CHARACTERIZING THE MARTENSITIC TRANSFORMATION IN A 10% NICKEL STEEL DURING DYNAMIC DEFORMATION USING *IN SITU* X-RAY DIFFRACTION

by

Paul Keslar Lambert

A dissertation submitted to The Johns Hopkins University in conformity with the requirements for the degree of Doctor of Philosophy.

Baltimore, Maryland

March, 2017

Abstract

Deformation-induced martensitic transformation (DIMT) is recognized in the steel industry as a deformation mechanism which can delay the onset of necking and fracture in steels containing metastable austenite. This transformation has recently been identified in an experimental steel containing 10 wt.% nickel (Ni) in the quenched, lamellarized, and tempered (QLT) heat treated condition. This steel is unusual in that it exhibits both superior strength and superior ballistic resistance. Understanding the surprising properties of this alloy requires a deeper understanding of the properties of the martensitic transformation of this steel during both low- and high-strain-rate deformation. We have endeavored to gain this understanding through the use of x-ray diffraction and several other characterization methods.

The first part of this investigation involves the development of a novel technique which allows for the simultaneous collection of quantitative information about both the bulk flow stress of a material, and information about a variety of microstructural features of the material as its microstructure evolves at high strain rates by synchronizing a compression Kolsky bar with time-resolved x-ray diffraction. We

demonstrate the technique's ability to measure elastic lattice strains, texture evolution, and phase volume fractions *in situ*. Comparisons to *ex situ* measurements are also made where appropriate, including a comparison of the *in situ* and *ex situ* measurement of austenite volume fraction present in 10% Ni steel during dynamic deformation.

In the second part of this investigation we use this technique and several complementary characterization tools to study the austenite transformation rate in 10% Ni steel in three different heat-treated conditions during dynamic compression. It was found that much more austenite transformed in the QLT-treated condition over a larger range of strain compared with the other two heat-treated conditions, which may help explain the QLT-treated alloy's excellent ballistic resistance.

Next, we further investigated the microstructural evolution of QLT-treated 10% Ni steel during low- and high-strain-rate compression. The strain-rate-dependent transformation behavior was found to differ from what other researchers have observed in some more common structural steels. This transformation behavior can be explained in the context of different subsets of austenite particles within the same material: larger particles which are transforming by both strain-induced martensitic transformation (SIMT) and stress-assisted martensitic transformation (SAMT), and ultrafine particles which are transforming primarily by SAMT.

Finally, we again utilize the *in situ* diffraction technique to investigate the evolution of phase-specific lattice strains in QLT-treated 10% Ni steel. While this mea-

surement provides some evidence of strain hardening in the steel's ferrite/martensite matrix at high strains, we find no evidence of strain hardening in the austenite phase. This may be attributable to the small size and high stacking fault energy of the austenite particles.

Primary Reader: Professor Todd Hufnagel

Secondary Reader: Professor Evan Ma

Acknowledgments

First and foremost I would like to extend my sincere thanks to my family, friends, and loved ones for their kindness and support. To my parents: thank you for always encouraging me and for teaching me the value of hard work and persistence. To Kevin and Megan: thank you for always being there for me and lifting my spirits, and for the numerous fresh chicken eggs. To Jen: I am sure I could not have successfully weathered the difficulties and uncertainties of graduate school without you by my side. You have made the hard times easier and the good times much more joyful. Thank you, and I look forward to our next adventure.

I would also like to thank my advisor, Professor Todd Hufnagel. For his skillful instruction on all aspects of crystallography and x-ray science, for his patience and guidance over these five years of study, and for his generosity in letting me use valuable beamtime on numerous synchrotron runs to complete this project, I owe him a debt of gratitude. Thank you also to the rest of my dissertation committee - Professors Tim Weihs, Evan Ma, and K.T. Ramesh, as well as Dr. Xian Jie Zhang - for the advice and guidance during this project. A special thanks goes to Jie, who devoted

countless hours to helping improve my knowledge of ferrous metallurgy, and who put his trust in me to continue his excellent work on this fascinating subject matter.

I certainly could not have gotten through graduate school with my sanity without the help and (more importantly) the friendship of the other members of my lab, both past and present. I am especially grateful to Caleb Hustedt, Mantong Zhao, Felicitee Kertis, Andrew Leong, Yonghao Sun, Ravi Shivaraman, and David Lee. Vignesh Kannan and Andrew Robinson of Professor K.T. Ramesh's lab are also gratefully acknowledged. A very special thanks goes to Eli Hustedt for sharing his apple juice.

The staff and other members of the Department of Materials Science and Engineering have done a wonderful job of making me feel like part of an academic family while at Johns Hopkins. To Marge Weaver, Dot Reagle, Ada Simari, Jeanine Majewski, Bryan Crawford, and all other department staff: thank you all for your time and assistance. To Darius Alix-Williams and Erin Gallagher: thank you for listening to me complain over coffee.

I am grateful that I have gotten to spend many months working with scientists and engineers at the Naval Surface Warfare Center, Carderock Division both during my studies at Johns Hopkins and before that as an NREIP intern. I would especially like to thank Nick Jones, Jim Restorff, Marilyn Wun-Fogle, Chuck Roe, Jin Yoo, Kristl Hathaway, and Art Clark for their instruction, mentoring, and encouragement. I am also grateful to the help provided by the scientists and engineers at the Army Research Laboratory over the course of this work, especially Dan Casem and Brian

Schuster. I would further like to thank Ken Vecchio and Emily Retzlaff (née Huskins) for their invaluable help with early synchrotron experiments.

Thomas Gnäupel-Herold of NIST is gratefully acknowledged for conducting the diffraction elastic constant measurements reported in Chapter 5. The beamline scientists at APS Sector 1, CHESS Hutch G3, and APS Sector 35 (DCS) are also acknowledged for their many hours of help with the *in situ* diffraction experiments.

Finally, I am extremely grateful to the funding agencies which have allowed me to complete my degree and to work on this fascinating subject matter. My time at Johns Hopkins was funded by the Department of Defense's Science, Mathematics & Research for Transformation (SMART) Scholarship Program and OSD-T&E (Office of Secretary Defense-Test and Evaluation), Defense-Wide / PE0601120D8Z National Defense Education Program (NDEP) / BA-1, Basic Research. This publication is based upon work performed at the Dynamic Compression Sector supported by the Department of Energy, National Nuclear Security Administration, under Award Number DE-NA0002442 and operated by Washington State University. This research used resources of the Advanced Photon Source, a U.S. Department of Energy (DOE) Office of Science User Facility operated for the DOE Office of Science by Argonne National Laboratory under Contract No. DE-AC02-06CH11357. This work is based upon research conducted at the Cornell High Energy Synchrotron Source (CHESS) which is supported by the National Science Foundation and the National Institutes of Health/National Institute of General Medical Sciences under NSF award DMR-

ACKNOWLEDGMENTS

1332208. Portions of this work were also funded by the Office of Naval Research, Code 332, thanks to Drs. William Mullins and Julie Christodoulou.

Dedication

This thesis is dedicated to Mr. Klingner.

Contents

List of Tables

List of Figures

Chapter 1

Introduction

Steel has been a technologically important material for centuries because of its range of desirable mechanical properties. From ancient tools and weaponry to modern automobiles and skyscrapers, steel has been prized for its strength, toughness, and wide availability. Although other impressive structural materials have been developed since the invention of steel, the excellent mechanical properties and relatively low production costs achievable with steels make them remain the material of choice in many structural applications today. "Steel" is also a broad term that can refer to a wide range of alloys, including those that are remarkable in an absolute sense. For example, a steel was recently developed that surpasses titanium alloys in specific strength and ductility [12].

As evidenced by the recent appearance of Reference [12] in a high-impact scientific journal, exciting breakthroughs in the mechanical properties of steel are still being

made today, despite its long history. These breakthroughs are made by gaining an ever-increasing understanding of the deformation mechanisms acting in the material and how to delay and/or exploit the evolution of these deformation mechanisms in order to delay yielding, necking, and/or fracture. One of the deformation mechanisms possible in steel is the martensitic transformation. This transformation has received a tremendous amount of research attention recently (again, despite its long history of acknowledgement in the literature) because of mounting evidence of its effectiveness at delaying necking and fracture. The transformation is influenced by a large number of variables, including those listed in section 1.3 and possibly others. This complexity explains the amount of time and research efforts which have been required to gain even our current, incomplete control over the transformation process. That knowledge has led to the development of various TRansformation-Induced Plasticity (TRIP) steels, TRIP-maraging steels, advanced austenitic stainless steels, nickel (Ni)-based cryogenic steels, and other advanced high-strength steels which are designed to exploit some form of deformation-induced martensitic transformation (DIMT). The first part of this chapter will introduce the necessary concepts needed to understand the martensitic transformation as it applies to steels generally.

The second part of this chapter will address the motivation for this dissertation: an experimental 10% Ni steel containing various carbide-forming elements and processed using a quenching, lamellarization, and tempering (QLT) heat treatment process. This alloy was developed for ballistic resistance applications and also undergoes a form

of DIMT. This steel has exhibited a number of surprising properties including superior strength, ballistic resistance, and impact toughness. This 10% Ni steel is the material receiving primary attention in this dissertation. The reader will therefore require more background knowledge of this material than of the other materials discussed in Chapter 2, which were tested to demonstrate the capabilities of a novel *in situ* x-ray diffraction technique we have developed during this work. Background information on this experimental steel will be discussed in the context of previous work done on other Ni steels. The concluding portion of this chapter will enumerate the aims of this dissertation.

1.1 Phases of steels

Although there are many possible non-equilibrium microconstituents of steel that are identified by specific morphological arrangement of two or more phases (*e.g.* bainite, pearlite) as well as numerous precipitates which can exist in steels, this section will focus on the three phases which will be most relevant later in this work. These phases are face-centered cubic (FCC) austenite, body-centered cubic (BCC) ferrite, and martensite which can be BCC or body-centered tetragonal (BCT) depending on its composition. Some important general characteristics of each phase will be discussed below.

1.1.1 Austenite

On the iron-carbon binary phase diagram, austenite (often identified as γ in shorthand) is only thermodynamically stable at high temperatures. The temperature above which austenite starts to form is referred to as the A_1 temperature (depicted in Figure 1.1 as blue), and at the temperature $A_3 > A_1$ (depicted in Figure 1.1 as red), austenite is the only stable phase, ignoring any carbides. (This distinction only applies for iron alloys; for pure iron, $A_1 = A_3$.) The addition of certain alloying elements can lower the temperature below which it become thermodynamically unfavorable for an iron crystal to remain FCC. Such "austenite-stabilizing" elements include Ni, carbon (C), manganese (Mn), cobalt (Co), and copper (Cu). Austenitic stainless steels contain so much of various austenite-stabilizing elements that virtually 100% of the material remains FCC even at room temperature. If cooled slightly below the A_3 temperature and held for extended time periods, some of the austenite will transform into ferrite via transformation mechanisms which involve diffusion. Any carbon that cannot remain dissolved in the ferrite will segregate to the austenite, and, if the temperature continues to drop slowly, the austenite will transform into ferrite and cementite (Fe_3C).

If, instead of being cooled slightly below A_3, the austenite is instead quenched rapidly below a characteristic M_s temperature (discussed in section 1.2), the carbon loses the driving force to diffuse out of the austenite and the austenite instead transforms by a diffusionless process into martensite.

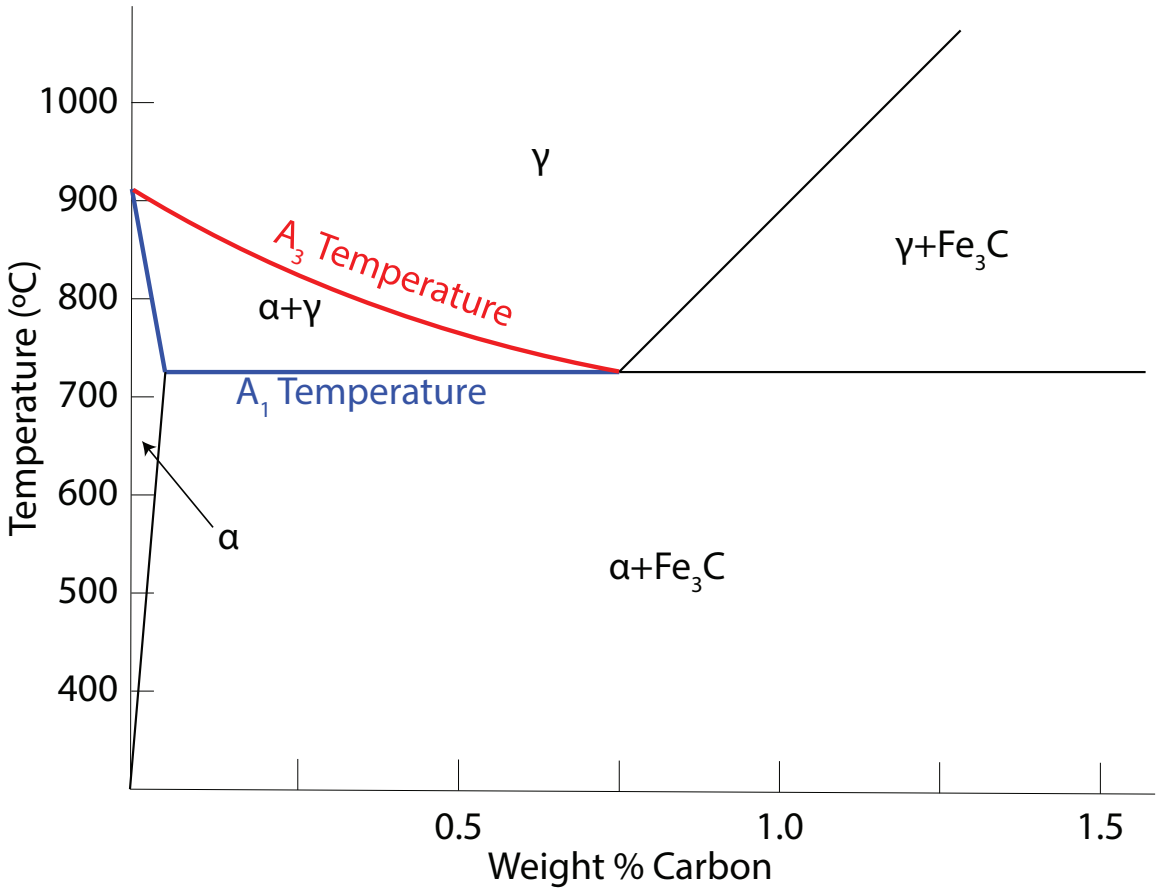

Figure 1.1: A schematic of the portion of the Fe-C phase diagram relevant to this dissertation. The phases depicted are austenite (γ), ferrite (α), and cementite (Fe_3C). The A_1 temperature line is shown in blue, and the A_3 temperature line is shown in red.

As an FCC crystal, austenite can normally undergo substantial strain hardening due to the ease of dislocation motion. The action of other deformation mechanisms will depend on the stacking fault energy (SFE) of the austenite. Austenite with higher SFE will tend to twin, whereas austenite with lower SFE will tend to form stacking faults [13]. Both twinning and stacking faults may in turn lead to strain-induced martensitic transformation (see section 1.2).

1.1.2 Ferrite

Ferrite (often identified as α in shorthand) is the thermodynamically stable phase at room temperature for iron-carbon alloys and many other steel compositions. Depending on its chemical composition and preexisting dislocation structure, it can be quite soft (in the case of mild steel, for example) or it can be significantly strengthened by carbides or other precipitates, as is the case for the 10% Ni steel discussed later in this work. The solubility of carbon in ferrite is extremely low because of the large mismatch between the size of a C atom and the interstitial site in the ferrite lattice.

1.1.3 Martensite

Martensite (or more specifically, α' martensite, as opposed to the hexagonally close-packed ϵ martensite which has little relevance later in this work) forms when

austenite grains are cooled below a characteristic M_s temperature and undergo a displacive transformation before carbon atoms in the austenite can diffuse away from their occupied sites. Martensite is a metastable phase, but practically speaking exists for a very long time at room temperature in the steels where it appears.

The aspect ratio of the martensite unit cell is either equal to or very close to 1 (depending on the carbon content), and the lattice parameters of ferrite and martensite are extremely similar, so ferrite and martensite can be extremely difficult to distinguish based on interatomic distances. The presence of interstitial carbon in the martensite unit cell may distort it from cubic to tetragonal if the carbon content is sufficiently high. Martensite also tends to be highly dislocated because of the strains associated with the martensitic transformation, so fresh (*i.e.* un-tempered) martensite is generally quite hard with little ductility. Some characteristics of martensite, which stem from the specifics of its formation, will be elaborated upon in section 1.2.

1.2 Martensitic transformation

Although the term is used in several material systems, in the context of steel a "martensitic transformation" is the fast, diffusionless transformation from the austenite phase to the martensite phase. This rapid transformation is possible due to the similarity of atomic positions in the austenite and martensite phases.

This crystallographic similarity can be visualized using the concept of a "Bain

strain," in which the FCC unit cell is compressed along one axis (the "Bain axis") and extended along the other two axes to reveal a BCC unit cell, as illustrated in Figure 1.2 [3, 14]. The Bain strain concept is simplistic, and the austenite unit cell does not necessarily transform to the martensite unit cell simply by undergoing this Bain strain in a straightforward manner. Nevertheless, there is an orientation relationship associated with the transformation which is usually very close to what is implied by the Bain strain. The most frequently observed orientation relationship is the Kurdjumov-Sachs (K-S) relation, which identifies the parallel planes:

$$\{111\}_\gamma \parallel \{110\}_{\alpha'} \tag{1.1}$$

and the parallel directions:

$$[110]_\gamma \parallel [111]_{\alpha'} \tag{1.2}$$

between parent austenite and daughter martensite. This habit plane, and the symmetry of FCC and BCC crystals, means that there are 24 possible variants of martensite that can form in a single austenite grain.

This transformation can be initiated either purely due to a thermal driving force, or through a combination of thermal and mechanical driving forces. When a steel is cooled below a characteristic temperature, M_s (determined by the local composition of the austenite grains in the material), there is enough of a free energy difference

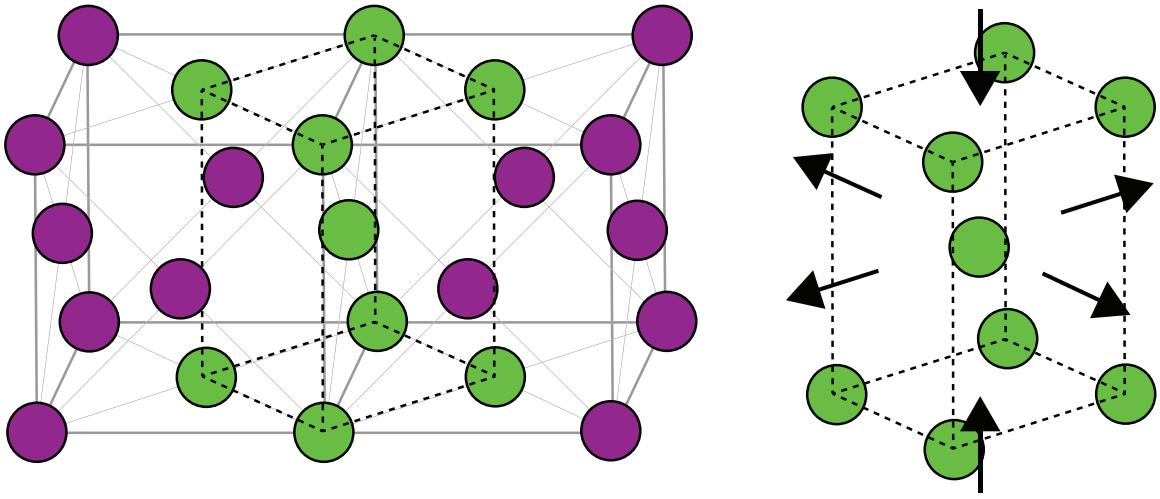

Figure 1.2: An illustration of the concept of Bain strain. The FCC unit cells (in magenta) are compressed along one axis (the Bain axis) and extended along the other two to form a BCC unit cell (in green). The necessary strains for this transformation are illustrated on the strained BCC unit cell on the right. Adapted from Ref. [3].

between the martensite and austenite phases to induce a spontaneous phase transformation. Transformation of a single austenite grain into a single martensite variant would cause a dramatic change in shape of the grain, as most steel compositions lead to $\sim 5\%$ normal expansion and $\sim 20\%$ shear strain when the austenite unit cell is transformed to the martensite unit cell [15]. Therefore, under stress-free circumstances, all 24 variants of daughter martensite occur within a parent austenite grain so as to minimize macroscopic shape change (at least in Ni steels, which is the class of steel focused on here) [3]. These daughter martensite variants will tend to form with a "packet," "block," and "lath" structure. At the largest scale, the region of the material formerly occupied by a parent austenite grain (a "prior austenite grain") will be divided into different martensite regions which have parallel $\{110\}_{\alpha'}$ planes

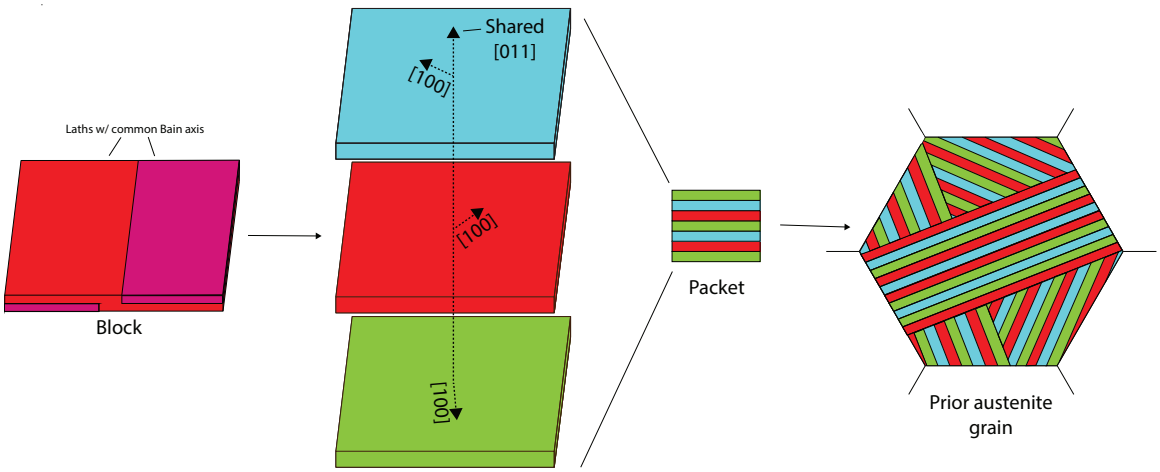

Figure 1.3: An illustration of the prior austenite grain, packet, block, and lath hierarchical structure which develops in martensitic steels such as quenched 9% Ni steels. Adapted from Ref. [3].

corresponding to one of the four crystallographically distinct $\{111\}_\gamma$ planes in the prior austenite grain. These regions are known as "packets." Each packet contains at least three "blocks" which has one of the possible Bain axes for that packet. Each block in turn contains two orientations of "laths" which are crystallographically twins of one another [3]. This hierarchical structure is illustrated in Figure 1.3. Thermally-induced martensite will generally nucleate along austenite grain boundaries, since the alternative is often the kinetically-unfavorable homogeneous nucleation inside an austenite grain [16].

As stated above, the martensitic transformation can also result from a combination of thermal as well as mechanical driving forces. If stress is applied to an austenitic material slightly above its M_s temperature, the elastic energy due to the lattice strain effectively adds to the chemical energy difference between the austenite

and martensite phases [17]. In this way, the activation energy for transformation can be reached and "stress-assisted" martensitic transformation (SAMT) can occur. This transformation generally begins at the same sites (along austenite grain boundaries) where purely thermally-driven transformations would have taken place at lower temperatures. The more the ambient temperature exceeds the M_s temperature for the austenite grain in question, the more stress must be applied to induce transformation. At a high enough temperature (dubbed M_s^σ), the stress required to cause transformation exceeds the yield strength of the parent austenite. In this case, plastic deformation in the austenite occurs in the austenite before transformation, but "strain-induced" martensitic transformation (SIMT) can still occur. This type of transformation differs from SAMT in terms of where martensite nucleations occurs. Instead of nucleating along grain boundaries, SIMT-created martensite tends to nucleate at the intersections of "shear bands" (which, in the steel literature, refers collectively to stacking faults, twins, and ϵ martensite formed within an austenite grain during deformation). A mechanism for nucleation at these sites was proposed by Olson and Cohen [11,18–20]. In addition to having differing martensite nucleation sites, SAMT and SIMT have other important differences which will be discussed later.

1.3 A (possibly incomplete) list of factors influencing DIMT

There are a wide variety of factors which influence the likelihood that an individual austenite grain will begin transforming to martensite, including:

- The amount of accumulated plastic strain: increasing the number of shear bands in the austenite grain will increase the average number of shear band intersections, which will create more favorable nucleation sights for martensite due to SIMT.

- The applied stress state: early studies of martensitic transformation [21] led to the conclusion that shear stress promotes the transformation process. Later, elastic bending experiments on austenitic steel [22] revealed that tensile stress promotes transformation of austenite more aggressively than compressive stress. In these experiments, the magnitudes of the normal and shear stress components were equal in both the tensile and compressive regions of the bent specimen, and the large number of possible habit planes for transformation made the sign of the shear stress essentially irrelevant, so it was made clear that normal stresses also influence the transformation. This was further demonstrated with hydrostatic compression experiments in which there is zero shear strain. This hydrostatic stress suppressed transformation [17]. These behaviors can be intuited based

on the stress state's aid or hindrance of the material expansion which occurs during transformation. (Daughter martensite is $\sim 6\%$ less dense than its parent austenite.)

- The local temperature: as explained above, higher ambient temperatures inhibit transformation of austenite into martensite. This is true at a local level as well, which is important to consider because adiabatic heat can cause local temperature rise in a material undergoing high-strain-rate deformation. In fact, within adiabatic shear bands, temperatures can rise so high that initially martensitic steel may reaustenitize within the band [23].

- The local composition: as explained above, certain chemical elements act as stabilizers for the austenite phase, lowering the austenite grain's M_s temperature. Chemical composition can be quite inhomogeneous within a steel and even within individual grains [24, 25], meaning that individual grains may be more or less chemically stabilized against transformation.

- The crystallographic orientation of the grain relative to the applied stress: the resolved shear stress on austenite grains with different orientations will change the likelihood of that grain to undergo slip and twinning, which will in turn have an effect on the probability of transformation [26].

- The grain size: larger austenite grains tend to transform with less accumulated plastic strain than smaller austenite grains. This has been attributed to a

larger work per unit volume needed to create martensite interfaces in smaller austenite grains [27]. In addition, shear bands are often confined to a single grain, so larger grains are more likely to form shear bands which intersect at some point within the grain to form a favorable martensite nucleation site.

- The neighboring microconstituents: it is possible for the grains surrounding a particular austenite grain to be beneficial or detrimental to the stabilization of that austenite grain against transformation. Stiffer and stronger phases (or even grains which are crystallographically oriented to be stiffer or less likely to undergo slip) surrounding an austenite grain can effectively "shield" that grain from transformation-inducing stress and strain [28]. At the same time, it has also been shown that interaction stresses between neighboring grains can promote plastic deformation in some alloy systems [29], and it is conceivable that this could occur in some steel microstructures as well.

Collectively, DIMT is recognized as assisting in the delay of both necking and fracture [30]. The rate of transformation as a function of strain (the "transformation kinetics") will affect how a material is likely to fail. Steels containing austenite which transforms rapidly as a function of strain (*i.e.* which has a low mechanical stability) may be susceptible to localized necking. Austenite which transforms less rapidly as a function of strain (*i.e.* which has a high mechanical stability) will not allow for the strain hardening needed to avoid more diffuse necking [30]. Therefore, in many cases the optimum DIMT-assisted microstructure will contain austenite of intermediate

stability, or different subsets of austenite having a spectrum of stabilities [31].

1.4 Previous work on Ni steels

Fe-Ni and Fe-Ni-C alloys, and Ni steels (*i.e.* a steel where Ni is the primary alloying element) have been the subject of research for decades [15, 17, 23, 25, 32–51]. Some of this research was quasi-fundamental in nature and led to improvements in the understanding of martensitic transformations in the steel community generally [3, 15, 17, 32]. A large amount of this research has also focused more practically on the impact toughness of these alloys, especially at low temperatures, and the processing required to optimize this impact performance [25, 37, 38, 40, 41, 48, 49]. This research has led to substantial use of 9% Ni steel today in stuctural applications where cryogenic temperatures are involved, such as in the storage and transportation of liquid nitrogen or liquid natural gas [52].

It is generally acknowledged in this research that the impact toughness and other mechanical properties of these steels are strongly influenced by the volume fraction, composition, and morphology of austenite particles within the steel. In the as-quenched condition, Ni steels contain very little austenite unless the steel contains large amounts of Ni and C. The fully-austenitic Fe-Ni-C alloys studied by Bolling and Richman [32], for example, all contained at least 15.9 wt.% Ni and, in most cases, more that 0.2 wt.% C. The fully-austenitic alloys they studied containing 0.11 wt.% C

or less contained at least 28.5 wt.% Ni. These alloys are undesirable from a practical perspective, because Ni is much more expensive than Fe and because large amounts of C can negatively impact ductility and weldability. Significant volume fractions of austenite can be created in alloys with lower Ni and C content through appropriate heat treatment, however. This has often been accomplished with a quenching and tempering (QT) process. The quenching step, which might more informatively be called a homogenization step, involves heating the material to high temperatures where austenite is the only thermodynamically stable phase, holding for some period of time (often $\sim$ 1 hour), and quenching in water. This partially homogenizes the material's chemical composition (although important inhomogeneities remain, as will be discussed later) and creates a final microstructure that is almost entirely fresh martensite. Varying the quenching step's time and temperature leads to different prior austenite grain sizes, which will in turn have some effect on the size of the martensite laths formed at the conclusion of the quenching step.

The tempering step is conducted in the two-phase coexistence region of the phase diagram (the "$\alpha+\gamma$" region of Figure 1.4). This partitions Ni and other stabilizing elements to regions of the microstructure (generally at prior austenite grain boundaries, packet and lath boundaries) where austenite particles form through processes involving diffusion. The tempering step is often also concluded with a water quench. This causes much of the austenite which existed during the tempering step to transform (in a diffusionless process) to fresh martensite within the tempered martensite/ferrite

matrix. Some of the austenite particles, however, have had enough stabilizing elements partitioned to them that they are "thermally stable" against transformation at room temperature. (The tempering step is not long enough for the material to reach thermodynamic equilibrium, so the composition of austenite is not the same everywhere in the microtructure.) The tempering time and temperature will determine the volume fraction of austenite at room temperature, as well as its propensity to resist DIMT (*i.e.* its "mechanical stability").

Some steel manufacturers have been introducing a third heat treatment step between quenching and tempering known as lamellarization [25, 34, 38, 46]. This intermediate step is done at higher temperatures within the two-phase coexistence region, where thermodynamically less Ni will be partitioned to the austenite phase but where kinetically the partitioning will happen more rapidly due to the added thermal energy. (The microstructure at the conclusion of the L process often also has a more pronounced "lamellar" structure compared with that of a QT-treated steel, which forms blockier austenite grains.) This 3-stage QLT process can produce larger volume fractions of thermally-stable austenite in less time compared with QT treatments, and can cause further improvements in impact toughness at cryogenic temperatures.

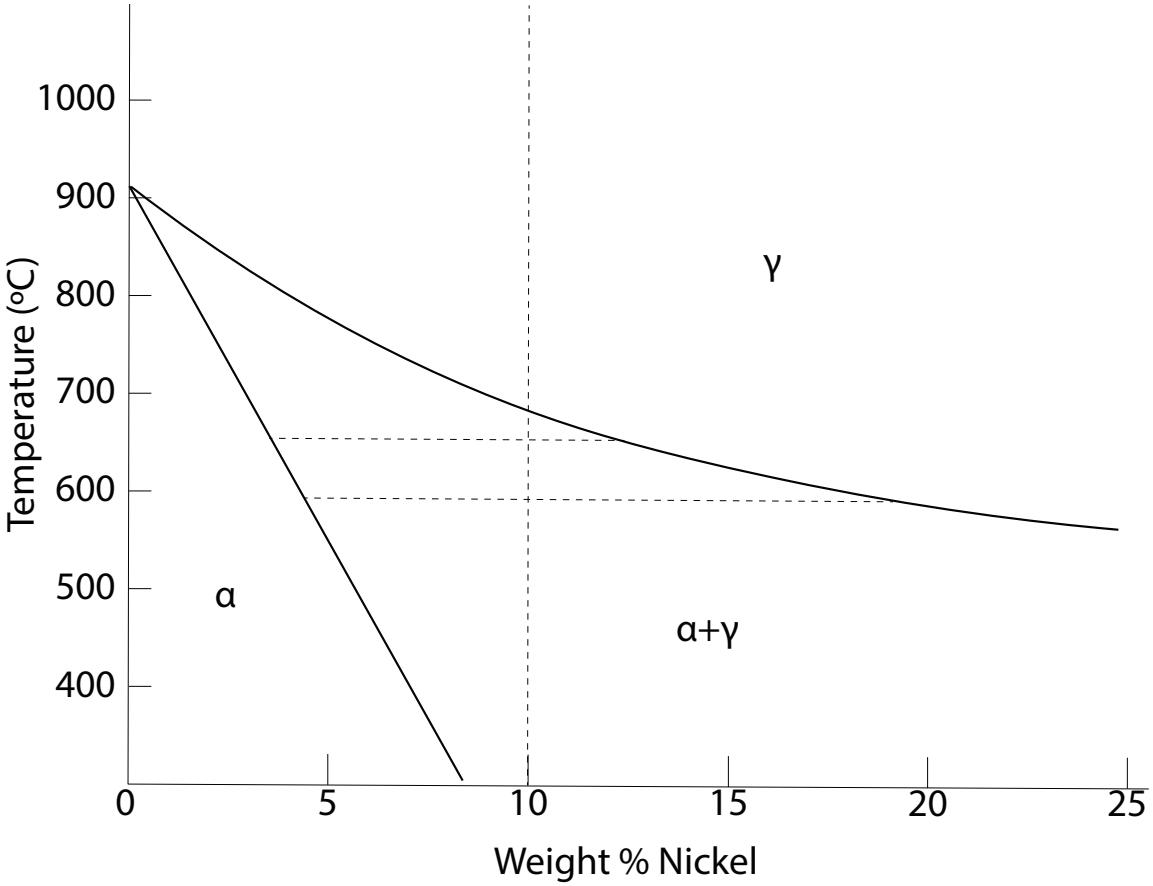

Figure 1.4: A schematic of the portion of the Fe-Ni phase diagram relevant to this dissertation. The phases depicted are austenite (γ) and ferrite (α). The dashed vertical line represents the bulk composition of the 10% Ni steel which is the material receiving primary attention in this work. The horizontal dashed lines are tie lines indicating the approximate compositions (at equilibrium) of austenite and ferrite formed during the heat treatments discussed in Chapter 2.

1.5 Project motivation: surprising high ballistic resistance of QLT-treated 10% Ni steel

Recently, this QLT process proved surprisingly effective at improving the ballistic resistance of an experimental 10% Ni steel [1]. Some of these results are shown in Figure 1.5. An experimentally-optimized heat treatment process for this steel led to improvements of over 10% in both strength and resistance to failure by ballistic impact in a 20 mm fragment simulating projectile (FSP) V_{50} test [53] compared with HSLA-100, a steel commonly used in naval structural applications. This FSP test involves blunt nosed-projectiles such as those pictured in Figure 1.6. The projectiles are fired at various velocities from a fixed distance at a plate of the test material. The resistance of the material to ballistic penetration is quantified as the V_{50} value, which is the average of five slowest velocities at which the projectile achieves complete penetration of the target and the five fastest velocities at which the projectile does not completely penetrate the target. The simultaneous improvements in strength and V_{50} value seen here could not be achieved in steels with lower Ni content, or in 10% Ni steels receiving a wide range of two-stage heat treatments.

The fact that the QLT-treated 10% Ni steel displayed superior ballistic resistance (having 115% of the V_{50} value of the baseline HSLA-100 steel) while maintaining

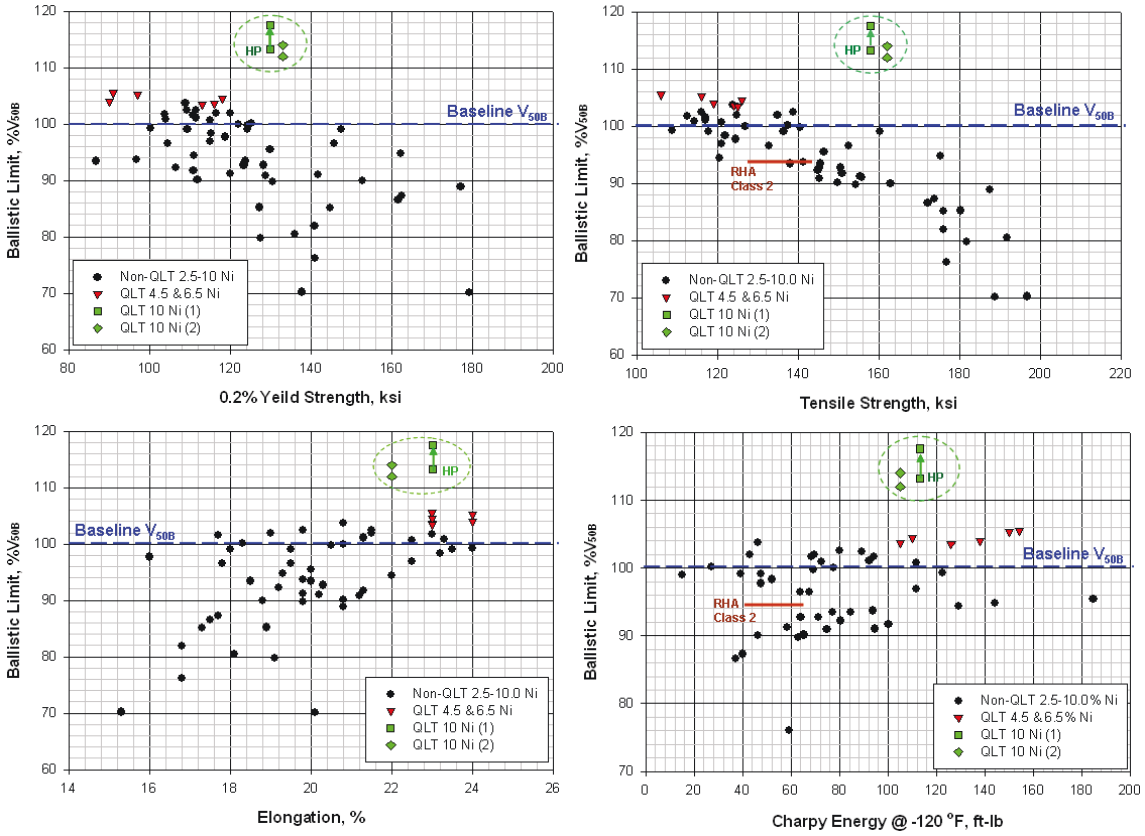

Figure 1.5: Ballistic resistance of various 2.5-10% Ni steels, including a 10% Ni steel with an experimentally optimized QLT heat treatment, plotted against (clockwise from top left) yield strength, ultimate tensile strength, Charpy impact energy at cryogenic temperatures, and tensile elongation. Adapted from Ref. [1]. *Image courtesy of Dr. X.J. Zhang.*

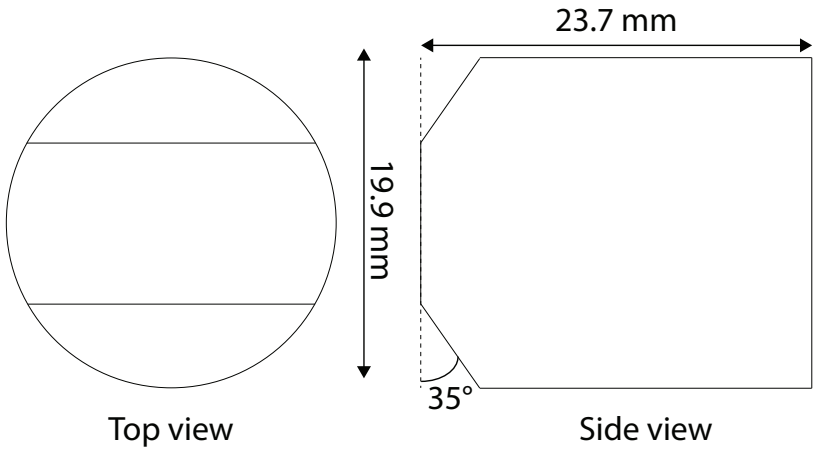

Figure 1.6: Schematic illustration of a fragment simulating projectile (FSP). Dimensions are approximate. Adapted from Ref. [4].

high yield and tensile strengths was particularly surprising, because this overcame the negative correlation between strength and ballistic resistance seen in most other materials (see Figure 1.5). Furthermore, analysis of the ballistic craters made during these V_{50} tests revealed that the QLT-treated 10% Ni steel had a decreased tendency to fail by plugging (*i.e.* the formation of adiabatic shear bands). Figure 1.7 serves as an example. It shows microhardness maps of craters from two ballistic plates. The left plate was a QL-treated 10% Ni steel plate, while the right plate was the experimentally-optimized QLT-treated 10% Ni steel plate. Both plates had nearly identical hardness in the as-heat-treated condition (332 H_v and 330 H_v, respectively). Both craters shown in Figure 1.7 were created at the respective plate's V_{50} velocity, which was approximately 30% higher in the QLT-treated plate than in the QL-treated plate. Two things are evident from the figure. First, the QL-treated plate formed an adiabatic shear band during impact, while the QLT-treated plate did not, de-

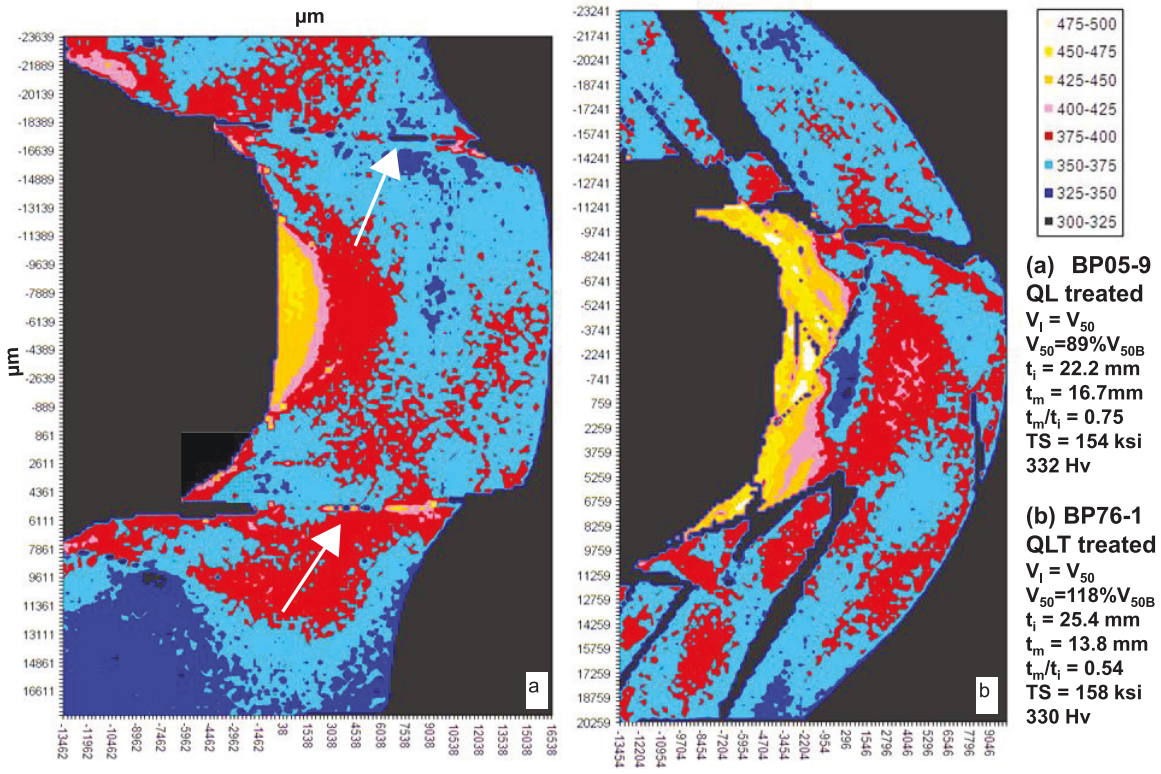

Figure 1.7: Microhardness maps of ballistic craters formed in (left) a 10% Ni steel having undergone a QL heat treatment, and (right) the same steel having undergone an experimentally optimized QLT heat treatment. The craters were produced using projectile moving at the V_{50} velocity of each plate, which was 30% higher in the QLT plate compared with the QL plate. The arrows indicate adiabatic shear bands. Adapted from Ref. [1]. *Image courtesy of Dr. X.J. Zhang.*

spite being impacted with a projectile moving 30% faster. Second, there is a much larger area of increased hardness in the QLT-treated crater. This suggests a larger amount of global plastic deformation occurring in this plate. This heightened ability to harden homogeneously, even under high-strain-rate loading, is another very desirable property of the QLT-treated 10% Ni steel.

There is substantial evidence that a primary mechanism behind the QLT-treated

10% Ni steel's desirable mechanical properties is some form of DIMT. For example, measurements of the volume fraction of austenite present in the steel reveal that the volume fraction drops after being deformed in various ways (see Table 1.1). As discussed previously, there is a large body of research linking DIMT to delaying necking and fracture in steels in general, and it is also recognized as a primary factor in the low-temperature impact toughness of Ni steels specifically. Nevertheless, DIMT acting in ballistic loading remains somewhat surprising, as impact loading has been observed to suppress martensitic transformation in TRIP steels [54]. In addition, there are currently few published works which discuss this experimental steel [1,23,24], especially those which consider deformation of the steel in its QLT-treated condition [1]. As such, the quantitative assessment of DIMT in this experimental alloy has been quite limited thus far, consisting mainly of before-and-after comparisons done on ballistic plates or fractured tensile specimens. These measurements shed no light on the kinetics of transformation (*i.e.* the austenite volume fraction as a function of strain).

QLT-treated Steel Condition	vol.%A (VSM)
Undeformed	19.0*
Fractured tensile specimen (uniform elongation region)	9.5*
Fractured tensile specimen (necked region)	4.5
FSP ballistic crater	0.03*

Table 1.1: Average vol.% of austenite present in 10% Ni steel specimens undergoing a QLT heat treatment process and various types of deformation. Measurements were made using vibrating sample magnetometry (VSM). Starred values are taken from Ref. [1].

Determining the design limits of this steel and creating similar steels with even better properties requires a more detailed understanding of the DIMT behavior in 10% Ni steel. This includes a baseline measurement of the current steel's transformation kinetics, as well as an understanding of what deformation mechanisms are acting and how the DIMT impacts the mechanical behavior of the material. That is the overarching objective of the present work. This objective was pursued in the following ways:

- Development of a technique for quantitative, time-resolved analysis of microstructure evolution in materials in real time during high-strain-rate deformation. This technique integrates Kolsky bar testing with x-ray diffraction at high-flux synchrotron sources (both of which will be described in the following chapter). This work, and a description of the other experimental methods employed in this dissertation, will be described in Chapter 2.

- Use of this technique to track the evolution of austenite volume fraction in 10% Ni specimens in the experimentally-optimized QLT heat treated condition. In addition, specimens heat treated with just the QL and just the QT portions of this experimentally-optimized QLT process were also tested. This was done to compare the dynamic compressive properties of each heat treatment with its ballistic resistance, and to possibly shed some light on how specific subsets of grains within the QLT-treated material behave under dynamic loading. This work will be described in Chapter 3.

- Analysis of the transformation kinetics of specific subsets of austenite particles within the QLT-treated microstructure as a function of strain rate. This analysis was intended to provide a deeper understanding of how the steel's microstructure is evolving during deformation, and also to provide insight into which deformation mechanisms are active in the austenite phase. This work will be described in Chapter 4.

- Use of the *in situ* diffraction technique developed above, as well as quasi-static loading with *in situ* neutron diffraction, to understand the evolution of lattice strain within each phase during deformation. A knowledge of the load partitioning between the constituent phases may help understand how deformation and defects accumulate in the material, and is valuable information for material modelers. This work will be described in Chapter 5.

Chapter 2

Experimental techniques

This chapter covers general procedures used in this investigation, including detailed descriptions of novel techniques developed during this investigation for *in situ* x-ray diffraction probing of a bulk metallic specimen undergoing high-strain-rate deformation. This chapter will describe the evolution of these *in situ* techniques, including (when appropriate) an explanation of lessons learned from the execution of each technique that may benefit future experimentalists. We will also summarize the advantages and disadvantages associated with each technique. Some of the techniques described here (especially *in situ* synchrotron techniques 1 and 2) were used to demonstrate the feasibility of the *in situ* experiment [55], but the materials examined using these techniques were not studied in more detail for this dissertation. However, the 10% Ni steel utilized in the most recently-developed *in situ* synchrotron technique (see Section 2.3.7) was also studied using a variety of other characterization

techniques. These other techniques are discussed throughout this chapter.

2.1 Specimen Preparation

2.1.1 Specimen preparation for synchrotron technique 1

The first technique we developed examined Monel®-400. This is a relatively well-characterized, single-phase Cu-Ni alloy which absorbs x-rays strongly due to its relatively high density. Monel®-400 specimens in the as-received state[1] were fabricated by electrical discharge machining (EDM) into $3 \times 3 \times 4$ mm (l/d ~ 1.3) rectangular prisms. The loading surfaces were polished using progressively finer grits of sand paper, down to a finishing step with 3 μm alumina particles.

2.1.2 Specimen preparation for synchrotron technique 2

The second technique we developed was used to examine the magnesium alloy AZ31 with a typical grain size of 3 μm produced by equal-channel angular extrusion[2]. We cut specimens from the extruded ingots by EDM and mechanically polished them

[1]Specimens were provided by Prof. Kenneth Vecchio.

[2]Caleb Hustedt is gratefully acknowledged as the experimentalist primarily responsible for the execution and data analysis of synchrotron technique 2.

into $\sim 0.6 \times 1 \times 1.5$ mm right rectangular prisms with loading surfaces polished to a finish of 5 μm. Specimens were loaded along the 1.5 mm direction and x-rays were transmitted through the 0.6 mm direction to minimize clipping of the x-ray beam by the bars and to maximize x-ray transmission, respectively.

2.1.3 Specimen preparation for synchrotron technique 3-1

The third technique we developed was used to examine undeformed specimens of the experimentally-optimized 10% Ni steel plates used in the ballistic resistance tests described in Chapter 1. The 10% Ni steel used here (and for the rest of this investigation) was formulated with the composition listed in Table 2.1. The steel was cast into a 227 kg ingot using vacuum induction melting by Mittal Steel USA. The ingots were hot rolled (also by Mittal Steel USA) from initial dimensions of $\sim$ 205 mm $\times$ 205 mm $\times$ 641 mm down to long plates that were 22 mm thick and 203 mm wide using a starting temperature of $\sim$ 1260 °C (2300 °F) and ending at 816 °C (1500 °F). These long plates were subsequently cut into 304.8 mm (12 in.) sections. This steel manufacturing process applies to all subsequent 10% Ni steel specimens described in this dissertation.

The experimentally-optimized QLT specimens (which had previously been heat treated in neutral salt baths) were EDM cut and polished into $\sim 0.65 \times 0.35 \times 0.9$ mm

Element	Fe	C	Ni	Mo	V	Mn	Cr
Nominal Composition (wt.%)	Balance	0.1	10.0	1.0	0.08	0.6	0.6

Table 2.1: Nominal composition of the 10% Ni steel which was studied using synchrotron techniques 3-1, 3-2, and 3-3, and which is the material given primary research attention in this work.

right rectangular prisms, with loading to be done along the 0.65 mm direction and with x-rays to be transmitted along the 0.35 mm direction. The loading surfaces were polished with progressively finer polishing papers, down to a finishing polish with 3 μm alumina particles.

2.1.4 Specimen preparation for synchrotron technique 3-2

The specimens tested using this technique were 10% Ni steel specimens in two different heat treatment conditions: the experimentally-optimized QLT condition, and a re-austenitized and quenched condition intended to contain little austenite. We cut specimens by EDM and mechanically polished them into $\sim 0.6\times0.3\times0.9$ mm right rectangular prisms using progressively finer polishing papers, with loading surfaces receiving a finishing polish with 3 μm alumina particles. Specimens were loaded along the 0.6 mm direction and x-rays were transmitted through the 0.3 mm direction.

2.1.5 Specimen preparation for synchrotron technique 3-3

10% Ni steel with the composition and manufacturing process described in Section 2.1.3 was studied using this technique. Instead of using previously-heat-treated specimens, we started with the as-hot-rolled material and heat treated it ourselves in three different conditions, described in Table 2.2. All specimens were heat treated in the same calibrated Ney Vulcan 3-1750 air furnace. Heat-treatment specimens had roughly the same volume and were all $\sim$ 12.5 mm thick in their smallest dimension. Each heat treatment was taken to begin when the specimen was inserted into the center of the pre-heated furnace and the temperature reported by the furnace returned to within 10 °C of the setpoint. At the conclusion of each heat treatment, the specimen was rapidly quenched into several gallons of room-temperature water and agitated until cool.

The steps of the QLT process we applied were very similar to the experimentally-optimized QLT heat treatment steps applied to the plates exhibiting superior ballistic resistance in Reference [1], but with slightly more time allotted for the specimens to warm up because we used an air furnace instead of a neutral salt bath. The QLT specimens were of primary interest, as they are the most representative of the steel microstructure which we seek to understand due to its excellent mechanical properties. The QL specimens were studied in hopes of understanding the stepwise microstruc-

tural evolution of the QLT-treated steel more completely. The QT specimens were prepared in an attempt to gain insight about the properties of specific subsets of grains within the QLT-treated microstructure which form during the T treatment. (Of course, no perfect comparison can be made between grains in the QT specimens and grains in the QLT specimens, because they have different thermal histories and steel microstructures are such a complicated product of heat treatment parameters as well as the pre-heat-treatment microstructure.)

Specimen Designation	790 °C 55 min. WQ (Water Quench)	650 °C 40 min. WQ	590 °C 70 min. WQ
"QL"	Step 1	Step 2	
"QT"	Step 1		Step 2
"QLT"	Step 1	Step 2	Step 3

Table 2.2: List of heat treatments applied to each group of specimens.

Heat treated specimens were then machined for mechanical testing using wire electrical discharge machining (EDM). Specimens were EDM cut so that they were connected together by a long "tab," making it easy to handle large numbers of very small specimens. Subsequently, they were glued to a South Bay Technology handheld lapping fixture designed for high parallelism of specimen surfaces and were mechanically ground and polished into $\sim 0.6 \times 0.4 \times 1.1$ mm right rectangular prisms. Polishing was done using 600 grit sandpaper lubricated with water (until the specimens were ~ 100 μm thicker than their desired dimensions), followed by 9μm Al_2O_3 particles lubricated with Struers DP-Lubricant Blue (until the specimens were a few tens of

microns thicker than their desired dimensions). The specimen loading surfaces and the surfaces with normals parallel to the incident x-ray beam were given a final polish with 3 μm Al_2O_3 particles. The "tab" was removed by sanding it away during the last polishing step, thus separating the individual specimens. The listed specimen dimensions corresponded with the rolling direction (RD), transverse direction (TD), and normal direction (ND) in the hot-rolled plate, respectively. After polishing, the specimens were examined along each each direction in an optical microscope, and any specimens more than $\sim 3^\circ$ out-of-square were discarded. Specimens were loaded along the 0.6 mm direction and x-rays were transmitted through the 0.4 mm direction. These specimen dimensions were chosen as a compromise between the competing experimental demands on the specimen, namely that the specimen thickness should be close to the absorption length (see Section 2.3.1.5), the volume of the specimen interrogated by the x-ray beam should contain enough grains for good powder averaging, and the specimen should have an aspect ratio which reduces the likelihood of buckling during the compression test.

2.1.6 Quasi-static compression specimen preparation

QLT heat-treated 10% Ni steel specimens prepared along with the specimens for synchrotron technique 3-3 were EDM cut into rectangular prisms with dimensions of

4.0 × 4.2 × 2.5 mm. These specimen dimensions correspond to the rolling direction (RD), normal direction (ND), and transverse direction (TD) in the as-rolled plate, respectively. Specimens were mechanically ground and polished to remove surface roughness. All compression specimen surfaces received a final polishing step with 3 μm Al_2O_3 particles.

2.1.7 Neutron diffraction specimen preparation

QLT heat-treated 10% Ni steel specimens prepared along with the specimens for synchrotron technique 3-3 were EDM cut into flat tensile testing specimens with dimensions of 120 mm (gage length) × 3 mm (thickness) × 10 mm (width). These specimen dimensions correspond to the rolling direction (RD), normal direction (ND), and transverse direction (TD) in the as-rolled plate, respectively. Specimens were mechanically ground and polished to remove surface roughness. The large flats of the specimen were polished using standard metallurgical polishing wheels and methods, with a final polishing step with 3 μm Al_2O_3 particles. The contoured sides of the specimen were polished using a Dremel 8220-1/28 cordless rotary tool and the sanding paper and polishing compound provided with that tool.

2.2 Mechanical Testing

2.2.1 Quasi-static compression testing

Specimens were compressed along the RD in an MTS Criterion™ model 43 mechanical load frame to pre-determined levels of strain[3]. Tests were conducted at a strain rate of 0.001 s^{-1}. The specimen faces in contact with the load frame were lubricated with lithium grease to minimize barreling.

2.2.2 Dynamic compression testing

Dynamic compression testing with a Kolsky bar apparatus was done in several slightly different ways throughout this work, due to the variety of materials and specimen sizes studied. Some of the specifics of the dynamic compression testing done with each synchrotron technique will be described in the context of that technique. However, here we will provide some specifics of the dynamic compression tests which apply to all our techniques, after first briefly explaining some important details of high-strain-rate mechanical testing in general.

[3]David Lee is gratefully acknowledged for the preparation and performance of these compression tests.

2.2.2.1 Fundamentals of high-strain-rate mechanical testing

Conventional servo-hydraulic load frames used for quasi-static mechanical testing generally cannot achieve strain rates higher than $\sim 10^1 - 10^2$ s^{-1} in a controlled manner. Achieving higher rates requires a different testing approach. One effective and well-developed way to reach these higher strain rates is to use a Kolsky bar (split Hopkinson pressure bar) apparatus [56], which is illustrated schematically in Figure 2.1. This technique works by introducing an elastic strain pulse into an "input" or "incident" bar by striking it with a projectile or "striker". This strain pulse propagates through the input bar and is partially transmitted into the specimen where, by careful experimental design, the specimen will be plastically deformed. Part of the incident strain pulse is reflected back into the input bar, and part of it is transmitted through the specimen and into an "output" or "transmitter" bar which is often the same material and diameter as the input bar.

The input and output bars are instrumented so that information about the waves propagating through the bars can be recorded as a function of time [5]. This is often accomplished with strain gauges, *i.e.* resistors firmly affixed to the bars which change resistance as they elastically deform along with the bars. Often, two strain gauges are affixed to each bar, on opposite sides of the bar so that any bending waves introduced into the bars are not reported in the final measurement[4]. The gauges are then connected to a Wheatstone bridge, such as the one seen in Figure 2.2, which

[4]Bending waves should be eliminated to the largest extent possible by properly aligning the apparatus, of course.

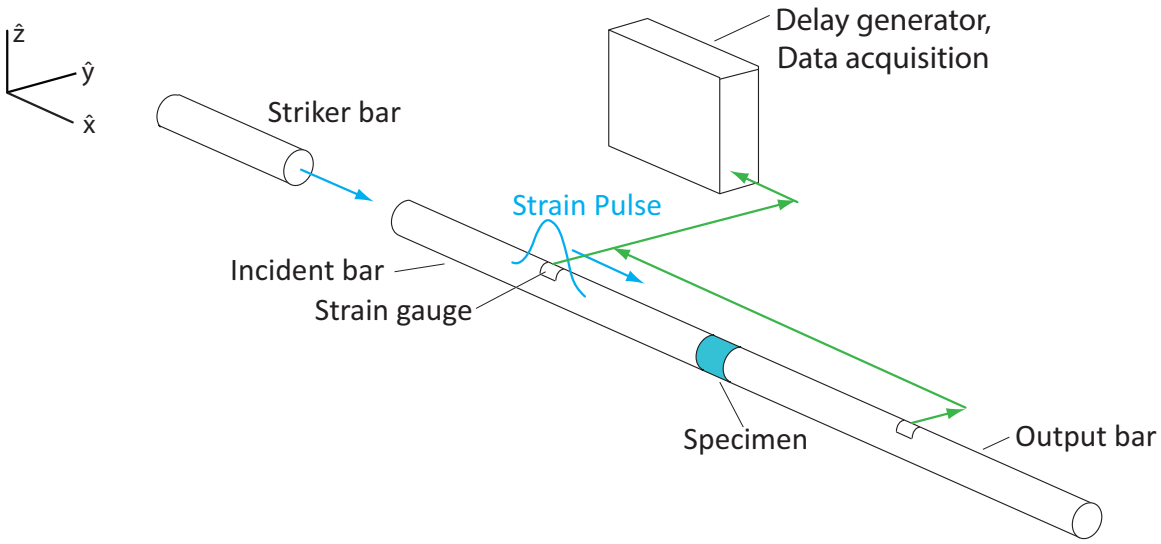

Figure 2.1: Schematic diagram of a Kolsky (split Hopkinson) bar apparatus.

allows for very accurate determination of changes in voltage and resistance. In the half-bridge configuration, the strain gauges are R_1 and R_4 in the diagram, and are balanced so that they have resistances identical to R_2 and R_3. The strains in the input and output bars can be determined from the observed change in voltage U_O from the Wheatstone bridge using the following equation:

$$\epsilon = \frac{2U_o}{G_F U_i} \tag{2.1}$$

where U_i is the applied excitation voltage and G_F is the gauge factor of the strain gauge being used [5].

As explained in Reference [5], stress and strain information about the specimen can be inferred from the measured strain from the input and output bars, as long as some prerequisite knowledge about the specimen and the bars can be applied. This

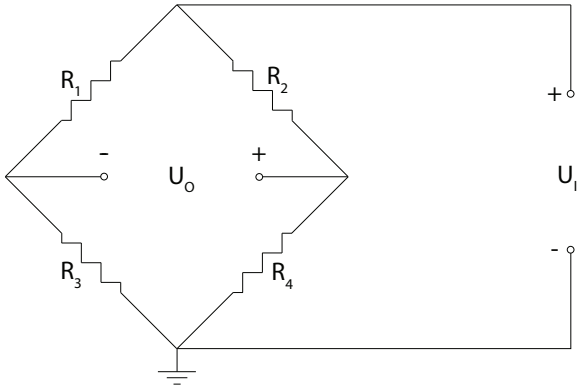

Figure 2.2: Diagram of a Wheatstone bridge. Adapted from Reference [5].

process assumes that one-dimensional elastic waves are propagating through the bars. The strain rate as a function of time $\dot{e}_s(t)$ experienced by the specimen during testing is:

$$\dot{e}_s(t) = -\frac{2c_b}{l_0}\epsilon_R(t) \tag{2.2}$$

where c_b is the speed of sound in the input and output bars, l_0 is the initial specimen length, and $\epsilon_R(t)$ is the strain as a function of time reported in the strain gauge of the input bar once the initial stress pulse has reflected off of the input bar-specimen boundary. The strain as a function of time $e_s(t)$ is then simply the integral of the strain rate from 0 (the arrival of the stress pulse at the specimen) to time t:

$$e_s(t) = \int_0^t \dot{e}_s(\tau)d\tau \tag{2.3}$$

The stress in the specimen as a function of time $s_s(t)$ is:

$$s_s(t) = \frac{E_b A_b}{A_s} \epsilon_T(t) \tag{2.4}$$

where E_b is the elastic modulus of the input and output bars, A_b is the cross-sectional area of the bars, A_s is the cross-sectional area of the specimen, and $\epsilon_T(t)$ is the strain as a function of time reported in the strain gauge of the output bar.

2.2.2.2 Dynamic compression testing procedures

Dynamic compression testing was done using several Kolsky bars provided courtesy of Prof. Kenneth Vecchio or Dr. Daniel Casem. With the exception of the experimental technique performed at Sector 1 of the Advanced Photon Source (technique 1, described below), data from the Kolsky bar strain gauges was collected using an HBM GEN3i data acquisition system. With the exception of sychrotron technique 1 performed at Sector 1 of the Advanced Photon Source, we used Kyowa KSP-2-1K-E4 1000-ohm semiconductor strain gauges to measure strain in the Kolsky bars. Foil strain gauges were employed for the Sector 1 technique. We utilized 8 mm maraging steel bars for sychrotron technique 1, 3 mm 7065-T6 aluminum bars for technique 2, and 4.8 mm high-strength steel bars for techniques 3-1, 3-2, and 3-3. Striker lengths and velocities were varied for each experiment based on the desired strain rate, which ranged from $\sim 1000 - 3000$ s^{-1}.

2.3 Time-resolved x-ray diffraction during dynamic compression

In the first part of this section, we will briefly explain some aspects of x-ray diffraction and synchrotron sources which are important to understand for the rest of this work. Then, we will explain the motivation for synchronizing time-resolved x-ray diffraction with dynamic loading. Next, we will provide a thorough description of several different experimental techniques we have employed to achieve this synchronization. Finally, we will summarize the positive and negative attributes of each technique for the experimentalist concerned with characterizing the microstructural evolution of different crystalline materials.

2.3.1 Important characteristics of x-ray diffraction and synchrotron sources

This section briefly summarizes a few aspects of x-ray diffraction and synchrotron sources which are essential to understanding the work described in this dissertation. Thorough elaboration on these and other topics of x-ray science can be found in References [57, 58].

2.3.1.1 Scattering vectors

When an incident x-ray plane wave with wave vector $\vec{k_0}$ ($\|\vec{k_0}\| = 2\pi/\lambda$, where λ is the x-ray wavelength) interacts with the atomic planes of a crystalline material, an elastically scattered wave $\vec{k}$ ($\|\vec{k}\| = \|\vec{k_0}\|$) will experience constructive interference if the crystal is oriented with respect to the incident wave vector such that it satisfies Bragg's law:

$$n\lambda = 2d\sin\theta \tag{2.5}$$

where d is the lattice spacing of the material. Figure 2.3 illustrates this concept. We can then define a scattering vector $\vec{q} = \vec{k} - \vec{k_0}$ ($\|\vec{q}\| = 4\pi\sin\theta/\lambda$). The information we can derive from the diffracted intensity on a detector formed by the wave vector $\vec{k}$ applies only to crystal planes whose plane normals are oriented parallel to $\vec{q}$. This concept is important to understanding specifically which subsets of planes within a material contribute to the diffraction data we collect for any given experimental geometry.

2.3.1.2 Generation of x-rays by synchrotron

Synchrotrons are large, circular particle accelerators. They circulate electrons and/or positrons, and the acceleration of these charged particles around the ring (achieved using "bending magnets") causes the emission of photons in a direction

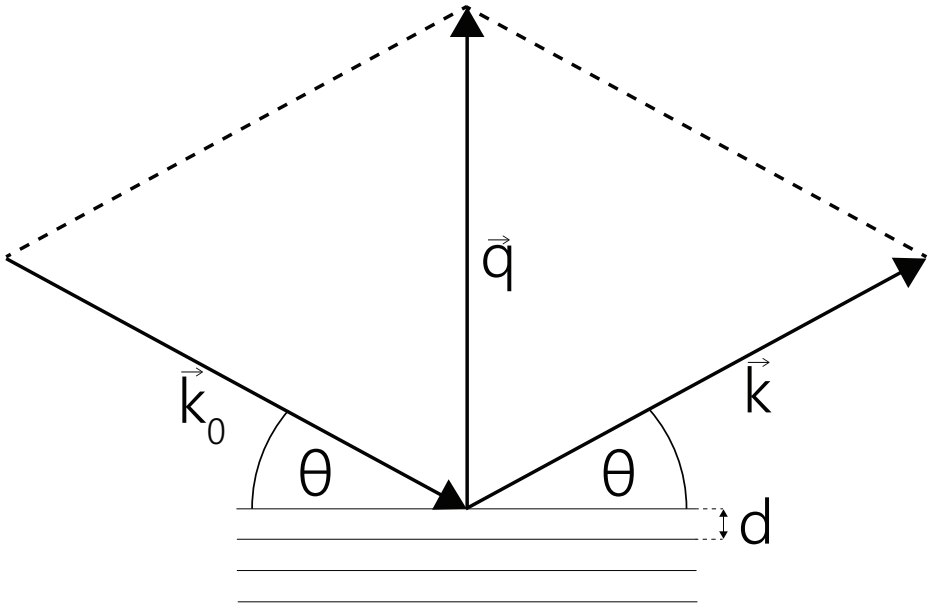

Figure 2.3: Illustration of the concept of a scattering vector relative to incident radiation, diffracted radiation, and the crystal planes causing the diffraction.

tangential to the particle storage ring. Synchrotrons can also contain straight portions of the storage ring where a collection of magnets (called "wigglers" and "undulators") accelerate the charged particles side-to-side, producing more photons. Experiment hutches are built downstream of these bending magnets, wigglers, and undulators so that the intense radiation can safely be directed onto a specimen of interest. These massive user facilities can generate x-ray streams with a wide range of characteristics, including spot sizes, brightness, and coherency which far exceed what laboratory x-ray sources can achieve.

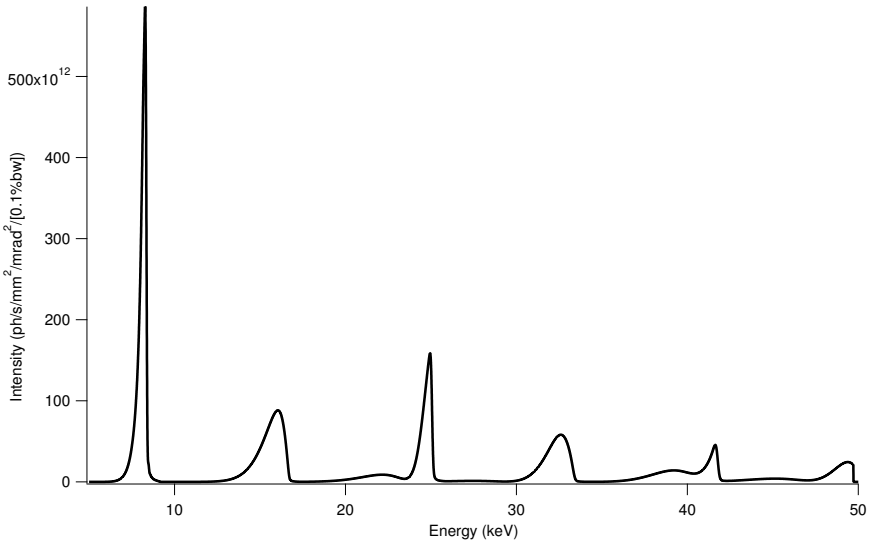

Figure 2.4: Example calculated x-ray output of a U30 undulator, calculated using the XOP software package [6]. Intensity information for the first six harmonics of the undulator can be seen here.

2.3.1.3 Synchrotron undulator energy spectra

A consequence of the way in which x-rays are produced in a synchrotron undulator is that, unlike in laboratory sources, there are higher harmonics of x-ray energies emitted in addition to the principal x-ray energy. These higher harmonics will be centered around energy values that are roughly integer multiples of the principal x-ray energy, although the harmonics will not all be produced with equal intensity. Instead, the intensity output of an undulator as a function of x-ray energy is often qualitatively similar to what is shown in Figure 2.4. This Figure portrays an undulator energy spectrum calculated using the XOP software [6] package and parameters associated with the U30 undulator at the Dynamic Compression Sector, Sector 35 of the Advanced Photon Source.

2.3.1.4 Bunch structure of synchrotron sources

An important feature of synchrotrons (which is especially important to bear in mind when doing experiments on short time scales) is the fact that they do not emit x-rays in a constant, continuous stream. Instead, they are emitted in short, isolated "bunches" associated with isolated groups of electrons travelling around the electron storage ring. The distribution of these bunches can be altered, but this affects every beamline at the synchrotron, so generally the bunch structure is held constant for several weeks. A particular beamline user has no say in the bunch structure being used during their experiment, although they can seek to obtain time at the synchrotron when the scheduled bunch structure best suits their experiment.

Examples of different bunch structures at the Advanced Photon Source (APS), for example, include "24 bunch mode," "324 bunch mode," and "1296 bunch mode." In these modes, the 102 mA of current stored in the storage ring is separated into 24, 324, or 1296 evenly spaced bunches, each of which contains an equal fraction of the total current. These bunches are usually tens of picoseconds in length and are separated in time by tens of nanoseconds. Other possible bunch structures involves dissimilar bunches. For example, "hybrid single mode" at APS involves one 16 mA bunch, followed by 8 groups of 7 bunches which each have much less current. Some important properties of the different operating modes at APS are summarized in Table 2.3 [2]. Other synchrotron facilities will generally have different operating modes as well.

Operating Mode	Bunch Current (mA)	RMS Bunch Duration (ps)	Bunch Separation (ns)
24 Bunch	4.25	33.5	153.4
324 Bunch	0.31	22	11.37
1296 Bunch	0.079	22	2.84
Hybrid Fill	16 (1 singlet) < 1.6 (8 septuplets)	50 (Singlet) 27 (septuplets)	1594 (around singlet) 51 (between septuplets)

Table 2.3: Some important properties of the different operating modes at the Advanced Photon Source. Information from Ref. [2].

The synchrotron operation mode can have important consequences for a high-strain-rate experiment. If the experiment duration and the desired diffraction pattern exposure duration are both ~ 1 μs or longer, then roughly the same number of photons will be recorded on the x-ray detector regardless of which mode is used. However, for very high-strain-rate Kolsky bar experiments and for even faster experiments such as gas gun or laser shock experiments, a mode with a high peak brightness (*i.e.* a large number of photons produced during a single bunch or over a similarly short time interval) must be selected. Examples of operation modes with high peak brightness are 24 bunch mode or hybrid fill mode at APS. Otherwise, very few (or zero) photons will be recorded on the x-ray detector during the very brief time it is collecting data. These modes have significant time gaps between bunches, which means it is important to synchronize detector gating with the "bunch clock" of the synchrotron to avoid collecting data while no x-rays are entering the experimental hutch. Finally, if the experimentalist wants to perform x-ray imaging in place of, or in addition to, x-ray diffraction [59], it is also important to use a mode with high peak brightness. This is

because it is desirable to have only one bunch per x-ray image, or else features of the image can be smeared by specimen movement.

2.3.1.5 X-ray absorption

Optimizing the time resolution of a diffraction experiment requires maximizing the diffracted intensity which can be observed for a given input x-ray intensity. An important part of maximizing this diffracted intensity (at least when the diffraction experiment is conducted in the transmission geometry) is picking the appropriate specimen thickness through which the x-rays are transmitted. This thickness is determined by considering absorption effects. If absorption did not exist, then the expected diffracted intensity at a Bragg angle from the specimen would scale linearly with the specimen thickness. Absorption counteracts this by causing exponential decay of the x-ray intensity as it propagates through the specimen (both before and after any diffraction which occurs). Consequently, the expected diffracted intensity I when accounting for absorption is [60]:

$$I/I_0 = \int_0^t \exp\left[-\mu\Big(z + \frac{t-z}{\cos[2\theta]}\Big)\right] dz \tag{2.6}$$

where I_0 is the incident intensity, θ is the scattering angle, t is the specimen thickness, and μ is the specimen's linear attenuation coefficient, which increases with increasing specimen density and an increasing wavelength of incident radiation. The best-case scenario for maximum diffracted intensity is when $t = 1/\mu$. This thickness t

is known as the specimen's "absorption length." For specimen thicknesses less than t, the diffracted intensity reaching a detector is sub-optimal because too many photons transmit directly through the specimen. For specimen thicknesses greater than t, the diffracted intensity reaching a detector is sub-optimal because too many photons are absorbed by the specimen before they can diffract, or before they can exit the specimen. For dense specimens (*i.e.* transition metals), the *in situ* diffraction experiments discussed below would require very small specimens in order to be near the absorption length of the material when the x-ray energy is below $\sim$ 25 keV, as is demonstrated in Table 2.4 for iron. The importance of specimen density to the ideal specimen size for these experiments is further demonstrated in Table 2.5 for materials of different densities exposed to 20 keV x-rays.

X-ray Energy (keV)	Absorption Length of Fe (μm)
10	7.5
20	49.8
30	157
40	354
50	655

Table 2.4: The absorption length of iron when using various x-ray energies.

X-ray Material	Absorption Length at 20 keV (μm)
Au	6.8
Fe	49.8
Ti	141
Al	1090
Mg	2120

Table 2.5: The absorption length of various metals when using a 20 keV x-ray beam.

2.3.1.6 Estimating signal quality during time-resolved diffraction

When designing *in situ* diffraction experiments it is useful to be able to estimate the expected signal given the experimental configuration and samples to be studied. This can guide the selection of the x-ray energy or other experimental parameters, and even help one decide whether a contemplated experiment is feasible. For powder x-ray diffraction experiments one important and easily-calculated quantity is the integrated intensity from the $\{hkl\}$ planes [57, 58]:

$$I = \frac{\Phi r_0^2 P A_\mathrm{s} F_{hkl}^2 a_0 \lambda^3 m_{hkl}}{v_\mathrm{uc}^2 8\pi L \sin^2\theta\cos\theta} \times (1 - A_\mathrm{d}) A_\mathrm{air} \Delta x \Delta t \tag{2.7}$$

where Φ is the incident beam flux (ph $\mathrm{s}^{-1}\mathrm{mm}^{-2}$), r_0 is the classical radius of an electron (2.82×10^{-15} m), P is the polarization factor ($\simeq 1$ for scattering in the vertical plane at a synchrotron), A_s is the absorption factor for the sample (discussed below), F_{hkl} is the structure factor, λ is the x-ray wavelength, v_uc is the volume of the unit cell, m_{hkl} is the multiplicity of the $\{hkl\}$ planes, L is the sample-to-detector distance, θ is one-half of the scattering angle, $(1 - A_\mathrm{d})$ is the efficiency of the detector (discussed below), A_air is the absorption factor for x-rays in air (from the sample to detector, for instance), Δx is the size of a pixel on the detector, and Δt is the integration time. Note that I represents the intensity of the peak integrated along $\vec{q}$ (transverse to a powder ring, analogous to integrating over 2θ for a conventional

diffraction pattern) while Δx is the pixel size in the transverse direction (*i.e.* around a ring). Equation 2.7 assumes a non-textured material, but it is still useful for assessing the feasibility of a diffraction experiment or estimating the expected intensity on the detector when studying a weakly-textured material. Highly-textured material (*e.g.* rolled magnesium) can produce intensities on certain regions of the detectors which are greatly underestimated or overestimated by equation 2.7. The detector geometry is also dealt with in a simplified way for ease of calculation.

For the experimental geometry we will consider in which the incident beam is normal to the sides of a flat planparallel specimen the absorption factor is [61]:

$$A_{\mathrm{s}} = A_{\mathrm{beam}} t \exp(-\mu t) \frac{\mu t(1 - \sec 2\theta)}{\exp[\mu t(1 - \sec 2\theta)] - 1} \tag{2.8}$$

where A_{beam} is the cross-sectional area of the incident x-ray beam, t is the specimen thickness, and μ is the linear absorption coefficient of the specimen.

The two parameters in Eqns. 2.7 and 2.8 most directly under the control of the experimenter are the x-ray wavelength and the sample thickness. For *in situ* loading experiments the optimal thickness must be balanced against the needs of the loading apparatus and the mechanical testing technique (*e.g.* the specimen should be proportioned so as to minimize the chances of buckling during a compression test).

2.3.2 Motivation for high-strain-rate mechanical testing with simultaneous x-ray diffraction

The response of materials to high-strain-rate mechanical deformation is of interest in many fields including the automotive, aerospace, and defense industries [62]. The compression Kolsky bar is commonly used to study the stress-strain behavior of materials over strain rates of $\sim 10^3 - 10^5$ s^{-1} [5, 56, 63–66]. Information about structural evolution in these experiments is usually inferred from the starting and ending microstructures, or by performing recovery experiments at various levels of strain. However, post-mortem microstructures may be different from the non-equilibrated structures present during the dynamic event. Certain microstructural attributes of dynamically deforming specimens, such as the presence of transient phases or the elastic strains present in specific phases or subsets of grains, can only be experimentally observed while deformation is taking place. An example of a transient phase is the monoclinic martensite phase which exists during loading of super-elastic nickel-titanium alloys.

Time-resolved x-ray diffraction can provide important insights into the evolution of the structure of a material during dynamic loading, such as the elastic strains in individual phases, crystallographic texture, and the development of new (possibly metastable) phases. Earlier work demonstrated the utility of x-ray diffraction studies of single crystals under shock loading [67–70]. Diffraction can also provide comple-

mentary information to imaging, which has previously been used to track damage evolution at similar strain rates [71]. We therefore endeavored to develop techniques for obtaining structural information via x-ray diffraction from polycrystalline materials during dynamic deformation at strain rates of $\sim 10^3$ s^{-1}.

Until recent years, the state of technological development severely limited researchers' abilities to characterize transient microstructural attributes using diffraction. However, recent improvements in synchrotron insertion devices and x-ray detector technology have allowed researchers to demonstrate that these microstructural attributes can now be observed *in situ* during Kolsky bar and gas gun experiments [55,59,69,71]. Methods for performing these measurements during compression Kolsky bar experiments on metals are described below.

2.3.3 Technique 1: Advanced Photon Source, Hutch 1-ID-C

At the time this experiment was done, fast x-ray detectors were even less readily available than they are now, especially detectors which were sensitive to strongly-penetrating x-rays above $\sim$ 25 keV. We therefore employed a technique in which we achieved temporal resolution on the microsecond scale by producing short x-ray pulses. A similar pulsed technique has been used for studies of irreversible transformations in materials in References [72–74].

We conducted these experiments at beamline 1-ID of the Advanced Photon Source (APS) using a monochromatic 86 keV x-ray beam vertically focused to a spot size of ~ 30 μm $\times$ 1 mm together with a large-format amorphous silicon detector centered on the transmitted beam (Fig. 2.5(a)). The beam had a bandpass of $\sim 0.01\%$ and a flux of $\sim 10^{12}$ ph s^{-1} mm^{-2}. The amorphous silicon detector is too slow (30 Hz) to capture multiple diffraction patterns during a single test, so to track the evolution of structure during deformation we performed separate tests on multiple, nominally identical specimens with different shutter delays to interrogate different times during the loading. We used a Kolsky bar apparatus with 8 mm diameter maraging steel bars.

To produce short x-ray pulses we positioned a fast shutter system [72, 75] in the incident beam upstream of the specimen. The pulses produced using this system had a full-width at half maximum of approximately 40 μs (Fig. 2.6) as measured by a PIN diode mounted on the beam stop in the transmitted beam. In previous experiments with smaller x-ray beams and lower x-ray energies the same shutters produced pulses of < 20 μs (Ref. [72]); the longer pulses here are due to a combination of a larger beam (requiring more time to occlude) and higher energy (which reduces the stopping power of the tungsten blades). Even with pulses of this length we are able to clearly observe the evolution of the structure, as described below.

In the pulsed experiments the critical timing event is the arrival of the strain pulse at the specimen, which must be synchronized with the timing of the x-ray pulse

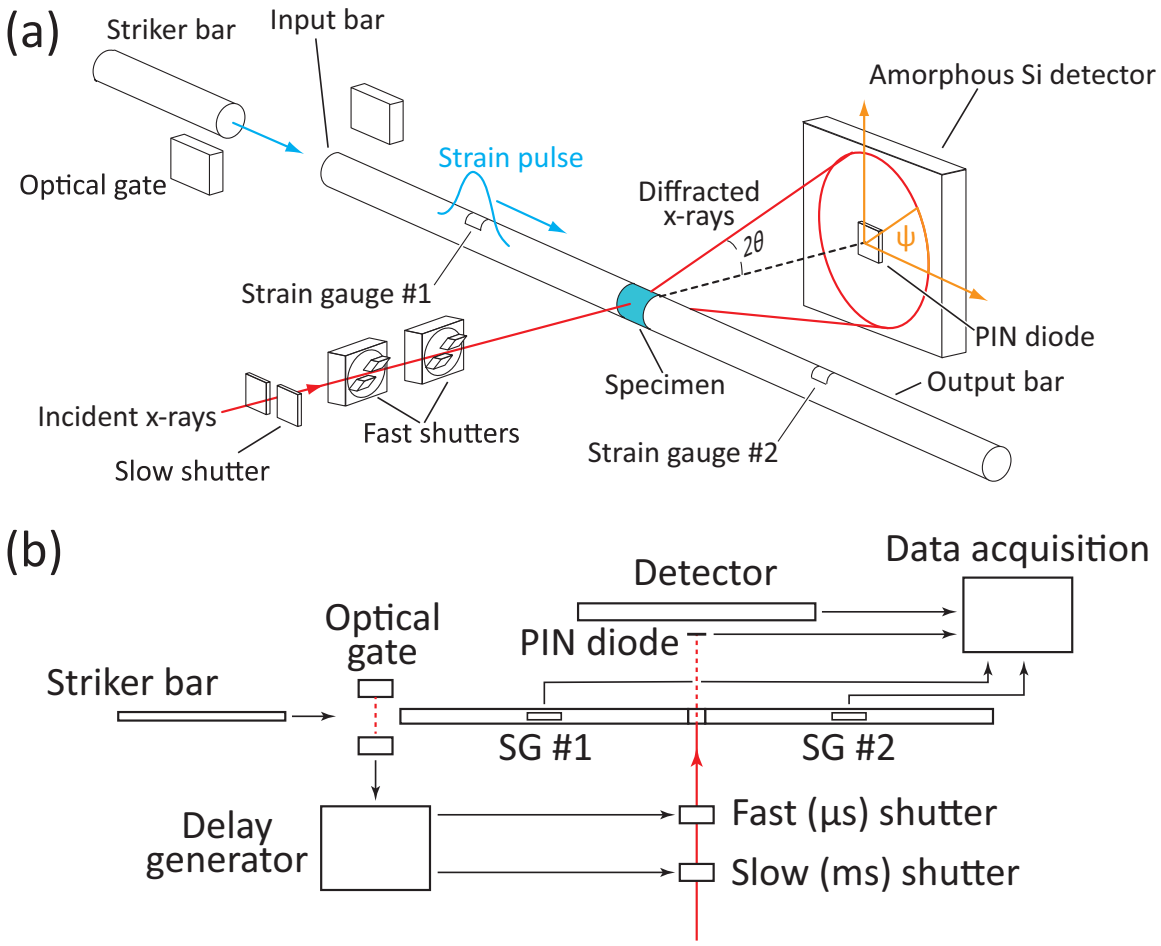

Figure 2.5: Schematic (a) and timing signals (b) for the fast detector experiments.

(Fig. 2.5(b)). In principle we could trigger the shutters from a strain gage signal on the incident bar, but in practice the time required to actuate the shutters (~ 350 μs) exceeds the time for the strain pulse to propagate down the input bar. Instead, we triggered the shutters off of an optical gate positioned to sense the movement of the striker bar toward the input bar (Fig. 2.5). Inevitable variations in the velocity of the striker bar, due to effects such as manual pressurization of the breech and variable amounts of breech depressurization we experienced while securing the beamline hutch, make the experimental timing with this approach less reliable than triggering off of the strain pulse. For various specimens tested with a fixed shutter delay, the arrival time of the strain pulse at the specimen relative to the timing of the diffraction pattern spanned a range of up to 220 μs. Because the opening of the shutters and the movement of the strain pulse down the incident bar both had little temporal variation from test to test, this means there was a variation in striker velocity of up to $\sim \pm 10\%$ over all tests. In subsequent experiments, we were able to measure the velocity of the striker bar (from two optical gate measurements) and adjust the shutter trigger delay accordingly on-the-fly, as will be describe in subsequent sections. This would be a particularly important improvement to future fast shutter-based experiments, because without two optical gates there was a substantial element of chance regarding the timing of the shutters. Many of the tests we ran were wasted effort, as the jitter of the striker velocity caused the diffraction pattern to be recorded before deformation had started or after the compression event was over.

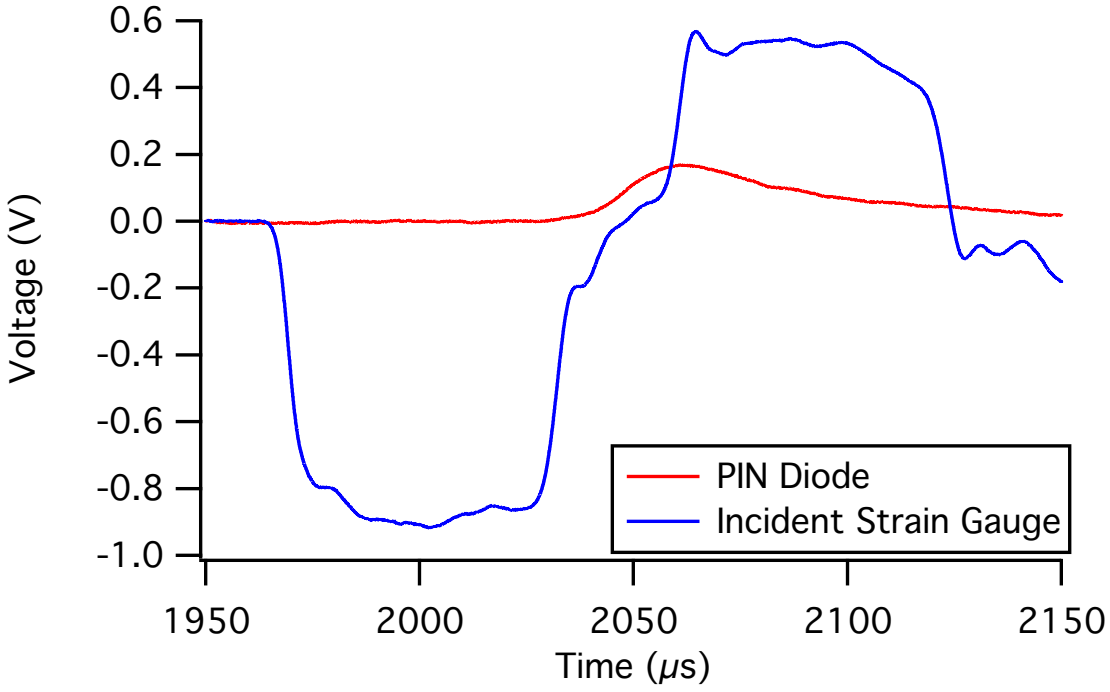

Figure 2.6: An example of the signal detected on the PIN diode (indicative of the number of photons passing through the specimen) as a function of time, superimposed with the incident bar strain gauge signal that was obtained simultaneously.

For these experiments, the synchrotron was operating in 24 bunch mode. Due to the length of the exposures, each diffraction pattern integrates over $\sim 10 - 20$ synchrotron ring cycles and thus hundreds of bunches. In principle, much improved temporal resolution would be possible with the higher flux ($\sim 10^{14}$ ph s^{-1} mm^{-2}) of a broad bandpass beam. Although this would decrease the accuracy of determining peak position, it would allow for shorter exposures, including the possibility of synchronization to single bunches in the APS hybrid fill mode. This would require use of a high-speed chopper [76, 77] similar to that used in high-speed imaging experiments in conjunction with the fast shutters we utilized, since the detector we utilized for these high-energy experiments cannot be gated.

2.3.3.1 Sample data

The amorphous silicon detector utilized during this experiment was relatively large, and one advantage of this, in combination with with the high x-ray energies (which compress the scattering into smaller angles 2θ) was that we could observe complete diffraction rings associated with {111}, {200}, and {220} reflections in the specimens. The complete diffraction rings meant that we were observing a wide range of scattering vectors $\vec{q}$ (one corresponding with the diffracted intensity at each point on the ring) ranging from those pointed perpendicular to the loading direction to those pointed nearly parallel to the loading direction. From the ring diameters we are able to determine the lattice spacings as a function of orientation around the

incident beam (corresponding to different orientations of the scattering vector) and thus calculate the elastic lattice strain in the loading and transverse directions [78].

A plot of the elastic strain in the loading direction as a function of time for {111} planes is shown in Fig. 2.7. Strains were calculated by dividing the diffraction ring into 60 bins spaced evenly in azimuthal angle, azimuthally integrating the intensity in each bin, fitting a Gaussian function to each diffraction peak to determine its peak position, averaging diametrically opposed positions to mitigate beam center errors, determining the average lattice strain for each bin by comparing the strained and unstrained peak positions, and extrapolating these strains as a function of azimuthal angle to an angle of zero (i.e. the loading direction) using the $\sin^2\psi$ method [79–81]. Using the time of maximum intensity from the PIN diode signal and the signal recorded by the strain gauges (Fig. 2.6), each diffraction pattern could be assigned a time point relative to the onset of deformation. We note, however, that each data point actually represents an integration over a longer period of time determined by the interval over which the shutter is open. Also shown in Fig. 2.7 is the lattice strain as a function of time for {111} planes with their normals along the loading direction, calculated from the global average stress (from the Kolsky bar strain gauge data) using the diffraction elastic constants for Monel®-400 (Ref. [7]). The measured strain agrees reasonably well with the calculation, allowing for the fact that the diffraction patterns average over a longer interval of time (during parts of which the sample sees lower load).

Figure 2.8 shows an intensity map of the {111} and {200} powder rings as a

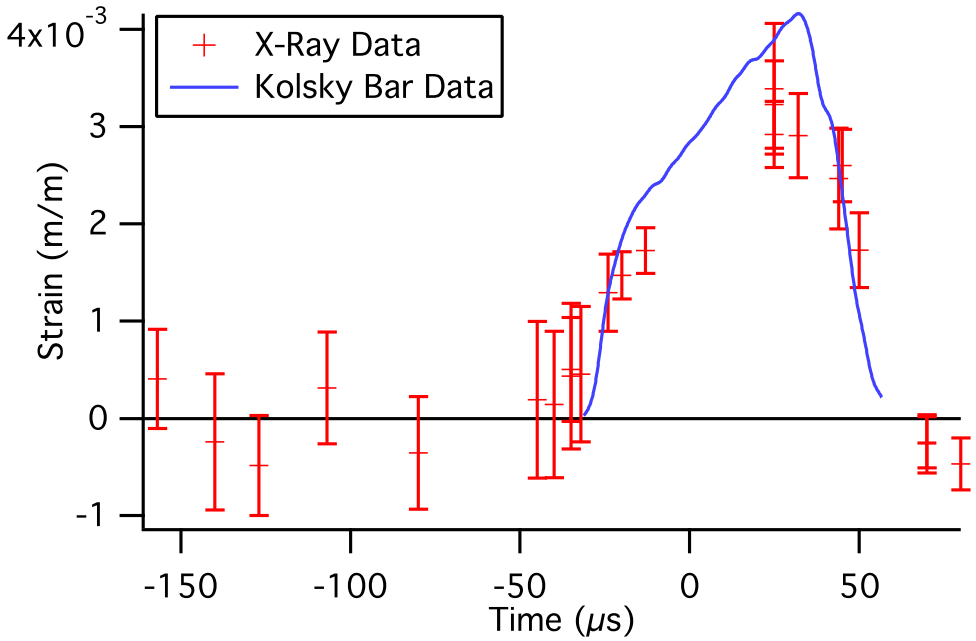

Figure 2.7: Measured elastic strain in the loading direction as a function of time for {111} planes in the Monel-400 specimens, superimposed with predicted strain in the loading direction for grains with their {111} plane normals aligned along the loading direction, based off of stress-strain data from the Kolsky bar strain gauges and the Kröner elasticity model [7].

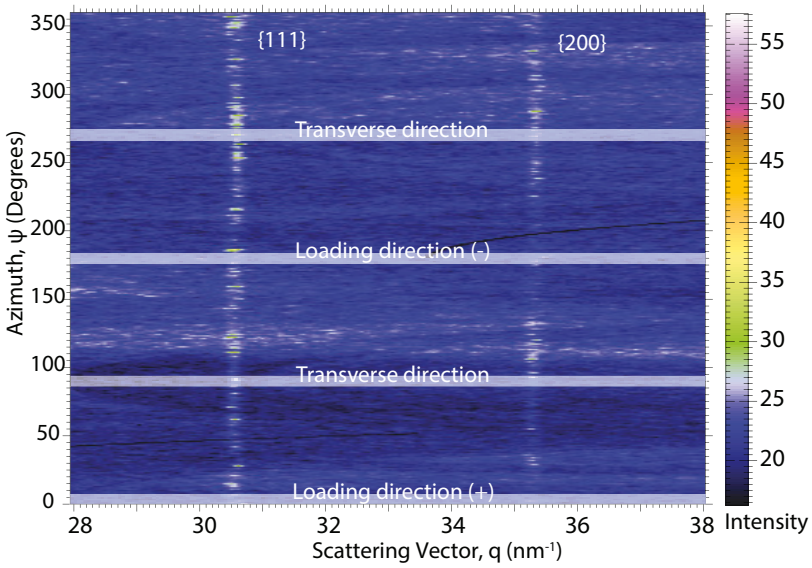

Figure 2.8: Intensity map as a function of scattering vector and azimuthal angle on the detector for the {111} and {200} planes of Monel®-400, made using a 40 μs exposure taken 107 μs before the onset of deformation in the specimen. $\psi = 0°$ corresponds with the direction of striker bar travel.

function of scattering vector magnitude q and azimuthal angle ψ made using a 40 μs exposure taken $\sim$107 μs before the onset of deformation, generated using the FIT2D x-ray data analysis program [82]. Figure 2.9 shows an intensity map of these same rings with the same exposure length, but the exposure was taken $\sim$32 μs after the onset of deformation. In the undeformed specimens the {111} and {200} rings are continuous and have nearly uniform intensity, indicative of a material that has little crystallographic texture. During dynamic loading crystallographic texture clearly develops, which appears most obviously as an increase in the intensity of the {111} ring near $\psi = \pm 45°$, $\pm 90°$, and $\pm 135°$. A similar but less pronounced variation in the {200} ring intensity can also be observed.

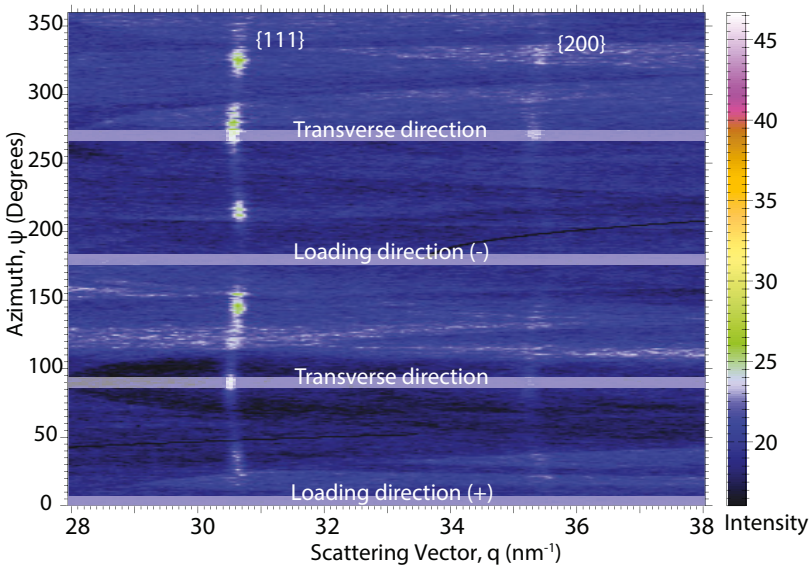

Figure 2.9: Intensity map as a function of scattering vector and azimuthal angle on the detector for the {111} and {200} planes of Monel®-400, made using a 40 μs exposure taken 32 μs after the onset of deformation in the specimen. $\psi = 0°$ corresponds with the direction of striker bar travel.

2.3.4 Technique 2: Cornell High Energy Synchrotron Source, Hutch G3

The specimen material we used while attempting the second experimental technique (AZ31 magnesium alloy) has a density which is sufficiently low that much lower x-ray energies could be utilized than in the first technique, allowing us to use the much more rapidly-framing direct-detection x-ray detector described below. With this change in detector came several improvements to the experimental procedure, also described below.

Figure 2.10(a) shows a schematic of the experimental setup associated with this

technique. We performed this technique in hutch G3 at the Cornell High Energy Synchrotron Source (CHESS) using a 1 mm $\times$ 1 mm beam of 10 keV x-rays. We used a multilayer monochromator which produced a bandpass of $\Delta E/E \simeq 2\%$, yielding a high flux of approximately 2×10^{13} ph s^{-1} mm^{-2}.

We positioned a Kolsky bar with 3 mm diameter aluminum bars in the incident beam. For most of our experiments, the incident beam was normal to the bar and the detector rotated in a vertical plane about the loading axis (i.e. the x- axis in Figure 2.10), so that the scattering plane was vertical and the scattering vector $\vec{q}$ perpendicular to the loading direction. In this geometry the structural information comes from scattering planes parallel to the loading direction. For some experiments we rotated the bar and detector about a vertical axis (the z axis in Figure 2.10(a)), making the scattering plane horizontal and choosing the incident and scattering angles so that the scattering vector was parallel to the loading direction; in this geometry the scattering planes were perpendicular to the loading direction.

We used a fast Keck Pixel Array Detector (PAD) [83] for this technique, which was a direct-detetion x-ray detector based on analog pixel array detector chips with a minimum integration time of 150 ns or less [83]. Each chip consists of a 128 $\times$ 128 array of 150 μm pixels. We used a 2 $\times$ 3 array of individual PAD chips to produce a detector with a total area of 57.6 $\times$ 38.4 mm, which covered an azimuthal angle range of $\sim 48^\circ$ in our experimental setup. The PAD can store eight frames before readout, so it was necessary to trigger the detector at an appropriate time relative to the arrival

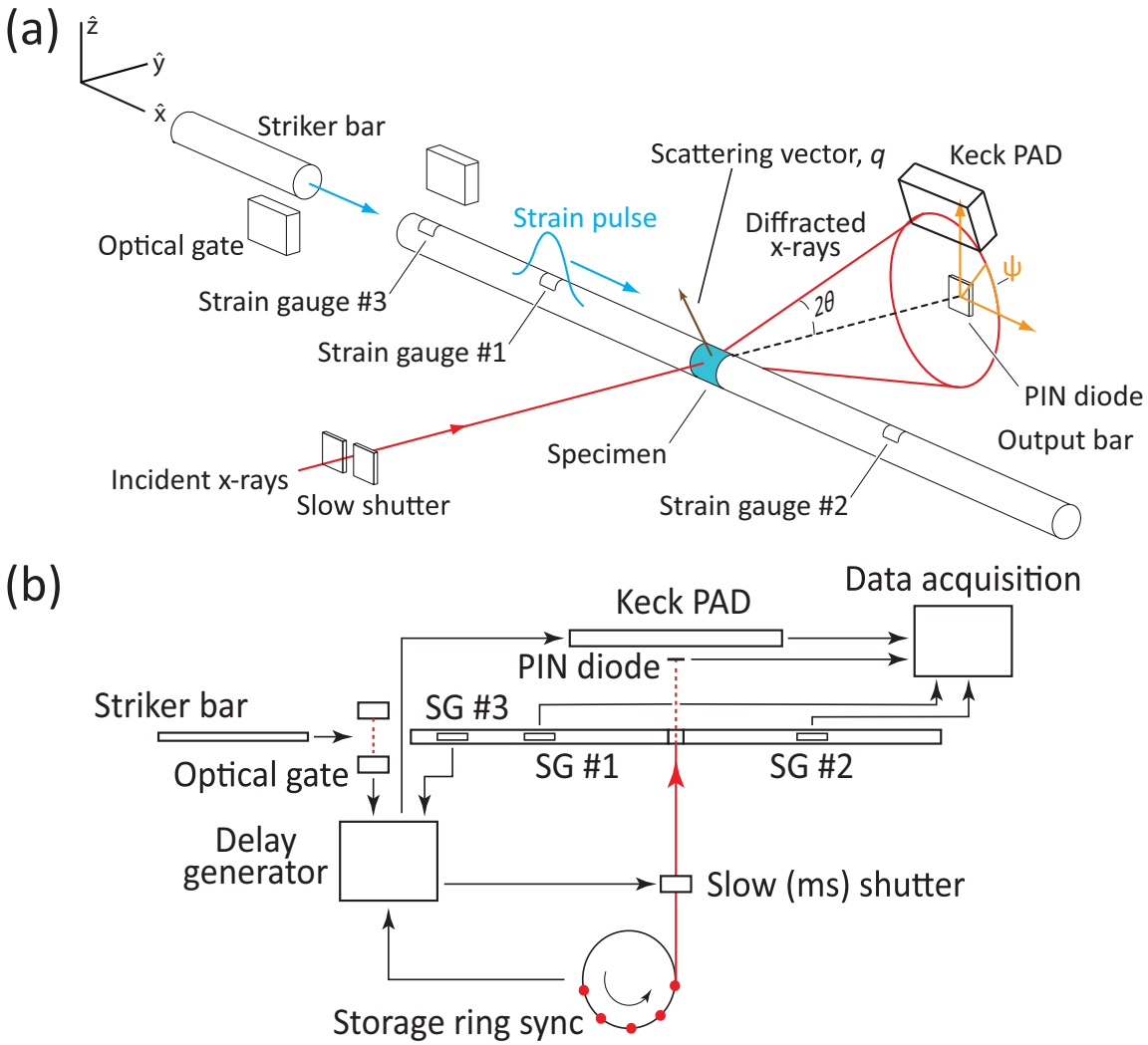

Figure 2.10: (a) Experimental setup used for fast detector experiments, showing scattering in a vertical plane and the scattering vector transverse to the loading axis. Strain gauges 1 and 2 were used to extract stress-strain data; strain gauge 3 was used to trigger the PAD. (b) Timing signals for the fast detector experiments.

of the strain pulse at the specimen. We did this by placing a semiconductor strain gauge (strain gauge 3 in Fig. 2.10) at the end of the input bar close to the projectile; the rise in signal from this strain gauge triggered a delay generator which in turn triggered the Keck PAD via a TTL pulse after a suitable delay (based on the speed of sound in the incident bar and the distance from strain gauge to specimen). By appropriate choices of delay time, integration time, and time between frames we were able to capture diffraction patterns during the entire course of deformation or during any portion of interest. In various experiments we used integration times ranging from the shortest possible with this detector (150 ns) to approximately 10 μs. A similar method of experimental timing, utilizing a piezoelectric pin for signal instead of a strain gauge, was recently used to synchronize gas gun shock experiments with phase contrast imaging techniques [84, 85].

Timing experiments on the microsecond scale require attention to the pulsed nature of synchrotron radiation. During these experiments the positron bunch structure in the Cornell Electron Storage Ring (CESR) consisted of five trains of bunches with each train having a duration of 70 ns. The five trains were equally spaced over a span of 1.19 μs followed by a 1.37 μs gap, for a ring period of 2.56 μs (Fig. 2.11). Under these conditions the x-ray exposure during the time the detector is counting can vary depending on when the integration time starts relative to the position of the bunches in the ring. For example, a 1 μs integration might occur during the 1.37 μs gap, when there are no x-rays incident on the specimen. To avoid this we implemented an

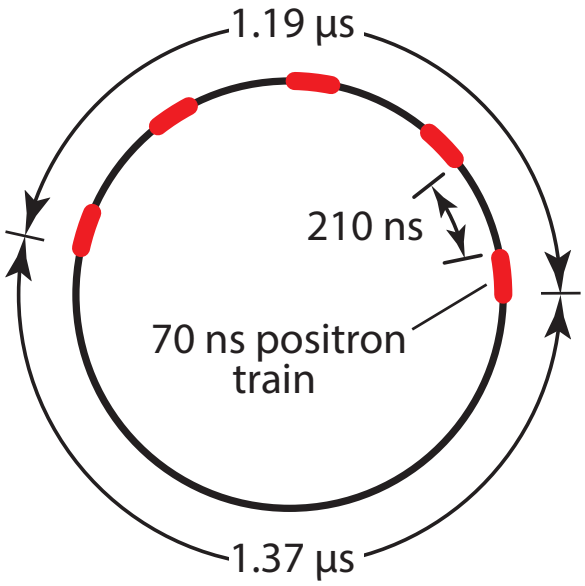

Figure 2.11: The bunch structure for the fast detector experiments consisted of five 70 ns positron trains separated by 210 ns, with an overall ring period of 2.56 μs.

additional delay that inhibited the detector from triggering until it received a timing signal indicating the arrival of the first bunch in the next ring period (Fig. 2.10(b)). Because we had no way to time the arrival of the strain pulse at the specimen relative to the positions of the positron bunches, this introduced a jitter in the timing of the first diffraction pattern of up to 2.56 μs (corresponding to the worst-case scenario where the detector has to wait a full ring period before beginning counting). We also arranged the timing so that each frame after the first occurred an integer number of ring periods after the preceding frame. In this way we were able to ensure consistent x-ray exposures for each frame.

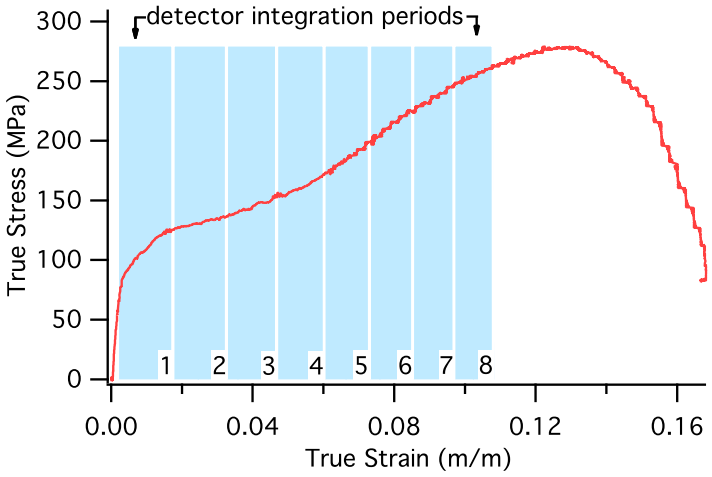

Figure 2.12: True stress-true strain curve of AZ31 magnesium alloy overlayed with Keck PAD signal indicating the start of data collection by the x-ray detector.

2.3.4.1 Sample data

Figure 2.12 shows a stress-strain curve obtained at CHESS along with the times over which each diffraction pattern was collected. The exposure time for these patterns was 3.75 μs, corresponding to two 2.56 μs ring periods minus the trailing 1.37 μs gap. After background subtraction, we azimuthally integrated the powder diffraction data from the Keck PAD to produce plots of scattered intensity *vs.* scattering vector magnitude $q = 4\pi \sin\theta/\lambda$, as shown in Fig. 2.13 for data collected with $\vec{q}$ transverse to the loading direction. The $\{10\bar{1}0\}$, $\{0002\}$, and $\{10\bar{1}1\}$ peaks from Mg are clearly defined, and we are able to track changes in peak position and peak area for all three. In particular the decrease in intensity of the $\{0002\}$ peak intensity coupled with the increase in the $\{10\bar{1}0\}$ peak is suggestive of deformation by $\{10\bar{1}2\}\langle\bar{1}011\rangle$ twinning of magnesium [86].

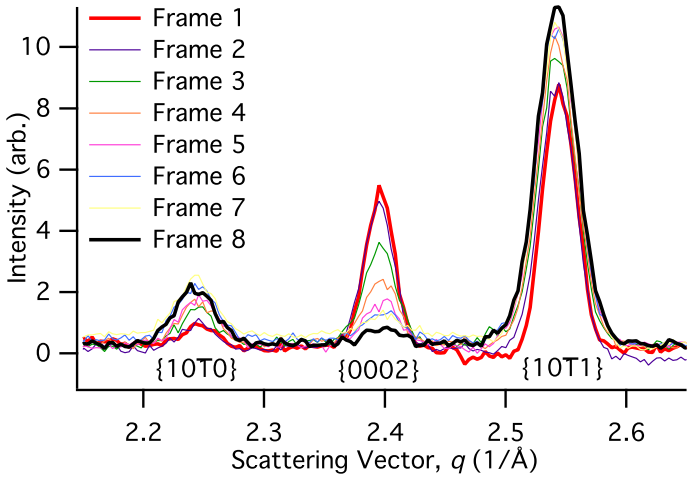

Figure 2.13: Plots of integrated intensity vs. scattering vector for the $\{10\bar{1}0\}$, $\{0002\}$, and $\{10\bar{1}1\}$ planes of AZ31 corresponding to the stress-strain curve in Figure 2.12, with exposure times of 3.75 μs.

Figure 2.14 shows examples of data collected with the shortest exposure time attempted, obtained with a 150 ns integration time synchronized to coincide with a single 70 ns positron bunch train (Fig. 2.11). As expected, the signal-to-noise ratio is poorer than for the longer exposures in Fig. 2.13, but, due to the pulsed synchrotron source, the x-ray intensity only drops by a factor of 10 between the two data sets while the temporal resolution is increased by a factor of 50. Here the $\{10\bar{1}0\}$ and $\{10\bar{1}1\}$ diffraction peaks are still clearly discernible, and changes in the peak area are apparent. The absence of the $\{0002\}$ peak is probably due to the initial crystallographic texture of the specific specimen being tested.

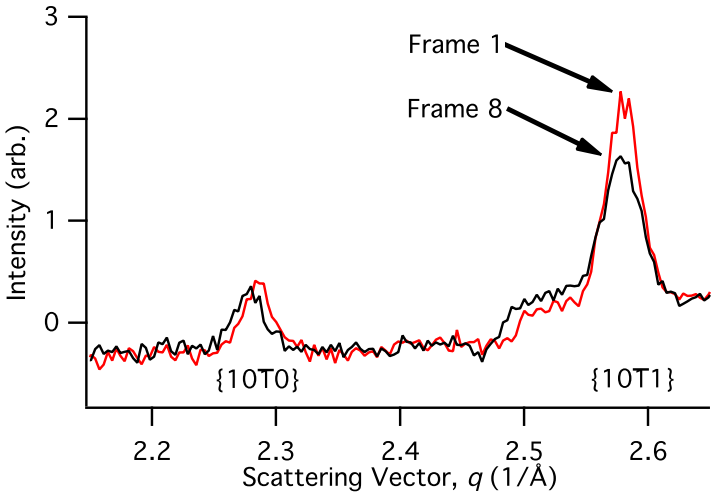

Figure 2.14: Example data collected with experimental parameters similar to those used in Figure 2.13 but with exposure times of 70 ns.

2.3.5 Technique 3-1: Advanced Photon Source, Hutch 35-ID-B

The third experimental technique was conducted at the Dynamic Compression Sector, which was specifically designed to output very high flux (up to $\sim 10^{16}$ photons/s). This high flux is very desirable for improving temporal resolution. However, the (logistically) more complex detector along with our attempts to integrate numerous experimental techniques into a newly-commissioned beamline resulted in a variety of experimental challenges the first time we employed this technique. Some of these challenges will be described below.

We positioned a Kolsky bar apparatus with 4.8 mm-diameter high-strength steel bars in the beamline with the DCS detector array positioned $\sim$ 113 mm behind the

bars in the transmission geometry. A schematic of the detector setup is shown in Figure 2.15 and a schematic of the whole experimental setup is shown in Figure 2.16. The experiments were conducted in 324 bunch mode using a U18 undulator with an 11.1 mm gap, so that the undulator's 1st harmonic was centered on 23.4 keV. The relatively wide scattering angles resulting from this x-ray energy required us to modify the support structure of the Kolsky bar, as the existing support structure partially obstructed diffracted x-rays from hitting the detector.

We recorded four 5 μs diffraction patterns during each test as the specimens were compressed at a strain rate of ~ 3000 s^{-1}. We also synchronized a high-speed optical camera with the experiment (not pictured in Figure 2.16 for visual clarity), positioning the optical camera above the beamline flight tube so that it looked down on the specimen at an angle of $\sim 60°$. The flash lamps associated with the optical camera caused a variety of experimental difficulties, such as severely increasing the level of noise in the x-ray detector and semiconductor strain gauge signal. In the future, more effective shielding of the detector and strain gauges would alleviate these problems, as would illuminating the specimen with pulsed laser light instead of flash lamps.

The detector used for these experiments and subsequent experiments at DCS was an array of four PI-MAX®4:2048f cameras (similar to the PI-MAX® camera arrays described elsewhere [84, 85]) that each record the appearance of an x-ray phosphor using a fiber optic taper and a series of beamsplitters. Each camera contains an array

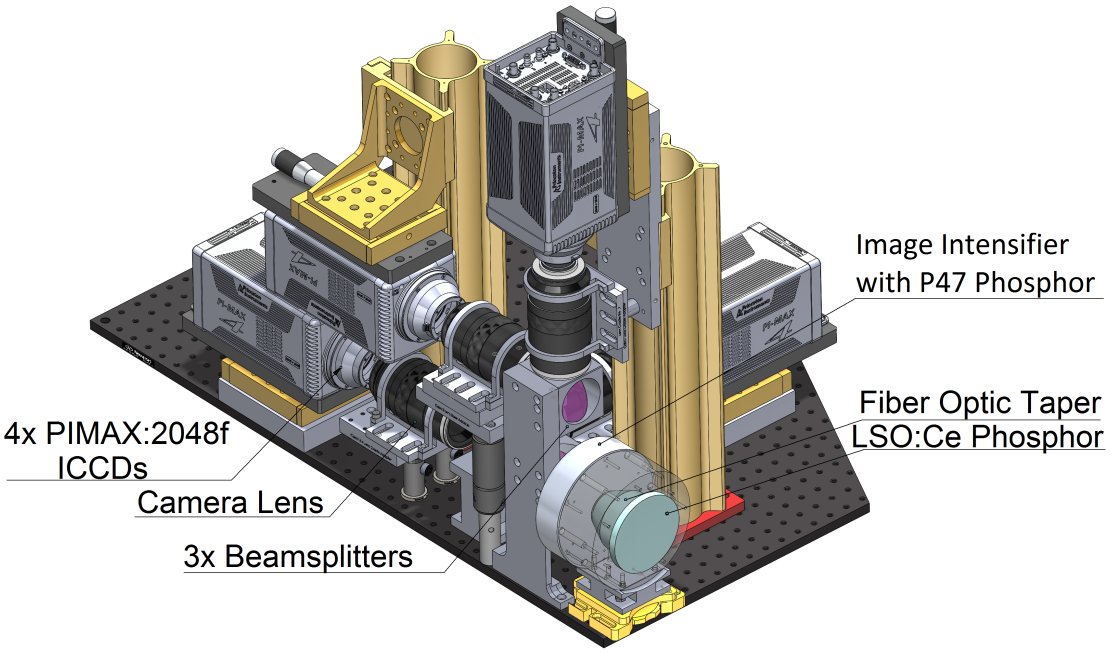

Figure 2.15: Schematic of the detector array used at the Dynamic Compression Sector. *Image courtesy of Dr. Nicholas Sinclair.*

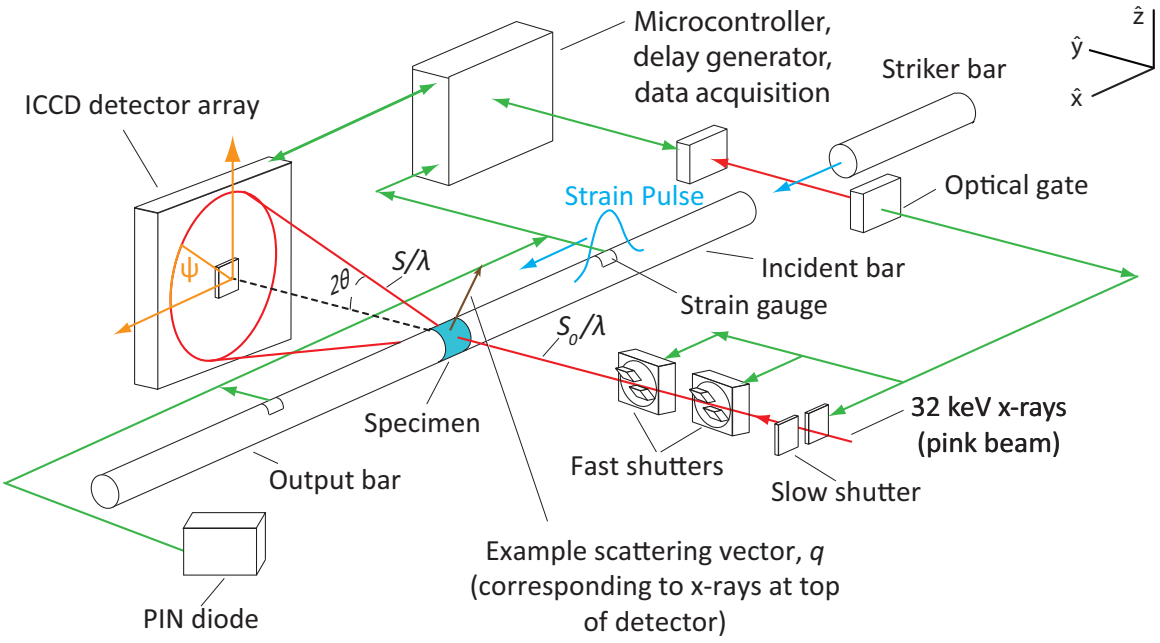

Figure 2.16: Schematic of the experimental setup used while performing the Hutch 35-ID-B technique.

of 2048 $\times$ 2048 pixels which are $\sim$ 13.5 μm wide. The effective area on the phosphor occupied by one camera pixel is $\sim$ 40 μm wide. Due to the low intensity of diffraction (compared with x-ray imaging), an image intensifier was needed to increase the signal observed by each camera. Each PI-MAX® camera can only record one image for each experiment, so triggering the detector at the appropriate time to observe deformation events in the sample was again required. The detector array was triggered using a semiconductor strain gauge on the incident bar, while the optical camera flash lamps were triggered by an optical gate in the path of the striker. We also used the fast shutters described earlier, but they were not utilized for temporal resolution. Instead, they were utilized to minimize the specimen's exposure to the high-flux x-ray beam.

This was done because the high-flux, high-energy x-ray beam can potentially damage the x-ray detector (and even the specimen, as described below) if the beam impinges on them for more than a few milliseconds. The shutters were also triggered off of the optical gate signal.

2.3.5.1 Sample data

Very few tests performed using this technique were complete successes, in which all diffraction data, strain gauge data, and optical camera data was collected at the intended time. This was mainly due to user error, stemming from the low level of automation we employed as well as our urgency to complete the large number of different tests (utilizing different experimental setups) planned for this synchrotron run. In addition, there were serious unforeseen difficulties with the steel specimens because they were far thicker than the absorption length for the undulator harmonic we intended to use. This meant that a very large fraction of the 1st harmonic's flux was absorbed by the specimen. When the beam was in its fully-focused condition, this actually led to such high energy input into the specimen that beam-induced oxidation and even small craters formed on the specimens during x-ray exposure. De-focusing the x-ray beam prevented these problems, but the specimen thickness still led to a dramatic decrease in the 1st harmonic's diffracted intensity on the detector.

Figure 2.17 is representative of most of the specimens we tested, and demonstrates that the 1st and 2nd harmonics produced comparable amounts of diffracted intensity

on the detector, despite the vastly larger flux ($\sim$ 20 times higher) produced by the undulator in the 1st harmonic. As the specimen became thicker during compression, there was sometimes more intensity on the detector coming from the 2nd harmonic than the 1st harmonic. This pronounced change in relative intensities for the same crystallographic plane generated by different harmonics during the course of a compression event is illustrated in Figure 2.18. One could imagine actually exploiting the appearance of multiple harmonics on the detector to determine the thickness of the specimen using the relative diffracted intensities of each harmonic. However, it is hard to imagine a scenario where this measurement could not be accomplished more easily through more conventional means. Since the scattering vectors associated with each ring are also slightly different (even through they both correspond to the same crystallographic family of planes), in principle one could also use multiple harmonics to extract additional texture information about a family of crystallographic planes from the same diffraction pattern.

2.3.6 Technique 3-2: Advanced Photon Source, Hutch 35-ID-B

In our second attempt of this experimental technique, we made a significant change to our approach in that we revisited the prospect of using monochromatic radiation. Although this greatly reduces the incident flux on the specimen (by $> 99\%$), thereby

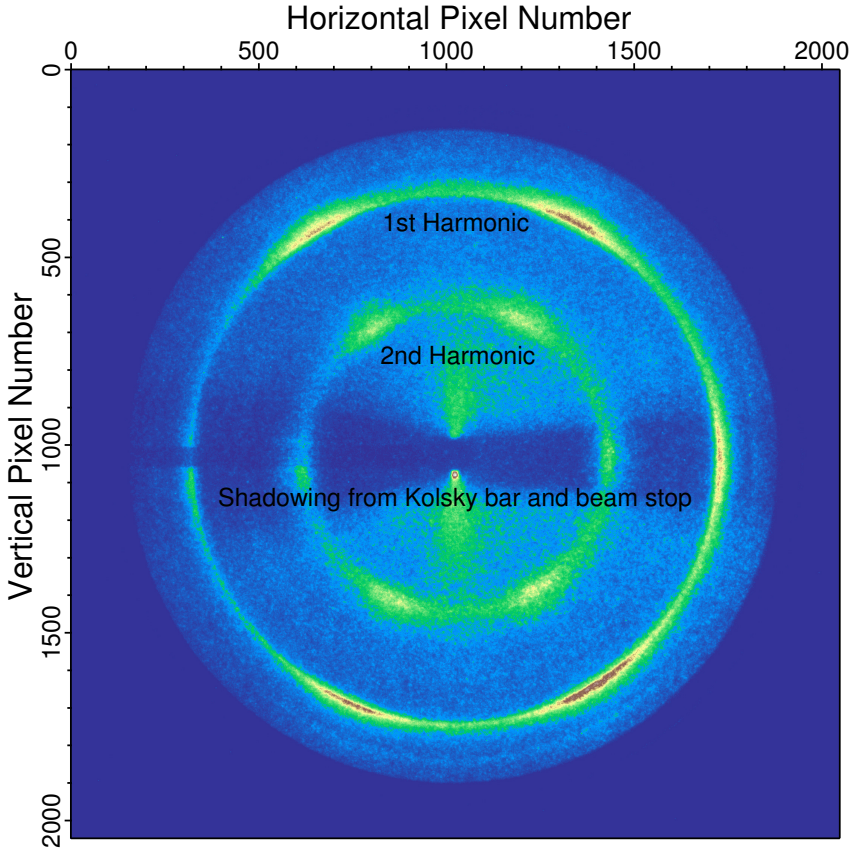

Figure 2.17: Example static diffraction pattern for a steel specimen collected using the U18 undulator. Despite the vast difference in intensity of the 1st and 2nd harmonics produced by the undulator, they show up with nearly equal intensity on the detector because of the specimen's very strong absorption of the 1st harmonic.

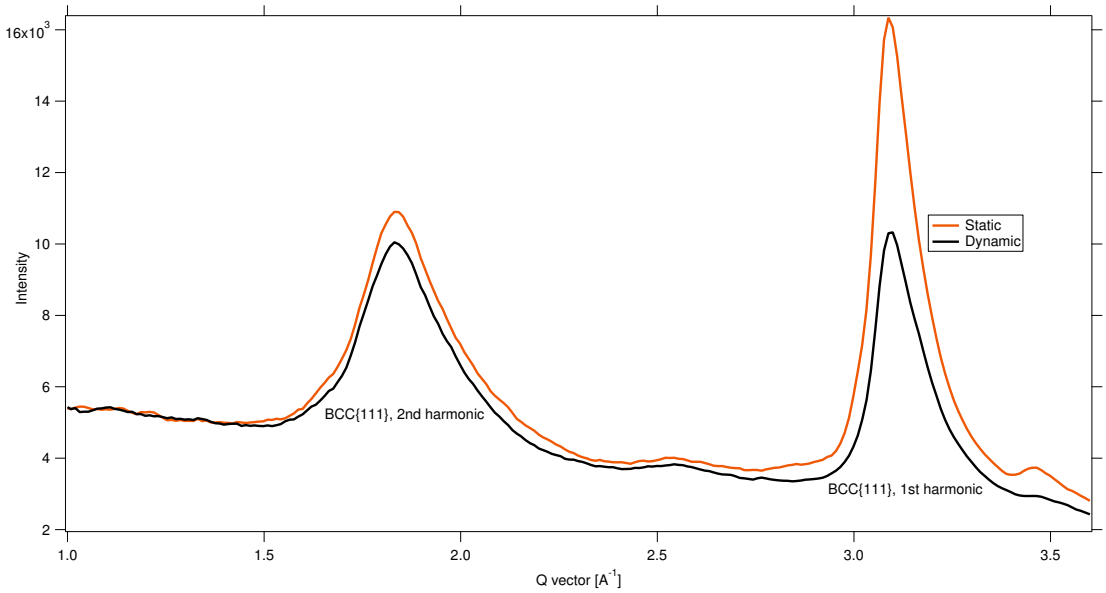

Figure 2.18: Integrated intensity plot of the {111} peaks generated by a steel specimen before compression (static) and during compression (dynamic). The reduction in diffracted intensity is much smaller for the 2nd harmonic, because of its longer absorption length.

decreasing the signal-to-noise ratio achievable in a given time period compared with a "pink" x-ray beam, it also improves the ease with which elastic strain information can be extracted from the data because of diffraction angle resolution which is superior to what is achieved using pink beam. The very high flux generated by the undulators at DCS allowed us to maintain acceptable time resolution (20 μs) even with the monochromatic beam and with the signal losses due to absorption in the specimen.

We utilized the U27 undulator at DCS with a monochromator isolating 30 keV x-rays and the synchrotron operating in 24 bunch mode for this iteration of the DCS technique. The Kolsky bar was essentially identical to what was used in the previously-described experiment. The positioning of the Kolsky bar and detector was also very similar to the previous experiment, except that the detector was closer to the Kolsky bar in order to observe more diffraction rings. The camera length was $\sim$ 6.5 cm, allowing us to observe 11 different diffraction rings on the detector. In part because of the high number of experimental problems we encountered the first time we employed this experimental technique, we did not utilize fast shutters or an optical camera so as to minimize the number of possible failure points in the experiment. The detector array was triggered using a semiconductor strain gauge on the input bar.

2.3.6.1 Sample data

While we utilized this technique with the intent to compare austenite transformation rates in various types of multi-phase steel, we did not account for a 50 μs

delay in the recording of our diffraction patterns due to a pulse suppression feature of the data acquisition system. This pulse suppression setting helps avoid false triggers by not sending a trigger-out signal for any voltage spikes that exceed the trigger-in voltage unless the spike also lasts a user-specified time (in our case, 50 μs). This will, of course, delay the timing of the trigger-out by the user-specified time, and we did not factor that delay into our calculations. This caused most of the diffraction patterns we recorded to correspond with much higher strains than originally intended. Consequently, almost all of the martensitic transformation had occurred before we could observe it. In addition, the movement of the input bar toward the x-ray beam during the test caused large fractions of the diffracted x-rays to be occluded before they could reach the detector when the diffraction pattern was taken at high levels of strain. Some of the specimens had such a short gage length that this beam blockage was unavoidable even before deformation had started. Nevertheless, some useful information can be drawn from the data.

The static (pre-experiment) diffraction patterns we recorded for the experimentally-optimized 10% Ni steel allowed us to determine a lower bound on the grain size of the particles in the steel. After processing the data (as described below) and fitting Gaussians to the observed peaks, we could then utilize the Scherrer equation [87]:

$$\tau = \frac{K\lambda}{\beta \cos\theta} \tag{2.9}$$

to define a lower limit on the size of the particles which were diffracting. In the

Scherrer equation, τ is the lower-bound size of the scattering crystalline domains, K is a shape factor, λ is the x-ray wavelength, θ is the Bragg angle, and β is the full-width-at-half-maximum line broadening of the observed peak. To determine the component of broadening coming from the specimen (as opposed to the measurement instrument), we subtracted the peak width generated by a National Institute of Standards and Technology (NIST) standard alumina powder from the peak width of the austenite peaks.

We know from microscopy that the ferrite/martensite particles have a mean size much larger than 1 μm, so the Scherrer equation does not accurately predict their size. Many of the austenite particles, on the other hand, are well below 200 nm in size (as will be shown in later chapters for similar steel specimens). Application of the Scherrer equation to the peaks observed in the experimentally-optimized 10% Ni steel produced a calculated grain size of $\sim$ 16 nm. This indicates that, if other microstructural features which can broaden diffraction peaks (*e.g.* high dislocation densities or chemical heterogeneities) are not present, then austenite particles as small as 16 nm in diameter are present in the specimen and contributing to the diffracted intensity. Work described in later chapters on a similarly heat-treated 10% Ni steel adds supporting evidence for the existence of these nano-scale austenite particles.

2.3.7 Technique 3-3: Advanced Photon Source, Hutch 35-ID-B

This third attempt at the DCS-based experimental technique applied all of the knowledge gained during previous attempts, and its execution was largely a success. The rest of this dissertation will focus heavily on data which was collected using this technique. The experimental setup was in many ways similar to what was used in the previous two iterations of the DCS technique. The synchrotron was operating in 24 bunch mode, and we utilized the U30 undulator with a 15.0 mm gap, causing the harmonic we utilized (the 4th) to be centered around 32 keV. We suppressed the higher and lower harmonics using the angle of a rhodium mirror and a 750 μm-thick aluminum attenuator, respectively. The specimen itself naturally attenuated some unwanted harmonics as well. The full, calculated spectrum of the U30 undulator is shown in Figure 2.19. It should be noted, however, that an impediment in the upstream x-ray optics was partially attenuating the beam during our experiment. This meant that the realized x-ray intensity during our experiment was lower than the achievable undulator output by a factor of at least 3 or 4, and also that the exact energy spectrum incident on the specimen is not known. It can be inferred, however, from the shape of the diffraction patterns we recorded for NIST standard alumina powders. The spot size for this experiment was 200 μm $\times$ 300 μm.

We positioned a Kolsky bar with 4.8 mm diameter maraging steel bars in the

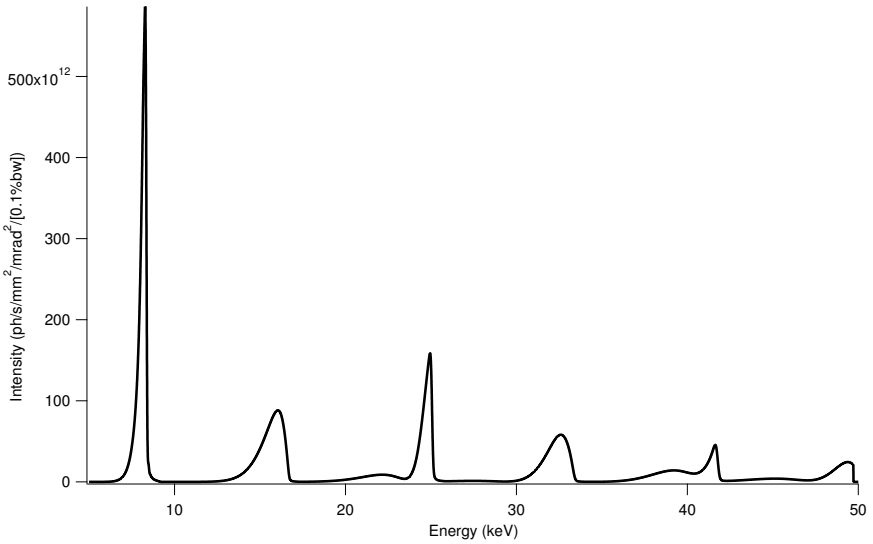

Figure 2.19: Output of the U30 undulator utilized for the 3rd iteration of the Hutch 35-ID-B experimental technique.

incident beam, perpendicular to the incident beam. To reduce blockage of diffracted x-rays by the steel bars, the ends of the bars in contact with the specimen were slightly tapered. We ensured that the specimen was always in the same place between the bars (and the same distance from the x-ray detector) using a custom-made specimen loading fixture. The shape of this fixture is illustrated schematically in Figures 2.20 and 2.21, along with the way it was used to consistently position specimens within the Kolsky bar apparatus and in line with the x-ray beam. The fixture's dimensions were such that, when pressed firmly against a bottom corner of the "V" notch supporting the Kolsky bar, a notch in the fixture designed to hold the specimen was in line with the axis of the input and output bars. The portion of the fixture supporting the specimen was narrower than the gage length of the specimen, which allowed us

to squeeze the specimen between the two bars to keep the specimen in its desired position as we carefully withdrew the loading fixture from the Kolsky bar apparatus. To ensure that the input bar was always the same distance from the gun barrel after the specimen had been positioned, the input bar was pressed firmly against a metal spacer placed between the input bar and the barrel while the specimen was being positioned. After the specimen was properly positioned between the input and output bars, we carefully removed this spacer without moving the input bar, thereby allowing the projectile to strike the input bar instead of the spacer. Besides ensuring a consistent uniaxial stress state was applied to each same from test to test, our use of this fixture and spacer also kept the timing of each experiment consistent. In addition, it minimized the amount of time spent positioning the small specimens between the bars and "searching" for the specimen with the x-ray beam before each test.

We placed the detector in two different positions for the compression of different specimens. First, the detector was centered on the transmitted x-ray beam with a camera length of $\sim$ 7.7 cm. This allowed us to record several full diffraction rings on the detector, but with limited angular resolution. This first experimental setup is pictured in Figure 2.16. Second, the detector was moved back to a camera length of $\sim$ 29.7 cm, and was translated in the direction of striker bar travel. This meant that we could only observe scattering vectors nearly aligned with the loading direction, but we could observe them with higher angular resolution.

The $\sim$ 7.7 cm camera length allowed us to record complete diffraction rings on

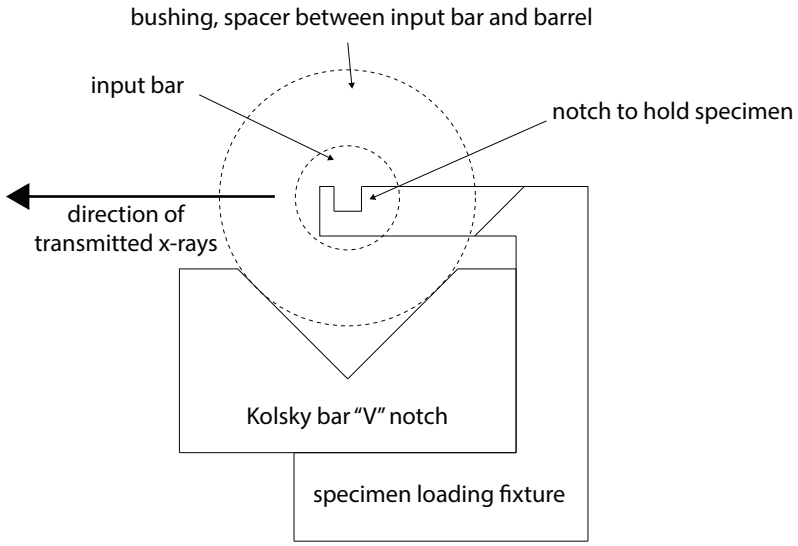

Figure 2.20: A schematic illustration of the specimen loading fixture positioned against the Kolsky bar apparatus so that the small specimen is consistently placed along the axis of the input and output bars. This illustration views the Kolsky bar apparatus along the axis of the input and output bars.

the detector for the {110}, {200}, and {211} planes of the martensite/ferrite phase and the {111}, {200}, {220}, and {311} planes of the austenite phase. (The martensite/ferrite {110} and austenite {111} rings were very strongly overlapping and could not be well resolved individually.) The $\sim$ 29.7 cm camera length allowed us to capture a portion of each of these rings ($\sim 40^\circ$ in azimuthal angle). We again utilized galvanometer shutters to minimize thermal load on the specimens. The galvanometer shutters open $\sim$ 350 μs after they receive an electronic signal to open, but this time exceeds the propagation time of a strain pulse in the incident bar. Jitter in the opening of the solenoid valve that releases the breach pressure was unacceptably large for the voltage pulse opening the solenoid valve to act as a signal to the

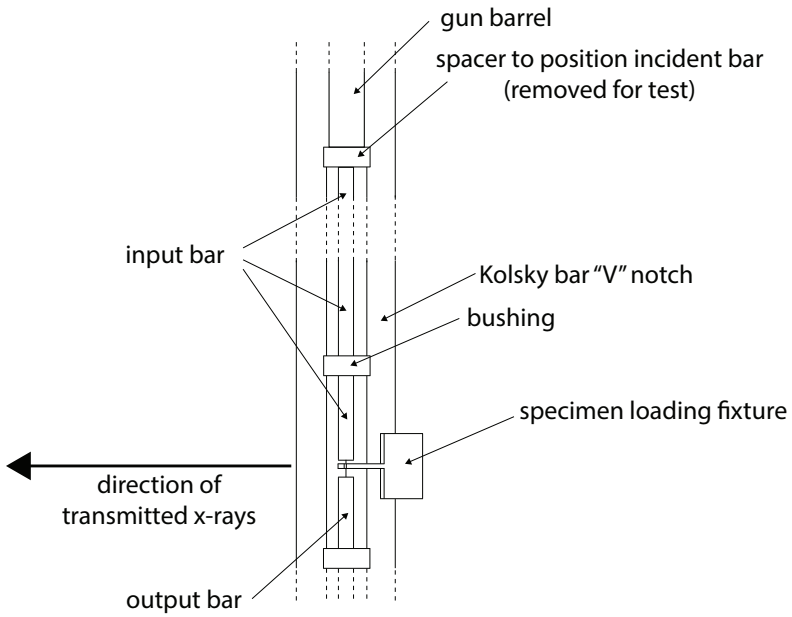

Figure 2.21: A schematic illustration of the specimen loading fixture positioned against the Kolsky bar apparatus so that the small specimen is consistently placed along the axis of the input and output bars. This illustration views the Kolsky bar apparatus from above.

galvanometer shutters, so we instead employed two optical gates in the path of the striker in conjunction with a microcontroller which calculated the appropriate time for the shutters to open. Details of this microcontroller system are provided in the Appendices. Specimen exposure to x-rays during each compression event was limited to a few hundred microseconds, and was limited by the speed at which the shutters could fully reveal and fully block the relatively tall x-ray beam.

Sample data from this experiment will be shown as necessary in later chapters.

2.3.8 Summary: Comparison of techniques

Table 2.6 summarizes several of the important attributes of each technique described above. Each technique had relative strengths and weaknesses. Due to the comparatively low flux of the undulator used in Technique 1, data collected with that technique simultaneously suffered from low diffracted intensity and undesirably long integration times. The inability to capture more than one diffraction pattern per specimen was also a disadvantage, especially since the timing of the diffraction pattern relative to the deformation event was largely up to chance. (Recent improvements to the experimental technique have largely removed that element of chance.) In contrast, the large detector format and high angular resolution achieved in Technique 1 allowed for surprisingly effective analysis of elastic lattice strains (given the very low diffracted intensity). The ability to test dense specimens which are several cubic millimeters in volume using Technique 1 was also advantageous.

The benefits of Technique 2 stem primarily from the fast, direct-detection x-ray detector. The Keck PAD's high dynamic range, high quantum efficiency at 10 keV, and ability to record 8 diffraction patterns per specimen was extremely advantageous for analyzing texture evolution in specific segments of diffraction peaks. The straightforward, highly automated way in which detector timing parameters can be changed was also very useful as it minimized user error. However, the small size/number of pixels on the detector prevented recording large azimuthal angles or large numbers of diffraction rings simultaneously. In addition, the quantum efficiency of the Keck PAD is much worse at the higher x-ray energies which would be needed to perform transmission experiments on materials denser than the magnesium alloys we tested. A larger-format pixel array detector with higher quantum efficiencies at high x-ray energies (*e.g.* through the use of a cadmium telluride detection layer) would be exceedingly desirable for these time-resolved diffraction studies.

The biggest benefit of the experiments performed at DCS is the high flux at high x-ray energies produced by the DCS undulators. This makes it possible to perform transmission diffraction experiments on dense materials (*e.g.* transition metals) of a manageable specimen size, while also having relatively short exposure durations. The detector array used at DCS has some advantages and disadvantages compared with the other two detectors. It is able to collect more diffraction patterns per specimen than the amorphous Si detector at Sector 1, but only half as many patterns per specimen as the Keck PAD. In addition, each high-speed camera in the detector

array has a unique beam center, camera length, pixel size, distortion correction, and relative intensity compared with the other cameras in the array. This makes analysis of data collected using this detector array much more tedious than analysis of Keck PAD data, which requires the determination of only one set of detector parameters. Further, the use of beamsplitters in the DCS detector array reduces the intensity seen by each camera by a factor of 4 compared with what a single camera would see in the absence of beam splitters. The DCS detector array also has a smaller dynamic range than the Keck PAD.

The combined effects of these last two points put some experimental constraints on the exposure durations we could employ while studying 10% Ni steel. The ferrite/martensite {110} peak in steel diffracts quite strongly, which meant we had to limit our exposure durations to avoid saturating the detector with diffraction from this peak. However, other peaks of interest in steel diffract much less strongly than the ferrite/martensite {110} peak, so these limited exposure durations resulted in a relatively low signal-to-noise ratio in these peaks of interest. The DCS detector array does offer two distinct advantages over the Keck PAD, however: it has more pixels and a better quantum efficiency at higher x-ray energies. This allowed us to examine full diffraction rings in steel in the transmission geometry, which we would not have been able to do effectively with the Keck PAD.

A comparison of the results obtained with monochromatic and "pink" x-ray radiation reveals mixed results in both cases. Pink beam is clearly more useful for mea-

surements of integrated peak intensity (*e.g.* for texture and phase evolution studies) with very short exposure durations. Monochromatic radiation offers distinct advantages in terms of angular resolution, and may be the only sensible choice if resolution of closely-spaced peaks is critical. However, pink beam can still be used to assess elastic lattice strains with some degree of precision. This has been demonstrated in the literature [59], and we have done some analysis (not shown here) of the data collected on magnesium alloys which provides useful insights on elastic strains despite the use of pink beam. Attempts to extract information about elastic strains from the pink beam data collected at DCS, however, has yielded only minimal success[5], as is discussed in Chapter 5. This implies that an x-ray beam bandpass much larger than $\sim 2\%$ greatly hinders one's efforts to extract elastic strain information from the resulting diffraction patterns.

2.4 X-ray diffraction data analysis

In order to convert the raw x-ray data into intelligible information about the microstructure of the specimen, the following steps were taken:

- Analysis of the Kolsky bar data, using the methods described in Reference [5].
- Determination of the amount of plastic strain the specimen had undergone when

[5]This comment only applies to the data collected in Technique 3-3 using the 4th undulator harmonic of the U30 undulator. So little usable data was collected in Technique 3-1 using that pink beam that we cannot draw real conclusions about our ability to extract elastic strain information from those diffraction patterns.

Technique	1 (APS Sector 1)	2 (CHESS Hutch G3)	3-1 (DCS)	3-2 (DCS)	3-3 (DCS)
Beam type	mono	pink	pink	mono	pink
Detector	Slow	Fast	Fast	Fast	Fast
Patterns/specimen	1	8	4	4	4
Temporal resolution used μs	42	2.5-5	5	20	1-5
Temporal resolution currently possible	42 μs	70 ns	40 ps	40 ps	40 ps
X-ray energy (keV)	86	10	23.4	30	32
Undulator harmonic used	N/A	1st	1st/2nd	N/A	4th
Bandpass	$\sim 0.01\%$	$\sim 2\%$	$\sim 2.7\%+$	$\sim 0.04\%$	$\sim 5.3\%$

Table 2.6: Table of some relevant experimental differences between each of the *in situ* diffraction techniques used in this work.

the x-ray data was collected. This was achieved by relating the x-ray detector signal-time curve recorded by the data acquisition system to the strain-time curve created using the strain gauge signals from the Kolsky bar.

- Approximation of the thickness of the specimen (along the direction of x-ray travel) at the time the x-ray data was collected. Because plastic strain does not change the specimen volume, the expansion strain in the thickness direction (and the vertical direction) will be approximately one-half the compressive strain in the loading direction. The specimen thickness is important for determining the absorption factor for the specimen.

- Subtraction of background from the data. We are only interested in the elastic scattering of x-rays by the specimen, but a variety of other scattering processes are happening simultaneously (*e.g* air scattering, inelastic scattering from the specimen, interaction of the tail ends of the x-ray beam with the incident and transmitted bars, etc.) and this scattered signal on the detector can erroneously influence the data analysis if it is not removed. To mitigate the effects of this background signal, we collected several detector captures with x-rays incident on the beamstop but with no specimen positioned between the incident and transmitted bars. We then subtracted the average of these detector captures from the static and dynamic diffraction patterns of the specimens.

- Determination of the x-ray beam center. Very accurate knowledge of the beam

center (*i.e.* with sub-pixel accuracy) is essential for correct interpretation of the elastic strains present in a specimen. There are several possible methods of determining this beam center. Software packages such as Nika [88] can accomplish this by converting the two-dimensional detector data into a series of line plots which show the intensity on the detector as a function of distance from some initial guess at the beam center. The software then fits the intensity from the diffraction peak using a Gaussian function and determines a beam center based on the variations in fitted peak position. Another method, similar to what is employed by Reference [89], is to fit a shape in three dimensions (*i.e.* pixels in the "x" detector direction, pixels in the "y" detector direction, and intensity on each pixel) to the entire diffraction ellipse. This method simultaneously determines the center of a diffraction ellipse and any eccentricity of the ellipse due to residual stresses or detector tilts/distortions. Because this fit considers the entire detector at once, it can also lead to more accurate results than methods similar to what is used by the Nika software, especially if spotty diffraction patterns are used. Reference [89] recommends a few possible ways to accomplish this fit [90, 91]. We have used a method similar to Reference [90] by fitting experimentally-collected diffraction data to a function which represents the intensity of an idealized diffraction ellipse having a Gaussian intensity profile. The well-known Gaussian function for a peak with height A, peak center r, and width described by the parameter w is:

$$y = Ae^{-\frac{\left(x-r\right)^2}{w^2}} \tag{2.10}$$

Utilizing this equation and the equation describing a circle centered at $[x_0, y_0]$, we can define a shape which has a Gaussian intensity profile swept in a circle with radius r about $[x_0, y_0]$:

$$z = Ae^{-\frac{\left(\sqrt{[(x-x_0)-(y-y_0)]^2+[(x-x_0)+(y-y_0)]^2}-r\right)^2}{w^2}} \tag{2.11}$$

Finally, we can generalize this equation to describe a Gaussian which is swept around $[x_0, y_0]$ in an ellipse of eccentricity B and semi-major axis tilt ω with respect to the detector reference frame [92]:

$$z = Ae^{-\frac{\left(\sqrt{[(x-x_0)\cos\omega-(y-y_0)\sin\omega]^2+B[(x-x_0)\sin\omega+(y-y_0)\cos\omega]^2}-r\right)^2}{w^2}} \tag{2.12}$$

Fitting the ferrite/martensite {211} peak in the 10% Ni steel data using this function yields a fitted beam center $[x_0, y_0]$ which is in good agreement with the beam center found using other methods such as those utilized in the software packages FIT2D [82] and Nika [88]. This function is plotted with example parameters in Figure 2.22.

- Transformation of the detector from Cartesian coordinates to polar coordinates, using the measured beam center as the origin. This puts the detector data into

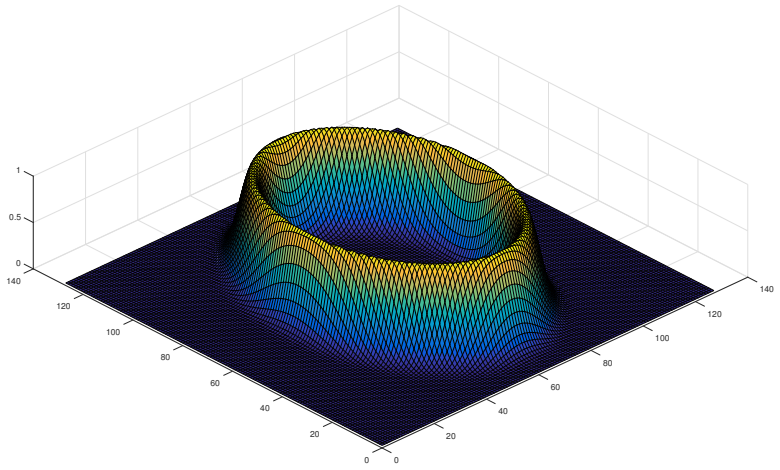

Figure 2.22: Plot of the function used to fit the diffraction pattern beam center, using example parameters. The ellipse eccentricity is highly exaggerated for illustrative purposes.

a more manageable format for creating one-dimensional diffraction patterns, and is very similar to the "caking" procedure available in the software package FIT2D [82].

- Binning and integration of the detector signal. For determining the volume fraction of austenite in the specimen, it is preferable to sample as many grains in the specimen as possible. This would ideally mean integrating the intensity of each diffraction ring around the entire circumference of the ring. However, on many of our experiments the incident bar of the Kolsky bar apparatus moved into the path of the diffracted x-rays during the course of the compression event, obscuring the signal on the right-hand side of the detector. Analysing the intensity of the peaks in this region of the detector would lead to inaccurate

volume fraction measurements, so we instead integrated only the peak intensity on the left-hand side of the detector for volume fraction measurements. Different binning and integration must be done for strain measurements, as the diffraction peak position varies continuously with azimuthal angle. It is therefore important to bin the detector data into relatively small segments so that the peak position (and consequently the elastic strain information) is not averaged over many different values. For the elastic strain measurements described later in this dissertation, integration over an azimuthal angle of 20° was done, although smaller azimuthal angle ranges are preferable for strain analysis. We used a 20° range in order to improve the definition and signal-tp-noise ratio of the integrated peaks.

- Performing corrections for polarization, geometrical factors, and absorption. The absorption correction we utilized is given in Equation 2.8. The corrected intensity $I_{corr,geo}$ accounting for the effects of specimen/detector geometry is [57]:

$$I_{corr,geo} = \frac{I_{obs}}{\cos^2 2\theta} \tag{2.13}$$

where I_{obs} is the uncorrected intensity and 2θ is the scattering angle. The corrected intensity $I_{corr,pol}$ accounting for the effects of polarization in the x-ray beam is [93]:

$$I_{corr,pol} = \frac{1}{2} I_{obs}(1 + \cos^2 2\theta)^2 - f \cos\psi \sin^2 2\theta \tag{2.14}$$

where ψ is the azimuthal angle on the detector and f is the polarization factor for synchrotrons. Typically, $f = 0.9 - 0.99$, and we have assumed a value of 0.98 for our analysis.

- Fitting of the diffraction peaks. Because no monochromator was used at DCS, the "pink" x-ray beam produces diffracted intensity which cannot be fitted with great accuracy using a Gaussian function (which is often used to fit monochromatic x-ray data). Therefore, we instead fitted each integrated, one-dimensional diffraction pattern to a convolution of a Gaussian and the instrument response function. This was done using the "conv" and "lsqcurvefit" commands (to perform the convolution and to fit the convoluted function to the experimental data, respectively) in MATLAB®. Figures 2.23-2.25 demonstrate this convolution process. Figure 2.23 shows an example instrument response function (expressed in terms of intensity as a function of scattering angle) which could be obtained from a synchrotron undulator harmonic. Figure 2.24 shows two example Gaussian functions of different amplitude. In this work, the shape of all diffraction peaks has been assumed to be Gaussian after all instrument response has been corrected for, so these Gaussians are expected to describe physically meaningful aspects of the specimen. Figure 2.25 shows the convolution of the

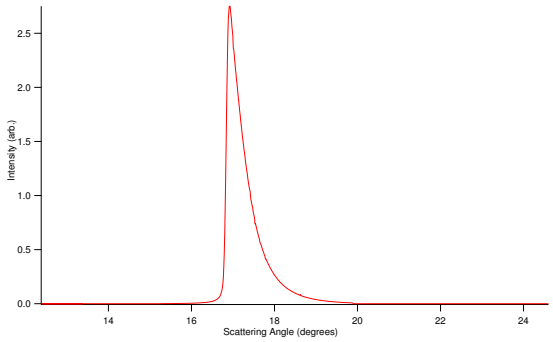

Figure 2.23: Example plot of an instrument response produced by a synchrotron undulator harmonic.

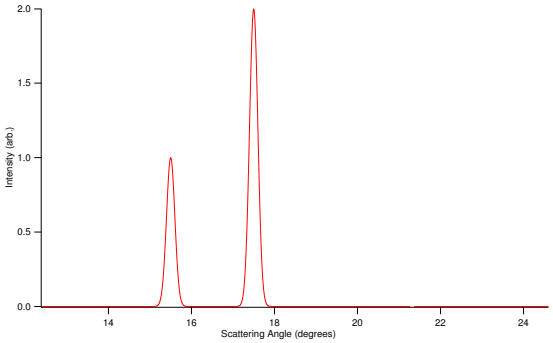

Figure 2.24: An example of two Gaussians (the assumed shaped of the diffraction peaks once the instrument response has been corrected for) of differing amplitudes.

instrument response function in Figure 2.23 and the Gaussians in Figure 2.24. The relative area under each example Gaussian is retained in the relative area under each convolved peak, as would be expected. The fitting algorithm allows the parameters describing each example Gaussian to be varied until the difference between the resulting convolved peak(s) and the experimental data is minimized.

To measure the instrument response function from our actual synchrotron ex-

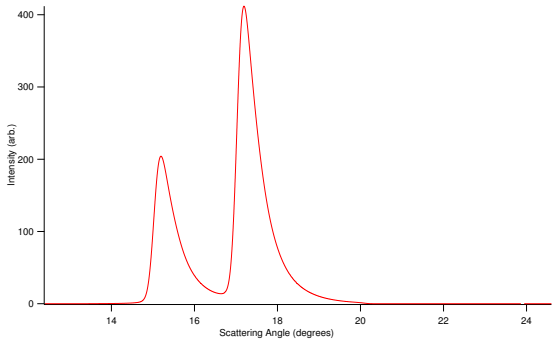

Figure 2.25: The convolution of the instrument repsonse shown in Figure 2.23 and the example Gaussians in Figure 2.24.

periment, we used a background-subtracted, integrated diffraction peak from a NIST 676 x-ray diffraction powder alumina standard reference material recorded using the same beam parameters that were used during the actual experiments. The standard was approximately the same thickness as the tested specimens, and was positioned the same distance from the detector as the specimens were by using the same custom-made fixture that was used to load each specimen into the Kolsky bar.

- Calculation of the time-resolved austenite volume fraction of the specimen based on the fitted integrated peak intensities. Quantitative measurement of austenite volume fraction can be made if two or more full diffraction peaks from each phase are observed through the following equation [94]:

$$V_\gamma = \frac{\left(\frac{1}{n}\sum_{l=1}^{n}\frac{I_l^{(\gamma)}}{R_l^{(\gamma)}}\right)}{\left(\frac{1}{m}\sum_{l=1}^{m}\frac{I_l^{(\alpha+m)}}{R_l^{(\alpha+m)}} + \frac{1}{n}\sum_{l=1}^{n}\frac{I_l^{(\gamma)}}{R_l^{(\gamma)}}\right)} = \frac{\overline{I}^{\gamma}}{\overline{I}^{(\gamma)} + \overline{I}^{(\alpha+m)}} \tag{2.15}$$

where V_γ is the volume fraction of austenite, n is the number of austenite peaks observed, m is the number of ferrite/martensite peaks observed (which are often strongly overlapping), I_l is the observed integrated intensity of peak l, R_l^γ is the predicted integrated intensity of austenite, and $R_l^{\alpha+m}$ is the predicted integrated intensity of ferrite/martensite peak l. The predicted integrated intensity of plane (hkl) from phase i is [94]:

$$R_{hkl}^{(i)} = \frac{K A_{hkl} V_i j \lambda^3 F_{hkl}^2 e^{-B\frac{\sin^2\theta}{\lambda^2}}}{v_i^2 \sin\theta \sin 2\theta} \tag{2.16}$$

where K is an experimental-setup-specific constant which can be neglected when all tests are conducted under the same conditions, V_i is the volume fraction of phase i, j is the multiplicity of plane (hkl), F_{hkl}^2 is the structure factor of plane (hkl), v_i is the unit cell volume of phase i, B is the Debye-Waller factor [95], θ is the Bragg angle, and A_{hkl} is an absorption factor. In these experiments, Equation 2.8 defines the applicable absorption factor.

- Calculation of the time-resolved elastic strain in various subsets of crystallographic planes within the specimen, as described in Chapter 5.

These steps were taken using a Matlab script written in-house. This script is reproduced in the Appendices.

2.5 Microstructural characterization

2.5.1 EBSD specimen preparation

10% Ni steel Specimens to be examined with EBSD were mounted in PolyFast conductive resin cylinders 25.4 mm in diameter. They were then mechanically ground and polished using a Struers© Abrapol-20 semi-automated polisher. Large specimens (*i.e.* the specimens that were tested outside the synchrotron) were polished using the following polishing steps:

- 120 grit sandpaper (until flat, water lubricated, 50 N force, 300 rpm platen rotation speed, 150 rpm specimen holder co-rotation speed)
- 240 grit, 320 grit, 600 grit, and 800 grit sandpaper (3 minutes each, water lubricated, 50 N force, 300 rpm platen rotation speed, 150 rpm specimen holder co-rotation speed)
- 3 μm and 1 μm Al_2O_3 polishing suspensions (7 minutes each, lubricated with Struers DP-Lubricant Blue, 50 N force, 300 rpm platen rotation speed, 150 rpm specimen holder co-rotation speed)
- 0.04 μm colloidal SiO_2 (7 minutes, 50 N force, 300 rpm platen rotation speed, 150 rpm specimen holder co-rotation speed)
- vibratory polishing in a Buehler Vibromet polisher containing 0.04 μm colloidal

SiO_2 (4 hours, maximum amplitude)

The specimens tested at the synchrotron were so small that this polishing procedure posed a serious risk of polishing away the entire specimen. Instead, specimens were polished with 600 grit paper until flat, and then the procedure above was followed starting with 800 grit.

Finally, the specimens were milled for 10 hours in a Fischione 1060 ion mill. Two ion sources were used, with an accelerating voltage of 6 kV, an angle of incidence of 2°, and a source focusing of 45%. The specimens rotated at a rate of 3 rotations per minute during milling. This specimen preparation procedure was chosen to minimize the possibility of both preferential etching of phases and of preparation-induced transformation of austenite occurring at the surface of the specimen, both of which would produce erroneous EBSD measurements. Other preparation techniques were tried, including a laser milling procedure, as well as the above procedure without the final ion milling step. These other procedures resulted in EBSD maps with measured austenite volume fractions which were lower than what was obtained with the ion milling procedure, and which were further from the expected value based on VSM and x-ray diffraction measurements of the austenite content. This may have been a result of DIMT of austenite on the specimen surface, even with very gentle mechanical polishing [96]. This hypothesis is supported by the fact that we have observed larger austenite particles in ion milled specimens (maximum observed size > 2 μm) than have been observed in vibratory polished specimens (maximum observed size

~ 1 μm). Because larger austenite particles are more likely to undergo DIMT, measurement of them is more likely to be influenced by insufficient specimen preparation.

2.5.2 EBSD data collection

Specimens were examined in a Hitachi SU6600 SEM[6]. Specimens were tilted to 70°. An accelerating voltage of 15 kV was used, with an extraction voltage of 2.00 kV, medium probe current, anode aperture "3," objective aperture "2," and a Condenser Lens 1 setting of 1.0. EBSD patterns were recorded using and EDAX Hikari EBSD detector and the EDAX OIM 7.0 software. The EBSD detector was binned using 5×5 bins, and patterns were collected at a rate of 70 patterns per second with 0 gain. Patterns received a static background subtraction and histogram normalization. Five reflectors were used to identify the austenite phase, while four reflectors were used for the ferrite phase. Data was collected with a 50 nm step size and a magnification of 2000x. The full Kikuchi patterns were saved at each pixel to aid in future data analysis.

These parameters (for both specimen preparation and data collection) were selected after a thorough optimization process intended to detect the austenite particles in the specimens as accurately as possible, while still gathering good statistics on the microstructure of the steel in a timely manner, which is critical for accurately understanding the microstructure of this steel given the amount of local microstructural

[6]This microscopy was performed using equipment at the Naval Surface Warfare Center, Carderock Division in Bethesda, Maryland.

inhomogeneity it has. This optimization process was undertaken because preliminary EBSD results measured an austenite volume fraction much lower than what was measured by both vibrating sample magnetometry (VSM) and synchrotron x-ray diffraction measurements. (These other measurements were in fairly good agreement with each other, which is detailed in Chapter 3 and illustrated most clearly in Figure 3.15. A comparison of the vol.% austenite measured by all three techniques for nominally-identical 10% Ni steel specimens can be found in Table 3.1.) There are several examples in the literature of EBSD measurements of austenite volume fraction being lower than the volume fraction measurements made in other ways [8, 97, 98], but the discrepancy was unusually large for the 10% Ni steel studied here. (The work done by Jacques *et al.* [8] on this matter is illuminating for an experimentalist studying multi-phase materials, as it rigorously compares the measured austenite volume fraction in TRIP steels of different compositions using different techniques, and illustrates the surprising difficulty of determining accurately even a "simple" material characteristic such as total phase fractions. A schematic representation of how one might expect different measurement techniques to differ in their reporting of austenite content is shown in Figure 2.26.)

During the EBSD optimization process, direct inspection of the patterns recorded on the EBSD camera revealed many obvious instances where a pattern was indexed with a low confidence index (CI) not because of poor pattern quality, but because of the strong overlapping of two or more distinct patterns. This indicates that the

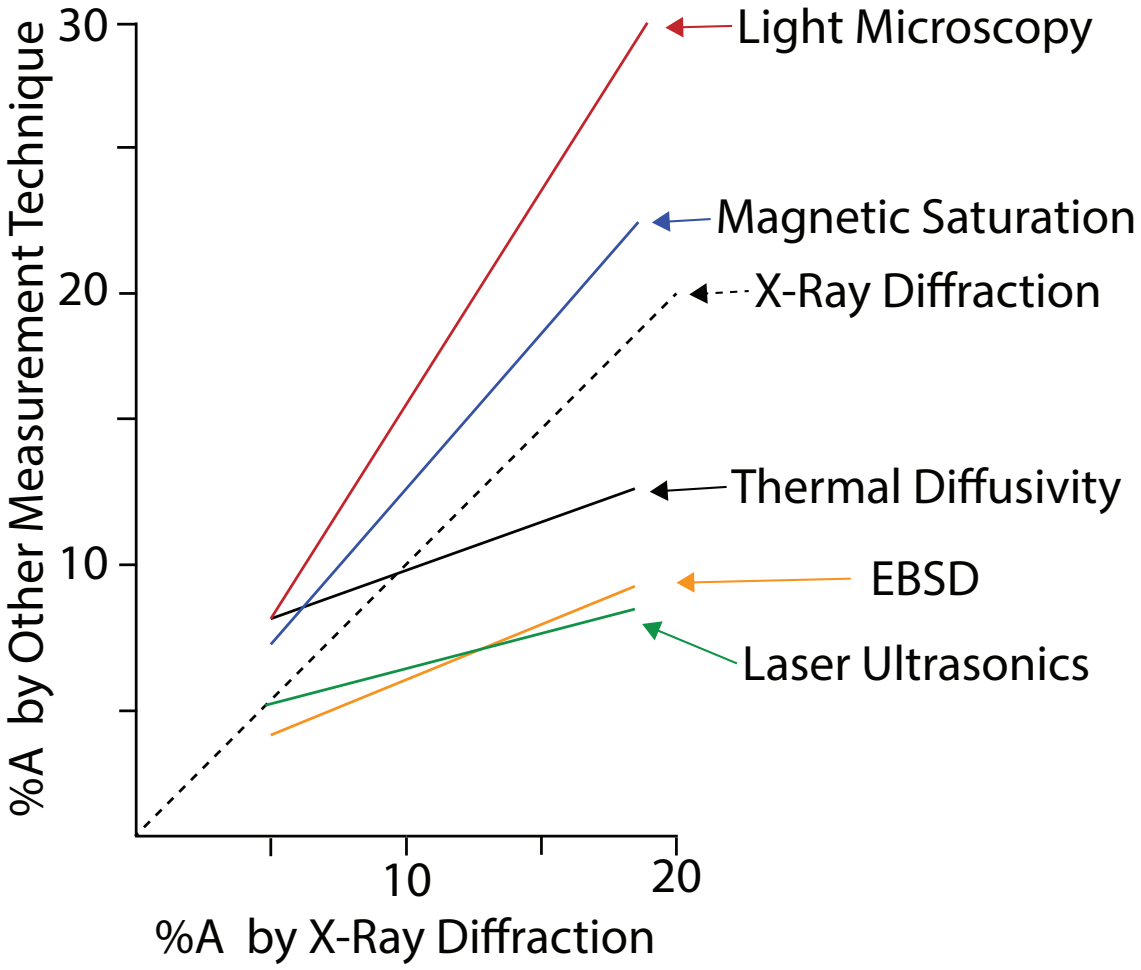

Figure 2.26: Schematic representation of the variation in vol.% austenite detected in the same collection of steels using different measurement techniques. Adapted from Ref. [8].

pattern was recorded at a grain boundary or phase boundary. The step size used (50 nm) is much smaller than the ferrite/martensite lath size, so the abundance of overlapping patterns suggests a very small austenite particle size. We attempted to mitigate this problem by reducing the accelerating voltage used (and hence the electron interaction volume in the specimen), but this caused no overall improvement in pattern indexing and dramatically decreased the data acquisition speed.

With this problem of overlapping patterns in mind, increasing the number of austenite reflectors checked for by the EBSD software tended to increase the measured austenite volume fraction closer to expected levels while still producing plausible maps of the microstructure (*i.e.* austenite was still measured in expected places within the microstructure and with plausible orientations relative to neighboring ferrite/martensite grains). In the future, using techniques such as transmission Kikichi diffraction (TKD) or precession electron diffraction (PED) may help resolve these small austenite particles more effectively. However, conventional EBSD measurements are still valuable, as it would take a very long time to gather representative data on the whole microstructure using these other methods. This is due to the combination of moderate pixel-per-second data collection speeds and the extremely small pixel spacing needed to resolve very small particles, as well as the fairly limited portion of each TKD or PED specimen which is thin enough to examine.

2.5.3 Scanning electron microscope (SEM) secondary electron imaging

Specimens being prepared for conventional SEM imaging in secondary electron mode were polished with a method similar to what was used for EBSD, although the ion milling was forgone[7]. Immediately after polishing, specimens were etched with a solution of 2% nitric acid in ethanol for ~ 5 seconds. (It is important that the etching be done immediately after polishing, as the steel tends to develop a passivated surface layer over time which makes the etchant work much less effectively and predictably.) Specimens were then examined in a Hitachi SU6600 SEM using an accelerating voltage of 5 kV. Some specimens were etched longer if the first etching did not reveal sufficient microstructural contrast.

2.5.4 Vibrating sample magnetometry (VSM)

We used a LakeShore model 7304 vibrating sample magnetometer (VSM) to rapidly obtain a bulk measurement of the austenite volume fraction present in steel specimens[8]. This is done by exploiting the fact that (in most circumstances) the ferrite and martensite phases of steel are ferromagnetic, while the austenite phase is not. To perform these measurements, first the VSM was calibrated using a NIST-produced

[7]This microscopy was performed using equipment at the Naval Surface Warfare Center, Carderock Division in Bethesda, Maryland.

[8]These measurements were performed using equipment at the Naval Surface Warfare Center, Carderock Division in Bethesda, Maryland.

Ni disk having known magnetic characteristics. Next, the specimen to be measured was suspended between the poles of the VSM, and a 14 kG magnetic field was applied so that the steel specimen was well into its saturation magnetization regime. After saddling the specimen, its magnetization was recorded. The magnetization per unit mass of the sample $M_{s,sat}$ was divided by $M_{f,sat}$, the saturation magnetization of purely ferromagnetic Fe containing 10 wt.% Ni, which was calculated to be 213.1 emu/g using Ref. [99]. This ratio represents the mass fraction of (ferrite + martensite) in the specimen, or, equivalently:

$$F_{\gamma,mass} = \frac{1 - M_{s,sat}}{M_{f,sat}} \tag{2.17}$$

represents the mass fraction of austenite $F_{\gamma,mass}$ in the specimen. (Strictly speaking, this number represents the sum of the mass fractions of austenite and of any other non-ferromagnetic phases such as carbides in the specimen, but the mass fraction of carbides was assumed negligible here. Carbide peaks are generally not observable in the x-ray diffraction patterns for this steel, suggesting that the volume fraction of carbides is well under $\sim 2 - 3\%$, and the mass fraction will be even lower due to the comparatively low density of the carbides.) Austenite is $\sim 6\%$ more dense than martensite and ferrite, so the volume fraction of austenite is then:

$$F_{\gamma,volume} = \frac{1}{1 + 1.06(\frac{1}{F_{\gamma,mass}} - 1)} \tag{2.18}$$

2.6 Stress factor measurements

Tensile specimens with a gage volume of $120 \times 10 \times 3$ mm were strained in a servo-hydraulic load frame while being irradiated with neutrons[9]. Measurements of the changes in peak positions from the unstrained state to the strained state were taken in order to determine the stress factor [9, 100–102] for each family of crystallographic planes. These stress factors F_{11} relate the macroscopically applied uniaxial stress to the measured elastic normal strains in certain crystal planes in certain directions in the specimen reference frame while that macroscopic stress is applied. Figure 2.27 provides a helpful reference frame for this discussion. If a uniaxial stress is applied along the "x" direction in Figure 2.27, then the stress factors relate elastic strains in specific subsets of crystal planes within the material to the macroscopically-applied stress in the following way [9]:

$$\epsilon(\phi, \psi, hkl) = F_{11}(\phi, \psi, hkl)\overline{\sigma}_{11} \tag{2.19}$$

where $\overline{\sigma}_{11}$ is the macroscopically applied uniaxial stress and $\epsilon(\phi, \psi, hkl)$ is the normal strain in a specific subset of planes $\{hkl\}$ which are oriented with the polar angles (ϕ, ψ) shown in Figure 2.27.

Measurements were conducted on a specimen at room temperature and on a specimen held at 200 °C. For each of these specimens, the stress factors for each peak were

[9]Thomas Gnäupel-Herold of NIST is gratefully acknowledged for conducting these measurements.

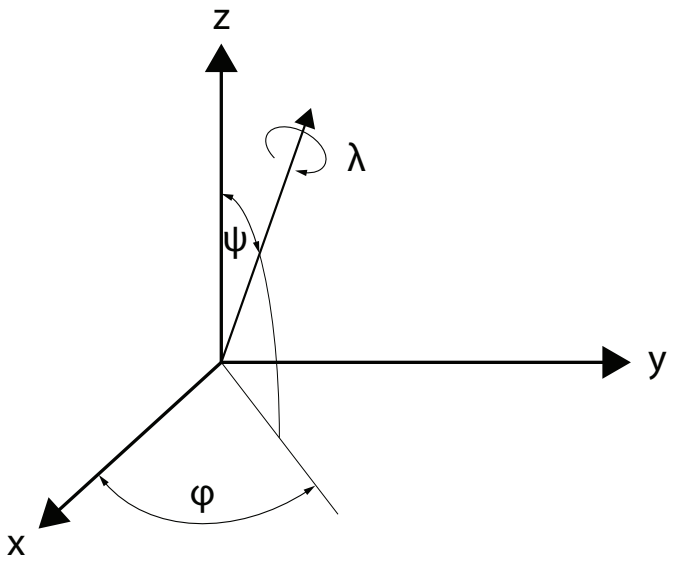

Figure 2.27: Reference frame used for Equation 2.19. Specimens were loaded along the "x" direction. Adapted from Reference [9].

measured at 0% plastic strain and at 7% plastic strain. The gage volume interrogated by neutrons was $2.5 \times 2.5 \times 10$ mm.

Depending on the scattering angle of the peak being observed, either the transmission geometry or the reflection geometry was used. For scattering angles $2\theta < 90°$, geometric restrictions imposed by the load frame make the transmission geometry preferable, while for scattering angles $2\theta > 90°$, the reflection geometry was used. In order to achieve proper geometric positioning of the beam slits close to the specimen, different neutron wavelengths from $\sim 90 - 200$ pm were chosen depending on the family of crystal planes being observed and the experiment geometry (transmission or reflection).

The results of the VSM measurements, synchrotron technique 3-3, and several

other experimental techniques described here will be discussed in the next chapter.

Chapter 3

Austenite evolution due to heat treatment and dynamic deformation in a 10% Ni steel

In the first part of this chapter, we will characterize the effect of previously-described QT, QL, and QLT heat treatments (with heat treatment parameters listed in Section 2.1.5) on the microstructure of an experimental 10% Ni steel. We will pay particular attention to the austenite phase in this analysis, given the relatively important role that mechanically-unstable austenite plays in the mechanical properties of steels where it exists. We will approach this task using both bulk measurement techniques (VSM and synchrotron x-ray diffraction) and local, surface techniques (SEM and EBSD).

In the second part of this chapter, we will discuss the transformation of austenite during dynamic deformation, which was quantified *in situ* using synchrotron diffraction and *ex situ* using VSM. The motivation for conducting both *in situ* and *ex situ* testing was to determine whether collecting data *in situ* can provide more accurate insights into the material's microstructural evolution related to the martensitic transformation. This transformation is promoted by increasing plastic strain, but is inhibited by increasing temperature. In dynamic deformation, the material simultaneously experiences increasing plastic strain and increasing temperature, followed by decreasing temperature after deformation has stopped. It is therefore possible (at least in principle) for some population of austenite particles within the material to remain stabilized against transformation *during* the deformation event, but then transform *after* deformation stops while the specimen returns to ambient temperature. If this occurred, *ex situ* measurements of the austenite volume fraction after various amounts of dynamic deformation would not be representative of real material behavior (or at least, not the type of material behavior which is relevant to designing microstructures that are more resistant to ballistic penetration). Knowledge of this behavior would have consequences for any micromechanical models developed to describe the material during dynamic deformation, and so we sought to determine if this behavior existed in the steel being studied.

Following a comparison of the *in situ* and *ex situ* measurements of transformation behavior (which was only conducted for the QLT specimens, as any discrepancy

between *in situ* and *ex situ* results was expected to be largest in this condition), we will discuss the effects that this transformation and the initial steel microstructures have on the compressive mechanical properties of each heat treatment. More detailed characterization of the deformed QLT microstructures using EBSD will be presented in Chapter 4.

3.1 Austenite evolution due to heat treatment

Before a detailed discussion of the microstructure resulting from each heat treatment, it is worthwhile to mention an important phenomenon which should be kept in mind when trying to characterize this steel's microstructure. This phenomenon is the banding structure which very often appears in hot-rolled steels. This phenomenon originates with the dendritic solidification of steel ingots, with early-solidified portions of the ingot containing fewer alloying elements than later-solidified portions. The hot-rolling process causes these dendrites to roughly align with the rolling direction of the plate. Although subsequent heat treatment processes will homogenize the steel's chemical composition to some extent, remnants of these compositional differences are almost impossible to eradicate in practical settings [103].

These minor compositional differences can translate into more pronounced local differences in thermally-stable austenite. These bands of austenite-rich and austenite-

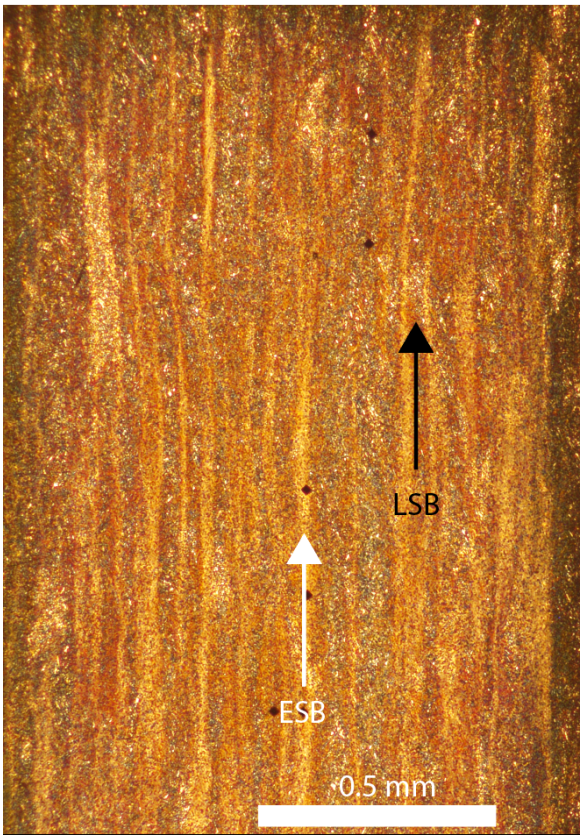

Figure 3.1: Light optical micrograph of an etched QLT-treated specimen showcasing early- and late-solidified bands (labelled with white and black arrows, respectively).

poor microstructure are particularly obvious in the QLT-treated condition, due to its higher total austenite content (which is quantified for each heat treatment in Table 3.1). Examples of these bands can be seen in Figure 3.1, and are on the size scale of $\sim 20-50$ μm. (In optical micrographs of etched specimens, the late-solidified bands appear darker due to increased scattering of light off of the more-prevalent austenite particles.)

In order to get an accurate picture of the total microstructure, any characterization technique used must look at the material on a large enough length scale to average

over (at a minimum) two of these bands. This put a lower limit on the x-ray spot size we could use to interrogate the specimens at the synchrotron. This also necessitates considering numerous micrographs taken from several positions on a given specimen, or using micrographs with relatively low magnification, in order to have representative information about the microstructure as a whole. In addition, it means that high-resolution investigations of the material with techniques such as TEM or atom probe tomography would require examining a very large number of specimens before one could develop a representative understanding of the whole microstructure.

The austenite content of each steel in the undeformed state, as determined using different characterization techniques, is summarized in Table 3.1[1]. These results, and other specifics of the microstructure of each specimen, are described in detail below.

Heat-treatment	vol.%A (VSM)	vol.%A (Synchrotron XRD)	vol.%A (EBSD)
QT	8.5 ± 0.7	5.8 ± 1.8	6.7 ± 3.5
QL	14.6 ± 0.3	11.1 ± 1.4	7.1 ± 2.4
QLT	20.8 ± 0.3	23.5 ± 2.8	13.3 ± 1.4

Table 3.1: Average vol.% of austenite present in each heat-treated steel, measured using different characterization tools.

3.1.1 QT heat treatment

VSM measurements of three QT-treated specimens from the same heat-treated workpiece and synchrotron diffraction measurements of the QT-treated specimens

[1]The uncertainties listed are the standard deviation of all measured values.

are summarized in Table 3.1. The numbers reflect a mild increase over the measured austenite volume fraction in the as-quenched ("Q-treated") steel of 4.6 vol.% as measured by VSM [1].

Figure 3.2 shows an SEM micrograph of the QT-treated material in the undeformed condition. The microstructure consists of a tempered martensite/ferrite matrix with a small fraction of austenite particles (appearing lighter in the micrograph) along prior austenite grain boundaries, and occasionally along martensite packet and lath boundaries.

Figure 3.3 is a representative EBSD inverse pole figure (IPF) map collected on a QT-treated specimen, showing the entire microstructure and the austenite phase only. The austenite volume fraction according to EBSD is 6.7%, which is in reasonable agreement with the bulk measurements. Close examination of the EBSD map and the accompanying austenite particle size distribution (see Figure 3.4) reveals that there are a few larger, blocky particles and many thinner, more film-like particles only a few pixels ($\sim$ 100 nm) in diameter.

3.1.2 QL heat treatment

VSM measurements of three QL-treated specimens from the same heat-treated workpiece and synchrotron diffraction measurements of the QL-treated specimens are summarized in Table 3.1. Figure 3.5 shows an SEM micrograph of the QL-treated material in the undeformed condition. It consists of a ferrite/tempered martensite

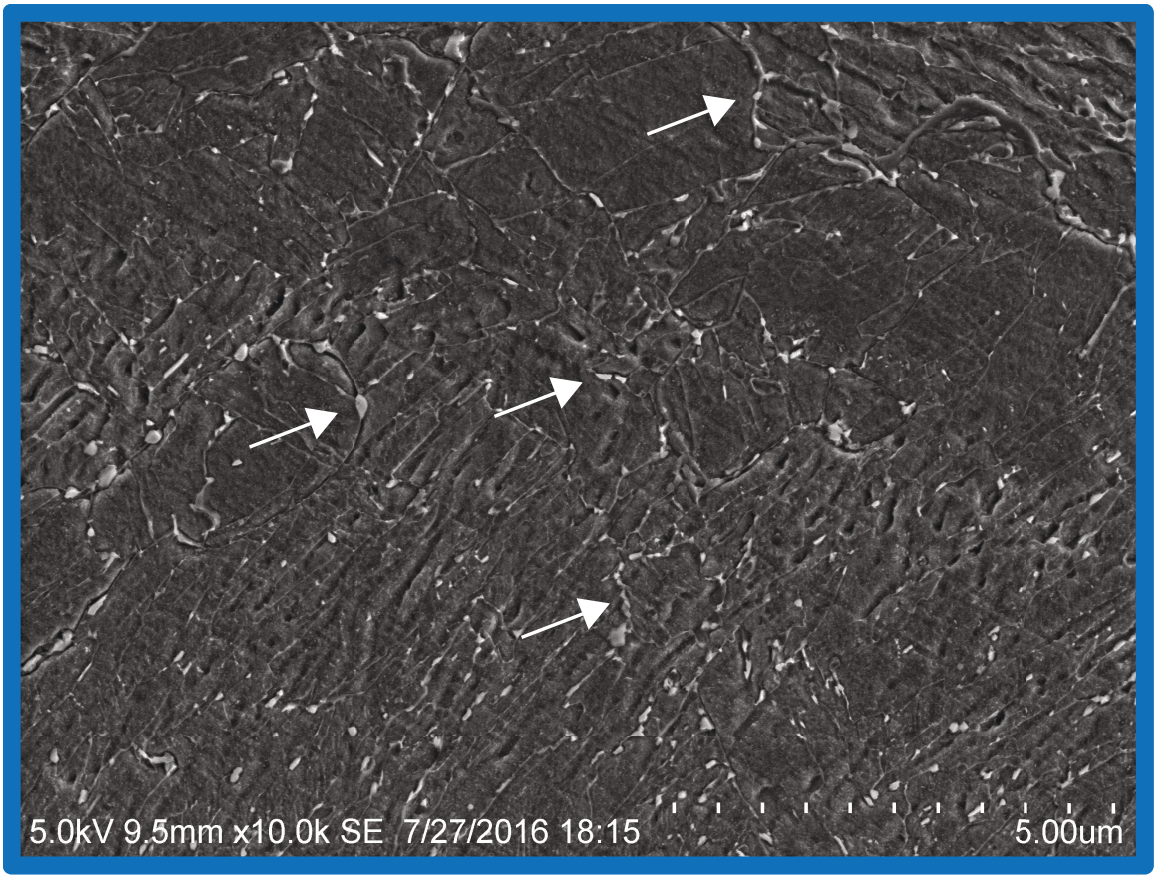

Figure 3.2: SEM micrograph of a specimen in the QT heat treated condition. Arrows indicate examples of austenite particles.

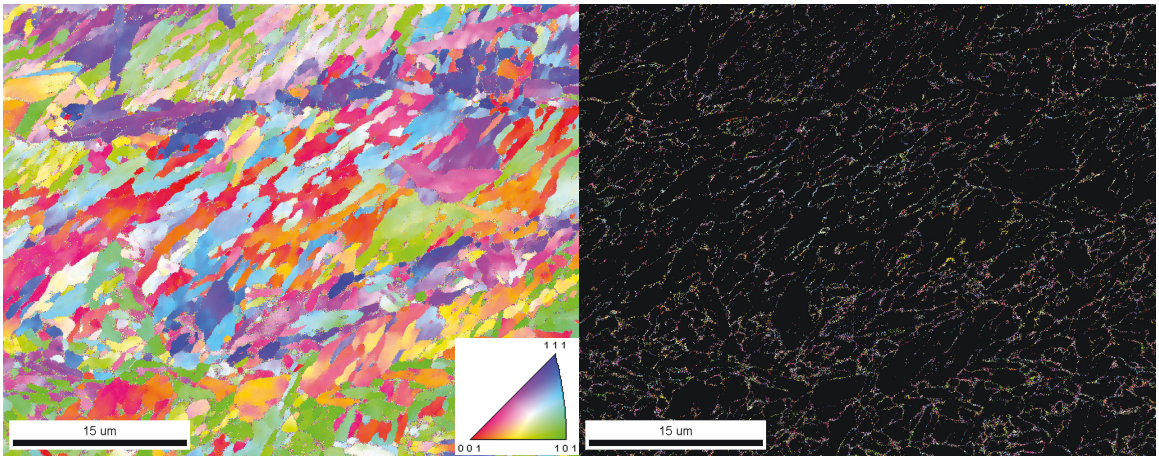

Figure 3.3: IPF map of a specimen in the QT heat treated condition.

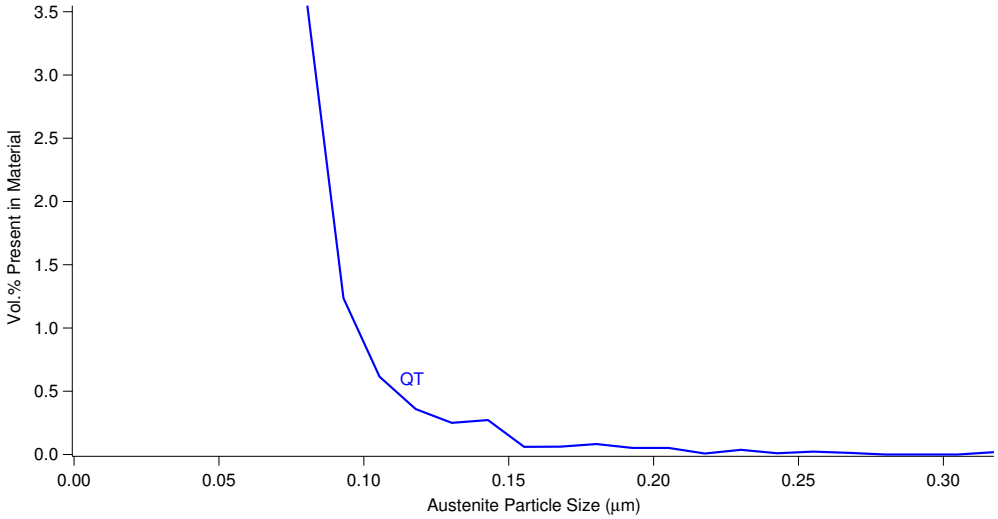

Figure 3.4: Grain size distribution of austenite particles in the QT-treated steel, expressed as a volume fraction that particles of a given size occupy in the specimen as a whole.

matrix and a light-shaded constituent along a large percentage of the packet and lath boundaries. This micrograph lends the impression that there is dramatically more austenite present in this material than in the QT-treated condition. Appearances can be deceiving, however. The light-shaded constituent covers far too large a fraction of the micrograph to be austenite, when compared with austenite volume fraction measurements made on this steel using VSM, XRD, and EBSD. In addition, SEM micrographs and EBSD maps collected on the same areas of the microstructure containing this light-shaded constituent in the QL material reveal that there is often negligible change in crystal orientation between the light-shaded constituent and the surrounding ferrite/martensite grains. This point is illustrated in Figure 3.6 using a specimen which received a slightly different QL treatment from what is receiving

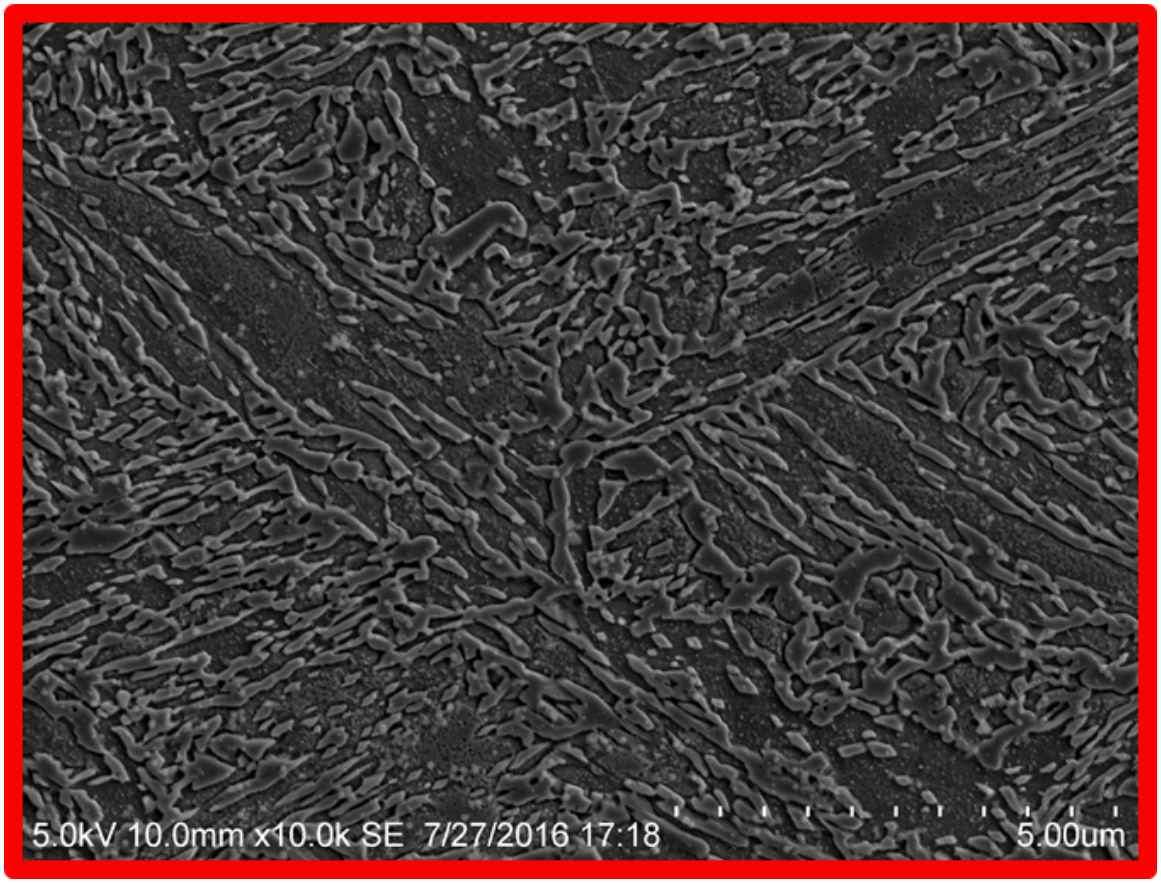

Figure 3.5: SEM micrograph of a specimen in the QL heat treated condition.

primary attention in this dissertation.

Much of this light-shaded constituent is, in fact, martensite which is chemically distinct from the surrounding ferrite/martensite. It may be fresh martensite that was austenite while at the L temperature but was not chemically stabilized with enough Ni and C to avoid transforming to martensite upon quenching from the L temperature. Dilatometry measurements made on a specimen undergoing a similar L heat treatment reinforce this point (see Figure 3.7). A substantial amount of austenite formed at L temperature (which will have a higher Ni content than the ferrite stable at L

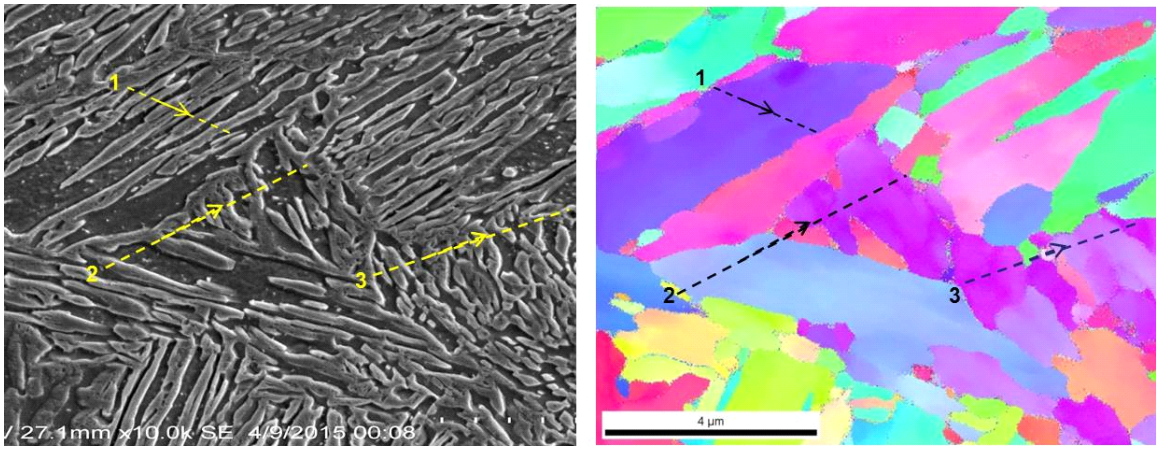

Figure 3.6: (Left) Secondary electron image and (right) EBSD scan of the same region of a 10% Ni specimen which received a QL heat treatment. Most of the features visible in the secondary electron image are not discernible in the EBSD scan. *Images courtesy of Dr. X.J. Zhang.*

temperature) undergoes a diffusionless transformation into martensite upon cooling to room temperature, which is suggested in the dilatometry data by the specimen dilation and the fact that austenite is $\sim 6\%$ more dense than martensite. Unfortunately, this bulk dilatometry measurement cannot verify that this transformation occurs in the regions of the microstructure where the light-shaded constituent is observed.

Figure 3.8 is a representative EBSD IPF map for the entire QL-treated material and for the austenite phase. Austenite particles appear to decorate the martensite packet and lath boundaries, similar to what is observed in the QT condition. Thus, while the light-shaded constituent is evidently not composed entirely of austenite, it also evidently must contain some austenite component. This ultrafine agglomeration of martensite and austenite is aptly described in the literature as an "M/A constituent" [1, 104, 105]. As seen in Figure 3.9, the maximum austenite particle size

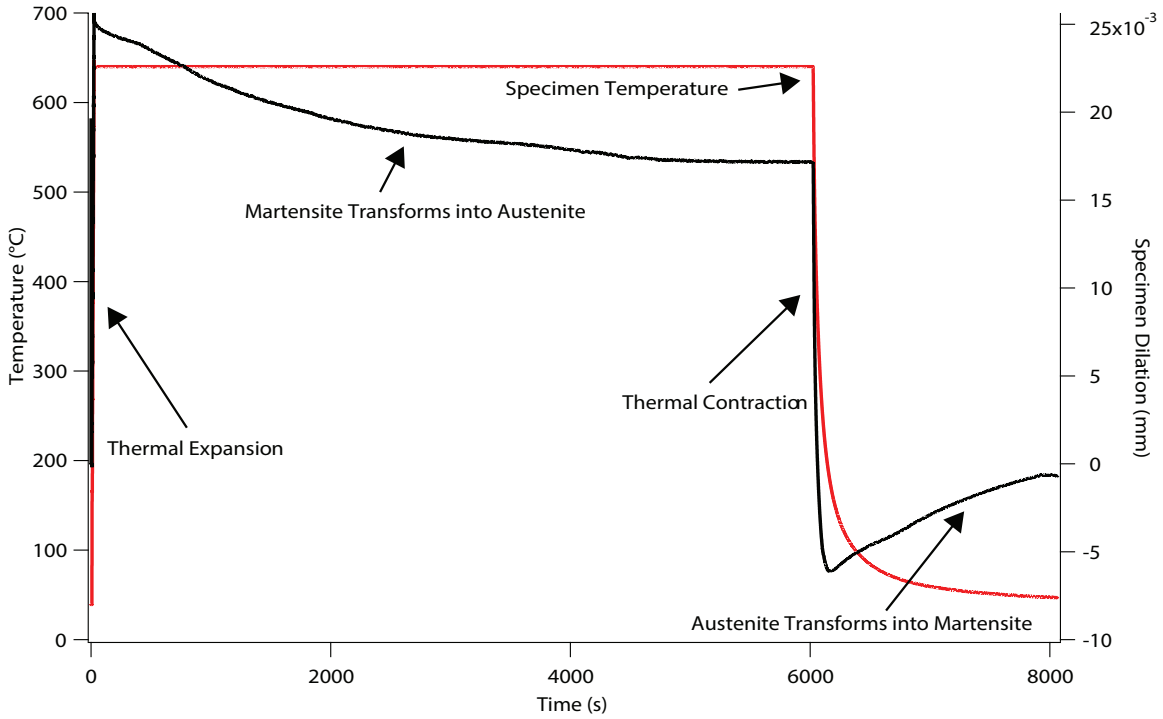

Figure 3.7: Dilatometry measurement of a 10% Ni steel specimen undergoing an example L treatment (at a slightly lower temperature and longer time than the L treatment focused upon in this dissertation).

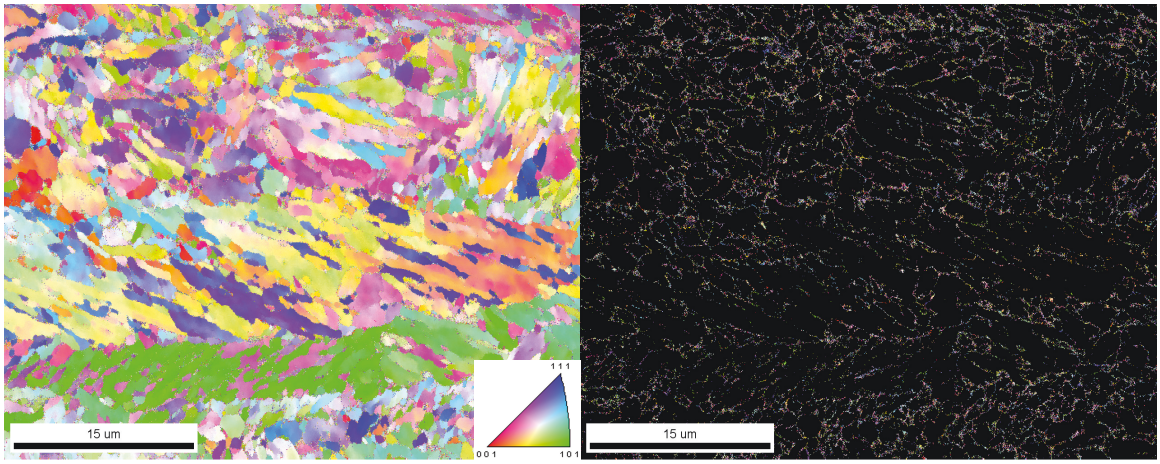

Figure 3.8: (left) IPF map of a specimen in the QL heat treated condition. (right) The same IPF showing the austenite phase only.

and relative austenite particle size distribution does not vary significantly between the QL- and QT-treated specimens, even though (according to bulk measurements) the total austenite volume fraction appears to be clearly higher in the QL-treated condition.

Unlike in the QT condition, in the QL condition the austenite volume fraction measured by EBSD is somewhat lower than what is measured by bulk measurements. As mentioned previously, EBSD often under-reports the volume fraction of austenite compared with other methods [8]. Based on the extensive EBSD optimization process we conducted, it seems unlikely that the discrepancy is due to specimen preparation-induced transformation of austenite particles at the specimen surface. As will be explained in the next chapter, our other EBSD measurements suggest that the calibration problems proposed in Reference [8] do not explain the discrepancy either.

The most likely explanation for the discrepancy is that a large portion of austenite

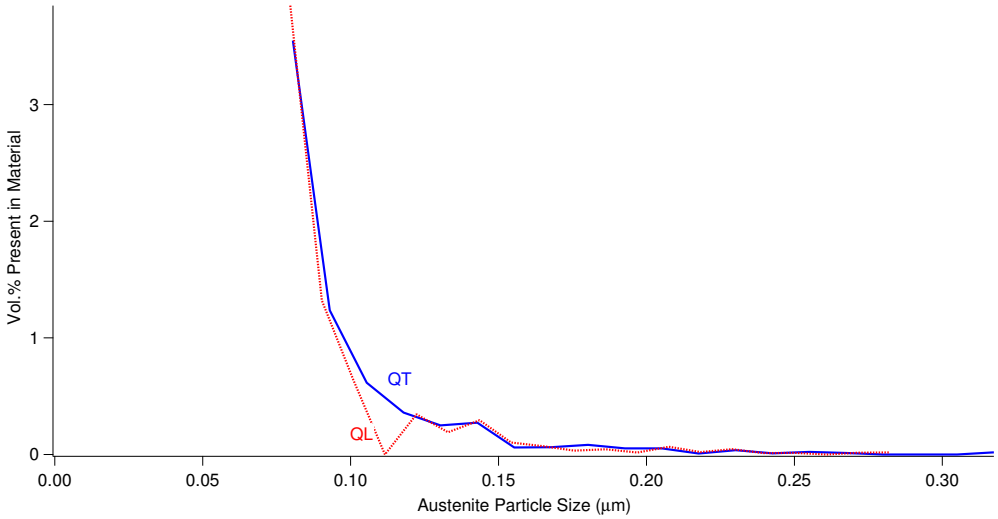

Figure 3.9: Grain size distribution of austenite particles in the QL-treated steel, expressed as a volume fraction that particles of a given size occupy in the specimen as a whole. Grain size information for the QT material is also included for comparison.

particles (apparently $\sim 4-7$ vol.%) are too small for the EBSD to detect. Unlike VSM and x-ray diffraction, which are not expected to suffer from detection errors due to small particle size in this steel[2], EBSD has a significant resolution limit which is mainly controlled by the electron beam parameters and the interaction volume of electrons in the specimen. The distribution of detected austenite particle sizes in the QL specimen (see Figure 3.9) reveals that the area fraction of particles increases more or less continuously as the particle size decreases, which lends credibility to the

[2]The VSM detects ferromagnetic ferrite/martensite, but if the particles were sufficiently small they could exhibit superparamagnetism instead. However, the particle size of ferromagnetic materials generally must be a few tens of nanometers or smaller before superparamagnetism takes hold [106], and this is far smaller than the average ferrite/martensite particle size here. Small particles lead to x-ray diffraction peaks with lower amplitude and larger widths, which can eventually cause signal-to-noise ratio issues depending on the experimental setup. However, the good agreement between our VSM and diffraction measurements suggests we are not failing to measure particles due to size with diffraction, either.

notion that there is a significant volume fraction of particles even smaller than what can be detected.

3.1.3 QLT heat treatment

VSM measurements of three QLT-treated specimens from the same heat-treated workpiece and synchrotron diffraction measurements of the QLT-treated specimens are summarized in Table 3.1. Figure 3.10 shows an SEM micrograph of the QLT-treated material in the undeformed condition. There is again a ferrite/tempered martensite matrix and a light-shaded constituent which is most likely a mixture of austenite and chemically distinct martensite. However, the morphology of this light-shaded constituent clearly differs from the light-shaded constituent in the QL material, and most likely consists to a much greater extent of austenite particles. The light-shaded constituent appears more refined, into particles with sizes in agreement with the austenite particle size measured using EBSD. In addition, dilatometry measurements indicate that, although there is transformation of austenite into fresh martensite upon cooling to room temperature after the L heat treatment, there is little or no transformation of austenite into fresh martensite upon cooling after the *subsequent* T heat treatment. Evidently, the L treatment must be preparing the microstructure for rapid stabilization of the austenite during the T treatment, for example by partitioning Ni atoms closer to the the austenite particles so that they can then then easily segregate to the austenite particles during the T treatment.

Figure 3.11 is a representative EBSD IPF map for the entire QLT-treated material and for the austenite phase. These maps indicate even more complete decoration of the martensite packet and lath boundaries with austenite particles than in the QT and QL conditions. There is also a noticeable increase in maximum austensite particle size compared with the other two heat treatments (displayed quantitatively in Figure 3.12), and yet simultaneously there is an increased volume fraction of particles which are apparently too small to detect. Figure 3.11 indicates an austenite volume fraction of 13.3%, which is up to $\sim$ 10 vol.% below the values reported by bulk measurement techniques. As with the other two heat treatments, the majority of detected particles are still close to or below the minimum detectable size for EBSD.

Although we have often observed grain size distributions in QLT specimens similar to what is seen in Figure 3.12, the previously-mentioned inhomogeneities in the microstructure do lead to some variation depending on where the measurement is made. For example, Figure 3.13 shows an austenite IPF map where particles up to $\sim$ 2.3 μm in effective diameter are observed in the center of the map, while only much smaller particles are observed around the periphery. Besides minor variations in Ni content throughout the steel due to early- and late-solidified dendrite bands, another explanation for this observed size variation may have to do with the austenite particle shape. If the steel contains austenite particles which develop a plate-like or film-like morphology between martensite laths - a morphology of austenite frequently observed in multi-phase steels [28, 31] - then the particle's orientation relative to the

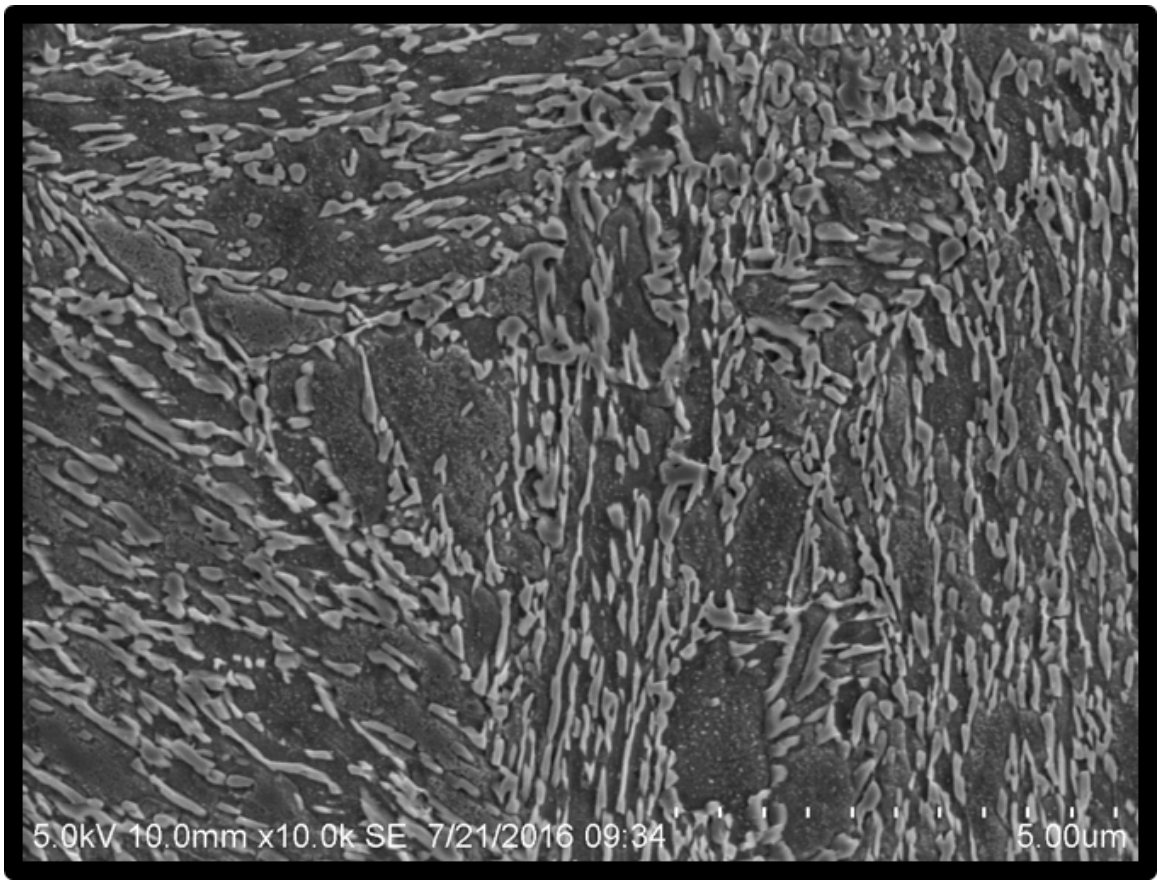

Figure 3.10: SEM micrograph of a specimen in the QLT condition.

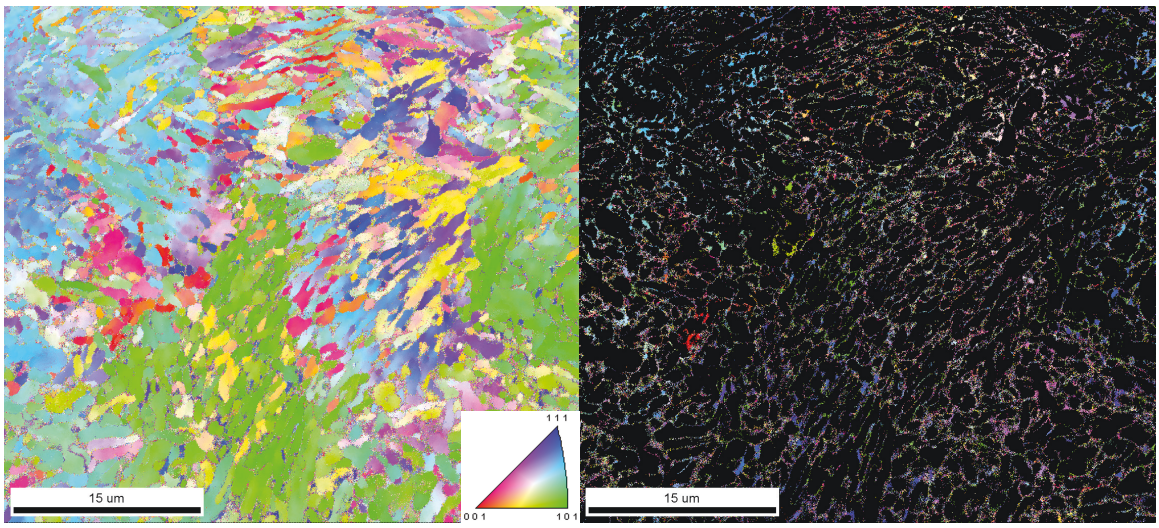

Figure 3.11: (left) IPF map of a specimen in the QLT heat treated condition. (right) The same IPF showing the austenite phase only.

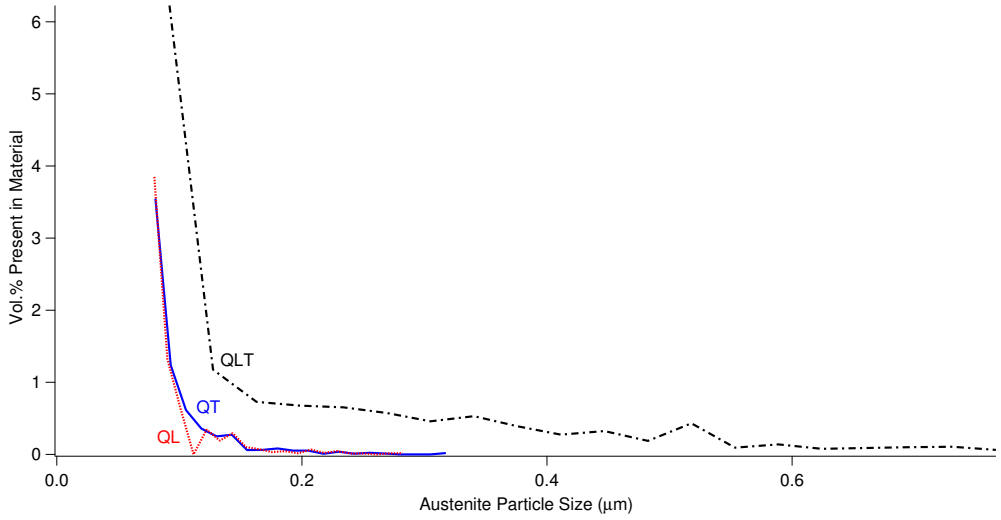

Figure 3.12: Grain size distribution of austenite particles in the QLT-treated steel, expressed as a volume fraction that particles of a given size occupy in the specimen as a whole. Grain size information for the QT and QL material is also included for comparison.

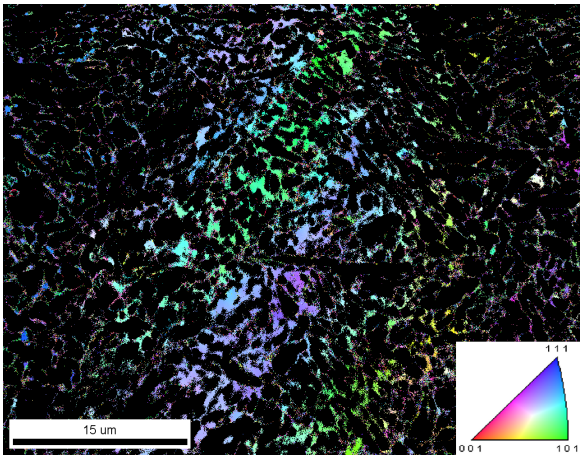

Figure 3.13: IPF map (austenite phase only) of a specimen in the QLT heat treated condition, showcasing unusually large particles.

specimen surface will determine the observed size in two dimensions. In the future, a three-dimensional EBSD study of this steel using serial sectioning could help determine the particles' full morphology, although the amount of material removed with each section would have to be extremely small in order to actually image the same austenite particle in multiple sections.

Another important observation about the microstructure of this steel is that retained austenite particles tend to have similar orientations with their neighbors, suggesting that they form with the same orientation as their prior austenite grains during heat treatment, and obeying the Kurdjumov-Sachs (K-S) relation with the martensite/ferrite particles against which they have nucleated [107]. This behavior is particularly obvious in both Figure 3.13 and Figure 3.14.

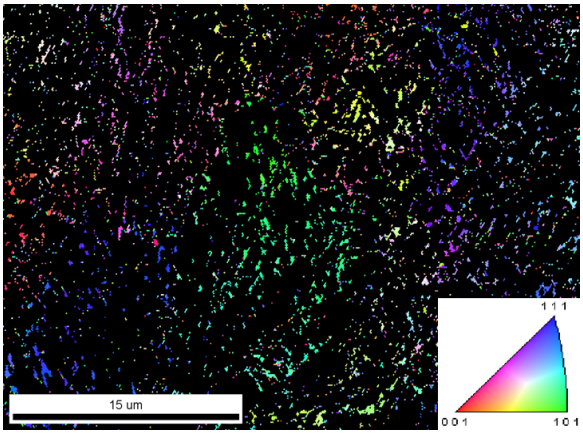

Figure 3.14: IPF map (austenite phase only) of a specimen in the QLT heat treated condition, showcasing the tendency of neighboring austenite particles to share similar orientations.

3.2 Austenite transformation during dynamic deformation

Figure 3.15 shows the austenite volume fraction as a function of strain for the QT, QL, and QLT specimens tested during the third iteration of the DCS synchrotron experiment (described in Section 2.3.7)[3]. Different transformation behaviors can be seen for each heat-treated condition. The low quantity of austenite ($\sim$ 5.8 vol.%) in the QT specimen appears highly resistant to transformation, as there is little if any change in average austenite volume fraction even at high strains. This stability is consistent with the small austenite particle size and the large concentration of

[3]The uncertainty in the diffraction volume fraction measurement is based off of the uncertainty in the fitted values for the amplitude and width of the peaks from each phase. The uncertainty in the strain corresponding to each volume fraction measurement is equal to the specimen strain over which the x-ray detector was collecting data.

austenite-stabilizing nickel which will be partitioned to the austenite phase at this temperature (see Figure 1.4).

The QL specimens initially contain somewhat more austenite ($\sim$ 11.1 vol.%), but this difference disappears relatively rapidly as some of the austenite undergoes DIMT. By the time the specimens have accumulated $\sim$ 10% plastic strain, both the QL- and QT-treated specimens contain $\sim 4-5$ vol.% austenite, and this values stays fairly constant at higher strains. With the exception of the FSP ballistic crater measured by Zhang [1] which seemingly contained almost no austenite, and the apparently negligible austenite content measurements made by Wang and Kumar [23], nearly every other measurement of the austenite content of this 10% Ni steel has yielded a value greater than $\sim$ 4%, regardless of heat treatment and deformation state. This includes specimens which were reaustenitized and quenched into liquid nitrogen [1], as well as measurements made on the necked region of tensile specimens which were deformed while in liquid nitrogen[4]. It is very difficult to promote the martensitic transformation more aggressively than with the low temperatures, high stresses, and stress state experienced by this necked specimen, indicating that this $\sim$ 4 vol.% of austenite is extremely mechanically stable.

The QLT-treated specimens exhibit substantially different transformation behavior from the other heat-treated specimens. Besides having a much higher initial austenite volume fraction ($\sim$ 23.5 vol.%), the austenite also transforms over a larger

[4]The mechanical testing which produced this necked tensile specimen was previously conducted by Dr. Xian Jie Zhang, and we quantified the austenite volume fraction in the necked region using VSM as supplementary work over the course of this dissertation

range of strain. While there are no obvious changes in the average austenite volume fraction of QL or QT specimens after $\sim 10 - 13\%$ strain, the austenite volume fraction in the QLT specimens clearly continues to decrease until at least 20% strain. This prolonged period of transformation gives the QLT-treated material ample opportunity to benefit from the localized hardening associated with the transformation, which could explain the material's high resistance to localized failure from adiabatic shear banding and failure during ballistic impact.

Another clear difference in the QLT specimens is that, even after almost 30% plastic strain, there is still nearly as much austenite present in the QLT specimens as in the undeformed QL specimens, and generally more than is present in the undeformed QT specimens. After 30% strain the rate of austenite transformation appears to drop drastically in the QLT specimens, so the remaining austenite may be mechanically stable (at least, under uniaxial compression). Some of this remaining austenite would likely have transformed if the stress state were different, however, meaning it could still be available to harden the material during a complicated loading condition such as ballistic impact. Regardless, the results shown here demonstrate that austenite particles in the QLT specimens possess a range of mechanical stability (*i.e.* some particles are highly susceptible to transformation and others are highly resistant to it). This range of stability has been linked to a desirable combination of strength, uniform elongation, and total elongation in other steels [30, 31].

Also seen in Figure 3.15 is VSM data collected on QLT specimens which were com-

pressed using the same Kolsky bar which was used for the *in situ* experiments, and which experienced a strain-rate history similar to the specimens tested *in situ*[5]. However, these specimens were recovered at various lower levels of strain. As explained in the introduction to this chapter, one motivation for conducting *in situ* tests was to determine if *in situ* tests are necessary to accurately assess the phase fractions that are present in this material *during* dynamic deformation, due to the temporary stabilization of austenite that could be caused by adiabatic heating. If this temporary stabilization were happening, then the austenite volume fraction measured *in situ* would become progressively higher than the austenite volume fraction measured *ex situ*. Clearly, this effect was not observed. Therefore, future measurements of the austenite volume fraction can be made with confidence using *ex situ* techniques, at least for steels with similar microstructures loaded in compression at strain rates not exceeding ~ 2500 s^{-1}.

3.3 Mechanical properties under dynamic compression

Figure 3.16 shows the average stress-strain behavior of the three heat-treated steels tested during the third iteration of the DCS synchrotron experiment. Stress-strain

[5]Uncertainty for the VSM volume fraction measurements is based off of the largest standard deviation we have obtained from measurements of nominally-identical specimens. The uncertainties in the mass and magnetization measurements which go into each individual VSM data point are much smaller than the uncertainty shown.

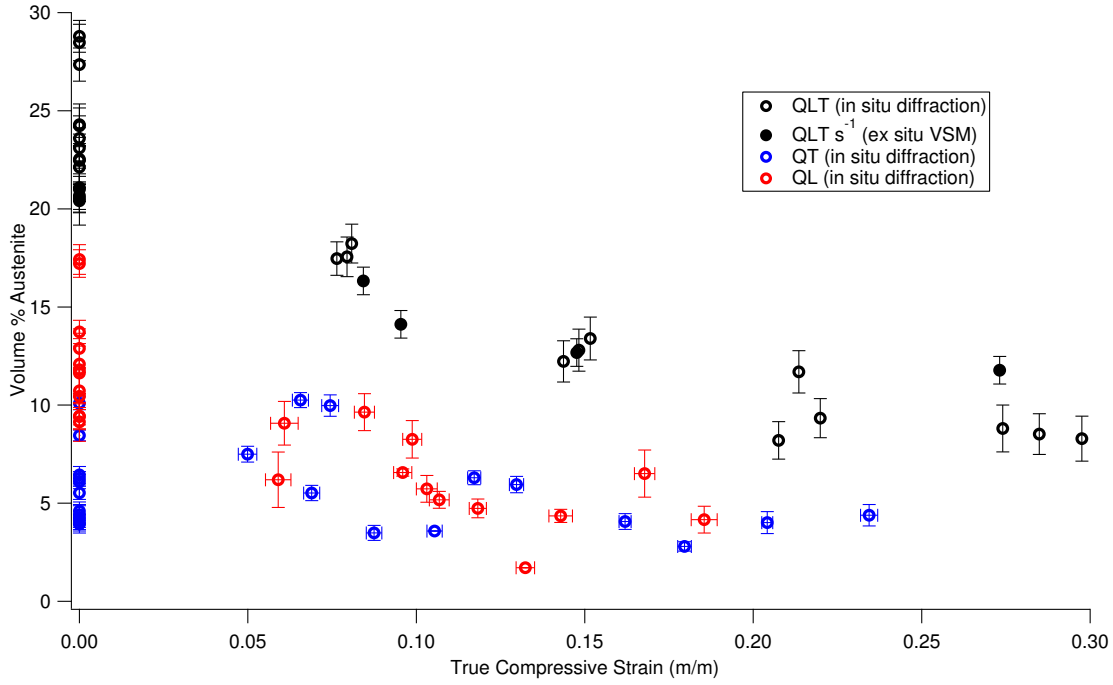

Figure 3.15: The volume fraction of austenite as a function of true strain for the specimens dynamically compressed in the synchrotron experiment discussed in Section 2.3.7. Corresponding stress-strain curves for these specimens are shown in Figure 3.16.

curves for individual specimens deviate from the average stress-strain behavior by as much as $\sim pm100$ MPa, as illustrated in Figure 3.17 for QLT-treated specimens. This data corresponds with compression along the material's rolling direction. Stress-strain data is derived from the Kolsky bar strain gauge data we recorded during the *in-situ* experiments and each curve represents the average of 3-4 specimens. The applied strain rates were ~ 1500 s^{-1} for the QL specimens, ~ 2000 s^{-1} for the QT specimens, and ~ 2500 s^{-1} for the QLT specimens. We made the logistical decision not to change the breech pressure or striker characteristics during the synchrotron experiment. This would have required time-consuming experimental changes in order to maintain the synchronization of all parts of the experiment, and it is often prudent to spend as much time collecting data as possible on the rare occasions one gets to use a synchrotron. This decision, in combination with small, systematic differences in specimen dimensions between each heat treatment, caused the differences in strain rate (and final strain).

No clear signs of catastrophic failure (*i.e.* fracture) were observed in the tested specimens. The end of each steel's stress-strain curve simply represents the final strain in the specimen when the strain pulse provided by the striker ended. In one of the few published works describing the mechanical properties of this experimental 10% Ni steel[6], Wang and Kumar [23] performed dynamic compression at a strain rate of $\sim 2200 - 3000$ s^{-1} and saw steep drops in specimen strength attributable to the

[6]The heat-treated condition of the 10% Ni steel in this publication was unspecified, but was evidently much different from the experimentally-optimized QLT condition due to the negligible amount of austenite present in the specimens.

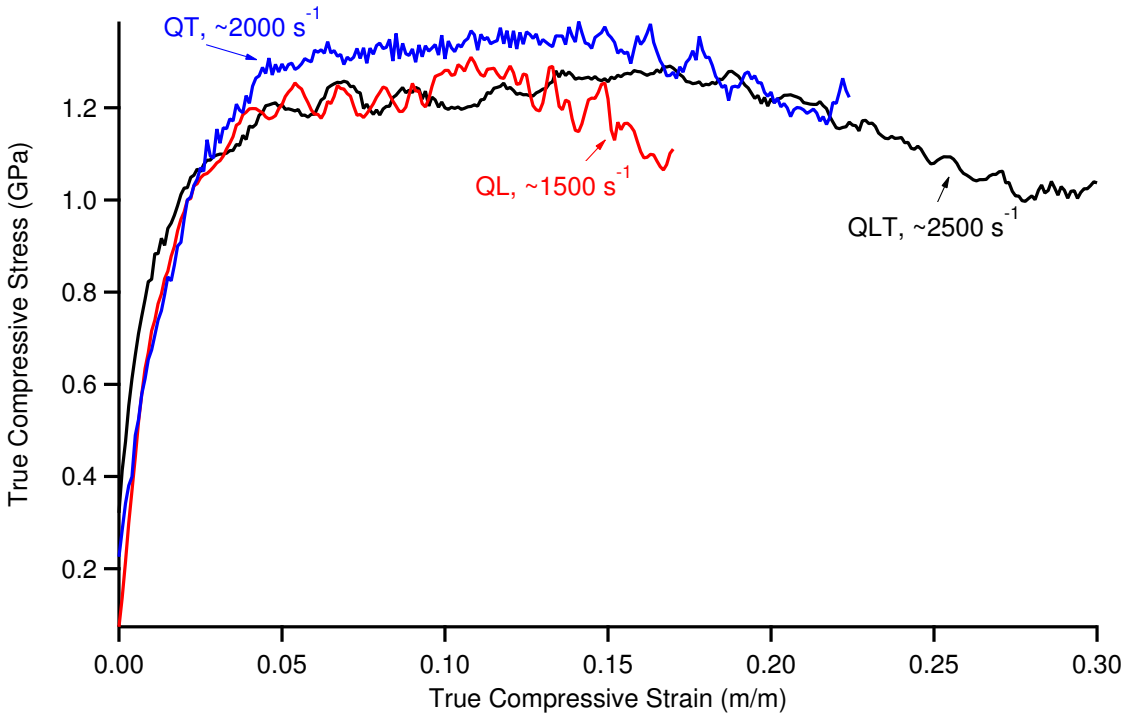

Figure 3.16: Averaged compressive true stress-true strain curves for the QT-, QL-, and QLT-treated specimens. The applied strain rates were $\sim$ 1500 s^{-1} for the QL specimens (average of 4 tests), $\sim$ 2000 s^{-1} for the QT specimens (average of 3 tests), and $\sim$ 2500 s^{-1} for the QLT specimens (average of 3 tests).

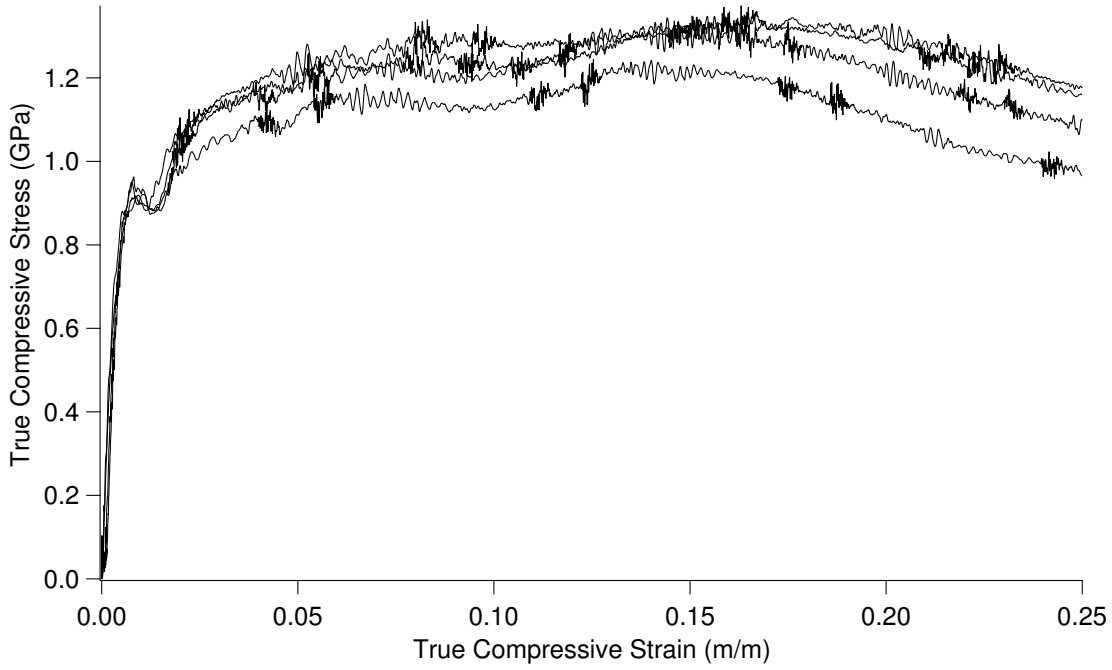

Figure 3.17: Stress-strain curves for individual QLT specimens, illustrating the fluctuation in flow stress from specimen to specimen.

formation of adiabatic shear bands. In contrast, our tested specimens exhibited only a mild drop in strength toward the end of each steel's stress-strain curve.

There are two possible explanations for this moderate drop in strength. The first would be an unusually severe susceptibility to thermal softening. We calculated a temperature rise of ∼80-90 K in the specimens by the end of compression, which is in reasonable agreement with measurements of temperature rise in steel undergoing dynamic deformation from the literature [108]. This calculation is based on the amount of energy supplied to the specimen during deformation, and standard assumptions about the generation of heat of plastic work. To elaborate: by calculating the area under the deformed specimen's stress-strain curve, we can determine the energy per unit volume supplied to the specimen during deformation. Because we know the undeformed specimen volume, we know the total amount of energy supplied to the specimen. Most, but not all, of this energy will be converted to heat; the fraction of energy converted to heat can be described by the Taylor-Quinney coefficient, which we have assumed to be 0.9 as is often assumed for metals [109, 110]. By factoring in the specimen's mass, the specific heat of iron, and the Taylor-Quinney coefficient, a temperature rise in the specimen under adiabatic conditions can thus be estimated.

The calculation described above ignores the exothermic character of the martensitic transformation, though, so the actual temperature rise in the specimen is likely a few degrees larger than what we have calculated [111]. This calculation also assumed uniform heating throughout the entire specimen, but in reality the local maximum

temperature rise may have been higher. Other research on high-strength steel [112] predicts a drop in strength of $\sim$ 100 MPa for a steel of comparable strength after a comparable increase in temperature, so a somewhat higher temperature sensitivity (*i.e.* susceptibility to thermal softening) in the 10% Ni steel could account for the strength drop seen here.

A second possible explanation could be non-uniform specimen deformation which did not result in fracture. Wang and Kumar [23] deformed 10% Ni steel specimens to different final strains at different strain rates and identified a "transition" region between strains/strain rates which resulted in shear bands and those which did not. In this transition region, localized deformation bands either traversed a portion of the specimen, or they traversed the entire specimen but did not result in fracture or the "white etching" commonly observed with adiabatic shear bands in steel. Signs of non-catastrophic localized deformation can be observed in some of our specimens deformed to high strains, even specimens (discussed in Chapter 4) which were deformed at quasi-static rates[7]. An example of this non-uniform deformation is shown in Figure 3.18. The QLT-treated specimens were deformed to final strains and strain rates which would lie very close to the "transition" region identified by Wang and Kumar [23], although the QL and QT specimens would be predicted to lie in the homogeneous deformation region.

[7]It should be noted, however, that unusual stress-strain measurements did not accompany this localized deformation of the quasi-statically-compressed specimens, so it is not currently clear whether this type of localized deformation would have a noticeable impact on bulk mechanical properties at high strain rates.

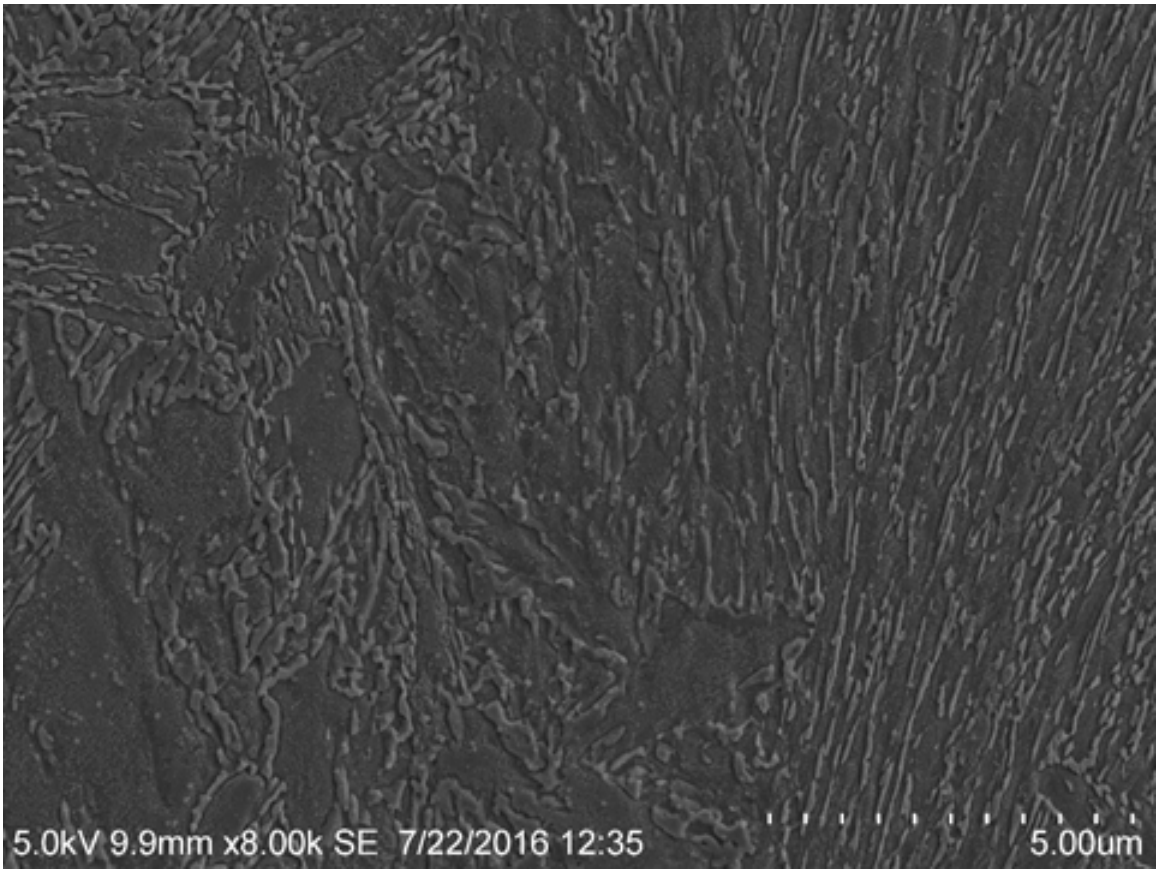

Figure 3.18: SEM micrograph of a deformed QLT compression specimen, showing highly-deformed grains (on the right) next to less-deformed grains (on the left).

Overall, the compressive stress-strain curves of the steel in each heat-treated condition are fairly similar. This is especially true when the specimen-to-specimen variation in flow stress is taken into consideration. Mechanically-unstable austenite tends to produce the most dramatic changes in material properties when considering necking and fracture, and in general compression testing causes neither necking nor fracture. Nevertheless, despite the specimen-to-specimen variation, the differences between each heat treatment's average stress-strain behavior are consistent with what is seen during quasi-static tensile testing of QL, QT, and QLT specimens[8]. In this context, there are a few differences in the stress-strain curves worthy of note. At low strains, the QT specimens are the strongest. This is most likely because there is relatively little austenite in the QT condition for Ni to preferentially partition to, meaning there is instead a substantial amount of Ni dissolved in the matrix. This high Ni content causes substitutional solid solution strengthening of the matrix [113].

The QL specimens are comparatively weaker, and this can similarly be attributed to the presence of more austenite compared with the QT phase, which partitions some of the solid solution strengthening Ni away from the matrix. According to Reference [113] (which summarizes and interprets data from References [114–116]), a change in the Ni content of ferrite from $\sim$ 3% to $\sim$ 4% leads to a solid solution strengthening of the ferrite by $\sim$ 100 MPa. This is the predicted change in Ni content of the steel's ferrite from the QL to the QT condition (based on the Fe-Ni phase

[8]Unpublished experiments conducted by Dr. Xian Jie Zhang.

diagram), and at low strains the QL steel is $\sim$ 100 MPa weaker than the QT steel.

The QLT material is initially comparable to the QL material in strength. Although the QLT specimen contains even more austenite than the QL specimen, and thus even less Ni in the ferrite/martensite matrix, much of the austenite is ultrafine-grained. The strength of austenite increases substantially when the grain size is reduced [117, 118]. There is also rapid transformation of austenite into the harder martensite at low strains, which causes strain hardening. These QLT specimens have the largest volume fraction of material undergoing martensitic transformation, and this transformation happens over a large range of strain, so this material hardens (or postpones softening) the longest. Indeed, by $\sim$ 17% true strain, the strength difference between the QT and QLT conditions essentially disappears. This extended window of strain hardening is likely a contributing factor to the QLT-treated steels resistance to localized failure under ballistic impact. The martensitic transformation of austenite particles in the QLT-treated steel produces a large portion of this hardening effect, which motivates a more detailed study of that transformation. This study will be detailed in the next chapter.

Chapter 4

The effects of strain rate on martensitic transformation in a QLT-treated 10% Ni steel

Having established the shape of the austenite transformation curve in QLT-treated 10% Ni steel during dynamic compression in the previous chapter, we then sought to understand the transformation behavior of this austenite in more detail. To do so, we proceeded to measure the transformation kinetics of the same steel compressed along the same direction (the rolling direction) at quasi-static rates. These measurements, and a post-mortem characterization of the dynamically- and quasi-statically-deformed microstructures, yielded some insights into the relative prevalence of strain-induced martensitic transformation (SIMT) and stress-assisted martensitic transformation

(SAMT) in this experimental 10% Ni steel. As discussed in Section 1.2, SIMT is characterized by nucleation of martensite particles within the intersections of "shear bands" (stacking faults, twins, and/or ϵ martensite) which form within austenite particles during plastic deformation. In contrast, SAMT is characterized by martensite nucleating at the same sites (typically along grain boundaries) at which martensite would have nucleated in the absence of stress upon cooling below the material's M_s temperature.

In general, the published literature on deformation-induced martensitic transformation (DIMT) in low-carbon Ni steels containing $\sim 4 - 14\%$ Ni does not mention these different transformation mechanisms [25, 34, 38, 39, 43, 44, 48]. Instead, the literature tends to describe the transformation only with the terms DIMT or with "the TRIP[1] effect." These terms are non-specific or ambiguous regarding the active mechanism. For example, some steels referred to as "TRIP steels" have been observed to undergo SIMT, and "transformation-aided plasticity" or "the TRIP effect" are sometimes used as synonyms for SIMT [32, 119]. Interpreted literally, though, "transformation-induced plasticity" is a more apt synonym for SAMT, and the transformation seen in some "TRIP steels" may actually be attributable to SAMT [120]. The results of our investigation into dynamically- and quasi-statically-deformed microstructures will be discussed in the context of these different transformation mechanisms.

[1] TRansformation-Induced Plasticity

4.1 Transformation behavior during quasi-static compression

To determine the austenite volume fraction present in QLT-treated specimens compressed at quasi-static rates, we compressed nominally-identical specimens to pre-determined levels of plastic strain at a strain rate of 0.001 s^{-1} and quantified the austenite volume fraction present in the deformed specimens using VSM. Figure 4.1 compares the transformation kinetics under quasi-static loading with the results shown in the previous chapter for dynamic loading. The austenite volume fraction during dynamic compression (according to both VSM and diffraction measurements) is always higher than the austenite volume fraction during quasi-static compression at a given amount of plastic strain. This contrasts with assessments in the literature of the effect of strain rate on transformation in some more common structural steels [10, 99, 119, 121], which revealed that those steels initially undergo more rapid martensitic transformation at high strain rates than at low strain rates. The austenite transformation behavior at low at high strain rates for these steels is schematically illustrated in Figure 4.2.

For pragmatic reasons, the quasi-static specimens and the specimens we tested at the synchrotron had substantially different volumes and slightly different aspect ratios, so it was conceivable that the unexpected transformation behavior we observed was a geometrical effect instead of an intrinsic property of the steel. To address

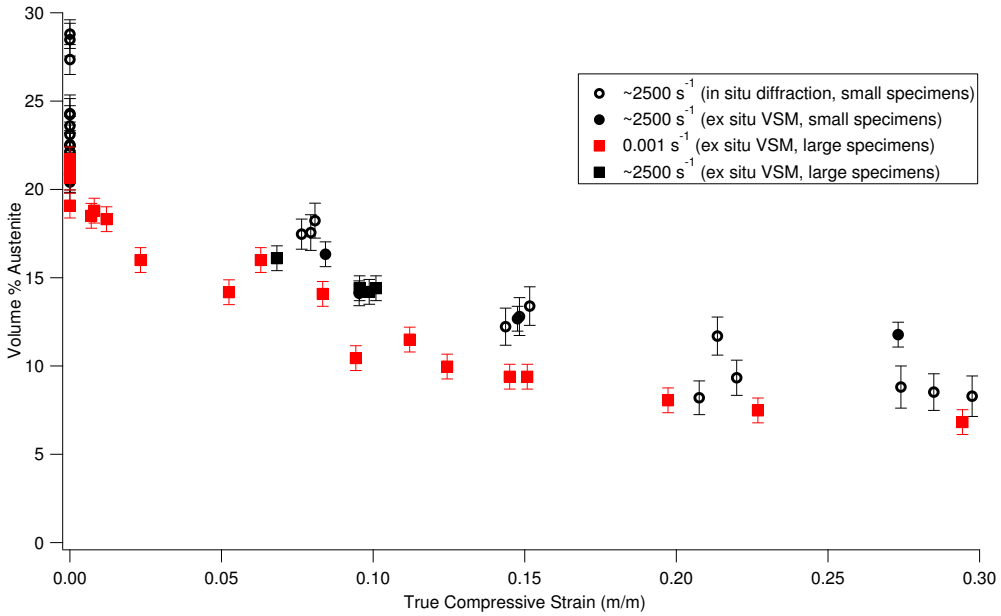

Figure 4.1: Volume fraction of austenite present in QLT-treated 10% Ni steel as a function of true compressive strain, tested at quasi-static and dynamic strain rates.

this concern, we prepared some additional specimens of the steel which were nominally identical to the quasi-statically compressed specimens and compressed them at a similar strain rate to what the synchrotron specimens experienced. The VSM-measured austenite volume fraction present in these specimens is shown in Figure 4.1 as well. These data points are in good agreement with the other values for dynamic compression, indicating that the difference in transformation behavior is indeed a characteristic of the steel and not due to the specimen geometry.

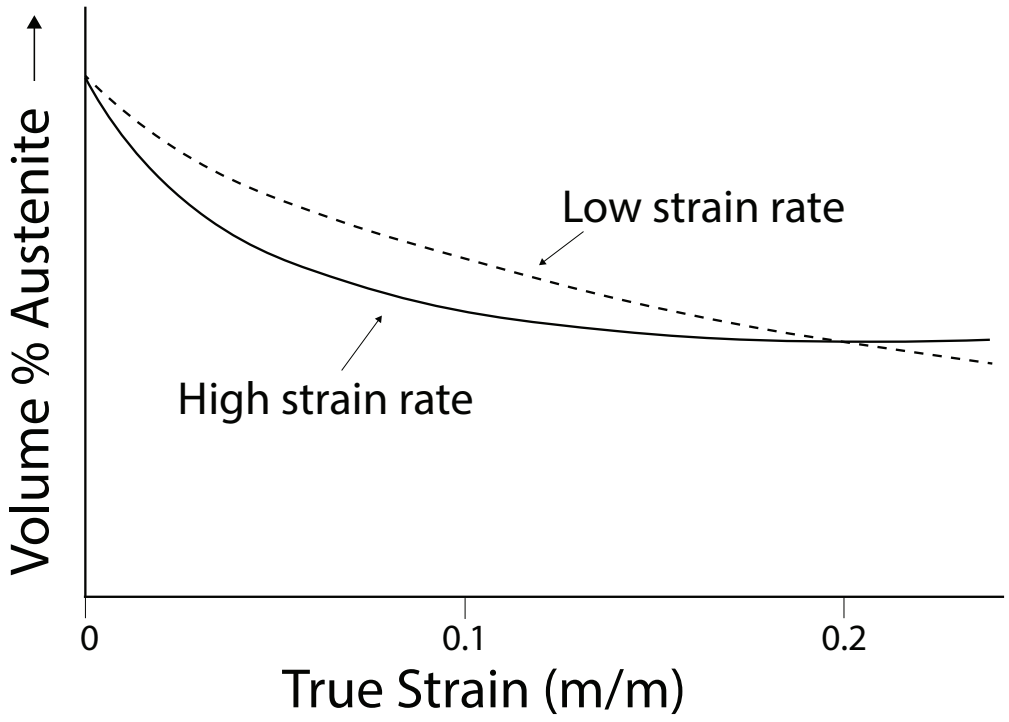

Figure 4.2: Schematic illustration of the austenite transformation behavior seen in Mn-Si TRIP steel at different strain rates. Similar transformation behavior can be seen in other common structural steels such as AISI 304, although in austenitic stainless steels there may not be measurable changes in austenite volume fraction at very low strains. Adapted from Ref. [10].

4.2 EBSD analysis of deformed austenite particle sizes

To shed more light on the cause of these differences in transformation rate, we conducted EBSD investigations on the deformed specimens. To ensure that the examined specimens were as similar as possible except for the strain rate which was applied to them, we examined two specimens which had the same specimen geometry and which had both been deformed by $\sim 9.5\%$. Examples of these EBSD maps displayed as inverse pole figures (IPFs) are shown in Figures 4.3 and 4.4 for specimens compressed to $\sim 9.5\%$ strain under quasi-static and dynamic conditions, respectively. Other EBSD maps (not shown here) that we have collected on other areas of each specimen's surface demonstrate the same general trends in austenite volume fraction and particle size distribution we are about to discuss.

The EBSD map for the quasi-statically compressed specimen reveals 7.0 vol.% austenite, in comparison with the 10.4 vol.% austenite measured in this specimen using VSM. This again reflects the systematic under-reporting of the austenite content using EBSD compared with other measurement techniques discussed in Section 2.5.2. Some authors (who perform *in situ* mechanical testing in the SEM) propose that the reason for this discrepancy is a greater propensity for austenite particles to transform when they are on the material's surface [98]. This may be true for measurements made on specimens deformed *in situ*, but the thorough surface preparation we have done

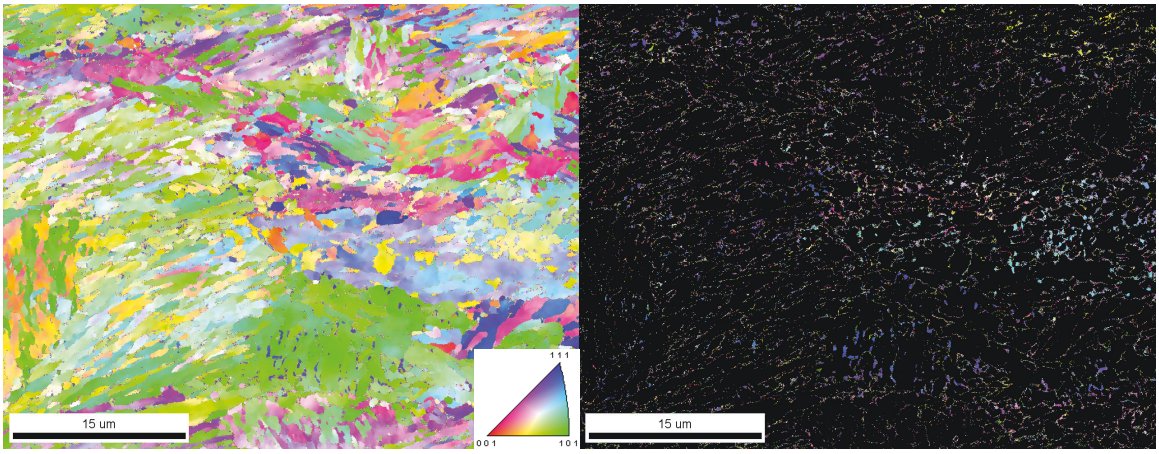

Figure 4.3: (left) Inverse pole figure (IPF) map for a QLT-treated 10% Ni steel compressed to 9.5% strain at a strain rate of 0.001 s^{-1}. (right) The same IPF map showing the austenite phase only.

between *ex situ* mechanical testing and EBSD makes it unlikely that we are looking at grains affected by surface effects. Jacques *et al.* [8] propose system calibration as a possible explanation for the discrepancy between EBSD measurements and other austenite volume fraction measurements, but we argue that in our case the resolution of EBSD is the actual source of the discrepancy, as will be explained throughout this section.

In contrast with the quasi-statically compressed specimen, the specimen compressed dynamically by nearly the same amount contains 14.4 vol.% austenite according to VSM, approximately 35% more than is present in the quasi-statically deformed specimen. However, the EBSD data indicates only 5.8 vol.% austenite, which is $\sim 24\%$ *less* than is reported by EBSD for the quasi-statically deformed specimen. Jacques *et al.* [8] found that the austenite volume fractions measured using EBSD

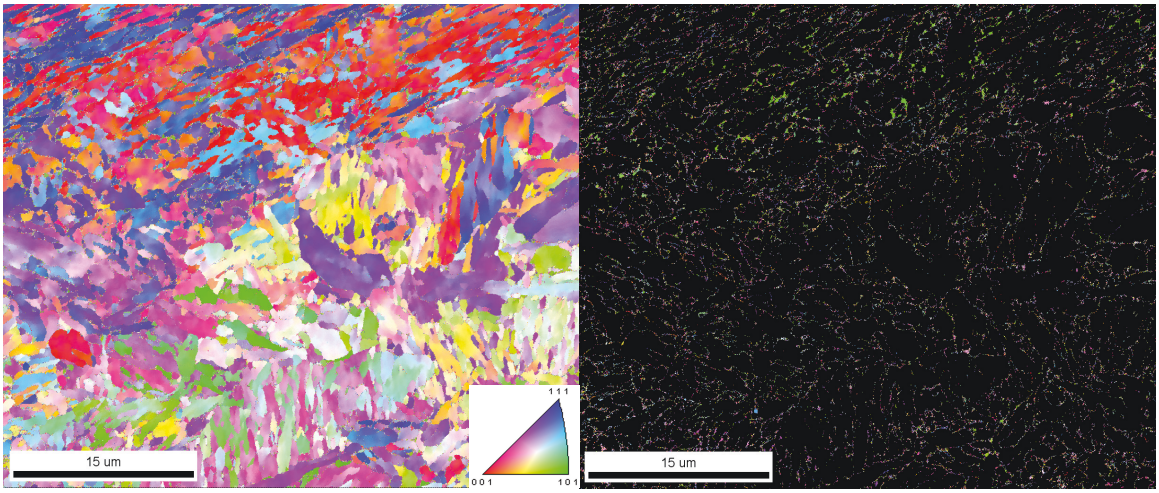

Figure 4.4: (left) IPF map for a QLT-treated 10% Ni steel compressed to 9.5% strain at a strain rate of $\sim 2500\ s^{-1}$. (right) The same IPF map showing the austenite phase only.

at least scaled proportionately with the austenite volume fractions measured using other techniques, which suggests that their proposed calibration issues are not the main source of the discrepancy we observe.

Examination of the austenite particle size distribution in each of the steels sheds more light on the source of the discrepancy. Figure 4.5 shows the austenite particle size distributions for the quasi-statically deformed specimen and the dynamically-deformed specimen. (The grain size distribution for an undeformed QLT specimen is also included for reference.) There is not a very clearly-defined local maximum in either distribution. Instead, the area fraction of particles with a certain effective radius increases more or less continuously as the effective radius decreases. The largest area fraction of austenite particles consists of particles which are only 2-3 pixels in size, and the pixel spacing in both maps is 50 nm, which is on the order of the

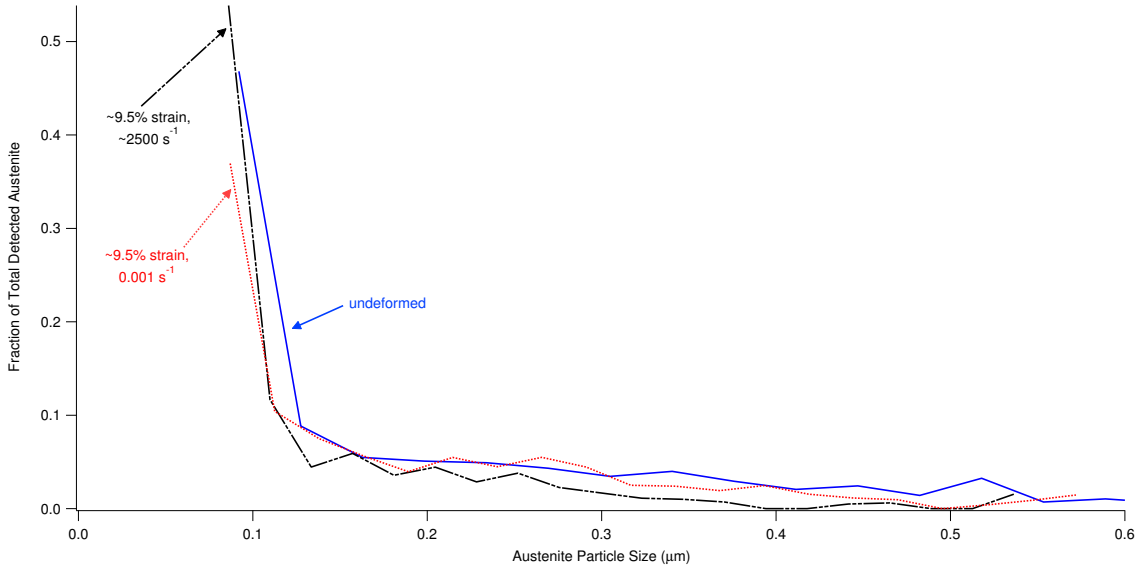

Figure 4.5: The distribution of austenite particle sizes found in undeformed QLT-treated 10% Ni steel, and in QLT-treated specimens compressed quasi-statically and dynamically by $\sim$ 9.5%, as a fraction of the total amount of austenite detected by EBSD. For ease of viewing, the axis range does not include all of the undeformed specimen's data.

resolution limit of EBSD using typical accelerating voltages [122]. (We experimented with the low accelerating voltages recommended in Reference [122] during our EBSD optimization process in order to achieve better resolution, but this only led to poorer pattern indexing and less plausible microstructure maps generated at a dramatically lower data acquisition speed.)

This particle size distribution suggests that there may be a very substantial fraction of austenite particles which are too small for EBSD to detect. The SEM observations described in Section 3.1.3 and the lower-bound particle size calculation on a similarly heat-treated 10% Ni steel described in Section 2.5.2 add support to this

hypothesis. Because neither VSM for x-ray diffraction are expected to suffer from problems with measuring the austenite volume fraction due to particle size in this steel (and because these two measurement techniques are in generally good agreement with one another), we take the VSM measurements to be the *total* austenite volume fraction in the specimen, and the EBSD measurement to be the volume fraction of austenite particles which are above the EBSD detection size limit. A comparison of the amount of austenite in the specimen which is visible to EBSD and the amount which is not can be found in Table 4.1.[2]

Specimen Strain	Total %A (VSM)	%A (Large Grains, Visible to EBSD)	%A (Small Grains, Invisible to EBSD)
0%	20.8 ± 0.7	13.3 ± 1.4	7.5 ± 1.6
$\sim 9.5\%$ (Quasi-Static)	10.4 ± 0.7	7.0 ± 1.1	3.4 ± 1.3
$\sim 9.5\%$ (Dynamic)	14.4 ± 0.7	5.8 ± 0.9	8.6 ± 1.2

Table 4.1: Austenite volume fraction of deformed and undeformed QLT-treated specimens, measured using VSM and EBSD.

It is unfortunate that the EBSD measurements were unable to resolve a substantial fraction of the austenite in the specimen even after an extensive optimization process, but they still provide a wealth of useful information about the transformation process

[2]It is interesting to note that, using these assumptions about the source of the discrepancy between VSM and EBSD measurements, the volume fraction of austenite in the specimen which is undetectable by EBSD seems to actually *increase* slightly during deformation. This is probably due to local variability in the microstructure influencing the EBSD measurements slightly. However, there are observations in the steel literature [98] of large austenite particles *partially* transforming to martensite at low strains, effectively replacing the large particle with a smaller one. This partial transformation, in combination with the relatively low susceptibility of small particles to transformation, means it is possible that the volume fraction of small particles could actually increase even while the total austenite volume fraction decreases.

when paired with other characterization techniques we have already described. For instance, careful examination of the particle size distributions for the two deformed specimens reveals that, despite having a larger *total* austenite volume fraction, there are fewer large austenite particles in the dynamically-deformed specimen. In fact, the disparity (on a percentage basis) between particles found in the dynamically- and quasi-statically-deformed specimens increases as the size of the particle being considered increases.[3]

This disparity can be discerned when comparing the direct output of the TSL OIM software (as reported in Figure 4.5), which displays the particle size distribution as a fraction of the total detected austenite. A more meaningful comparison, however, is the specimen's austenite particle size distribution in terms of the volume fraction that austenite particles of a certain size occupy *in the specimen as a whole*. (This is done simply by multiplying the TSL OIM software-generated particle size distribution by the austenite volume fraction reported in the EBSD map.) This information is displayed in Figure 4.6 for the undeformed QLT-treated metal and the specimens which were quasi-statically or dynamically compressed by $\sim 9.5\%$. Also shown in Figure 4.6 is the expected volume fraction of small particles undetectable by EBSD, based on the VSM austenite volume fraction measurements.

These data suggest that large austenite particles in the steel transform more

[3]This observation is important, since the EBSD is most likely to be reporting accurate information about particles which are large. The EBSD maps shown here have had no "cleanup" done on them, so some of the 1- or 2-pixel particles reported by the EBSD are undoubtedly noise instead of real particles. The likelihood of a larger particle being reported inaccurately is much lower, though.

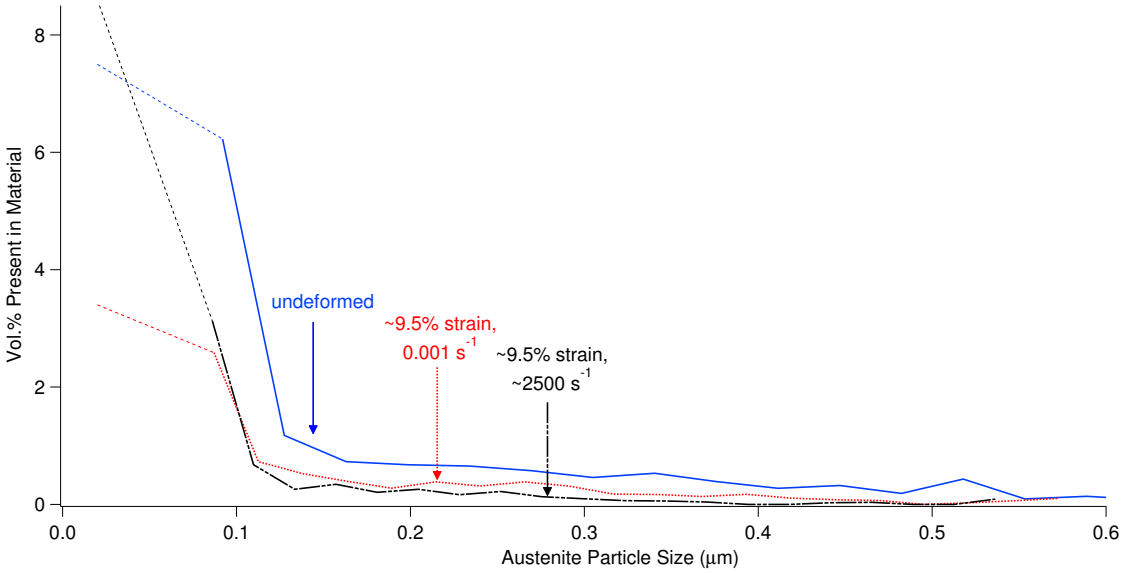

Figure 4.6: The distribution of austenite precipitate sizes found in the underformed and deformed specimens, as a percentage of the whole specimen, with projections (dotted lines below ~ 90 nm) for the volume fraction of small particles based on the discrepancy between VSM and EBSD measurements. For ease of viewing, the axis range does not include all of the undeformed specimen's data.

rapidly with an increased strain rate, even though the totality of austenite particles transform *less* rapidly with an increasing strain rate. This is illustrated using Figure 4.7 and Table 4.2. Figure 4.7 shows the fraction of austenite particles in the quasi-statically and dynamically deformed specimens which have transformed, as a function of particle size. This figure only considers grain sizes which could be quantified using EBSD, so the fraction of very small particles which have transformed is not shown. Table 4.2 complements this plot by summarizing the fraction of transformed particles within different size regimes, considering both EBSD and VSM data. Table 4.2 demonstrates that the fraction of austenite which has transformed after quasi-static loading is fairly constant across all particle size regimes, except for the very largest particles in the steel. In contrast, under dynamic loading the fraction of transformed austenite steadily increases as the particle size increases.

Particle Size	% Transformed (Quasi-Static)	% Transformed (Dynamic)
All	50	31
< 100 nm	59	22
$100 - 250$ nm	53	68
$250 - 450$ nm	57	87
> 450 nm	86	92

Table 4.2: The fraction of austenite in various size ranges which transformed after $\sim 9.5\%$ strain at quasi-static and dynamic strain rates.

A possible explanation for this behavior can be found in emerging research on Mn-based duplex and TRIP-maraging steels performed by Yen *et al.* and Wang *et al.* [98, 123]. This recent research had the explicit goal of gaining a better understanding

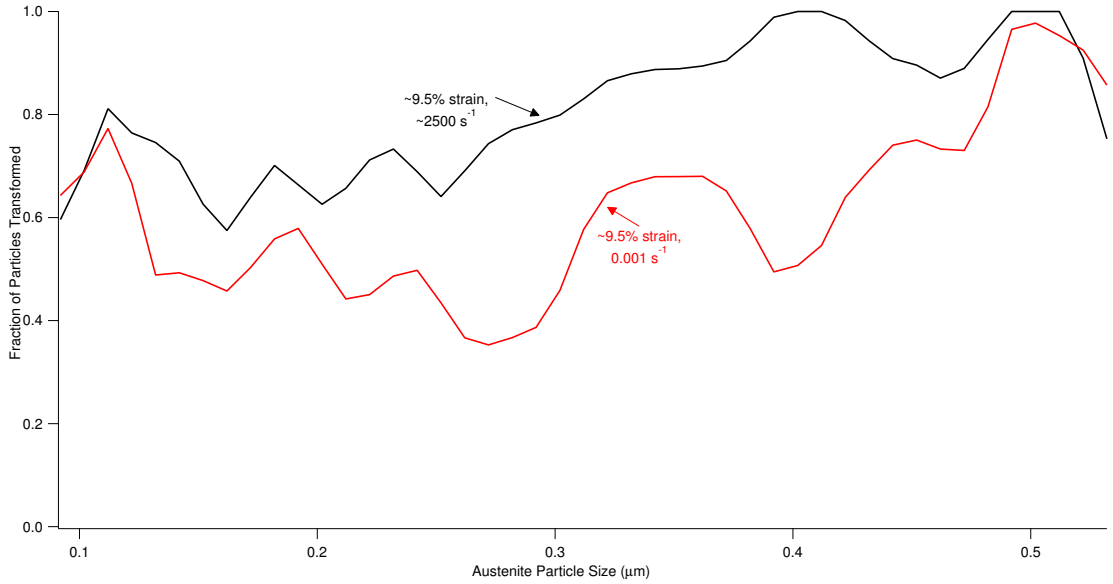

Figure 4.7: The fraction of austenite particles of different sizes which have transformed after quasi-static and dynamic compression.

of how DIMT in ultrafine-grained austenite compares with DIMT in coarse-grained austenite, a subject which has not received much attention in the past [124]. This research indicated that there may be a size dependence, not only to the susceptibility of an austenite particle to transformation, but also to the transformation mechanisms. It was observed that austenite particles below a certain size (both Yen *et al.* and Wang *et al.* specify a size of $\sim$ 300 nm) exhibited different deformation morphology than larger particles. Yen *et al.* in particular finds that, while the larger austenite particles were observed to contain the intersecting shear bands (particularly stacking faults) that are characteristic of SIMT, the smaller particles did not exhibit this behavior. Instead, stacking faults in the smaller particles were predominantly co-planar (*i.e.* non-intersecting) and the transformed martensite tended to originate

from the austenite grain boundaries. This is characteristic of SAMT.

This work from other researchers we have just described was only conducted on quasi-statically deformed specimens. However, the mechanism (SIMT or SAMT) by which austenite particles of a given size transform has implications for the strain rate dependence of the transformation of those particles. Specifically, SIMT is known to occur more rapidly (as a function of strain) at higher strain rates, at least at low strains where the specimen has not had enough adiabatic heat buildup to suppress further transformation. The strain-rate-dependence studies of austenite transformation behavior cited at the beginning of this chapter [10, 99, 119, 121] attributed the more rapid transformation they observed at high strain rates at low strains to the SIMT mechanism (or "the TRIP effect," which some authors seem to use interchangeably with "SIMT"). In References [10, 99], the transformation rate appears higher at high strain rates than at low strain rates until the specimens have accumulated $\sim 15\%$ strain, so it is probably around this level of strain that adiabatic heat starts to significantly influence the transformation rate in the dynamically-deformed specimens.[4] Olson and Cohen [125] developed an early model for SIMT in which the volume fraction of martensite $f^{\alpha'}$ depends on plastic strain ϵ in the following way:

[4]The level of strain at which adiabatic heating starts to become important to the transformation rate will of course depend on many factors, including the composition, morphology, and volume fraction of the austenite as well as the overall strength of the steel and the testing temperature. This impact of specimen temperature on the stress required to cause transformation is illustrated in Figure 4.8.

$$f^{\alpha'} = 1 - \exp\left(- p\frac{\bar{v}^{\alpha'}\pi^2 d^2}{16(\bar{v}^{sb})^n}[1 - \exp\left(-\alpha\epsilon\right)]^n \right) \tag{4.1}$$

where p is the probability of a martensitic embryo forming in a given shear band intersection, $\bar{v}^{\alpha'}$ is the average volume of a martensite unit, $\bar{v}^{sb}$ is the average volume of a shear band (assumed constant), d is the average shear band diameter (on the order of the austenite grain size), $n = 2$ based on the assumption of randomly oriented thin shear bands, and α is a fitted constant which represents the low-strain shear band formation rate. The parameter α, Olson and Cohen explain, is expected to increase with increasing strain rate (as well as decreasing temperature or stacking fault energy), based on the tendency of high-strain-rate deformation to increase the rate of shear band formation compared with slip. Increasing this α parameter leads to a faster increase of $f^{\alpha'}$ (or, equivalently, a faster decrease in austenite volume fraction) with strain. Subsequent theorists have improved the accuracy and applicability of this formula, but the strain-rate dependence remains qualitatively the same as what was outlined by Olson and Cohen, and this appears to be the strain-rate dependence we observe in the largest particles of QLT-treated 10% Ni steel.

The rate of SAMT exhibits a different strain-rate dependence than that of SIMT. While SIMT leads to higher initial martensitic transformation rates at high strain rates than at low strain rates, the rate of transformation during SAMT is always expected to be lower at high strain rates. The first reason for this is the buildup of adiabatic heat caused by both plastic work and the exothermic transformation process,

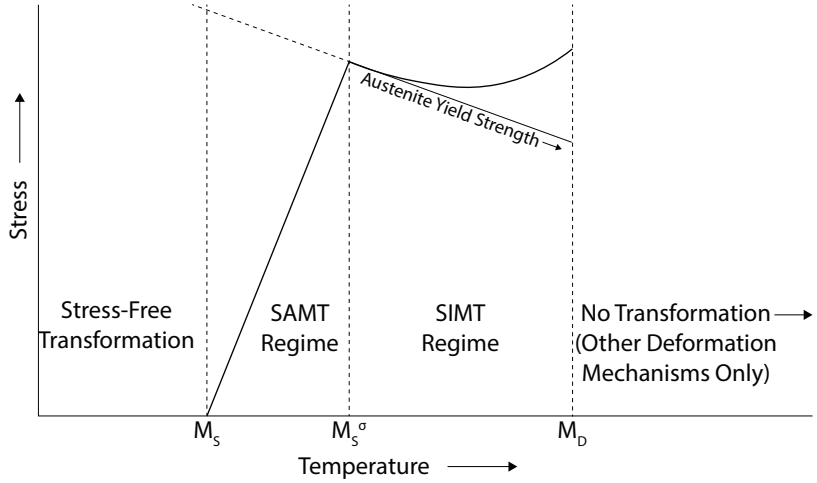

Figure 4.8: Schematic illustration of the stress required to cause martensitic transformation in several Fe-Ni-C austenitic steels as a function of temperature. Adapted from Ref. [11].

which will suppress continued transformation. This adiabatic heat buildup also occurs in alloys undergoing SIMT, of course. However, the response of mechanically-unstable austenite to an increase in temperature is very different depending upon whether the austenite is in the SAMT-dominated temperature regime or the SAMT-dominated temperature regime. Figure 4.8 serves as an example. This figure schematically illustrates the stress required to cause transformation in several Fe-Ni-C austenitic steels as a function of temperature. In the SAMT regime, the change in stress required to cause transformation due to an increase in temperature is large and positive. In the SIMT region, the change in required stress for the same amount of temperature increase is smaller, or even negative.

The second reason for the expected slowdown of transformation at high strain rates is the intrinsic rate sensitivity of the stress needed to cause transformation.

This was expressed by Olson and Cohen [126] as:

$$\frac{\delta\sigma}{\delta \ln \dot{\epsilon}} = -\frac{RT}{B\frac{\delta\Delta G}{\delta\sigma}} \tag{4.2}$$

where ΔG is the transformation free energy change per mole, T is the testing temperature, and R is the molar constant. B is a constant relating ΔG to the activation energy for isothermal martensite nucleation Q in the following way:

$$Q = A + B\Delta G \tag{4.3}$$

where A is also a constant. Using the more customary notation of a strain-rate sensitivity parameter m:

$$m = \frac{\delta \ln \sigma}{\delta \ln \dot{\epsilon}} = \frac{1}{\sigma}\frac{\delta\sigma}{\delta \ln \dot{\epsilon}} \tag{4.4}$$

we can then describe a material's flow stress (or transformation stress) σ as a function of strain rate $\dot{\epsilon}$ in the usual way:

$$\sigma = K\dot{\epsilon}^m \tag{4.5}$$

where K is a material-dependent constant. This sensitivity parameter has been found experimentally to be positive in the SAMT regime, meaning that higher stresses are required to initiate transformation at higher strain rates [32, 126]. Thus, SAMT is

expected to lead to a transformation rate which is always lower (as a function of strain) at high strain rates than at low strain rates, a behavior we observe in the totality of the austenite present in QLT-treated 10% Ni steel because of the large volume fraction of small particles.

Additional evidence that SAMT is occurring in at least some of the austenite particles in QLT-treated 10% Ni steel comes from one of the quasi-statically deformed specimens. This specimen was loaded elastically, but there was no bulk plastic strain in the specimen detectable by micrometer measurements. Nevertheless, VSM measurement of this elastically-loaded specimen revealed an austenite volume fraction lower than the undeformed condition by ~ 1.7 vol.%, well outside the standard deviation of the undeformed measurements. Steels which only undergo SIMT must accumulate enough plastic strain to have intersecting shear bands before any transformation of austenite can be detected.

Our results add supporting evidence for the size-dependent difference in transformation mechanisms we have described above from Yen *et al.* and Wang *et al.* [98,123], using a different steel composition and demonstrating that different-sized particles transform at different rates within the same microstructure depending on the applied strain rate. Our results do suggest a smaller size range where SAMT is favored, as only particles which are smaller than 100 nm appear to transform less rapidly at high strain rates. However, the percentage of transformed austenite in the range of $100 - 250$ nm is fairly similar at quasi-static and dynamic rates. This contrasts with

the size range of $250 - 500$ nm, in which substantially more austenite transformed during dynamic compression compared with quasi-static compression. (Almost no austenite particles larger than 500 nm remained in either deformed specimen.) This might suggest a range over which the austenite transitions from SAMT-dominated transformation to SIMT-dominated transformation.

It is also noteworthy that the primary alloying element in the steels studied in References [98, 123] is $9 - 11\%$ manganese, and they also contain either aluminum or silicon. A recent, thorough review of stacking fault energy (SFE) in steel [127] illustrates that, while the scatter in the measured SFE for steels of a given composition is distressingly large in the literature, it is fairly clear that nickel raises the SFE of steel more strongly than manganese (and any other common alloying element), while silicon and aluminum tend to lower the SFE. A higher SFE leads to narrower stacking faults [127]. Perhaps intersecting stacking faults can more readily form in smaller grains when the stacking faults themselves are smaller, because the energy cost associated with a new stacking fault traversing an existing stacking fault (as discussed by Yen *et al.* [123]) is lower. The ability of intersecting stacking faults to form in smaller austenite particles in the QLT-treated 10% Ni steel would explain the apparent smaller transition size between SAMT-like and SIMT-like transformation. Additionally, Reference [128] observed that the primary deformation mechanism in a 17Cr-7Ni steel transitions from SIMT to twinning below a grain size of 225 nm (compared with the $\sim$ 300 nm size range discussed by Yen *et al.* and Wang *et al.*),

illustrating that the particle size regime where different mechanisms are dominant is clearly composition- and/or process-dependent.

Chapter 5

Measurement of lattice strains during deformation of a QLT-treated 10% Ni steel

In this chapter, we will attempt to draw additional insights about the martensitic transformation and microstructural evolution of the experimental QLT-treat 10% Ni steel discussed throughout this dissertation by using diffraction-based elastic strain measurements. We will approach this by doing a higher-resolution examination of the diffraction rings we measured for the dynamically-compressed specimens at the synchrotron. We will also report on neutron diffraction measurements of the lattice strains present in the material under quasi-static tensile loading, intended for use in better understanding how load is partitioned between each phase within the mate-

rial during deformation. The results discussed in this chapter are more preliminary than those discussed in previous chapters. Due to the experimental constraints associated with time-resolved diffraction during high-strain-rate loading, as well as the complexity of this material's microstructure, we are not able to draw conclusions about the microstructural evolution of this material with the level of detail that has been achieved in the literature using diffraction measurements on quasi-statically-deforming materials. Nevertheless, these results lay the groundwork for future work on the load partitioning which can occur in multi-phase materials during dynamic loading.

5.1 Quantification of lattice strains in deforming families of grains

Elastic inter-atomic normal strains for specific subsets of crystallographic planes within a crystalline material can be measured using radiation such as x-rays or neutrons. The lattice strain ϵ_{hkl} of a particular plane is defined as:

$$\epsilon_{hkl} = \frac{d_{hkl} - d^0_{hkl}}{d^0_{hkl}} \tag{5.1}$$

where d_{hkl} is the measured interactomic spacing (d-spacing) of the particular atomic plane while under stress, and d^0_{hkl} is the measured d-spacing of that plane in the

absence of stress. This strain measurement only applies to the lattice planes which are oriented to diffract the incident radiation onto the detection device, *i.e.* the lattice planes which satisfy Bragg's Law:

$$\vec{q} = \vec{G}^{\star}_{hkl} \tag{5.2}$$

where $\vec{q}$ is the scattering vector introduced in Chapter 2 and $\vec{G}^{\star}_{hkl}$ is a reciprocal lattice vector with magnitude $\|\vec{G}^{\star}_{hkl}\| = 1/d_{hkl}$, where d_{hkl} is the interplanar spacing of a particular lattice plane $\{hkl\}$. The experimentalist can therefore determine the amount of strain in specific lattice planes oriented in specific directions within the material by using this measurement technique.

These elastic lattice strain measurements are of great use, both for determining the magnitude of residual stress present in materials intended for fatigue resistance or for some other critical load-bearing application [129], and for assessing the load partitioning between different phases and different crystallographic orientations of a material during deformation. This second use aids in microstructure design, as it yields insights about the relative importance of each phase to the material's mechanical properties at each stage of deformation and enables researchers to exploit this knowledge in the optimization of material processing [130, 131].

As opposed to the diffraction measurements described earlier in this dissertation, which utilized the short-camera-length setup described in Section 2.3.7, for the measurements of lattice strain described below we utilized the long-camera-length setup

which is also described in Section 2.3.7. This was done in an attempt to improve the angular resolution of the measurement, as a given deflection of a diffraction peak will move the peak across a greater number of detector pixels (or a larger fraction of one pixel) when the camera length is longer. A given lattice strain is therefore more likely to be resolved with a longer camera length. The downside to increasing the camera length with a detector of fixed size, of course, is that the solid angle covered by the detector decreases. In our case, this meant we could no longer observe complete diffraction rings on the detector, but instead could observe an azimuthal angle range of $\sim 40°$. We chose to observe diffraction from grains which had scattering vectors roughly aligned with the loading direction of the Kolsky bar specimens, although in the best case the scattering vectors were misaligned with the loading direction by $\sim 6 - 10°$, depending on the diffraction peak being considered. For this analysis we have azimuthally integrated intensity on the detector for all points within $\pm 10°$ of the part of the diffraction ring oriented closest to the loading direction.

5.2 Strain measurement during dynamic compression

The measured lattice strain as a function of bulk plastic strain in planes roughly aligned with the loading direction is shown for five nominally-identical QLT-treated 10% Ni steel specimens in Figures 5.1, 5.2, and 5.3. These Figures show the measured

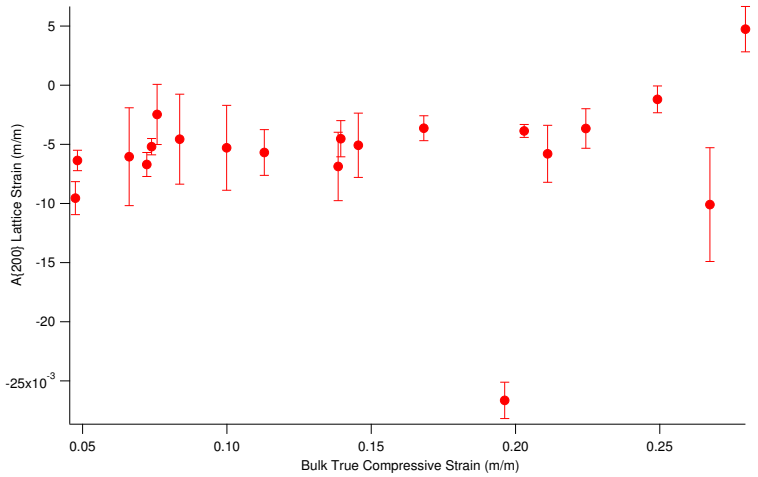

Figure 5.1: Measured lattice strains in the A{200} peak as a function of bulk plastic strain for 5 dynamically-deforming QLT-treated specimens.

lattice strain for the austenite {200} peak (A{200}), the ferrite/martensite {200} peak (F/M{200}), and the ferrite/martensite {211} peak (F/M{211}), respectively[1]. There is substantial scatter in the data, and the calculated error bars for many of the data points are quite large. This uncertainty is due to the fitting algorithm's low confidence in the fitted peak position. Example diffraction data that was used to make these strain calculations is shown in Figure 5.4. The signal-to-noise ratio in the data is clearly rather low, particularly in the dynamically-captured data, and many of the peaks are also not fully separated due to the wide bandpass of the undulator. Specific factors contributing to the peak position uncertainty (and ways to reduce that uncertainty in future experiments) will be discussed in more detail below.

Despite the large scatter in the data, some general trends can be observed. First,

[1]In general, ferrite and martensite peaks are extremely difficult to differentiate due to their very similar lattice constants, so here they are considered collectively.

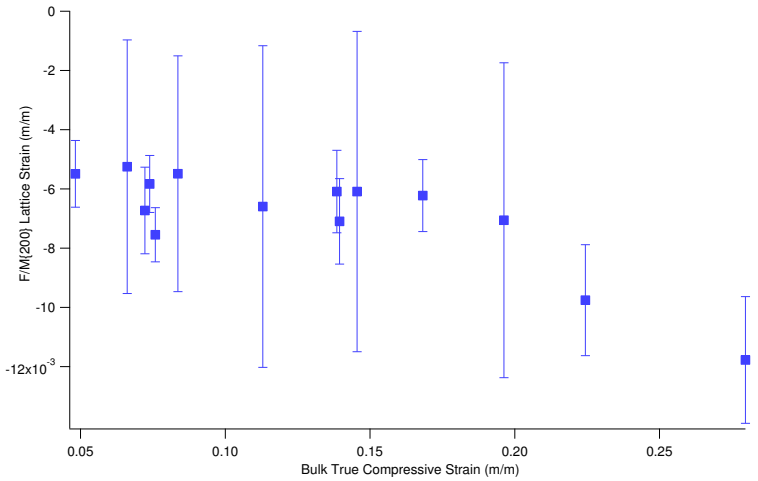

Figure 5.2: Measured lattice strains in the F/M{200} peak as a function of bulk plastic strain for 5 dynamically-deforming QLT-treated specimens.

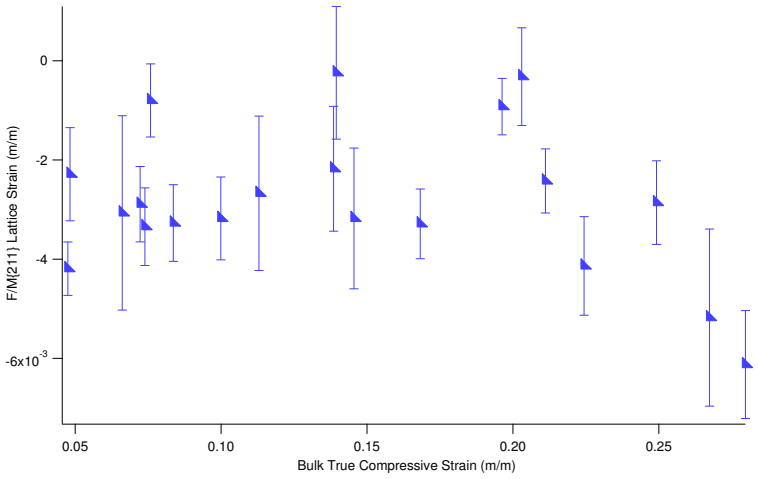

Figure 5.3: Measured lattice strains in the F/M{211} peak as a function of bulk plastic strain for 5 dynamically-deforming QLT-treated specimens.

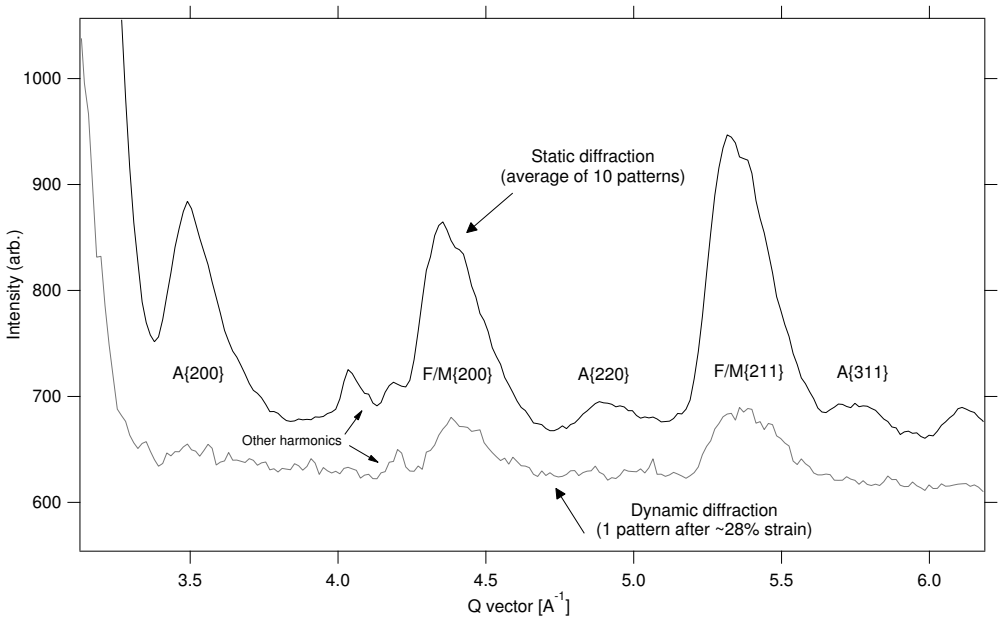

Figure 5.4: Representative diffraction data corresponding to the patterns collected before deformation and while deformation is occurring.

the lattice strain in all three peaks appears roughly constant until $\sim 17\%$ bulk plastic strain has accumulated. This suggests that there is not severe strain hardening happening in either phase happening at low strains. After $\sim 17\%$ bulk plastic strain, the compressive lattice strain in both ferrite/martensite peaks appears to increase in magnitude (*i.e.* become more negative). In contrast, the elastic strain in what remains of the austenite phase appears to drop. This point in the deformation process ($\sim 17\%$ bulk plastic strain) corresponds loosely with two other occurrences observed in Chapter 3: the near-cessation of martensitic transformation, and the softening of the bulk material.

The bulk softening of the material and the apparently increasing lattice strain in

the ferrite/martensite matrix may both be related to specimen heating. Experiments conducted by Fu *et al.* [132] in which quasi-static loading was combined with *in situ* diffraction measurements of the lattice strains in a Mn-Al-Si TRIP steel at temperatures differing by ~ 60 °C revealed that increasing the temperature led to a $\sim 7\%$ drop in bulk strength of the steel at high strains, while at the higher temperature the lattice strain in the ferrite phase rose by as much as $\sim 20\%$. These trends in material behavior are qualitatively similar to what we observe here, while the predicted temperature rise of our specimens over the course of testing was even higher (in excess of 80 °C). It is therefore conceivable that the noticeable drop in strength we observed in the latter part of the QLT-treated steel's stress-strain curve is related to the rising temperature of the specimen. This same work by Fu *et al.* also revealed an increase in lattice strain ($\sim 13\%$) in the austenite phase. Our data suggests that the austenite lattice strain may be decreasing at high strains instead of increasing, although the scatter in our austenite data is very large at high strains. This scatter is no doubt due, in part, to the greatly reduced intensity and signal-to-noise ratio of the austenite phase at high strains.

Regardless of testing temperature, Fu *et al.* observed a lattice strain in the austenite which roughly doubled in magnitude over the course of plastic deformation. Similar lattice strain behavior for the austenite phase of a multi-phase steel has been observed elsewhere as well [108, 131, 133], which is suggestive of significant strain hardening in the austenite. We see no evidence of this increasing lattice strain in the austenite

phase in QLT-treated 10% Ni steel. One possible explanation for this difference in behavior is the austenite peak we have chosen to analyze. Researchers often perform strain analysis on the F/M{211} peak and the A{311} peak in multi-phase steel, because the measured lattice strains in these peaks have been experimentally found to be the least sentitive to local intergranular strains [132, 134, 135]. However, in our case the A{311} peak had a very low initial signal-to-noise ratio, was overlapping with nearby peaks, and disappeared rapidly with deformation, so we were forced to consider the A{200} peak instead.

Another possible explanation for the lack of an increase in observed lattice strain has to do with the austenite particle size. References [108, 131, 133] all discuss steels where the average austenite particle size is at least 1 μm, and relatively coarse-grained FCC materials such as austenite will usually undergo substantial strain hardening (which in turn leads to increases in elastic lattice strains with continued deformation) based on dislocation entanglement. This is not necessarily true for nanocrystalline/ultrafine-grained austenite, though. Reference [136] explains that nanocrystalline metals often have very low strain hardening because they experience rapid dynamic recovery of dislocations. This dynamic recovery can even happen during high-strain-rate deformation, albeit to a decreased extent compared with quasi-static deformation [137]. Reference [138] discusses quasi-static deformation and *in situ* observations of lattice strains in a TRIP steel containing a substantial volume fraction of austenite particles smaller than 1 μm, and in this study the weighted

average lattice strain in the austenite phase increases at a far slower rate than the lattice strains reported in References [108, 131, 133]. The behavior of this relatively fine-grained austenite in Reference [138] is thus more in line with the negligible increase in strain we observe in the ultrafine-grained austenite particles of QLT-treated 10% Ni steel.

Dynamic recovery is particularly easy during deformation of nanocrystalline or ultrafine-grained materials with a high stacking fault energy (SFE) [139], and the high Ni content of the ultrafine-grained austenite in QLT-treated 10% Ni steel raises its SFE [127]. Recent compression experiments on single-phase ultrafine-grained aluminum (an FCC metal with a high SFE for which martensitic transformation is *not* a possible deformation mechanism) revealed negligible strain hardening or even strain softening occurred for tests done at room temperature and above [140], suggesting that similar negligible strain hardening is possible in the ultrafine-grained austenite we have studied.

5.3 Strategies for improved lattice strain measurements during dynamic deformation

Normally, when researchers conduct synchrotron diffraction-based strain measurements on a material as a function of deformation, they utilize a monochromatic x-ray beam of very high energy (usually ranging from $\sim$ 50 keV and to over 100 keV) which results in very high angular resolution. They also employ long exposure durations which are allowable due to the very slow or intermittent straining they apply to the specimen. Our dynamic experiments are inherently limiting in terms of the exposure durations we can employ, which means we must instead do everything else possible to maximize both signal-to-noise ratio and angular resolution.

One improvement for future experiments in this regard would be to employ a different undulator and/or undulator harmonic. The experiment described here utilized the relatively low-peak-intensity, relatively broad 4th undulator harmonic of the U30 undulator. (Use of this harmonic was not by choice, but instead resulted indirectly from another beamline malfunction outside of our control.) The aforementioned impediment in the beampath exacerbated these problems, especially the problem of low intensity. This low intensity necessitated longer exposure durations to get clearly-defined peaks, which no doubt resulted in some "smearing" of the peak

position as the specimen was continuously deforming. The peak broadness hinders the differentiation between neighboring peaks, and disincentivizes fitting algorithms from determining the peak position with very high accuracy compared with narrower peaks. In the future, use of an undulator harmonic with a narrower bandpass would certainly improve data quality. As mentioned in Chapter 2, we have had more success interpreting elastic strain information contained in x-ray diffraction data which was collected using pink beam which had a bandpass of $\sim 2\%$. In contrast, the bandpass from the 4th harmonic of the U30 undulator is substantially higher, at $\sim 5.3\%$.

If elastic strain measurements are the main priority of the synchrotron diffraction experiment, a monochromatic beam should also be considered. Despite the longer integration times this would require and the associated "smearing" of strain information that might result, it would offer significant advantages in terms of angular resolution. As we demonstrated with Monel®-400 in Chapter 2, we were able to obtain interpretable strain measurements even with integration times which spanned roughly half of the entire deformation event thanks to the high angular resolution of the high-energy, monochromatic beam we used. If the objective is to resolve peaks with very similar d-spacings such as 10% Ni steel's A{111} and F/M{110} peaks, or to individually resolve both ferrite and martensite peaks that have essentially the same d-spacing, then high angular resolution becomes even more important. In these cases, use of a monochromatic beam might be the only viable option.

Another strategy which might yield more easily-interpreted strain information is

to test a thinner specimen. This would have benefited the experiment described in this work by bringing the specimen's initial thickness closer to the material's absorption length, which would result in more diffracted intensity on the detector. The grain size of the specimens we tested was so small that decreasing the specimen thickness somewhat would not have caused experimental problems associated with poor powder averaging, but making the compression specimens we used thinner would increase the chances of buckling during deformation. Thus, all the dimensions of the compression specimen would have to be smaller for this strategy to be holistically effective. Considering the experimental difficulties already associated with the specimens we used due to their small size, this strategy might work better for dynamic tension tests. Tension testing allows for the testing of long, tall, thin specimens without the risk of buckling, and offers the added benefit that the input and output bars move away from the x-ray beam during testing. This would eliminate the problems we encountered in some experiments where the input bar occluded a significant fraction of the diffracted x-rays during deformation.

Given the numerous negative aspects of the "pink" beam radiation we used with regard to the measurement of elastic strains, and the low signal-to-noise ratio obtained in the time-resolved x-ray diffraction experiments described above, one might reasonably wonder if the differences in fitted peak position we have obtained are attributable to lattice strains at all. In principle, they might be attributable to some systematic bias in the data analysis process we have used, or some other process

which is irrelevant to the mechanical properties of the material. While we cannot address that concern rigorously here, we offer below a simple demonstration that the measured peak shifts are at least approximately the magnitude one would expect based on elastic lattice strains, indicating that improved pink beam measurements might lead to more useful quantitative results in the future. To do so, we will utilize measured stress factors for the material, discussed in the next section.

5.4 Stress factor measurement

In order to assist future analyses of the load partitioning between phases in 10% Ni steel, we have measured the stress factors [9, 100–102] for this steel in the QLT-treated condition under uniaxial tensile stress[2]. As explained in Chapter 2, these stress factors F_{11} relate the macroscopically applied uniaxial stress to the measured elastic normal strains in certain crystal planes in certain directions in the specimen reference frame while that macroscopic stress is applied. In general, these lattice strains in response to an applied stress will differ from what would be predicted based on either single-crystal elastic constants or the material's bulk elastic constants. This is because specific grains within the material will be elastically confined in specific ways by neighboring crystallites, such that those specific grains do not deform in response to a macroscopically-applied stress the same way that a single crystal or an

[2]These measurements were conducted under tension, despite all of our other measurements being conducted under compression, because doing so dramatically improved the feasibility of stress factor measurements in the experimental apparatus which was available to us.

isotropic medium would.

Factors which influence the real elastic strains exhibited in a particular grain include that grain's single-crystal elastic properties, that grain's orientation relative to the applied stress, that grain's shape and shape orientation, as well as the single-crystal elastic constants, orientations, shapes and shape orientations of the crystallites surrounding the grain in question. Stress factors are based on direct measurement of the real normal lattice strains of specific crystal planes, meaning they automatically account for all these factors which influence a grain's deformation. (They are, however, averages over all the crystal planes oriented in a certain direction in the volume interrogated by radiation. In general, these planes will belong to grains which have a variety of different shapes, shape orientations, and confinement by neighboring crystallites.) Because stress factors are influenced by all the above factors, they will change based on testing temperature, texture evolution, and phase evolution within a material [101, 141, 142]. Several models of varying complexity have been developed over the years to calculate stress factors based on these material parameters [9, 143, 144]. Because they provide a more realistic understanding of how grains of an anisotropic material deform due to an applied stress, stress factors are valuable for the measurement of residual stresses in materials and can also be used for load partitioning studies.

For the measurement of stress factors in 10% Ni steel, we performed neutron diffraction on a specimen undergoing a uniaxial tensile test, as described in Sec-

tion 2.6. The tensile axis of the specimen (aligned with the plate's rolling direction) corresponds to the "x" axis in Figure 2.27. The plate's transverse direction was aligned with the "y" axis in Figure 2.27. For the measurements we have conducted, the tilt angle of the specimen was not varied ($\psi = 0$), and measurements of lattice strains were made with scattering vectors parallel and perpendicular to the loading direction ($\phi = 0, \pi$). The stress factors measured at room temperature along the loading direction (the steel's rolling direction) during elastic loading of the steel are shown in Table 5.1. The measured stress factors under the same conditions, but measured after the specimen had undergone 7% plastic tensile strain, are shown in Table 5.2. Tables 5.3 and 5.4 show the measured stress factors along the transverse direction under the same testing condition specified in Tables 5.1 and 5.2, respectively.

Crystal Plane Family	F_{11}, 0% Strain (TPa)	F_{11}, 7% Strain (TPa)
F/M{200}	168 ± 1.34	161 ± 0.795
F/M{211}	232 ± 2.28	216 ± 1.23
A{200}	173 ± 1.40	155 ± 1.61
A{220}	216 ± 2.39	293 ± 1.54
A{311}	201 ± 1.76	237 ± 7.41

Table 5.1: Measured stress factors along the tensile loading direction at room temperature for various ferrite/martensite and austenite crystal planes in QLT-treated 10% Ni steel.

Using the measured stress factors for QLT-treated 10% Ni steel along the loading direction (rolling direction) at room temperature, and the measured lattice strains from our time-resolved x-ray diffraction experiment, we have recalculated the stress acting on specific lattice planes approximately aligned with the specimen loading di-

Crystal Plane Family	F_{11}, 0% Strain (TPa)	F_{11}, 7% Strain (TPa)
F/M{200}	180 ± 1.06	197 ± 1.00
F/M{211}	220 ± 6.42	262 ± 1.42
A{200}	179 ± 1.2	238 ± 4.4
A{220}	214 ± 3.74	399 ± 2.15
A{311}	186 ± 6.93	342 ± 10.3

Table 5.2: Measured stress factors along the tensile loading direction at 200 °C for various ferrite/martensite and austenite crystal planes in QLT-treated 10% Ni steel.

Crystal Plane Family	F_{11}, 0% Strain (TPa)	F_{11}, 7% Strain (TPa)
F/M{211}	-800 ± 22.5	-680 ± 17.8
F/M{220}	-920 ± 50.3	-1120 ± 69.2
A{220}	-620 ± 14.4	-950 ± 223
A{311}	-750 ± 26.9	-761 ± 94

Table 5.3: Measured stress factors along the transverse direction at room temperature for various ferrite/martensite and austenite crystal planes in QLT-treated 10% Ni steel.

rection during dynamic compression. An example of this data (for F/M{200} planes) is shown in Figure 5.5 as a function of bulk plastic strain in the specimen. Plotted in the same Figure is the average bulk true stress-true strain curve for the dynamically-compressed QLT-treated material. Although the uncertainty in the recalculated stress is very large, the most likely values of recalculated stress below $\sim$ 17% bulk plastic strain are at least roughly the magnitude one would expect them to be in the ferrite/martensite matrix. (Because ferrite/martensite makes up the large majority of the material, it stands to reason that the stress acting on the ferrite/martensite phase should be close to the stress acting on the material as a whole.)

The analysis is obviously simplistic and incomplete, but the very large uncertainty

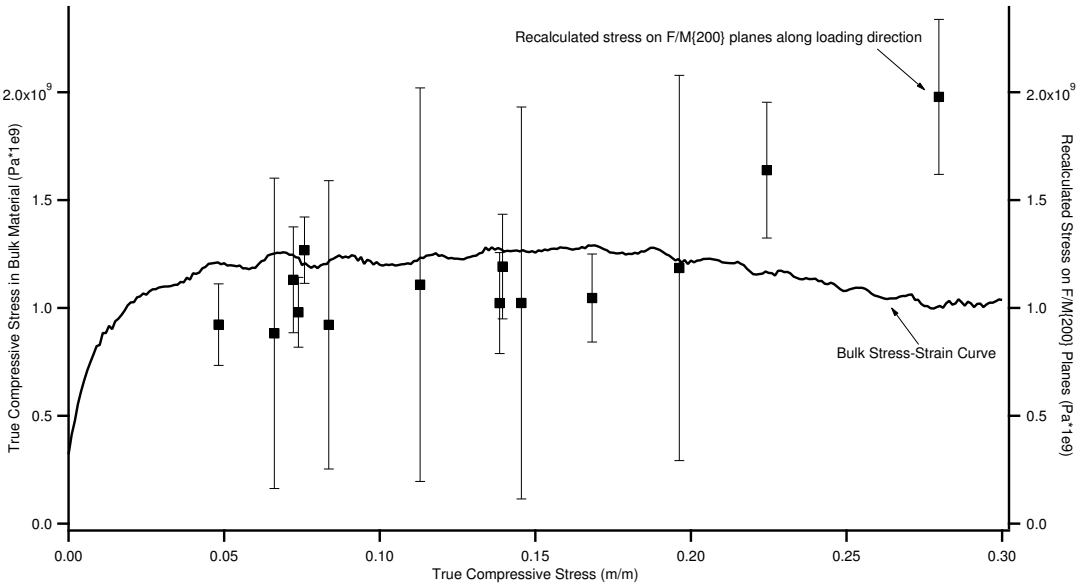

Figure 5.5: Recalculated stress acting on the F/M{200} planes oriented along the loading direction of the dynamically-compressed QLT-treated 10% Ni steel specimens described in Chapters 3-4. The average bulk true stress-true strain curve for the dynamically-compressed QLT specimens is also shown, plotted on the same scale.

Crystal Plane Family	F_{11}, 0% Strain (TPa)	F_{11}, 7% Strain (TPa)
F/M{220}	-980 ± 74	-1180 ± 12.8
F/M{211}	-730 ± 29.1	780 ± 10.9
A{220}	-640 ± 26.4	-1180 ± 107
A{311}	-800 ± 37.9	-1140 ± 77.7

Table 5.4: Measured stress factors along the transverse direction at 200 °C for various ferrite/martensite and austenite crystal planes in QLT-treated 10% Ni steel.

in the lattice strain data suggests that any more rigorous analysis would not be appropriate at this time. This analysis does at least indicate that future time-resolved elastic strain measurements using high-flux pink x-ray sources will be more effective for rigorous analysis of the load partitioning in dense, multi-phase materials deforming at high rates.

Chapter 6

Conclusions and suggestions for future work

In the first part of this chapter, we will briefly summarize the primary research outcomes of this dissertation. In the second part of this chapter, we will propose some future research that seems to be the logical next step following the results of the work presented here.

6.1 Conclusions

Over the course of this work, we have developed a novel technique for interrogating dense dynamically-deforming polycrystalline specimens with high-energy synchrotron radiation to record time-resolved diffraction patterns. This technique was validated

as an effective way to measure phase transformation, texture evolution, and lattice strain evolution in metallic specimens of both low and intermediate density, utilizing either fast shutters or a fast detector to achieve the temporal resolution.

We employed the above technique, along with numerous other characterization techniques, to characterize the starting microstructures, bulk stress-strain behavior, and austenite transformation behavior of 10% Ni steel specimens in selected QT, QL, and QLT heat treatment conditions during dynamic compression. The QLT specimens contained much more thermally-stable austenite than the other two heat-treated conditions, and portions of this austenite transformed over a large range of strain. In contrast, a somewhat smaller volume fraction of austenite in the QL specimens transformed over a smaller range of strain, and what little austenite exists in the QT specimens appears almost completely mechanically stable. Although the compressive stress-strain curves are fairly similar for each of the three heat-treated conditions, the QLT condition avoids losing strength longer than the other conditions, and maintains a strength at high strains which is higher than the QL condition and comparable to the QT condition. This prolonged maintenance of hardness, in combination with the substantial ability to undergo transformation hardening even at high strains, is likely a contributing factor in the QLT-treated steel's high resistance to shear banding and failure during FSP ballistic tests.

During the *in situ* characterization of this austenite transformation behavior, we further determined that the competing factors of increasing plastic strain and increas-

ing temperature do not lead to discrepancies between the austenite volume fractions which are measured *in situ* and *ex situ* for this steel. Therefore, further characterization of the austenite transformation behavior in this steel during dynamic compression can be carried out *ex situ* with confidence in the measurements. This result may not necessarily generalize to every steel and every loading condition, however.

To gain further insights into the nature of the austenite transformation of the QLT-treated steel, we further characterized the austenite transformation behavior in the QLT-treated steel during quasi-static compression. The strain-rate-dependent austenite transformation behavior in the steel we studied differed from what is seen in several more common steels including AISI 304 austenitic stainless steel and Mn-Si TRIP steel. Specifically, the volume fraction of austenite in this QLT-treated 10% Ni steel is always higher during dynamic compression than during quasi-static compression, whereas the austenite transformation rate in AISI 304 and Mn-Si TRIP steel is initially higher at high strain rates.

Quantitative microstructural analysis of the deformed specimens using EBSD, in conjunction with bulk measurements of the austenite volume fraction using VSM and synchrotron x-ray diffraction, revealed that the austenite grain size distribution evolves in different ways during quasi-static and dynamic compression. In quasi-statically compressed specimens, the volume fraction of austenite particles which are larger than ~ 100 nm is higher than the volume fraction of equivalently-sized austenite particles in dynamically compressed specimens, even while the total volume fraction

of austenite is higher in the dynamically compressed specimens. This suggests two subsets of austenite particles with different strain-rate-dependent behaviors: particles larger than $\sim$ 100 nm which transform *more* rapidly with increasing strain rate, and particles smaller than $\sim$ 100 nm which transform *less* rapidly with strain rate. Particles in the size range of $100 - 250$ nm transformed at fairly comparable rates under both loading conditions, while particles larger than 250 nm transformed much more rapidly at high strain rates.

Based on these observations, the behavior of the larger particles could be explained by the combined occurrence of strain-induced martensitic transformation (SIMT), which is the mechanism of transformation recognized in AISI 304 and Mn-Si TRIP steels, and stress-assisted martensitic transformation (SAMT). The behavior of the smaller particles is more consistent with a primarily SAMT-like transformation. Recent quasi-static experiments by other researchers on experimental duplex and TRIP-maraging steels revealed evidence of a transition from SIMT-like deformation to SAMT-like deformation as the austenite particle size fell below $\sim$ 300 nm. The strain-rate-dependent transformation behavior of the two subsets of austenite particles observed in our work is consistent with this size-based transition between deformation mechanisms. The smaller length scale ($\sim$ 100 nm vs. $\sim$ 300 nm) of the inferred crossing-over point between SAMT-dominated transformation and SIMT-dominated transformation in 10% Ni steel might be explained by the strong effect that Ni has on raising the stacking fault energy, and thus decreasing the stacking

fault width, in austenite.

Finally, we again utilized the newly-developed time-resolved diffraction technique to characterize the evolution of elastic strains within specific subsets of crystal planes of the austenite and ferrite/martensite phases in QLT-treated 10% Ni steel during dynamic compression. The average lattice strain in all measured phases appears to remain roughly constant until $\sim 17\%$ strain, at which point the average lattice strain in the ferrite/martensite phase appears to increase while the strain in the austenite phase appears to decrease. The lack of hardening observed in the austenite phase may be due to dynamic recovery which is facilitated by the small particle size and high stacking fault energy of the austenite. The apparent increase in ferrite/martensite lattice strains at high bulk plastic strains may be attributable to adiabatic heating of the specimen.

6.2 Suggestions for future work

The work done in this dissertation has raised a number of scientific questions which could be addressed in future work. For example, while we have presented evidence to suggest different transformation mechanisms acting in different-sized austenite particles, there is very little discussion of transformation mechanisms specifically in the literature on low-carbon Ni steel containing $\sim 4-14\%$ Ni. There is thus ample opportunity to contribute to our body of knowledge in that area. Similarly, studies related

to the size dependence of the transformation mechanism are apparently in their early stages for many (or possibly all) classes of steel, so there is ample opportunity for discovery in this area of study too.

Further, little or no work has been done thus far on load partitioning in multi-phase steels during dynamic deformation (for good pragmatic reasons, as the very large uncertainties in the measurements presented here demonstrate). However, continued refinement of the experimental techniques we have developed at DCS or CHESS could allow for very significant improvements in lattice strain data quality. The load partitioning information which would come from this lattice strain data would be of great use for the validation of crystal plasticity models. These models, incidentally, have also received very little attention in the low-carbon Ni steel community (at least to our knowledge), but would be of great assistance for better understanding the evolution of this experimental QLT-treated 10% Ni steel's particularly complicated microstructure.

Listed below are some specific recommendations for future work:

1. Experimental observation of the deformation-induced lattice defects characteristic of stress-assisted and strain-induced martensitic transformation in individual deformed austenite particles. Observation of these defects in individual particles (*e.g.* through the use of transmission electron microscopy or electron channeling contrast imaging) would reveal whether the strain-rate-dependent transformation behavior we have documented is indeed due to different transformation

mechanisms, or due to some other cause. If different mechanisms are indeed acting, this microstructural study would help to more accurately determine the size threshold which determines the change in deformation mechanism. In addition, observation of the dislocation structures within the austenite particles could help determine if the diffraction measurements indicating negligible/negative strain hardening in the austenite phase are accurate.

2. More detailed characterization of load partitioning in each phase over the course of quasi-static and dynamic deformation under different stress states. This information can be used to develop more detailed phase-specific stress-strain curves which would be valuable for the development of a crystal plasticity model.

3. Assessment of the austenite transformation behavior under different stress states at quasi-static and dynamic rates.

4. Experimental determination of the M_s and M_s^σ temperatures for the room-temperature-stable austenite particles in QLT-treated 10% Ni steel. There may in fact be M_s and M_s^σ temperature *ranges*, as opposed to discrete temperatures, due to the variation in austenite particle sizes, both above and below the $\sim$ 100 nm size which is apparently dividing the transformation behavior between stress-assisted and strain-induced character at room temperature. At the very least, there are evidently different M_s^σ temperatures for the different-sized subsets of grains.

5. Implementation of a crystal plasticity model that accounts for the observed load partitioning between different phases, as well as the different strain-rate-dependent transformation behavior of different subsets of austenite particles.

Appendix A

Microcontroller Code

The microcontroller used to help synchronize the fast shutter opening with the arrival of the strain pulse at the sample was a Teensy 3.1. This is an inexpensive device that can be programmed using the Arduino® open-source electronic prototyping platform.

The microcontroller was programmed to calculate the speed of the striker bar based on the times when two optical gates in the path of the striker are triggered. Then, based on this speed, the distance from the downstream optical gate to the incident bar, the length of the incident bar, the speed of sound in the incident bar, the opening time required for the fast shutter, and an experimentally-determined correction factor for acceleration of the striker, the microcontroller calculates a delay time. Then, after this calculated delay time has elapsed, the microcontroller sends a TTL voltage signalling the fast shutters to begin opening. When the breech pressure

was held nominally constant, this allowed us to open the fast shutters at the desired time relative to the start of specimen deformation with a time jitter of ~ 25 μs. This jitter was quite small relative to the several hundred microseconds needed to open the fast shutters, complete the compression event, and close the fast shutters again. Example code for programming the microcontroller is shown below. It is important to note that this code exploits a fast read/write functionality of the Teensy that requires the read and write pins to be specified in advance. The upstream optical gate output signal should be connected to pin 7 on the Teensy, the downstream optical gate output signal should be connected to pin 8, and the Trigger In cable for the fast shutters should be connected to pin 9.

```
const unsigned long laserSeparation = 40.0;
const unsigned long barDistance = 113;
const unsigned long pulsePropagationTime = 200;
const unsigned long velocityChangeFactor = 1.3;
void setup() {
Serial.begin(38400);
pinMode(7, INPUT);
pinMode(8, INPUT);
pinMode(9, OUTPUT);
}
void loop()
{
  while (digitalReadFast(7) == HIGH) {
    continue;
  }
unsigned long Time1 = micros();
Serial.print("Time1 is: ");
Serial.print(Time1);
while (digitalReadFast(8) == HIGH) {
  continue;
}
unsigned long Time2 = micros();
Serial.print("Time2 is: ");
Serial.print(Time2);
unsigned long elapsedTime = Time2 - Time1;
Serial.print("Elapsed Time is: ");
Serial.print(elapsedTime);
unsigned long delayTime = velocityChangeFactor*barDistance/
```

```
    laserSeparation*elapsedTime + pulsePropagationTime;
delayMicroseconds(delayTime);
digitalWriteFast(9, HIGH);
Serial.print("Delay time is: ");
Serial.print(delayTime);
delay(100000);
}
```

Appendix B

Mathematica Detector Signal Calculator Code

Displayed below is the code written for Wolfram Mathematica used to help predict the scattered intensity on a detector pixel from an iron specimen, to be used for planning the setup of future time-resolved synchrotron experiments. This code accounts for the effects of absorption, atomic scattering factor, the multiplicity of the peak being observed, detector efficiency, beamline flux, detector pixel size, air scattering, and beamline polarization.

```
intensity[θ_, λ_, μ_, t_, flux_, ao_, rdiff_, musi_] := flux ro^2 polarization
  absorption[θ, μ, t] 4 fhkl^2 (ao/va) (λ^3/va) mhkl (1/(8 π rdiff Sin[θ]^2 Cos[θ])) detector[musi]

ro = 2.82*^-15;

energy = 34;
λ = 12.398 / energy / 1*^10;

mhkl = 6;

θ = ArcSin[λ/(2 * 2.8665 * 1.732 * 0.333 * 10^-10)];
q = 4 * π * Sin[θ]/λ;
a1 = 11.7695; a2 = 7.3573; a3 = 3.5222; a4 = 2.3045;
b1 = 4.7611; b2 = 0.3072; b3 = 15.3535; b4 = 76.8805;
c = 1.0369;
fhkl = a1 Exp[-b1 ((q * 1 * 10^-10)/(4 π))^2] + a2 Exp[-b2 ((q * 1 * 10^-10)/(4 π))^2] +
  a3 Exp[-b3 ((q * 1 * 10^-10)/(4 π))^2] + a4 Exp[-b4 ((q * 1 * 10^-10)/(4 π))^2] + c
16.6716

μ = 4464;

va = (2.8665*^-10)^3;

polarization = 1;

absorption[θ_, μ_, t_] := ∫_0^t Exp[-μ (z + (t - z)/Cos[2 θ])] dz

detector[musi_] = 1. - Exp[-musi 500*^-6];

musi = 7692;

intensityPerPixel[θ_, λ_, μ_, t_, flux_, ao_, rdiff_, musi_, air_, pixelSize_, time_] :=
  intensity[θ, λ, μ, t, flux, ao, rdiff, musi] air pixelSize time;
```

Appendix C

Kolsky Bar Strain Gauge and Synchrotron Diffraction Pattern Analysis Code

Displayed below are some of the most important programs produced in the Hufnagel lab over the course of this work which were used to analyze the 2-dimensional x-ray diffraction patterns we recorded using our synchrotron techniques. These programs perform background subtraction, fit the beam center of the diffraction pattern, convert the detector data from Cartesian to polar coordinates, azimuthally integrate peak intensity, fit the data using convolutions of Gaussian functions with the instrument response function, calculate the measured volume fraction of austenite, and determine elastic strains during loading. Additional code used for data analysis (not

shown here) was provided by Vignesh Kannan and by Reference [145].

Main program:

```
function DCSFeb2016Analyzer( baseDataDir, material,
   materialID, numStatic, dezingerRadius1,
   dezingerProportion1, dezingerRadius2,
   dezingerProportion2, dezingerRadius3,
   dezingerProportion3, Ws, Hs, Ls, maxFreq, ciLevel,
   detectorClose )
%For analyzing in-situ Kolsky bar experiments at DCS
%{
Last updated: Paul Lambert, 29 April 2016
REQUIRED SCRIPTS:
KolskyBar_dataprocessing
BridgeCktAnalysis
Filter_Kannan_realsignal
Disp_corr_latest_Bancroft
DCSbacksubtract2016_2
FitStrainEllipseMethod2016
PolarTransformationAll
NewConvolutionFitQAll
VolumeFractionCalculatorAll
INPUT PARAMETERS:
baseDataDir = the name of the overall directory where the
   data is saved
material = the name of the specific type of material being
    analyzed, e.g.
"rolledMg" or "ECAEMg"
materialID = the number of the specific sample being
   analyzed
numStatic = the number of static images to be averaged
dezingerRadius1 = the radius of pixels to be examined
   during the
dezingering process for the averaged dark image.
dezingerProportion1 = if the proportional difference
   between a given pixel in the averaged dark image and
the average of its surrounding pixels exceeds this number,
    the pixel value
will be changed to the average of its surrounding pixels.
dezingerRadius2 = like dezingerRadius1, but for the
   averaged static image.
```

```
In principle, we might want these numbers to be different.
dezingerProportion2 = like dezingerProportion1, but for
   the averaged static
image.
dezingerRadius3 = like dezingerRadius1, but for the
   dynamic image.
dezingerProportion3 = like dezingerProportion1, but for
   the dynamic image.
Ws = initial sample size in the direction of the x-ray
   beam
Hs = initial sample size in the vertical direction
Ls = inital sample size in the loading direction
maxFreq = cutoff frequency for noise in the Kolsky bar
   data analysis
ciLevel = (a value between 0 and 1) the size of the
   confidence interval
that you want Matlab to calculate in the fitting
   procedures
detectorClose = detector position (1 for close, 0 for far)
%}
lambda = 3.8685e-11;
Aso = Ws*Hs;
nu = 0.3;
%Creating stress-strain curve and other Kolsky bar stuff
[time,timeAdjusted,displacement,force,trueStress,
   trueStrain,trueStrainRate,monitor,cam1startstrain,
   cam1endstrain,cam2startstrain,cam2endstrain,
   cam3startstrain,cam3endstrain,cam4startstrain,
   cam4endstrain]=KolskyBar_dataprocessing(Aso,Ls,maxFreq,
   baseDataDir,material,materialID);
%Determining the strain at which each x-ray camera turned
   on and off
dataDir4 = strcat(baseDataDir,'Camera4/');
camerastrains = dlmread(sprintf('%s%s_%s_camera_strains.
   txt',dataDir4,material,materialID));
cam1startstrain = camerastrains(1,1); cam1endstrain =
   camerastrains(1,2);
cam2startstrain = camerastrains(2,1); cam2endstrain =
   camerastrains(2,2);
cam3startstrain = camerastrains(3,1); cam3endstrain =
   camerastrains(3,2);
cam4startstrain = camerastrains(4,1); cam4endstrain =
```

```
   camerastrains(4,2);
%Determining the strain at (roughly) the middle of each
   detector capture,
%dubbed Strain1, Strain2, Strain3, and Strain4
Strain1 = (cam1endstrain + cam1startstrain)./2;
Strain2 = (cam2endstrain + cam2startstrain)./2;
Strain3 = (cam3endstrain + cam3startstrain)./2;
Strain4 = (cam4endstrain + cam4startstrain)./2;
StrainErrorBars = zeros(4,2);
StrainErrorBars(5,1) = cam1endstrain - Strain1;
StrainErrorBars(6,1) = cam2endstrain - Strain2;
StrainErrorBars(7,1) = cam3endstrain - Strain3;
StrainErrorBars(8,1) = cam4endstrain - Strain4;
StrainErrorBars(5,2) = Strain1 - cam1startstrain;
StrainErrorBars(6,2) = Strain2 - cam2startstrain;
StrainErrorBars(7,2) = Strain3 - cam3startstrain;
StrainErrorBars(8,2) = Strain4 - cam4startstrain;
if size(force,1) > size(force,2)
   force = force';
   displacement = displacement';
end
size(time)
size(timeAdjusted)
size(displacement)
size(force)
size(trueStress)
size(trueStrain)
size(trueStrainRate)
kolskyData = vertcat(time,timeAdjusted,displacement,force,
   trueStress,trueStrain,trueStrainRate);
kolskyDataInfo = horzcat(Ws, Hs, Ls, maxFreq,
   cam1startstrain, cam1endstrain, cam2startstrain,
   cam2endstrain, cam3startstrain, cam3endstrain,
   cam4startstrain, cam4endstrain);
%Prep for the for loop that analyzes each camera
counter = 1;
AusteniteVsStrain = zeros(8,2);
AusteniteVsStrainPost = zeros(4,2);
UpperErrorBars = zeros(8,1);
LowerErrorBars = zeros(8,1);
UpperErrorBarsPost = zeros(4,1);
LowerErrorBarsPost = zeros(4,1);
```

```
M200strain = zeros(4,2);
M200Shearstrain = zeros(4,2);
M211strain = zeros(4,2);
M211Shearstrain = zeros(4,2);
A200strainvsStrain = zeros(4,2);
F200strainvsStrain = zeros(4,2);
F211strainvsStrain = zeros(4,2);
A200StrainErrorBars = zeros(4,2);
F200StrainErrorBars = zeros(4,2);
F211StrainErrorBars = zeros(4,2);
F110width = zeros(4,2);
A200width = zeros(4,2);
F200width = zeros(4,2);
F211width = zeros(4,2);
F211StrainLowerErrorBars = zeros(4,1);
F211StrainUpperErrorBars = zeros(4,1);
filename = strcat(material,'_',materialID);
for CAMNUM = 1:4
    dataDir = sprintf('%sCamera%s/',baseDataDir,num2str(
       CAMNUM));
    %Approximating the thickness of the sample in the
       direction of the x-ray
    %beam during each detector capture
    Ws1 = Ws * (1 + 0.5*Strain1);
    Ws2 = Ws * (1 + 0.5*Strain2);
    Ws3 = Ws * (1 + 0.5*Strain3);
    Ws4 = Ws * (1 + 0.5*Strain4);
    %Saving Kolsky bar info (in each camera folder, for
       convenience)
    dlmwrite(sprintf('%s%s_%
       s_Bulk_StressStrainCurve_Results.txt',dataDir,
       material,materialID),kolskyData,'delimiter','\t','
       precision',7);
    dlmwrite(sprintf('%s%s_%
       s_Bulk_StressStrainCurve_MetaData.txt',dataDir,
       material,materialID),kolskyDataInfo,'delimiter','\t
       ','precision',4);
    close all
    if detectorClose == 0
        if CAMNUM == 1
            pixelSize = (41.5e-6);
            beamCenterApproxX = 3000.93;
```

```
    beamCenterApproxY = 1066.7;
    cameraLength = (286.989e-3);
end
if CAMNUM == 2
    pixelSize = (42.0e-6);
    beamCenterApproxX = 2996.34,;
    beamCenterApproxY = 1063.52;
    cameraLength = (286.063e-3);
end
if CAMNUM == 3
    pixelSize = (42.5e-6);
    beamCenterApproxX = 2990.87;
    beamCenterApproxY = 1079.55;
    cameraLength = (289.018e-3);
end
if CAMNUM == 4
    pixelSize = (41.1e-6);
    beamCenterApproxX = 3000;
    beamCenterApproxY = 1086.69;
    cameraLength = (284.20e-3);
end
%Specifies parameters for the fitting and
   austenite volume fraction for
%each image
if CAMNUM == 1
    thickness = Ws1;
    currentStrain = Strain1;
end
if CAMNUM == 2
    thickness = Ws2;
    currentStrain = Strain2;
end
if CAMNUM == 3
    thickness = Ws3;
    currentStrain = Strain3;
end
if CAMNUM == 4
    thickness = Ws4;
    currentStrain = Strain4;
end
[strainA200, WidthSA200, WidthDA200,
   FracStrainUncertaintyA200 ] =
```

```
    DetectorFarStrain10A200( filename, dataDir,
    pixelSize, cameraLength, beamCenterApproxX,
    beamCenterApproxY, CAMNUM, thickness )
[strain, WidthS, WidthD, FracStrainUncertaintyF200
    ] = DetectorFarStrain10( filename, dataDir,
    pixelSize, cameraLength, beamCenterApproxX,
    beamCenterApproxY, CAMNUM, thickness )
[strain211, WidthS211, WidthD211,
    FracStrainUncertaintyF211] =
    DetectorFarStrain10F211( filename, dataDir,
    pixelSize, cameraLength, beamCenterApproxX,
    beamCenterApproxY, CAMNUM, thickness )
pause();
%[strain, WidthS, WidthD] = DetectorFarStrain15(
    filename, dataDir, pixelSize, cameraLength,
    beamCenterApproxX, beamCenterApproxY, CAMNUM,
    thickness )
%[strain211, WidthS211, WidthD211] =
    DetectorFarStrain15F211( filename, dataDir,
    pixelSize, cameraLength, beamCenterApproxX,
    beamCenterApproxY, CAMNUM, thickness )
A200strainvsStrain(CAMNUM,1) = currentStrain;
F200strainvsStrain(CAMNUM,1) = currentStrain;
F211strainvsStrain(CAMNUM,1) = currentStrain;
A200strainvsStrain(CAMNUM,2) = strainA200(1);
F200strainvsStrain(CAMNUM,2) = strain(1);
F211strainvsStrain(CAMNUM,2) = strain211(1);
A200StrainErrorBars(CAMNUM,1) = currentStrain;
F200StrainErrorBars(CAMNUM,1) = currentStrain;
F211StrainErrorBars(CAMNUM,1) = currentStrain;
A200StrainErrorBars(CAMNUM,2) =
    FracStrainUncertaintyA200;
F200StrainErrorBars(CAMNUM,2) =
    FracStrainUncertaintyF200;
F211StrainErrorBars(CAMNUM,2) =
    FracStrainUncertaintyF211;
A200width(CAMNUM,1) = 0;
F200width(CAMNUM,1) = 0;
F211width(CAMNUM,1) = 0;
A200width(CAMNUM,2) = WidthSA200(1);
F200width(CAMNUM,2) = WidthS(1);
F211width(CAMNUM,2) = WidthS211(1);
```

```
        A200width(4+CAMNUM,1) = currentStrain;
        F200width(4+CAMNUM,1) = currentStrain;
        F211width(4+CAMNUM,1) = currentStrain;
        A200width(4+CAMNUM,2) = WidthDA200(1);
        F200width(4+CAMNUM,2) = WidthD(1);
        F211width(4+CAMNUM,2) = WidthD211(1);
    end

    if detectorClose == 1
        %camera parameters
        if CAMNUM == 1
            pixelSize = (41.5e-6);
            beamCenterApproxX = 1077.3; %Average of fitted
                beam centers for QLT_R_#18 and QLT_R_#21,
               which look good
            beamCenterApproxY = 1055.7; %Average of fitted
                beam centers for QLT_R_#18 and QLT_R_#21,
               which look good
            cameraLength = (76.36e-3);
        end
        if CAMNUM == 2
            pixelSize = (42.0e-6);
            beamCenterApproxX = 1074.7;
            beamCenterApproxY = 1056.7;
            cameraLength = (77.61e-3);
        end
        if CAMNUM == 3
            pixelSize = (42.5e-6);
            beamCenterApproxX = 1081.4;
            beamCenterApproxY = 1053.5;
            cameraLength = (78.04e-3);
        end
        if CAMNUM == 4
            pixelSize = (41.1e-6);
            beamCenterApproxX = 1077.3;
            beamCenterApproxY = 1062.4;
            cameraLength = (76.71e-3);
        end
        %Background subtraction
        if counter == 1
            maxIntensity = 1;
        end
```

```
        [ staticBkgdSubWithPeaks, dynamicBkgdSub,
           maxIntensity ] = DCSbacksubtract2016_2(
           baseDataDir, material, materialID, CAMNUM,
           beamCenterApproxX, beamCenterApproxY, numStatic
           , maxIntensity );
        %Refining the beam center (comment out the last 3
           lines for time
        %efficiency if precise beam center is not
           important)
        x = [1:1:2048];
        y = [1:1:2048];
        X0staticM211 = beamCenterApproxX;
        Y0staticM211 = beamCenterApproxY;
        %
%         if exist(sprintf('%s%s_%s_C%
   s_BeamCenter_for_M211.txt',dataDir,material,materialID,
   num2str(CAMNUM)), 'file') == 2
%             FittedBeamCenter = dlmread(sprintf('%s%s_%
   s_C%s_BeamCenter_for_M211.txt',dataDir,material,
   materialID,num2str(CAMNUM)))
%             X0staticM211 = FittedBeamCenter(1);
%             Y0staticM211 = FittedBeamCenter(2);
%         else
 %             [fitresult1, gof1, coefvals1, ci1] =
    FitStrainEllipseMethod2016_M211(x, y,
    staticBkgdSubWithPeaks, 0.6, beamCenterApproxX,
    beamCenterApproxY );
 %             X0staticM211 = coefvals1(end - 2)
 %             Y0staticM211 = coefvals1(end - 1)
%         end
%
         BeamCenterM211 = horzcat(X0staticM211,
            Y0staticM211);
         dlmwrite(sprintf('%s%s_%s_C%s_BeamCenter_for_M211
            .txt',dataDir,material,materialID,num2str(
            CAMNUM)),BeamCenterM211,'delimiter','\t','
            precision',7);
        X0dynamic = X0staticM211;
        Y0dynamic = Y0staticM211;
        X0post = X0staticM211;
        Y0post = Y0staticM211;
        %Caking the static images
```

```
[ Zinterp1 ] = PolarTransformationAll_M200(
   X0staticM211, Y0staticM211, dataDir, material,
   materialID, dezingerRadius2,
   dezingerProportion2, CAMNUM, 's' );
[ Zinterp2 ] = PolarTransformationAll_M200(
   X0dynamic, Y0dynamic, dataDir, material,
   materialID, dezingerRadius2,
   dezingerProportion2, CAMNUM, 'd' );
if exist(sprintf('%s%s_%s_C%s_p.tif',dataDir,
   material,materialID,num2str(CAMNUM)), 'file')
   == 2
    [ Zinterp3 ] = PolarTransformationAll_M200(
       X0post, Y0post, dataDir, material,
       materialID, dezingerRadius2,
       dezingerProportion2, CAMNUM, 'p' );
end
%Caking the static images
[ Zinterp1 ] = PolarTransformationAll(
   X0staticM211, Y0staticM211, dataDir, material,
   materialID, dezingerRadius2,
   dezingerProportion2, CAMNUM, 's' );
[ Zinterp2 ] = PolarTransformationAll( X0dynamic,
   Y0dynamic, dataDir, material, materialID,
   dezingerRadius2, dezingerProportion2, CAMNUM, '
   d' );
if exist(sprintf('%s%s_%s_C%s_p.tif',dataDir,
   material,materialID,num2str(CAMNUM)), 'file')
   == 2
    [ Zinterp3 ] = PolarTransformationAll( X0post,
       Y0post, dataDir, material, materialID,
       dezingerRadius2, dezingerProportion2,
       CAMNUM, 'p' );
end
%Specifies parameters for the fitting and
   austenite volume fraction for
%each image
if CAMNUM == 1
    thickness = Ws1;
    currentStrain = Strain1;
end
if CAMNUM == 2
    thickness = Ws2;
```

```
        currentStrain = Strain2;
    end
    if CAMNUM == 3
        thickness = Ws3;
        currentStrain = Strain3;
    end
    if CAMNUM == 4
        thickness = Ws4;
        currentStrain = Strain4;
    end
    %Fitting the data to a convolution of the
       instrument response and a
    %series of Gaussians
    %M200
        [ coefvalsstaticstrain, resnormstaticstrain ]
           = NewConvolutionFitQAllStrain( dataDir,
           material, materialID, pixelSize,
           cameraLength, dezingerRadius2,
           dezingerProportion2, X0dynamic, Y0dynamic,
           CAMNUM, Ws, lambda, 's' )
        for n = 1:size(coefvalsstaticstrain,1)
            k = 1;
            %for j = 1:9
            for j = 1:1
                for i = 1:3
                    peakFitDataStatic(j,i,n) =
                       coefvalsstaticstrain(n,k);
                    k = k + 1;
                end
            end
        end
        [ coefvalsdynamicstrain, resnormdynamicstrain
           ] = NewConvolutionFitQAllStrain( dataDir,
           material, materialID, pixelSize,
           cameraLength, dezingerRadius3,
           dezingerProportion3, X0dynamic, Y0dynamic,
           CAMNUM, thickness, lambda, 'd' )
        for n = 1:size(coefvalsdynamicstrain,1)
            k = 1;
            %for j = 1:9
            for j = 1:1
                for i = 1:3
```

```
                    peakFitDataDynamic(j,i,n) =
                        coefvalsdynamicstrain(n,k);
                    k = k + 1;
                end
            end
        end
    qStatic = zeros(1,size(peakFitDataDynamic,3));
    %qStatic(1,:) = peakFitDataStatic(6,2,:)
    qStatic(1,:) = peakFitDataStatic(1,2,:)
    qStatic = qStatic';

    figure
    plot((1:size(coefvalsstaticstrain,1)),qStatic)
    title(strcat(material,num2str(materialID),'-C',
        num2str(CAMNUM),' Variation in Static M{211}
        Fitted Peak Position for Each Azimuthal Range')
        );
    savefig(sprintf('%s%s_%s_C%
        s_Static_Variation_in_M211_Peak_Position',
        dataDir,material,materialID,num2str(CAMNUM)))

    thetaStatic = asin(1e10.*qStatic.*lambda./(4.*pi))
        ;
    dStatic = lambda./(2.*sin(thetaStatic));

    qDynamic = zeros(1,size(peakFitDataDynamic,3));
    %qDynamic(1,:) = peakFitDataDynamic(6,2,:)
    qDynamic(1,:) = peakFitDataDynamic(1,2,:)
    qDynamic = qDynamic';

    figure
    plot((1:size(coefvalsdynamicstrain,1)),qDynamic)
    title(strcat(material,num2str(materialID),'-C',
        num2str(CAMNUM),' Variation in Dynamic M{211}
        Fitted Peak Position for Each Azimuthal Range')
        );
    savefig(sprintf('%s%s_%s_C%
        s_Dynamic_Variation_in_M211_Peak_Position',
        dataDir,material,materialID,num2str(CAMNUM)))

    thetaDynamic = asin(1e10.*qDynamic.*lambda./(4.*pi
        ));
```

```
dDynamic = lambda./(2.*sin(thetaDynamic));
twothetaDynamic = thetaDynamic*2;

strains = (dDynamic - dStatic)./dStatic;

azimuth = [0:(360/size(peakFitDataDynamic,3)):(360
    - 360/size(peakFitDataDynamic,3))].*pi./180;
azimuth = azimuth';
ellipsetilt = 0;
if CAMNUM == 4
    ellipsetilt = 0.*pi./180;
end
sinsquared = sin(azimuth + ellipsetilt).^2;

figure
plot(azimuth,strains)
title(strcat(material,num2str(materialID),'-C',
   num2str(CAMNUM),' (dM{211}-sM{211})/sM{211} for
    Each Azimuthal Range'));
savefig(sprintf('%s%s_%s_C%s_M211_strain_simple',
   dataDir,material,materialID,num2str(CAMNUM)))

figure
plot(sinsquared,strains)
title(strcat(material,num2str(materialID),'-C',
   num2str(CAMNUM),' Un-corrected M211 sin^2 plot'
   ));
savefig(sprintf('%s%s_%s_C%
   s_M211_uncorrected_sinsquared',dataDir,material
   ,materialID,num2str(CAMNUM)))
%direction cosines between sample coordinate
   system and laboratory
%coordinate system
cos22prime = cos(azimuth).*ones(size(
   peakFitDataDynamic,3),1);
cos33prime = cos(azimuth).*ones(size(
   peakFitDataDynamic,3),1);
cos23prime = cos(azimuth + pi/2).*ones(size(
   peakFitDataDynamic,3),1);
cos32prime = cos(azimuth - pi/2).*ones(size(
   peakFitDataDynamic,3),1);
```

```
eprime22 = strains;
eprime22_addon = eprime22(1:(size(strains,1)/2),:)
   ;
eprime33 = [eprime22;eprime22_addon];
eprime33 = eprime33((1+size(strains,1)/2):end,:);
eprime23 = zeros(size(peakFitDataDynamic,3),1);

%resolves strains onto laboratory coordinate
   system
e22 = cos22prime.*cos22prime.*eprime22 +
   cos23prime.*cos23prime.*eprime33 + cos22prime.*
   cos23prime.*eprime23;
e33 = cos32prime.*cos32prime.*eprime22 +
   cos33prime.*cos33prime.*eprime33 + cos32prime.*
   cos33prime.*eprime23;

for k = 1:(size(strains,1)/2)
    e22Diametric(k,:) = (e22(k,:) + e22(k+(size(
       strains,1)/2),:))/2;
    qDynamicDiametric(k,:) = (qDynamic(k,:) +
       qDynamic(k+(size(strains,1)/2),:))/2;
end
twothetaDynamicDiametric = 2.*asin(
   qDynamicDiametric.*lambda./(4.*pi));

incrementDiametric = 0:(360/size(
   peakFitDataDynamic,3)):(180 - 360/size(
   peakFitDataDynamic,3));

azimuthDiametric = incrementDiametric.*pi./180;
azimuthDiametric = azimuthDiametric';
sinsquaredDiametricStatic = sin((
   incrementDiametric + ellipsetilt).*pi./180).^2;
sinsquaredDiametricDynamic = sin((
   incrementDiametric + ellipsetilt).*pi./180).^2;
sinsquaredDiametricDynamic =
   sinsquaredDiametricDynamic';

figure
plot(sinsquaredDiametricDynamic,e22Diametric)
title(strcat(material,num2str(materialID),'-C',
   num2str(CAMNUM),' Elastic Strain Plot for M211
```

```
    (no correction)'));

figure
plot(sinsquaredDiametricDynamic,e22Diametric)
title(strcat(material,num2str(materialID),'-C',
    num2str(CAMNUM),' Elastic Strain Plot for M211'
    ));
weightslinearfit = ones(size(e22Diametric));

%[fitresult, gof, linearFitCoef, ci] =
    weightedLinearFit(sinsquaredDiametricDynamic,
    e22Diametric, weightslinearfit, 0.6);

weightslinearfit = ones(size(e22));
sinsquared = sinsquared(37:108);
e22old = e22;
e22 = e22./(cos(twothetaDynamic.*cos(azimuth)).^2
    + nu.*sin(twothetaDynamic.*cos(azimuth)).^2);
(e22-e22old)./e22old
e22 = e22(37:108);
weightslinearfit = weightslinearfit(37:108);
[fitresult, gof, linearFitCoef, ci] =
    weightedLinearFit(sinsquared, e22,
    weightslinearfit, 0.95);

F211StrainLowerErrorBars(CAMNUM,1) = linearFitCoef
    (1) - ci(1,1);
F211StrainUpperErrorBars(CAMNUM,1) = ci(2,1) -
    linearFitCoef(1);

M211strain(CAMNUM,1) = currentStrain;
M211strain(CAMNUM,2) = linearFitCoef(1);
M211Shearstrain(CAMNUM,1) = currentStrain;
M211Shearstrain(CAMNUM,2) = linearFitCoef(2);
title(strcat(material,num2str(materialID),'-C',
    num2str(CAMNUM),' Elastic Strain Plot for M211
    with Fit'));
savefig(sprintf('%s%s_%s_C%
    s_Elastic_Strain_Plot_for_M211',dataDir,
    material,materialID,num2str(CAMNUM)))

dlmwrite(sprintf('%s%s_%s_C%
```

```
    s_Strain_Fit_Results_for_M211.txt',dataDir,
    material,materialID,num2str(CAMNUM)),
    linearFitCoef,'delimiter','\t','precision',7);
%Fitting the data to a convolution of the
    instrument response and a
%series of Gaussians
[ coefvalsstaticfirsttwo, resnormstaticfirsttwo ]
    = NewConvolutionFitQAllAusteniteFirstTwo(
    dataDir, material, materialID, pixelSize,
    cameraLength, dezingerRadius2,
    dezingerProportion2, X0dynamic, Y0dynamic,
    CAMNUM, Ws, lambda, 's' )
[ coefvalsdynamicfirsttwo, resnormdynamicfirsttwo
    ] = NewConvolutionFitQAllAusteniteFirstTwo(
    dataDir, material, materialID, pixelSize,
    cameraLength, dezingerRadius3,
    dezingerProportion3, X0dynamic, Y0dynamic,
    CAMNUM, thickness, lambda, 'd' )
if exist(sprintf('%s%s_%s_C%s_p.tif',dataDir,
    material,materialID,num2str(CAMNUM)), 'file')
    == 2
      [ coefvalspostfirsttwo, resnormpostfirsttwo ]
        = NewConvolutionFitQAllAusteniteFirstTwo(
        dataDir, material, materialID, pixelSize,
        cameraLength, dezingerRadius3,
        dezingerProportion3, X0dynamic, Y0dynamic,
        CAMNUM, thickness, lambda, 'p' )
end
%Fitting the data to a convolution of the
    instrument response and a
%series of Gaussians
[ coefvalsstatic, resnormstatic ] =
    NewConvolutionFitQAllAustenite( dataDir,
    material, materialID, pixelSize, cameraLength,
    dezingerRadius2, dezingerProportion2, X0dynamic
    , Y0dynamic, CAMNUM, Ws, lambda, 's' )
[ coefvalsdynamic, resnormdynamic ] =
    NewConvolutionFitQAllAustenite( dataDir,
    material, materialID, pixelSize, cameraLength,
    dezingerRadius3, dezingerProportion3, X0dynamic
    , Y0dynamic, CAMNUM, thickness, lambda, 'd' )
if exist(sprintf('%s%s_%s_C%s_p.tif',dataDir,
```

```
        material,materialID,num2str(CAMNUM)), 'file')
        == 2
          [ coefvalspost, resnormpost ] =
             NewConvolutionFitQAllAustenite( dataDir,
             material, materialID, pixelSize,
             cameraLength, dezingerRadius3,
             dezingerProportion3, X0dynamic, Y0dynamic,
             CAMNUM, thickness, lambda, 'p' )
    end

    coefvalsstatic(4:6) = coefvalsstaticfirsttwo
        (10:12);
    coefvalsdynamic(4:6) = coefvalsdynamicfirsttwo
        (10:12);
    %Calculate the austenite volume fraction from the
        fitted peak
    %parameters
    [percentAusteniteDistinctStatic,
        percentAusteniteDistinctStaticUpper,
        percentAusteniteDistinctStaticLower] =
        VolumeFractionCalculatorAll( coefvalsstatic,
        dataDir, material, materialID, dezingerRadius2,
         dezingerProportion2, X0staticM211,
        Y0staticM211, CAMNUM, lambda, 0, 's' )
    UpperErrorBars(CAMNUM,1) =
        percentAusteniteDistinctStaticUpper -
        percentAusteniteDistinctStatic;
    LowerErrorBars(CAMNUM,1) =
        percentAusteniteDistinctStatic -
        percentAusteniteDistinctStaticLower;
    AusteniteVsStrain(CAMNUM,2) =
        percentAusteniteDistinctStatic;

    savefig(sprintf('%s%s_%s_C%
        s_Peak_Fitting_for_Volume_Fraction_Static',
        dataDir,material,materialID,num2str(CAMNUM)))

    [percentAusteniteDistinctDynamic,
        percentAusteniteDistinctDynamicUpper,
        percentAusteniteDistinctDynamicLower] =
        VolumeFractionCalculatorAll( coefvalsdynamic,
        dataDir, material, materialID, dezingerRadius3,
```

```
    dezingerProportion3, X0dynamic, Y0dynamic,
    CAMNUM, lambda, currentStrain, 'd' )
UpperErrorBars(4+CAMNUM,1) =
    percentAusteniteDistinctDynamicUpper -
    percentAusteniteDistinctDynamic;
LowerErrorBars(4+CAMNUM,1) =
    percentAusteniteDistinctDynamic -
    percentAusteniteDistinctDynamicLower;

savefig(sprintf('%s%s_%s_C%
    s_Peak_Fitting_for_Volume_Fraction_Dynamic',
    dataDir,material,materialID,num2str(CAMNUM)))

if exist(sprintf('%s%s_%s_C%s_p.tif',dataDir,
    material,materialID,num2str(CAMNUM)), 'file')
    == 2
     [percentAusteniteDistinctPost,
        percentAusteniteDistinctPostUpper,
        percentAusteniteDistinctPostLower] =
        VolumeFractionCalculatorAll( coefvalspost,
        dataDir, material, materialID,
        dezingerRadius3, dezingerProportion3,
        X0dynamic, Y0dynamic, CAMNUM, lambda,
        currentStrain, 'p' )
     UpperErrorBarsPost(CAMNUM,1) =
        percentAusteniteDistinctPostUpper -
        percentAusteniteDistinctPost;
     LowerErrorBarsPost(CAMNUM,1) =
        percentAusteniteDistinctPost -
        percentAusteniteDistinctPostLower;
end
CAMNUM
currentStrain
AusteniteVsStrain(4+CAMNUM,1) = currentStrain;
AusteniteVsStrain(4+CAMNUM,2) =
    percentAusteniteDistinctDynamic;
if exist(sprintf('%s%s_%s_C%s_p.tif',dataDir,
    material,materialID,num2str(CAMNUM)), 'file')
    == 2
     AusteniteVsStrainPost(CAMNUM,1) = 0.5;
     AusteniteVsStrainPost(CAMNUM,2) =
        percentAusteniteDistinctPost;
```

```
        end
        counter = counter + 1;
        close all
    end
end
    if detectorClose == 1
    figure
    plot(M200strain(:,1),M200strain(:,2))
    title(strcat(material,num2str(materialID),'-C',num2str
       (CAMNUM),' Compressive Strain in the Loading
       Direction for M200 as a Function of Plastic Strain'
       ));
    dlmwrite(sprintf('%s%s_%s_C%s_M200StrainVsStrain.txt',
       dataDir,material,materialID,num2str(CAMNUM)),
       M200strain,'delimiter','\t','precision',7);
    savefig(sprintf('%s%s_%s_C%s_M200StrainPlot',dataDir,
       material,materialID,num2str(CAMNUM)))
    figure
    plot(M200Shearstrain(:,1),M200Shearstrain(:,2))
    title(strcat(material,num2str(materialID),'-C',num2str
       (CAMNUM),' Shear Strain in M200 as a Function of
       Plastic Strain'));
    dlmwrite(sprintf('%s%s_%s_C%s_M200ShearStrainVsStrain.
       txt',dataDir,material,materialID,num2str(CAMNUM)),
       M200Shearstrain,'delimiter','\t','precision',7);
    savefig(sprintf('%s%s_%s_C%s_M200ShearStrainPlot',
       dataDir,material,materialID,num2str(CAMNUM)))

    figure
    errorbar(M211strain(:,1),M211strain(:,2),
       F211StrainLowerErrorBars,F211StrainUpperErrorBars)
    title(strcat(material,num2str(materialID),'-C',num2str
       (CAMNUM),' Compressive Strain in the Loading
       Direction for M211 as a Function of Plastic Strain'
       ));
    dlmwrite(sprintf('%s%s_%s_C%s_M211StrainVsStrain.txt',
       dataDir,material,materialID,num2str(CAMNUM)),
       M211strain,'delimiter','\t','precision',7);
    savefig(sprintf('%s%s_%s_C%s_M211StrainPlot',dataDir,
       material,materialID,num2str(CAMNUM)))

    figure
```

```
plot(M211Shearstrain(:,1),M211Shearstrain(:,2))
title(strcat(material,num2str(materialID),'-C',num2str
   (CAMNUM),' Shear Strain in M211 as a Function of
   Plastic Strain'));
dlmwrite(sprintf('%s%s_%s_C%s_M211ShearStrainVsStrain.
   txt',dataDir,material,materialID,num2str(CAMNUM)),
   M211Shearstrain,'delimiter','\t','precision',7);
savefig(sprintf('%s%s_%s_C%s_M211ShearStrainPlot',
   dataDir,material,materialID,num2str(CAMNUM)))

AusteniteVsStrain
AusteniteVsStrainPost
%Plots the measured austenite content as a funtion of
   strain for the
%sample, along with the uncertainty in the measurement
figure
errorbar(AusteniteVsStrain(:,1),AusteniteVsStrain(:,2)
   ,LowerErrorBars,UpperErrorBars,'kx')
title(strcat(material,num2str(materialID),'-C',num2str
   (CAMNUM),' Austenite Volume Fraction as a Function
   of True Compressive Strain'));
if exist(sprintf('%s%s_%s_C%s_p.tif',dataDir,material,
   materialID,num2str(CAMNUM)), 'file') == 2
    hold on
    errorbar(AusteniteVsStrainPost(:,1),
       AusteniteVsStrainPost(:,2),LowerErrorBarsPost,
       UpperErrorBarsPost,'bx')
end
title(strcat(material,num2str(materialID),'-C',num2str
   (CAMNUM),' Austenite Content as a Function of
   Strain'));
savefig(sprintf('%s%s_%s_C%s_AusteniteVsStrainPlot',
   dataDir,material,materialID,num2str(CAMNUM)))
%Save the volume fraction data
dlmwrite(sprintf('%s%s_%s_AusteniteVsStrain.txt',
   dataDir,material,materialID),AusteniteVsStrain,'
   delimiter','\t','precision',7);
dlmwrite(sprintf('%s%s_%s_AusteniteUpperErrorBars.txt'
   ,dataDir,material,materialID),UpperErrorBars,'
   delimiter','\t','precision',7);
dlmwrite(sprintf('%s%s_%s_AusteniteLowerErrorBars.txt'
   ,dataDir,material,materialID),LowerErrorBars,'
```

```
    delimiter','\t','precision',7);
dlmwrite(sprintf('%s%s_%s_F211StrainLowerErrorBars.txt
    ',dataDir,material,materialID),
    F211StrainLowerErrorBars,'delimiter','\t','
    precision',7);
dlmwrite(sprintf('%s%s_%s_F211StrainUpperErrorBars.txt
    ',dataDir,material,materialID),
    F211StrainUpperErrorBars,'delimiter','\t','
    precision',7);
dlmwrite(sprintf('%s%s_%s_StrainErrorBars.txt',dataDir
    ,material,materialID),StrainErrorBars,'delimiter','
    \t','precision',7);

if exist(sprintf('%s%s_%s_C%s_p.tif',dataDir,material,
    materialID,num2str(CAMNUM)), 'file') == 2
     dlmwrite(sprintf('%s%s_%s_C%
         s_AusteniteVsStrainPost.txt',dataDir,material,
         materialID,num2str(CAMNUM)),
         AusteniteVsStrainPost,'delimiter','\t','
         precision',7);
end
end

if detectorClose == 0
     A200StrainErrorBars
     figure
     errorbar(A200strainvsStrain(:,1),
         A200strainvsStrain(:,2),A200StrainErrorBars
         (:,2),A200StrainErrorBars(:,2))
     title('A200 strain vs. strain')
     figure
     errorbar(F200strainvsStrain(:,1),
         F200strainvsStrain(:,2),F200StrainErrorBars
         (:,2),F200StrainErrorBars(:,2))
     title('F200 strain vs. strain')
     figure
     errorbar(F211strainvsStrain(:,1),
         F211strainvsStrain(:,2),F211StrainErrorBars
         (:,2),F211StrainErrorBars(:,2))
     title('F211 strain vs. strain')
     figure
     plot(A200width(:,1),A200width(:,2))
```

```
            title('A200 width vs. strain')
            figure
            plot(F200width(:,1),F200width(:,2))
            title('F200 width vs. strain')
            figure
            plot(F211width(:,1),F211width(:,2))
            title('F211 width vs. strain')
            dlmwrite(sprintf('%s%s_%s_A200strainVsStrain_10.
               txt',dataDir,material,materialID),
               A200strainvsStrain,'delimiter','\t','precision'
               ,7);
            dlmwrite(sprintf('%s%s_%s_F200strainVsStrain_10.
               txt',dataDir,material,materialID),
               F200strainvsStrain,'delimiter','\t','precision'
               ,7);
            dlmwrite(sprintf('%s%s_%s_F211strainVsStrain_10.
               txt',dataDir,material,materialID),
               F211strainvsStrain,'delimiter','\t','precision'
               ,7);
            dlmwrite(sprintf('%s%s_%s_A200StrainErrorBars_10.
               txt',dataDir,material,materialID),
               A200StrainErrorBars,'delimiter','\t','precision
               ',7);
            dlmwrite(sprintf('%s%s_%s_F200StrainErrorBars_10.
               txt',dataDir,material,materialID),
               F200StrainErrorBars,'delimiter','\t','precision
               ',7);
            dlmwrite(sprintf('%s%s_%s_F211StrainErrorBars_10.
               txt',dataDir,material,materialID),
               F211StrainErrorBars,'delimiter','\t','precision
               ',7);
            dlmwrite(sprintf('%s%s_%s_A200Width_10.txt',
               dataDir,material,materialID),A200width,'
               delimiter','\t','precision',7);
            dlmwrite(sprintf('%s%s_%s_F200Width_10.txt',
               dataDir,material,materialID),F200width,'
               delimiter','\t','precision',7);
            dlmwrite(sprintf('%s%s_%s_F211Width_10.txt',
               dataDir,material,materialID),F211width,'
               delimiter','\t','precision',7);
    end
end
```

Sub-programs: Background subtraction of data:

```
function [ staticBkgdSub, dynamicBkgdSub, maxIntensity ] =
    DCSbacksubtract2016_2( baseDataDir, material,
   materialID, CAMNUM, beamCenterApproxX,
   beamCenterApproxY, numStatic, maxIntensity )

sampleName = strcat(material,'_',materialID);
dataDir = sprintf('%sCamera%s/',baseDataDir,num2str(CAMNUM
   ));
%Masks of various kinds:
[rows columns] = meshgrid(1:2048);
maskBeamCenter = sqrt((rows-beamCenterApproxX).^2+(columns
   -beamCenterApproxY).^2)<=180;
maskBeamStop = rows > beamCenterApproxX & abs(columns -
   beamCenterApproxY) < 40;
%create bright field image
for k = 1:10
    A = imread(sprintf('%sBrightfield_C%s_shift150um.tif',
       dataDir,num2str(CAMNUM)), k);
    brightstack(:,:,k) = A;
end
brightAverage = mean(brightstack,3);
%open all static images
for k = 1:10
    A = imread(sprintf('%s%s_C%s_s.tif',dataDir,sampleName
       ,num2str(CAMNUM)), k);
    staticstack(:,:,k) = A;
end
%average static images
staticAverage = mean(staticstack,3);
staticAverage = uint16(staticAverage);
imwrite(staticAverage,sprintf('%s%s_%s_C%s_s_avg.tif',
   dataDir,material,materialID,num2str(CAMNUM)))
staticAverage = double(staticAverage);
%subtract average bright field from average static.
if min(min(staticAverage)) < min(min(brightAverage))
   staticAverage = staticAverage + min(min(brightAverage))
       - min(min(staticAverage));
end
staticBkgdSub = staticAverage - brightAverage;
staticBkgdSub = uint16(staticBkgdSub);
```

```
imwrite(staticBkgdSub,sprintf('%s%s_%s_C%s_s_avg_bsub1.tif
   ',dataDir,material,materialID,num2str(CAMNUM)))
staticBkgdSub = double(staticBkgdSub);
%load dynamic image and subtract average bright field.
dynamic = imread(sprintf('%s%s_C%s_d.tif',dataDir,
   sampleName,num2str(CAMNUM)));
dynamic = double(dynamic);
if min(min(dynamic)) < min(min(brightAverage))
    dynamic = dynamic + min(min(brightAverage))- min(min(
       dynamic));
end
dynamicBkgdSub = dynamic - brightAverage;
%Masks
dynamicBkgdSub(maskBeamCenter) = NaN;
dynamicBkgdSub(maskBeamStop) = NaN;
%save prior to de-zingering
dynamicBkgdSub = uint16(dynamicBkgdSub);
imwrite(dynamicBkgdSub,sprintf('%s%s_%s_C%s_d_bsub1.tif',
   dataDir,material,materialID,num2str(CAMNUM)))
figure
imagesc(staticBkgdSub,([0 max(max(staticBkgdSub))])); axis
    square;
title(strcat(material,num2str(materialID),'-C',num2str(
   CAMNUM),' Bright-subtracted Static image'));
figure
imagesc(dynamicBkgdSub); axis square;
title(strcat(material,num2str(materialID),'-C',num2str(
   CAMNUM),' Bright-subtracted Dynamic image'));
%check for post-mortem images
if exist(sprintf('%s%s_C%s_p.tif',dataDir,sampleName,
   num2str(CAMNUM)), 'file') == 2
%open all post images
for k = 1:10
    A = imread(sprintf('%s%s_C%s_p.tif',dataDir,sampleName
       ,num2str(CAMNUM)), k);
    poststack(:,:,k) = A;
end
%average post images
postAverage = mean(poststack,3);
postAverage = uint16(postAverage);
imwrite(postAverage,sprintf('%s%s_%s_C%s_p_avg.tif',
   dataDir,material,materialID,num2str(CAMNUM)))
```

```
postAverage = double(postAverage);
%subtract average bright field from average post.
if min(min(postAverage)) < min(min(brightAverage))
    postAverage = postAverage + min(min(brightAverage)) -
       min(min(postAverage));
end
postBkgdSub = postAverage - brightAverage;
postBkgdSub = uint16(postBkgdSub);
imwrite(postBkgdSub,sprintf('%s%s_%s_C%s_p_avg_bsub1.tif',
   dataDir,material,materialID,num2str(CAMNUM)))
figure
imagesc(dynamicBkgdSub); axis square;
title(strcat(material,num2str(materialID),'-C',num2str(
   CAMNUM),' Bright-subtracted Post-mortem image'));
end
end
```

Sub-programs: Determination of beam center using ellipse fit:

```
function [fitresult, gof, coefvals, ci] =
   FitStrainEllipseMethod2016_M211(x, y, M, ciLevel,
   beamCenterApproxX, beamCenterApproxY )
%% Fit: 'untitled fit 1'.
[xData, yData, zData, weights] = prepareSurfaceData( x, y,
    M, M );
BeamCenterLimit = 0.5;
lowerBounds = [0.8 10 610 0.5 (beamCenterApproxX -
   BeamCenterLimit) (beamCenterApproxY - BeamCenterLimit)
   -30];
upperBounds = [ 1.2 Inf 650 16 (beamCenterApproxX +
   BeamCenterLimit) (beamCenterApproxY + BeamCenterLimit)
   30];
coefvalsinit = [1 75 655 1 beamCenterApproxX
   beamCenterApproxY 0];
coefvalsmod = coefvalsinit;
% Set up fittype and options.
ft = fittype( 'peakHeight1*exp(-(2*(sqrt(((x-zcenterX)*cos
   (zphase*pi/180)-(y-zcenterY)*sin(zphase*pi/180)).^2+B1
   *((x-zcenterX)*sin(zphase*pi/180)+(y-zcenterY)*cos(
   zphase*pi/180)).^2)-radius1).^2/(w1.^2)))', '
   independent', {'x', 'y'}, 'dependent', 'z' );
opts = fitoptions( 'Method', 'NonlinearLeastSquares' );
```

```
opts.Display = 'Off';
opts.Lower = lowerBounds;
opts.StartPoint = coefvalsmod;
opts.Upper = upperBounds;
opts.Weights = weights;
% Fit model to data.
[fitresult, gof] = fit( [xData, yData], zData, ft, opts );
coefvals = coeffvalues(fitresult);
ci = confint(fitresult,ciLevel);
```

Sub-programs: Conversion of detector data into polar coordinates:

```
function [ Zinterp1 ] = PolarTransformationAll( X0, Y0,
   dataDir, material, materialID, dezingerRadius2,
   dezingerProportion2, CAMNUM, SDorP )
filename = 's_avg';
if SDorP == 'd'
    filename = 'd';
end
if SDorP == 'p'
    filename = 'p_avg';
end
%Opens raw data file and cakes it, using the largest
   circle that can fit in
%the image while centered on the beam center.  The "720"
   means that the
%azimuthal bins are 0.5 degrees wide, and "pointer" causes
    the radial bins
%to be the number of pixels between the beam center and
   the edge of the
%circle
TheImage = imread(sprintf('%s%s_%s_C%s_%s.tif',dataDir,
   material,materialID,num2str(CAMNUM),SDorP));
xdist = abs(1024-X0);
ydist = abs(1024-Y0);
pointer = 1024 - max(xdist,ydist);
Zinterp1 = polartrans(TheImage,pointer,720,X0,Y0,'linear',
   'valid')';
%Offsets the intensity so it is always positive.  This
   ensures that no
%negative values get truncated to zero when the data is
   converted to uint16
```

```
%for saving as a TIFF
if min(min(Zinterp1)) < 0
    Zinterp1 = Zinterp1 - min(min(Zinterp1));
end
%Saves the cake, creates an integration of the cake around
    the entire ring,
%and defines an x axis for plotting this integration as a
   function of
%pixels from the beam center
Zinterp1 = uint16(Zinterp1);
imwrite( Zinterp1 , sprintf('%s%s_%s_C%s_%
   s_PolarTransformation_X%s_Y%s.tif',dataDir,material,
   materialID,num2str(CAMNUM),filename,num2str(X0),num2str
   (Y0)))
ZinterpmeanRaw = mean(Zinterp1,1);
size_ZinterpmeanRaw = size(ZinterpmeanRaw);
x_axis1 = (1:1:size_ZinterpmeanRaw(2));
%Plot of raw data, caked
figure
imagesc(Zinterp1,([0 max(max(Zinterp1))]))
title(strcat(material,num2str(materialID),'-C',num2str(
   CAMNUM),' Raw Static image converted to polar
   coordinates (caked)'));
if SDorP == 'd'
    title(strcat(material,num2str(materialID),'-C',num2str
       (CAMNUM),' Raw Dynamic image converted to polar
       coordinates (caked)'));
end
if SDorP == 'p'
    title(strcat(material,num2str(materialID),'-C',num2str
       (CAMNUM),' Raw Post-mortem image converted to polar
        coordinates (caked)'));
end
%Opens bright-subtracted data file and cakes it, using the
    largest circle that can fit in
%the image while centered on the beam center.  The "720"
   means that the
%azimuthal bins are 0.5 degrees wide, and "pointer" causes
    the radial bins
%to be the number of pixels between the beam center and
   the edge of the
%circle
```

```
TheImage = imread(sprintf('%s%s_%s_C%s_%s_bsub1.tif',
   dataDir,material,materialID,num2str(CAMNUM),filename));
xdist = abs(1024-X0);
ydist = abs(1024-Y0);
pointer = 1024 - max(xdist,ydist);
Zinterp2 = polartrans(TheImage,pointer,720,X0,Y0,'linear',
   'valid')';
%Offsets the intensity so it is always positive.  This
   ensures that no
%negative values get truncated to zero when the data is
   converted to uint16
%for saving as a TIFF
if min(min(Zinterp2)) < 0
    Zinterp2 = Zinterp2 - min(min(Zinterp2));
end
%Saves the cake, creates an integration of the cake around
    the entire ring,
%and defines an x axis for plotting this integration as a
   function of
%pixels from the beam center
Zinterp2 = uint16(Zinterp2);
imwrite( Zinterp2 , sprintf('%s%s_%s_C%s_%
   s_bsub1_PolarTransformation_X%s_Y%s.tif',dataDir,
   material,materialID,num2str(CAMNUM),filename,num2str(X0
   ),num2str(Y0)))
ZinterpmeanBright = mean(Zinterp2,1);
size_ZinterpmeanBright = size(ZinterpmeanBright);
x_axis2 = (1:1:size_ZinterpmeanBright(2));
%Plot of bright-subtracted data, caked
figure
imagesc(Zinterp2,([0 max(max(Zinterp2))]))
title(strcat(material,num2str(materialID),'-C',num2str(
   CAMNUM),' Bright-subtracted Static image converted to
   polar coordinates (caked)'));
if SDorP == 'd'
    title(strcat(material,num2str(materialID),'-C',num2str
       (CAMNUM),' Bright-Subtracted Dynamic image
       converted to polar coordinates (caked)'));
end
if SDorP == 'p'
    title(strcat(material,num2str(materialID),'-C',num2str
       (CAMNUM),' Bright-Subtracted Post-mortem image
```

```
        converted to polar coordinates (caked)'));
end
%Figure comparing raw and bright-subtracted data
figure
plot(x_axis1,ZinterpmeanRaw,'k-',x_axis2,ZinterpmeanBright
   ,'r-')
title(strcat(material,num2str(materialID),'-C',num2str(
   CAMNUM),' Raw (black) and Bright-subtracted (red)
   Static image integrated over entire ring'));
if SDorP == 'd'
    title(strcat(material,num2str(materialID),'-C',num2str
       (CAMNUM),' Raw (black) and Bright-subtracted (red)
       Dynamic image integrated over entire ring'));
end
if SDorP == 'p'
    title(strcat(material,num2str(materialID),'-C',num2str
       (CAMNUM),' Raw (black) and Bright-subtracted (red)
       Post-mortem image integrated over entire ring'));
end
end
```

Sub-programs: Fitting of data to a convolution of a Gaussian with the instrument response function:

```
function [ coefvalsx, resnorm ] =
   NewConvolutionFitQAllAustenite( dataDir, material,
   materialID, pixelSize , cameraLength, dezingerRadius3,
   dezingerProportion3, X0, Y0, CAMNUM, thickness, lambda,
    SDorP )
%absorption coefficient for steel:
mu = 4644;
format long
%For saving files based on whether they're static or
   dynamic
filename = 's_avg';
if SDorP == 'd'
    filename = 'd';
end
if SDorP == 'p'
    filename = 'p_avg';
end
```

```
%loop over the number of sectors you want to divide the
   data into
for n = 1:1
    %Open the file containing the instrument response...in
        this case, an
    %isolated, background-subtracted peak measured from
       the silicon standard,
    %integrated all the way around the detector
    SiStandardPixels = dlmread(sprintf('%sInstRespCam%
       sSi600microns3rdharmonic.txt',dataDir,num2str(
       CAMNUM)));
    PixelsInstrumentResponse = SiStandardPixels(:,1)';
    SiStandardIntensity = SiStandardPixels(:,2);
    NormIntensity = SiStandardIntensity./max(
       SiStandardIntensity);
    intensityInstrumentResponse = NormIntensity';
    TwoThetaInstrumentResponse = atan(pixelSize.*
       PixelsInstrumentResponse./cameraLength);
    QInstrumentResponse = 4.*pi.*sin(
       TwoThetaInstrumentResponse./2)./lambda;

    marker = find(intensityInstrumentResponse == max(
       intensityInstrumentResponse));
    intensityInstrumentResponse = [
       intensityInstrumentResponse(marker:end)
       intensityInstrumentResponse(1:marker-1)];
    %open the caked image
    cake = imread(sprintf('%s%s_%s_C%s_%
       s_bsub1_PolarTransformation_X%s_Y%s.tif',dataDir,
       material,materialID,num2str(CAMNUM),filename,
       num2str(X0),num2str(Y0)));
    %In case you want to automate binning of rows that
       would include both row
    %720 and row 1, for example, I've just replicated the
       cake 3 times and only
    %use the center one for fitting
    cake = repmat(cake,3,1);
    %depending on the beam center used and the way the
       data caking was done, the
    %instrument response vector is probably longer than
       the data vector, so
    %this brings them into agreement
```

```
QInstrumentResponse = QInstrumentResponse(1:size(cake
   ,2));
TwoThetaInstrumentResponse =
   TwoThetaInstrumentResponse(1:size(cake,2));
%polarization correction, found in "Area detector
   correcions for high
%quality synchrotron x-ray structure factor
   measurements", in the journal
%"Nuclear Instruments and Methods in Physics Research
   A"
f = 0.98;
phi = [0.5:1:719.5].*0.5.*pi./180;
phi = repmat(phi,size(cake,2),3)';
TwoThetaInstrumentResponseRep = repmat(
   TwoThetaInstrumentResponse,720*3,1);
cake = double(cake);
cake = cake.*0.5.*(1 + cos(
   TwoThetaInstrumentResponseRep).^2 - f.*cos(phi).*
   sin(TwoThetaInstrumentResponseRep).^2);
%Select which rows of the cake to integrate over.
   Currently, there are 720
%rows that are 0.5 degrees wide
%to integrate over the left half of the detector
%set n = 1:1
dataIntensity= mean(cake(720+180+1+(n-1)*10:720+540+(n
   -1)*10,:),1);
%To integrate over the whole detector
%set n = 1:1
%dataIntensity= mean(cake(720+0+1+(n-1)*10:720+720+(n
   -1)*10,:),1);
%to integrate over the left half of the detector, at
   10 degree increments
%set n = 1:18
%dataIntensity= mean(cake(720+180+1+(n-1)
   *20:720+180+20+(n-1)*20,:),1);
%to integrate over the left half of the detector, at
   10 degree increments
%set n = 1:36
%dataIntensity= mean(cake(720+0+1+(n-1)*20:720+0+20+(n
   -1)*20,:),1);
%zero padding to avoid problems of circular
   convolution
```

```
    extrazeros = zeros(1,1020);
    intensityInstRespInterp = intensityInstrumentResponse;
    intensityInstRespInterp = [extrazeros
       intensityInstrumentResponse];
    dataIntensityInterp = dataIntensity;
    %Various corrections depending only on 2theta (or Q,
       or d)
    %geometrical correction
    dataIntensityInterp = dataIntensityInterp./(cos(
       TwoThetaInstrumentResponse).^2);
    %Lorentz factor correction...check this!
    %dataIntensityInterp = dataIntensityInterp.*sin(
       TwoThetaInstrumentResponse./2).^2.*cos(
       TwoThetaInstrumentResponse./2);
    %absorption correction
    dataIntensityInterp = dataIntensityInterp./((exp(mu.*
       thickness.*(1-sec(TwoThetaInstrumentResponse)))-1)
       ./(mu.*thickness.*(1-sec(TwoThetaInstrumentResponse
       ))));
    %Weights for the fitting function
    Weights = ones(size(dataIntensityInterp));
    Weights(1:250) = 0;
    %Weights(900:end) = 0;
    %The function that will be fit to the measured data (
       in this
    %case, {the Weights function * [a background + (a
       convolution of the instrument response with a
       series of Gaussians) ] } )
    fun1 = @(x,Pixels)Weights.*(1e-20*x(28)*(Pixels-1e10*x
       (39)).^2 ...
+x(29) ...
+conv(x(1)*exp(-((Pixels-1e10*x(2)).^2/(2*1e16*x(3).^2)))
   ...
+x(4)*exp(-((Pixels-1e10*x(5)).^2/(2*1e16*x(6).^2))) ...
+x(7)*exp(-((Pixels-1e10*x(8)).^2/(2*1e16*x(9).^2))) ...
+x(10)*exp(-((Pixels-1e10*x(11)).^2/(2*1e16*x(12).^2))) ...
+x(13)*exp(-((Pixels-1e10*x(14)).^2/(2*1e16*x(15).^2))) ...
+x(16)*exp(-((Pixels-1e10*x(17)).^2/(2*1e16*x(18).^2))) ...
+x(19)*exp(-((Pixels-1e10*x(20)).^2/(2*1e16*x(21).^2))) ...
+x(22)*exp(-((Pixels-1e10*x(23)).^2/(2*1e16*x(24).^2))) ...
+x(25)*exp(-((Pixels-1e10*x(26)).^2/(2*1e16*x(27).^2))) ...
+x(30)*exp(-((Pixels-1e10*x(31)).^2/(2*1e16*x(32).^2))) ...
```

```
+x(33)*exp(-((Pixels-1e10*x(34)).^2/(2*1e16*x(35).^2))) ...
+x(36)*exp(-((Pixels-1e10*x(37)).^2/(2*1e16*x(38).^2))) ...
,intensityInstRespInterp,'same'));
    A111 = [400,3.0,6];
    M110 = [1500,3.06,6];
    A200 = [60,3.516,8];
    Weird2ndHarmonicPeak = [60,4.06,10];
    M200 = [100,4.35,6];
    A220 = [20,4.85,6];
    M211 = [100,5.3,6];
    A311 = [0,5.6,9];
    A222 = [];
    M220 = [100,5.85,10];
    HigherPeaks = [10,6.9,10];
    slopex = [0];
    offsetx = [0];
    HigherHarmonic1 = [30,2.45,4];
    HigherHarmonic2 = [30,2.64,4];
    HigherHarmonic3 = [30,2.75,4];
    curvepos = [4.5];

    A111lower = [0,2.8,1.5];
    M110lower = [200,2.9,1.5];
    A200lower = [0,3.3,1.5];
    Weird2ndHarmonicPeaklower = [0,3.85,1.5];
    M200lower = [0,4.25,1.5];
    A220lower = [0,4.8,1.5];
    M211lower = [0,5.2,1.5];
    A311lower = [0,5.6,1.5];
    A222lower = [];
    M220lower = [0,5.82,1.5];
    HigherPeakslower = [0,6.5,1.5];
    slopelowerx = [-30];
    offsetlowerx = [-40];
    HigherHarmonic1lower = [0,2.35,1.5];
    HigherHarmonic2lower = [0,2.55,1.5];
    HigherHarmonic3lower = [0,2.55,1.5];
    curveposlower = [3];

    A111upper = [400,3.05,8];
    M110upper = [20000,3.3,11];
    A200upper = [6000,3.6,17];
```

```
Weird2ndHarmonicPeakupper = [500,4.05,6];
M200upper = [5000,4.55,17];
A220upper = [2000,5.05,17];
M211upper = [2000,5.35,17];
A311upper = [4000,5.85,15];
A222upper = [];
M220upper = [1000,6.1,13];
HigherPeaksupper = [1000,7.3,13];
slopeupperx = [-7];
offsetupperx = [500];
%if SorD == 's'
    %offsetupperx = [300];
%end
HigherHarmonic1upper = [1000,2.51,6];
HigherHarmonic2upper = [1000,2.7,6];
HigherHarmonic3upper = [1000,2.9,6];
curveposupper = [6.5];
%Assembling all of the above parameters into vectors
   describing the initial
%guess, lower bounds, and upper bounds that get fed
   into the curve fitting
%operation
x0 = [M110 A200 Weird2ndHarmonicPeak M200 A220 M211
   A311 M220 HigherPeaks slopex offsetx
   HigherHarmonic1 HigherHarmonic2 HigherHarmonic3
   curvepos ];
xlowerbounds = [M110lower A200lower
   Weird2ndHarmonicPeaklower M200lower A220lower
   M211lower A311lower M220lower HigherPeakslower
   slopelowerx offsetlowerx HigherHarmonic1lower
   HigherHarmonic2lower HigherHarmonic3lower
   curveposlower ];
xupperbounds = [M110upper A200upper
   Weird2ndHarmonicPeakupper M200upper A220upper
   M211upper A311upper M220upper HigherPeaksupper
   slopeupperx offsetupperx HigherHarmonic1upper
   HigherHarmonic2upper HigherHarmonic3upper
   curveposupper ];
%Performs the fitting
[x,resnorm,residual,exitflag,output,fitlambda,J] =
   lsqcurvefit(fun1,x0,QInstrumentResponse,Weights.*
   dataIntensityInterp,xlowerbounds,xupperbounds);
```

```
%Information about the quality/uncertainty of the fit
resnorm
ci = nlparci(x,residual,'jacobian',J);
covariance = inv(J.'*J)*var(residual);
%Plotting the measured data (line), along with the
   convolution of the fitted
%Gaussians with the instrument response (dots).  If
   the fitting has gone
%well, these two plots should overlap nicely
figure
plot(QInstrumentResponse,dataIntensityInterp)
hold on
plot(QInstrumentResponse,1e-20*x(28)*(
   QInstrumentResponse-1e10*x(39)).^2 +x(29)+conv(x(1)
   *exp(-((QInstrumentResponse-1e10*x(2)).^2/(2*1e16*x
   (3).^2)))+x(4)*exp(-((QInstrumentResponse-1e10*x(5)
   ).^2/(2*1e16*x(6).^2)))+x(7)*exp(-((
   QInstrumentResponse-1e10*x(8)).^2/(2*1e16*x(9).^2))
   )+x(10)*exp(-((QInstrumentResponse-1e10*x(11))
   .^2/(2*1e16*x(12).^2)))+x(13)*exp(-((
   QInstrumentResponse-1e10*x(14)).^2/(2*1e16*x(15)
   .^2)))+x(16)*exp(-((QInstrumentResponse-1e10*x(17))
   .^2/(2*1e16*x(18).^2)))+x(19)*exp(-((
   QInstrumentResponse-1e10*x(20)).^2/(2*1e16*x(21)
   .^2)))+x(22)*exp(-((QInstrumentResponse-1e10*x(23))
   .^2/(2*1e16*x(24).^2)))+x(25)*exp(-((
   QInstrumentResponse-1e10*x(26)).^2/(2*1e16*x(27)
   .^2)))+x(30)*exp(-((QInstrumentResponse-1e10*x(31))
   .^2/(2*1e16*x(32).^2)))+x(33)*exp(-((
   QInstrumentResponse-1e10*x(34)).^2/(2*1e16*x(35)
   .^2)))+x(36)*exp(-((QInstrumentResponse-1e10*x(37))
   .^2/(2*1e16*x(38).^2))) ...

plot(QInstrumentResponse,x(1)*exp(-((
   QInstrumentResponse-1e10*x(2)).^2/(2*1e16*x(3).^2))
   ))
plot(QInstrumentResponse,x(4)*exp(-((
   QInstrumentResponse-1e10*x(5)).^2/(2*1e16*x(6).^2))
   ))
plot(QInstrumentResponse,x(7)*exp(-((
   QInstrumentResponse-1e10*x(8)).^2/(2*1e16*x(9).^2))
   ))
```

```
    plot(QInstrumentResponse,x(10)*exp(-((
       QInstrumentResponse-1e10*x(11)).^2/(2*1e16*x(12)
       .^2))))
    plot(QInstrumentResponse,x(13)*exp(-((
       QInstrumentResponse-1e10*x(14)).^2/(2*1e16*x(15)
       .^2))))
    plot(QInstrumentResponse,x(16)*exp(-((
       QInstrumentResponse-1e10*x(17)).^2/(2*1e16*x(18)
       .^2))))
    plot(QInstrumentResponse,x(19)*exp(-((
       QInstrumentResponse-1e10*x(20)).^2/(2*1e16*x(21)
       .^2))))
    plot(QInstrumentResponse,x(22)*exp(-((
       QInstrumentResponse-1e10*x(23)).^2/(2*1e16*x(24)
       .^2))))
    plot(QInstrumentResponse,x(25)*exp(-((
       QInstrumentResponse-1e10*x(26)).^2/(2*1e16*x(27)
       .^2))))
    plot(QInstrumentResponse,x(30)*exp(-((
       QInstrumentResponse-1e10*x(31)).^2/(2*1e16*x(32)
       .^2))))
    plot(QInstrumentResponse,x(33)*exp(-((
       QInstrumentResponse-1e10*x(34)).^2/(2*1e16*x(35)
       .^2))))
    plot(QInstrumentResponse,x(36)*exp(-((
       QInstrumentResponse-1e10*x(37)).^2/(2*1e16*x(38)
       .^2))))

    title(strcat(material,num2str(materialID),'-C',num2str
       (CAMNUM),' Bright-subtracted Static image
       integrated over entire ring, with fit'));
    if SDorP == 'd';
        title(strcat(material,num2str(materialID),'-C',
           num2str(CAMNUM),' Bright-subtracted Dynamic
           image integrated over entire ring, with fit'));
    end
    %Stores the fitted parameters from this sector, and
       prepares to fit the
    %next sector
    coefvalsx(n,:) = x;
    n = n+1
end
```

```
%Saving all the fit information
dlmwrite(sprintf('%s%s_%s_C%s_%s_bsub1_dzr_r%s_p%
   s_bsub2_PolarTransformation_X%s_Y%s_bsub2_coefvals.txt'
   ,dataDir,material,materialID,num2str(CAMNUM),filename,
   num2str(dezingerRadius3),num2str(dezingerProportion3),
   num2str(X0),num2str(Y0)),coefvalsx,'delimiter','\t','
   precision',13)
dlmwrite(sprintf('%s%s_%s_C%s_%s_bsub1_dzr_r%s_p%
   s_bsub2_PolarTransformation_X%s_Y%s_bsub2_resnorm.txt',
   dataDir,material,materialID,num2str(CAMNUM),filename,
   num2str(dezingerRadius3),num2str(dezingerProportion3),
   num2str(X0),num2str(Y0)),resnorm,'delimiter','\t','
   precision',13)
dlmwrite(sprintf('%s%s_%s_C%s_%s_bsub1_dzr_r%s_p%
   s_bsub2_PolarTransformation_X%s_Y%s_residual.txt',
   dataDir,material,materialID,num2str(CAMNUM),filename,
   num2str(dezingerRadius3),num2str(dezingerProportion3),
   num2str(X0),num2str(Y0)),residual,'delimiter','\t','
   precision',13)
dlmwrite(sprintf('%s%s_%s_C%s_%s_bsub1_dzr_r%s_p%
   s_bsub2_PolarTransformation_X%s_Y%s_ci.txt',dataDir,
   material,materialID,num2str(CAMNUM),filename,num2str(
   dezingerRadius3),num2str(dezingerProportion3),num2str(
   X0),num2str(Y0)),ci,'delimiter','\t','precision',13)
dlmwrite(sprintf('%s%s_%s_C%s_%s_bsub1_dzr_r%s_p%
   s_bsub2_PolarTransformation_X%s_Y%s_covariance.txt',
   dataDir,material,materialID,num2str(CAMNUM),filename,
   num2str(dezingerRadius3),num2str(dezingerProportion3),
   num2str(X0),num2str(Y0)),full(covariance),'delimiter','
   \t','precision',13)
end
```

Sub-programs: Calculation of austenite volume fraction based on fitted peak areas:

```
function [percentAusteniteDistinct,
   percentAusteniteDistinctUpper,
   percentAusteniteDistinctLower] =
   VolumeFractionCalculatorAll( coefvals, dataDir,
   material, materialID, dezingerRadius2,
   dezingerProportion2, X0, Y0, CAMNUM, lambda,
   currentStrain, SorD )
```

```
lambda = repmat(lambda,9,1);
%For saving files based on whether they're static or
   dynamic
filename = 's_avg';

if SorD == 'd'
    filename = 'd';
end
%Some parameters used in the calculation: K = experimental
    setup-dependent
%constant; V = expected volume fraction; B = Debye-Waller
   factor quoted in
%S.K. Mohanlal's 1979 paper in J. Phys. C; multiplicity =
   multiplicity of
%A111/M110, A200, M200, A220, M211, A311, A222/M220, and
   higher peaks (set
%to 1, but they don't get used in the calculation anyway)
K = ones(9,1);
V = ones(9,1);
B = 3.5e-21*ones(9,1);
multiplicity = [12; 6; 6; 12; 24; 24; 12; 1; 1];
%Assembles information from the convolution fit for
   uncertainty calculation
covariance = dlmread(sprintf('%s%s_%s_C%s_%s_bsub1_dzr_r%
   s_p%s_bsub2_PolarTransformation_X%s_Y%s_covariance.txt'
   ,dataDir,material,materialID,num2str(CAMNUM),filename,
   num2str(dezingerRadius2),num2str(dezingerProportion2),
   num2str(X0),num2str(Y0)));
FitUncertainty = zeros(7,2);
AmplitudeA200 = covariance(4,4);
FWHMA200 = covariance(6,6);
FitUncertainty(2,1) = AmplitudeA200;
FitUncertainty(2,2) = FWHMA200;
AmplitudeM200 = covariance(10,10);
FWHMM200 = covariance(12,12);
FitUncertainty(4,1) = AmplitudeM200;
FitUncertainty(4,2) = FWHMM200;
AmplitudeA220 = covariance(13,13);
FWHMA220 = covariance(15,15);
FitUncertainty(5,1) = AmplitudeA220;
FitUncertainty(5,2) = FWHMA220;
AmplitudeM211 = covariance(16,16);
```

```
FWHMM211 = covariance(18,18);
FitUncertainty(6,1) = AmplitudeM211;
FitUncertainty(6,2) = FWHMM211;
AmplitudeA311 = covariance(19,19);
FWHMA311 = covariance(21,21);
FitUncertainty(7,1) = AmplitudeA311;
FitUncertainty(7,2) = FWHMA311;
%Fitted data: peak amplitudes, q vector amplitude, and q
   values
k = 1;
for j = 1:9
   for i = 1:3
      peakFitData(j,i) = coefvals(1,k);
      k = k + 1;
   end
end
%Calculated measured peak areas
peakArea(:,1) = peakFitData(:,1).*peakFitData(:,3).*sqrt(
   pi);
peakPosition(:,1) = peakFitData(:,2)
for p = 1:7
    FracAreaUncertainty(p,1) = sqrt( sqrt( FitUncertainty(
       p,1)./peakFitData(p,1) ).^2 +  sqrt( FitUncertainty
       (p,2)./peakFitData(p,3) ).^2 );
end
%Establish the q vector magnitude, theta, and 2theta value
    of each peak
qA(:,1) = peakFitData(:,2);
q(:,1) = qA*(1e10);
theta(:,1) = asin(lambda(:,1).*q(:,1)./(4*pi));
twotheta(:,1) = 2.*theta(:,1);
%Atomic form factor coefficients taken from http://lampx.
   tugraz.at/~hadley/ss1/crystaldiffraction/
   atomicformfactors/formfactors.php
FeA1 = 11.7695;
FeB1 = 4.7611;
FeA2 = 7.3573;
FeB2 = 0.3072;
FeA3 = 3.5222;
FeB3 = 15.3535;
FeA4 = 2.3045;
FeB4 = 76.8805;
```

```
FeC = 1.0369;
fhklFe(:,1) = FeA1*exp(-FeB1*(qA(:,1)/(4*pi)).^2)+FeA2*exp
   (-FeB2*(qA(:,1)/(4*pi)).^2)+FeA3*exp(-FeB3*(qA(:,1)/(4*
   pi)).^2)+FeA4*exp(-FeB4*(qA(:,1)/(4*pi)).^2)+FeC;
NiA1 = 12.8376;
NiB1 = 3.8785;
NiA2 = 7.292;
NiB2 = 0.2565;
NiA3 = 4.4438;
NiB3 = 12.1763;
NiA4 = 2.38;
NiB4 = 66.3421;
NiC = 1.0341;
fhklNi(:,1) = NiA1*exp(-NiB1*(qA(:,1)/(4*pi)).^2)+NiA2*exp
   (-NiB2*(qA(:,1)/(4*pi)).^2)+NiA3*exp(-NiB3*(qA(:,1)/(4*
   pi)).^2)+NiA4*exp(-NiB4*(qA(:,1)/(4*pi)).^2)+NiC;
fhkl(:,1) = 0.9*fhklFe(:,1) + 0.1*fhklNi(:,1);
%Structure factor for austenite and martensite
Fhkl = zeros(9,1);
Fhkl2 = zeros(9,1);
%austenite
for l = [2,5,7]
    Fhkl(l,1) = 4*fhkl(l,1);
    Fhkl2(l,1) = Fhkl(l,1)^2;
end
%martensite
for m = [4,6]
    Fhkl(m,1) = 2*fhkl(m,1);
    Fhkl2(m,1) = Fhkl(m,1)^2;
end
dAustenite = lambda/(2*sin(theta(2,1)));
dMartensite = lambda/(2*sin(theta(4,1)));
aAustenite = 2*dAustenite;
aMartensite = 2*dMartensite;
%aAustenite = 0.3571e-9;
aAustenite = repmat(aAustenite,9,1);
%aMartensite = 0.2886e-9;
aMartensite = repmat(aMartensite,9,1);
vAustenite = aAustenite.^3;
vMartensite = aMartensite.^3;
v = zeros(9,1);
for n = [2,5,7]
```

```
    v(n,1) = vAustenite(n,1);
end
for p = [1,3,4,6,8,9]
    v(p,1) = vMartensite(p,1);
end
predictedArea(:,1) = K(:,1).*V(:,1).*multiplicity(:,1).*
   lambda.^3.*Fhkl2(:,1).*exp(-B(:,1).*sin(theta(:,1))
   .^2./(lambda.^2))./(v(:,1).^2.*sin(theta(:,1)).*sin(
   twotheta(:,1)));
%Computes volume fraction of austenite
summationAusteniteDistinct = 0;
counter3 = 0;
%for r = [2,5,7]
for r = [2,5]
    summationAusteniteDistinct =
       summationAusteniteDistinct + peakArea(r,1)/
       predictedArea(r,1);
    counter3 = counter3 + 1;
end
summationMartensiteDistinct = 0;
counter4 = 0;
for s = [4,6]
    summationMartensiteDistinct =
       summationMartensiteDistinct + peakArea(s,1)/
       predictedArea(s,1);
    counter4 = counter4 + 1;
end
percentAusteniteDistinct = 100*(summationAusteniteDistinct
   /counter3)/((summationAusteniteDistinct/counter3) + (
   summationMartensiteDistinct/counter4))
peakArea
predictedArea
FitUncertainty
FracAreaUncertainty(4,1)
FracAreaUncertainty(5,1)
FracAreaUncertainty(6,1)
AreaError = sqrt(((FracAreaUncertainty(5,1))).^2)/( ((
   FracAreaUncertainty(5,1))).^2 + ((FracAreaUncertainty
   (4,1) + FracAreaUncertainty(6,1))/2).^2 )
percentAusteniteDistinctLower = percentAusteniteDistinct -
    AreaError;
percentAusteniteDistinctUpper = percentAusteniteDistinct +
```

```
    AreaError
Strain_and_Austenite = horzcat(currentStrain,
   percentAusteniteDistinct);
dlmwrite(sprintf('%s%s_%s_C%s_%s_bsub1_dzr_r%s_p%
   s_PolarTransformation_X%s_Y%s_PercentAustenite.txt',
   dataDir,material,materialID,num2str(CAMNUM),filename,
   num2str(dezingerRadius2),num2str(dezingerProportion2),
   num2str(X0),num2str(Y0)),Strain_and_Austenite,'
   delimiter','\t','precision',4)
end
```

Bibliography

[1] X. J. Zhang, "Microhardness characterisation in developing high strength, high toughness and superior ballistic resistance low carbon Ni steel," *Materials Science and Technology*, vol. 28, no. 7, pp. 818–822, July 2012.

[2] "Storage Ring Operation Modes". Advanced Photon Source, Argonne National Laboratory, 2010. [Online]. Available: http://www.aps.anl.gov/Accelerator_Systems_ Division/Accelerator_ Operations_ Physics/SRparameters/node5.html

[3] C. C. Kinney, K. R. Pytlewski, A. G. Khachaturyan, and J. W. Morris, Jr., "The microstructure of lath martensite in quenched 9Ni steel," *Acta Materialia*, vol. 69, pp. 372–385, May 2014.

[4] L. Nguyen, S. Ryan, S. Cimpoeru, A. Mouritz, and A. Orifici, "The efficiency of ultra-high molecular weight polyethylene composite against fragment impact," *Experimental Mechanics*, vol. 56, no. 4, pp. 595–605, April 2016.

BIBLIOGRAPHY

[5] W. Chen and B. Song, *Split Hopkinson (Kolsky) Bar: Design, Testing, and Applications*. Springer Science + Business Media, 2011.

[6] [Online]. Available: https://www1.aps.anl.gov/science/scientific-software/xop

[7] T. Holden, A. Clarke, and R. Holt, "Neutron diffraction measurements of intergranular strains in MONEL-400," *Metallurgical and Materials Transactions A-Physical Metallurgy and Materials Science*, vol. 28, no. 12, pp. 2565–2576, December 1997.

[8] P. J. Jacques, S. Allain, O. Bouaziz, A. De, A. Gourgues, B. Hance, Y. Houbaert, J. Huang, A. Iza-Mendia, S. Kruger, M. Radu, L. Samek, J. Speer, L. Zhao, and S. van der Zwaag, "On measurement of retained austenite in multiphase TRIP steels - results of blind round robin test involving six techniques," *Materials Science and Technology*, vol. 25, no. 5, pp. 567–574, May 2009.

[9] T. Gnaeupel-Herold, A. A. Creuziger, and M. Iadicola, "A model for calculating diffraction elastic constants," *Journal of Applied Crystallography*, vol. 45, no. 2, pp. 197–206, April 2012.

[10] W. Dabboussi and J. A. Nemes, "Systematic characterization of the crashworthiness properties of low alloys silicon bearing trip steels," *ISIJ International*, vol. 53, no. 8, pp. 1462–1470, April 2013.

[11] G. B. Olson and M. Cohen, "A Mechanism for the Strain-Induced Nucleation

of Martensitic Transformations," *Journal of the Less-Common Metals*, vol. 28, no. 1, pp. 107–118, 1972.

[12] S. H. Kim, H. Kim, and N. J. Kim, "Brittle intermetallic compound makes ultrastrong low-density ssteel with large ductility," *Nature*, vol. 518, no. 7537, p. 77, February 2015.

[13] K. Limmer, J. Medvedeva, D. Van Aken, and N. Medvedeva, "Ab initio simulation of alloy effect on stacking fault energy in fcc Fe," *Computational Materials Science*, 2015.

[14] E. Bain, "The nature of martensite," *Transactions of the American Institute of Mining and Metallurgical Engineers*, vol. 70, pp. 25–46, 1924.

[15] E. Machlin and M. Cohen, "Habit phenomenon in the martensitic transformation," *Transactions of the American Institute of Mining and Metallurgical Engineers*, vol. 191, no. 11, pp. 1019–1029, 1951.

[16] C. Magee, "Kinetics of martensite formation in small particles," *Metallurgical Transactions*, vol. 2, no. 9, 1971.

[17] J. Patel and M. Cohen, "Criterion for the action of applied stress in the martensitic transformation," *Acta Metallurgica*, vol. 1, no. 5, pp. 531–538, 1953.

[18] G. B. Olson and M. Cohen, "A general mechanism of martensitic nucleation: Part i. general concepts and the fcc - hcp transformation," *Metallurgical and*

Materials Transactions A-Physical Metallurgy and Materials Science, vol. 7, no. 12, pp. 1897–1904, 1976.

[19] ——, "A general mechanism of martensitic nucleation: Part ii. fcc - bcc and other martensitic transformations," *Metallurgical and Materials Transactions A-Physical Metallurgy and Materials Science*, vol. 7, no. 12, pp. 1905–1914, 1976.

[20] ——, "A general mechanism of martensitic nucleation: Part iii. kinetics of martensitic nucleation," *Metallurgical and Materials Transactions A-Physical Metallurgy and Materials Science*, vol. 7, no. 12, pp. 1915–1923, 1976.

[21] E. Scheil, "On the transformation of austenite in martensite in iron-nickel alloys during stress," *Zeitschrift fuer Anorganische und Allgemeine Chemie*, vol. 207, no. 1, pp. 21–40, July 1932.

[22] S. Kulin, M. Cohen, and B. Averbach, "Effect of applied stress on the martensitic transformation," *Journal of Metals*, vol. 4, no. 6, pp. 661–668, 1952.

[23] P. Wang and K. S. Kumar, "Dynamic deformation response of a high-strength, high-toughness Fe-10Ni-0.1C steel," *Materials Science & Engineering, A: Structural Materials: Properties, Microstructure and Processing*, vol. 519, no. 1-2, pp. 184–197, August 2009.

[24] D. Isheim, A. H. Hunter, X. J. Zhang, and D. N. Seidman, "Nanoscale Analyses

of High-Nickel Concentration Martensitic High-Strength Steels," *Metallurgical and Materials Transactions A-Physical Metallurgy and Materials Science*, vol. 44A, no. 7, pp. 3046–3059, July 2013.

[25] T. Pan, J. Zhu, H. Su, and C.-F. Yang, "Ni segregation and thermal stability of reversed austenite in a Fe-Ni alloy processed by QLT heat treatment," *Rare Metals*, vol. 34, no. 11, pp. 776–782, November 2015.

[26] M. Eskandari, A. Zarei-Hanzaki, M. Mohtadi-Bonab, Y. Onuki, R. Basu, A. Asghari, and J. Szpunar, "Grain-orientation-dependent of $\gamma-\epsilon-\alpha'$ transformation and twinning in a super-high-strength, high ductility austenitic Mn-steel," *Materials Science & Engineering, A: Structural Materials: Properties, Microstructure and Processing*, vol. 674, pp. 514–528, September 2016.

[27] S. Turteltaub and A. S. J. Suiker, "Grain size effects in multiphase steels assisted by transformation-induced plasticity," *International Journal of Solids and Structures*, vol. 43, no. 24, pp. 7322–7336, November 2006.

[28] P. J. Jacques, J. Ladriere, and F. Delannay, "On the influence of interactions between phases on the mechanical stability of retained austenite in transformation-induced plasticity multiphase steels," *Metallurgical and Materials Transactions A-Physical Metallurgy and Materials Science*, vol. 32, no. 11, pp. 2759–2768, November 2001.

[29] A. Jaworski and S. Ankem, "Influence of the second phase on the room-

temperature tensile and creep deformation mechanisms of alpha-beta titanium alloys: Part 1. Tensile deformation," *Metallurgical and Materials Transactions A-Physical Metallurgy and Materials Science*, vol. 37A, no. 9, pp. 2739–2754, September 2006.

[30] F. Lani, Q. Furnemont, T. Van Rompaey, F. Delannay, P. J. Jacques, and T. Pardoen, "Multiscale mechanics of TRIP-assisted multiphase steels: II. Micromechanical modelling," *Acta Materialia*, vol. 55, no. 11, pp. 3695–3705, June 2007.

[31] M.-M. Wang, C. Tasan, D. Ponge, and D. Raabe, "Spectral TRIP enables ductile 1.1 GPa martensite," *Acta Materialia*, vol. 111, pp. 262–272, June 2016.

[32] G. F. Bolling and R. H. Richman, "The Plastic Deformation-Transformation of Paramagnetic F.C.C. Fe-Ni-C Alloys," *Acta Metallurgica*, vol. 18, pp. 673–681, 1970.

[33] J. Kim and J. Morris, "The composition of precipitated austenite in 5.5Ni steel," *Metallurgical Transactions A-Physical Metallurgy and Materials Science*, vol. 12, no. 11, 1981.

[34] S. J. Wu, G. J. Sun, Q. S. Ma, Q. Y. Shen, and L. Xu, "Influence of QLT treatment on microstructure and mechanical properties of a high nickel steel," *Journal of Materials Processing Technology*, vol. 213, no. 1, pp. 120–128, January 2013.

[35] X. Q. Zhao, T. Pan, Q. F. Wang, H. Su, C. F. Yang, Q. X. Yang, and Y. Q. Zhang, "Effect of intercritical quenching on reversed austenite formation and cryogenic toughness in QLT-processed 9%Ni steel," *Journal of Iron and Steel Research International*, vol. 14, no. 1, pp. 240–244, September 2007.

[36] T. Kobayashi, H. Tachibana, W. Yagi, and Y. Ueda, "Effect of the QLT treatment on the toughness of 13-percent Cr cast stainless-steel," *Journal of the Japan Institute of Metals*, vol. 46, no. 4, pp. 433–440, 1982.

[37] H. Kim, Y. Kim, and J. Morris, "Thermal mechanisms of grain and packet refinement in a lath martensitic steel," *ISIJ International*, vol. 38, no. 11, pp. 1277–1285, 1998.

[38] J. Kim, H., C. Syn, C., and J. Morris, "Microstructural sources of toughness in a QLT-treated 5.5Ni cryogenic steel," *Metallurgical Transactions A-Physical Metallurgy and Materials Science*, vol. 14, no. 1, pp. 93–103, 1983.

[39] Z. Guo and J. Morris, "Martensite variants generated by the mechanical transformation of precipitated interlath austenite," *Scripta Materialia*, vol. 53, no. 8, pp. 933–936, October 2005.

[40] B. Fultz, J. Kim, Y. Kim, and J. Morris, "The Chemical Composition of Precipitated Austenite in 9Ni Steel," *Metallurgical Transactions A-Physical Metallurgy and Materials Science*, vol. 17, no. 6, pp. 967–972, June 1986.

[41] B. Fultz, J. Kim, Y. Kim, H. Kim, G. Fior, and J. Morris, "The Stability of Precipitated Austenite and the Toughness of 9Ni Steel," *Metallurgical Transactions A-Physical Metallurgy and Materials Science*, vol. 16, no. 12, pp. 2237–2249, December 1985.

[42] J. W. Morris, Jr., C. Kinney, K. Pytlewski, and Y. Adachi, "Microstructure and cleavage in lath martensitic steels," *Science and Technology of Advanced Materials*, vol. 14, no. 1, FEB 2013.

[43] S. H. Chen, M. J. Zhao, X. Y. Li, and L. J. Rong, "Compression Stability of Reversed Austenite in 9Ni Steel," *Journal of Materials Science and Technology*, vol. 28, no. 6, pp. 558–561, June 2012.

[44] B. Fultz and J. Morris, "The mechanical stabilty of precipitated austenite in 9Ni steel," *Metallurgical Transactions A-Physical Metallurgy and Materials Science*, vol. 16, no. 12, pp. 2251–2256, December 1985.

[45] ——, "A Mossbauer spectrometry study of the mechanical transformation of precipitated austenite in 6Ni steel," *Metallurgical Transactions A-Physical Metallurgy and Materials Science*, vol. 16, no. 2, pp. 173–177, 1985.

[46] X. Zhao, T. Pan, Q. Wang, H. Su, C. Yang, and Q. Yang, "Effect of tempering temperature on microstructure and mechanical properties of steel containing Ni of 9%," *Journal of Iron and Steel Research International*, vol. 18, no. 5, p. 47, May 2011.

[47] R. Fonda and G. Spanos, "Effects of cooling rate on transformations in a Fe-9 Pct Ni steel," *Metallurgical and Materials Transactions A-Physical Metallurgy and Materials Science*, vol. 45A, no. 13, pp. 5982–5989, 2014.

[48] N. Nakada, J. Syarif, T. Tsuchiyama, and S. Takaki, "Improvement of strength-ductility balance by copper addition in 9%Ni steels," *Materials Science & Engineering, A: Structural Materials: Properties, Microstructure and Processing*, vol. 374, no. 1-2, pp. 137–144, June 2004.

[49] C. Syn, S. Jin, and J. Morris, "Cryogenic fracture toughness of Ni-9 Steel enhanced through grain refinement," *Metallurgical Transactions A-Physical Metallurgy and Materials Science*, vol. 7, no. 12, pp. 1827–1832, 1976.

[50] D. Delagnes, F. Pettinari-Sturmel, M. Mathon, R. Danoix, F. Danoix, C. Bellot, P. Lamesle, and A. Grellier, "Cementite-free martensitic steels: A new route to develop high strength/high toughness grades by modifying the conventional precipitation sequence during tempering," *Acta Materialia*, vol. 60, no. 16, pp. 5877–5888, September 2012.

[51] H. Na, S. Nambu, M. Ojima, J. Inoue, and T. Koseki, "Crystallographic and microstructural studies of lath martensitic steel during tensile deformation," *Metallurgical and Materials Transactions A-Physical Metallurgy and Materials Science*, vol. 45A, no. 11, pp. 5029–5043, October 2014.

[52] "9% Nickel Steel: For use at cryogenic tem-

peratures". ArcelorMittal USA, 2016. [Online]. Available: http://www.usa.arcelormittal.com/~/media/Files/A/Arcelormittal-USA-V2/what-we-do/steel-products/plate-products/9-percent-nickel.pdf

[53] *Ballistic Tests of Armor Materials*, U.S. Army Test and Evaluation Command Std., February 1984.

[54] J. A. Rodriguez-Martinez, R. Pesci, A. Rusinek, A. Arias, R. Zaera, and D. Pedroche, "Thermo-mechanical behaviour of TRIP 1000 steel sheets subjected to low velocity perforation by conical projectiles at different temperatures," *International Journal of Solids and Structures*, vol. 47, no. 9, pp. 1268–1284, May 2010.

[55] P. K. Lambert, C. J. Hustedt, K. S. Vecchio, E. L. Huskins, D. T. Casem, S. M. Gruner, M. W. Tate, H. T. Philipp, A. R. Woll, P. Purohit, J. T. Weiss, V. Kannan, K. T. Ramesh, P. Kenesei, J. S. Okasinski, J. Almer, M. Zhao, A. G. Ananiadis, and T. C. Hufnagel, "Time-resolved x-ray diffraction techniques for bulk polycrystalline materials under dynamic loading," *Review of Scientific Instruments*, vol. 85, no. 9, September 2014.

[56] H. Kolsky, "An investigation of the mechanical properties of materials at very high rates of loading," *Proceedings of the Physical Society, Section B*, vol. 62, no. 302, pp. 676–700, 1949.

[57] H. Klug and L. Alexander, *X-Ray Diffraction Procedures for Polycrystalline and Amorphous Materials*. Wiley, 1974.

[58] J. Als-Nielson and D. McMorrow, *Elements of Modern X-ray Physics*, 2nd ed. Wiley, 2011.

[59] M. Hudspeth, T. Sun, N. Parab, Z. Guo, K. Fezzaa, S. Luo, and W. Chen, "Simultaneous X-ray diffraction and phase-contrast imaging for investigating material deformation mechanisms during high-rate loading," *Journal of Synchrotron Radiation*, vol. 22, no. 1, pp. 49–58, January 2015.

[60] A. Hull, "A new method of x-ray crystal analysis," *Physical Review*, vol. 10, no. 6, pp. 661–696, December 1917.

[61] L. Alexander, *X-Ray Diffraction Methods in Polymer Science*. Wiley-Interscience, 1969.

[62] M. Meyers, *Dynamic Behavior of Materials*. John Wiley and Sons, 1994.

[63] W. Chen and G. Ravichandran, "Dynamic compressive failure of a glass ceramic under lateral confinement," *Journal of the Mechanics and Physics of Solids*, vol. 45, no. 8, pp. 1303–1328, August 1997.

[64] D. Chichili, K. Ramesh, and K. Hemker, "The high-strain-rate response of alpha-titanium: Experiments, deformation mechanisms and modeling," *Acta Materialia*, vol. 46, no. 3, pp. 1025–1043, January 1998.

[65] T. P. M. Johnson, S. S. Sarva, and S. Socrate, "Comparison of Low Impedance Split-Hopkinson Pressure Bar Techniques in the Characterization of Polyurea," *Experimental Mechanics*, vol. 50, no. 7, pp. 931–940, September 2010.

[66] D. Jia and K. Ramesh, "A rigorous assessment of the benefits of miniaturization in the Kolsky bar system," *Experimental Mechanics*, vol. 44, no. 5, pp. 445–454, October 2004.

[67] Q. Johnson, A. Mitchell, and L. Evans, "X-ray diffraction evidence for crystalline order and isotropic compression during shock-wave process," *Nature*, vol. 231, no. 5301, pp. 310–&, 1971.

[68] P. Rigg and Y. Gupta, "Real-time x-ray diffraction to examine elastic-plastic deformation in shocked lithium fluoride crystals," *Applied Physics Letters*, vol. 73, no. 12, pp. 1655–1657, September 1998.

[69] Y. M. Gupta, S. J. Turneaure, K. Perkins, K. Zimmerman, N. Arganbright, G. Shen, and P. Chow, "Real-time, high-resolution x-ray diffraction measurements on shocked crystals at a synchrotron facility," *Review of Scientific Instruments*, vol. 83, no. 12, December 2012.

[70] M. J. Suggit, A. Higginbotham, J. A. Hawreliak, G. Mogni, G. Kimminau, P. Dunne, A. J. Comley, N. Park, B. A. Remington, and J. S. Wark, "Nanosecond white-light Laue diffraction measurements of dislocation microstructure

in shock-compressed single-crystal copper," *Nature Communications*, vol. 3, November 2012.

[71] M. Hudspeth, B. Claus, S. Dubelman, J. Black, A. Mondal, N. Parab, C. Funnell, F. Hai, M. L. Qi, K. Fezzaa, S. N. Luo, and W. Chen, "High speed synchrotron x-ray phase contrast imaging of dynamic material response to split Hopkinson bar loading," *Review of Scientific Instruments*, vol. 84, no. 2, February 2013.

[72] S. T. Kelly, J. C. Trenkle, L. J. Koerner, S. C. Barron, N. Walker, P. O. Pouliquen, M. W. Tate, S. M. Gruner, E. M. Dufresne, T. P. Weihs, and T. C. Hufnagel, "Fast X-ray microdiffraction techniques for studying irreversible transformations in materials," *Journal of Synchrotron Radiation*, vol. 18, no. 3, pp. 464–474, May 2011.

[73] P. Fuoss, D. Kisker, F. Lamelas, G. Stephenson, P. Imperatori, and S. Brennan, "Time-resolved x-ray-scattering studies of layer-by-layer epitaxial-growth," *Physical Review Letters*, vol. 69, no. 19, pp. 2791–2794, November 1992.

[74] T. Irving and D. Maughan, "In vivo X-ray diffraction of indirect flight muscle from Drosophila melanogaster," *Biophysical Journal*, vol. 78, no. 5, pp. 2511–2515, May 2000.

[75] K. Goetze and U. Lienert, "A galvanometer based fast shutter," Presented

at *10th International Conference on Synchrotron Radiation Instrumentation*, Melbourne, Australia, 27 September - 2 October 2009.

[76] M. Wulff, F. Schotte, G. Naylor, D. Bourgeois, K. Moffat, and G. Mourou, "Time-resolved structures of macromolecules at ESRF: single-pulse Laue diffraction, stroboscopic data collection and femtosecond flash photolysis," *Nuclear Instruments & Methods in Physics Research, Section A: Accelerators, Spectrometers, Detectors, and Associated Equipment*, vol. 398, no. 1, pp. 69–84, October 1997.

[77] A. Rousse, C. Rischel, and J. Gauthier, "Colloquium: femtosecond x-ray crystallography," *Reviews of Modern Physics*, vol. 73, no. 1, pp. 17–31, January 2001.

[78] J. C. I.C. Noyan, *Residual Stress*, N. G. B. Ilschner, Ed. Springer-Verlag, 1987.

[79] A. Wanner and D. Dunand, "Synchrotron x-ray study of bulk lattice strains in externally loaded Cu-Mo ccomposite," *Metallurgical and Materials Transactions A-Physical Metallurgy and Materials Science*, vol. 31, no. 11, pp. 2949–2962, November 2000.

[80] A. Korunsky, K. Wells, and P. Withers, "Mapping two-dimensional state of strain using synchrotron x-ray diffraction," *Scripta Materialia*, 1998.

[81] I. Noyan and J. Cohen, *Residual Stress: Measurement by Diffraction and Interpretation*, B. Ilschner and N. Grant, Eds. Springer-Verlag, 1987.

[82] A. Hammersly, "Fit2d: An introduction and overview," 1997.

[83] L. J. Koerner, M. W. Tate, and S. M. Gruner, "An Accumulating Pixel Array Detector for Single-Bunch Synchrotron Experiments," *IEEE Transactions on Nuclear Science*, vol. 56, no. 5, pp. 2835–2842, October 2009.

[84] S. N. Luo, B. J. Jensen, D. E. Hooks, K. Fezzaa, K. J. Ramos, J. D. Yeager, K. Kwiatkowski, and T. Shimada, "Gas gun shock experiments with single-pulse x-ray phase contrast imaging and diffraction at the Advanced Photon Source," *Review of Scientific Instruments*, vol. 83, no. 7, July 2012.

[85] B. J. Jensen, C. T. Owens, K. J. Ramos, J. D. Yeager, R. A. Saavedra, A. J. Iverson, S. N. Luo, K. Fezzaa, and D. E. Hooks, "Impact system for ultrafast synchrotron experiments," *Review of Scientific Instruments*, vol. 84, no. 1, January 2013.

[86] M. R. Barnett, "Twinning and the ductility of magnesium alloys Part I: "Tension" twins," *Materials Science and Engineering A-Structural Materials Properties Microstructure and Processing*, vol. 464, no. 1-2, pp. 1–7, August 2007.

[87] A. Patterson, "The Scherrer formula for x-ray particle size determination," *Physical Review*, vol. 56, no. 10, pp. 978–982, November 1939.

[88] J. Ilavsky, "Nika: software for two-dimensional data reduction," *Journal of Applied Crystallography*, vol. 45, pp. 324–328, April 2012.

[89] A. Borbely, L. Renversade, and P. Kenesei, "On the calibration of high-energy X-ray diffraction setups. I. Assessing tilt and spatial distortion of the area detector," *Journal of Applied Crystallography*, vol. 47, pp. 1042–1053, June 2014.

[90] R. Brown. *fitellipse.m*. [Online]. Available: https://www.mathworks.com/matlabcentral/fileexchange/15125-fitellipse-m

[91] P. Kenesei. *DIGIgrain Manual*. [Online]. Available: https://sourceforge.net/p/digigrain/wiki/Home/

[92] D. Kalman. *General equation of an ellipse*. [Online]. Available: http://www.maa.org/external˙archive/joma/Volume8/Kalman/General.html

[93] L. Skinner, C. Benmore, and J. Parise, "Area detector corrections for high quality synchrotron x-ray structure factor measurements," *Nuclear Instruments & Methods in Physics Research, Section A: Accelerators, Spectrometers, Detectors, and Associated Equipment*, vol. 662, no. 1, pp. 61–70, January 2012.

[94] T. Gnaeupel-Herold and A. Creuziger, "Diffraction study of the retained austenite content in TRIP steels," *Materials Science and Engineering A-Structural*

Materials Properties Microstructure and Processing, vol. 528, no. 10-11, pp. 3594–3600, April 2011.

[95] S. Mohanlal, "An experimental determination of the Debye-Waller factor for iron by neutron diffraction," *Journal of Physics C-Solid State Physics*, vol. 12, no. 17, pp. L651–L653, 1979.

[96] P. Nowakowski, J. Schlenker, M. Ray, and P. Fishchione, "Sample preparation using broad Argon ion beam milling for electron backscatter diffraction (EBSD) analysis," C. U. Press, Ed., vol. 22, no. S3. Microscopy and Microanalysis, 2016.

[97] G. Tirumalasetty, M. van Huis, C. Kwakernaak, J. Sietsma, W. Sloof, and H. Zandbergen, "Deformation-induced austenite grain rotation and transformation in TRIP-assisted steel," *Acta Materialia*, vol. 60, no. 3, pp. 1311–1321, February 2012.

[98] M.-M. Wang, C. Tasan, D. Ponge, A. Kostka, and D. Raabe, "Smaller is less stable: Size effects on twinning vs. transformation of reverted austenite in TRIP-maraging steels," *Acta Materialia*, vol. 79, pp. 268–281, 2014.

[99] S. S. Hecker, M. G. Stout, K. P. Staudhammer, and J. L. Smith, "Effects of Strain State and Strain Rate on Deformation-Induced Transformation in 304 Stainless-Steel: Part 1. Magnetic Measurement and Mechanical Behavior," *Met-*

allurgical Transactions A-Physical Metallurgy and Materials Science, vol. 13, no. 4, pp. 619–626, 1982.

[100] M. Barral, J. Lebrun, J. Sprauel, and G. Maeder, "X-ray macrostress determination on texture material - use of the ODF for calculating the x-ray compliances," *Metallurgical and Materials Transactions A-Physical Metallurgy and Materials Science*, 1987.

[101] N. Koch, U. Welzel, H. Wern, and E. Mitteneijer, "Mechanical elastic constants and diffraction stress factor of macroscopically elastic anisotropic polycrystals: the effect of grain-shape (morphological) texture," *Philosophical Magazine*, 2004.

[102] B. Ortner, "Symmetry properties and transformation behaviour of the x-ray stress factor," *Journal of Applied Crystallography*, 2006.

[103] X. J. Zhang and E. Czyryca, "The effect of banded structure on the fracture behavior of a low-carbon 10% Ni steel." TMS, 2002, pp. 295–300.

[104] C. Li, L. Han, X. Luo, Q. Liu, and J. Gu, "Fine structure characterization of martensite/austenite constituent in low-carbon low-alloy steel by transmission electron forward scatter diffraction," *Journal of Microscopy*, vol. 264, no. 2, pp. 252–258, November 2016.

[105] L. Fan, D. Zhou, T. Wang, S. Li, and Q. Wang, "Tensile properties of an

acicular ferrite and martensite/austenite constituent steel with varying cooling rates," *Materials Science & Engineering, A: Structural Materials: Properties, Microstructure and Processing*, vol. 590, pp. 224–231, January 2014.

[106] M. Raghasudha, D. Ravinder, and P. Veerasomaiah, "Investigation of superparamagnetism in pure and chromium substituted cobalt nanoferrite," *Journal of Magnetism and Magnetic Materials*, vol. 420, pp. 45–50, December 2016.

[107] N. Nakada, T. Tsuchiyama, S. Takaki, and S. Hashizume, "Variant selection of reversed austenite in lath martensite," *ISIJ International*, vol. 47, no. 10, pp. 1527–1532, 2007.

[108] J. A. Rodriguez-Martinez, R. Pesci, and A. Rusinek, "Experimental study on the martensitic transformation in AISI 304 steel sheets subjected to tension under wide ranges of strain rate at room temperature," *Materials Science & Engineering, A: Structural Materials: Properties, Microstructure and Processing*, vol. 528, no. 18, pp. 5974–5982, July 2011.

[109] W. Farren and G. Taylor, "The heat developed during plastic extension of metals," *Proceedings of the Royal Society of London Series A*, vol. 107, no. 743, pp. 422–451, March 1925.

[110] G. Taylor and H. Quinney, "The latent energy remaining in a metal after cold working," *Proceedings of the Royal Society of London Series A*, vol. 143, no. A849, pp. 0307–0326, January 1934.

[111] A. Rusinek and J. Klepaczko, "Experiments on heat generated during plastic deformation and stored energy for TRIP steels," *Materials and Design*, vol. 30, no. 1, pp. 35–48, January 2009.

[112] W. Lee and C. Liu, "The effects of temperature and strain rate on the dynamic flow behaviour of different steels," *Materials Science & Engineering, A: Structural Materials: Properties, Microstructure and Processing*, vol. 426, no. 1-2, pp. 101–113, June 2006.

[113] S. Takaki, K. Ngo-Huynh, N. Nakada, and T. Tsuchiyama, "Strengthening Mechanism in ultra low carbon martensitic steel," *ISIJ International*, vol. 52, no. 4, pp. 710–716, 2012.

[114] G. Speich and P. Swann, "Yield strength and transformation substructure of quenched iron-nickel alloys," *Journal of the Iron and Steel Institute*, vol. 203, 1965.

[115] W. Rees, B. Hopkins, and H. Tipler, "Tensile and impact properties of Fe-Si, Fe-Ni, Fe-Cr, and Fe-Mo alloys of high purity," *Journal of the Iron and Steel Institute*, vol. 177, 1954.

[116] H. Kranzlein, M. Burton, and G. Smith, "Solid solution strength in iron-nickel and iron-platinum alloys," *Transactions of the Metallurgical Society of AIME*, vol. 223, no. 1, 1965.

[117] A. Di Schino and J. Kenny, "Grain size dependence of the fatigue behaviour of a ultrafine-grained AISI 304 stainless steel," *Materials Letters*, vol. 57, no. 21, pp. 3182–3185, July 2003.

[118] A. Bohner, T. Niendorf, D. Amberger, H. Hoppel, M. Goken, and H. Maier, "Martensitic transformation in ultrafine-grained stainless steel AISI 304L under monotonic loading," *Metals*, vol. 2, no. 1, pp. 56–64, March 2012.

[119] S. Oliver, T. Jones, and G. Fourlaris, "Dual phase versus TRIP strip steels: microstructural changes as a consequence of quasi-static and dynamic testing," *Materials Characterization*, vol. 58, no. 4, pp. 390–400, April 2007.

[120] S. Chatterjee and H. Bhadeshia, "Transformation induced plasticity assisted steels: stress or strain affected martensitic transformation?" *Materials Science and Technology*, vol. 23, no. 9, pp. 1101–1104, September 2007.

[121] P. Hëdstrom, L. Lindgren, J. Almer, U. Lienert, J. Bernier, M. Terner, and M. Odén, "Load partitioning and strain-induced martensite formation during tensile loading of a metastable austenitic stainless steel," *Metallurgical and Materials Transactions A-Physical Metallurgy and Materials Science*, vol. 40A, no. 5, pp. 1039–1048, May 2009.

[122] D. Steinmetz and S. Zaefferer, "Towards hultrahigh resolution EBSD by low accelerating voltage," *Materials Science and Technology*, vol. 26, no. 6, pp. 640–645, June 2010.

[123] H.-W. Yen, S. Ooi, M. Eizadjou, A. Bree, C.-Y. Huang, H. Bhadeshia, and S. Ringer, "Role of stress-assisted martensite in the design of strong ultrafine-grained duplex steels," *Acta Materialia*, vol. 82, pp. 100–114, 2015.

[124] S. Sadeghpour, A. Kermanpur, and A. Najafizadeh, "Investigation of the effect of grain size on the strain-induced martensitic transformation in a high-Mn stainless steel using nanoindentation," *Materials Science & Engineering, A: Structural Materials: Properties, Microstructure and Processing*, vol. 612, pp. 214–216, August 2014.

[125] G. B. Olson and M. Cohen, "Kinetics of Strain-Induced Martensitic Nucleation," *Metallurgical Transactions*, vol. A6, no. 4, pp. 791–795, 1975.

[126] ——, "Stress-assisted Isothermal martensitic transformation: Application to TRIP steels," *Metallurgical Transactions A-Physical Metallurgy and Materials Science*, vol. 13, no. 11, pp. 1907–1914, 1982.

[127] A. Das, "Revisiting stacking fault energy of steels," *Metallurgical and Materials Transactions A-Physical Metallurgy and Materials Science*, vol. 47A, no. 2, pp. 748–768, February 2016.

[128] R. Misra, V. Challa, P. Venkatsurya, Y. Shen, M. Somani, and L. Karjalainen, "Interplay between grain structure, deformation mechanisms and austenite stability in phase-reversion-induced nanograined/ultrafine-grained austenitic ferrous alloy," *Acta Materialia*, vol. 84, pp. 339–348, February 2015.

[129] R. Dutta, R. Huizenga, M. Amirthalingam, A. King, H. Gao, M. Hermans, and I. Richardson, "In situ diffraction studies on the temperature-dependent plane-specific elastic constants in a high-strength quenched and tempered structural steel," *Scripta Materialia*, vol. 69, pp. 187–190, 2013.

[130] N. Jia, Z. H. Cong, X. Sun, S. Cheng, Z. H. Nie, Y. Ren, P. K. Liaw, and Y. D. Wang, "An in situ high-energy X-ray diffraction study of micromechanical behavior of multiple phases in advanced high-strength steels," *Acta Materialia*, vol. 57, no. 13, pp. 3965–3977, August 2009.

[131] K. S. Choi, W. N. Liu, X. Sun, M. A. Khaleel, Y. Ren, and Y. D. Wang, "Advanced micromechanical model for transformation-Induced plasticity steels with application of in-situ high-energy x-ray diffraction method," *Metallurgical and Materials Transactions A-Physical Metallurgy and Materials Science*, vol. 39A, no. 13, pp. 3089–3096, December 2008, Symposium on Neutron and X-Ray Studies for Probing Materials Behavior held at the 137th TMS Annual Meeting and Exhibition, New Orleans, LA, March 09-September 13, 2008.

[132] B. Fu, W. Y. Yang, Y. D. Wang, L. F. Li, Z. Q. Sun, and Y. Ren, "Micromechanical behavior of TRIP-assisted multiphase steels studied with in situ high-energy X-ray diffraction," *Acta Materialia*, vol. 76, pp. 342–354, September 2014.

[133] J. Bouquerel, K. Verbeken, and B. de Cooman, "Microstructure-based model for

the static mechanical behaviour of multiphase steels," *Acta Materialia*, vol. 54, no. 6, pp. 1443–1456, April 2006.

[134] Z. H. Cong, N. Jia, X. Sun, Y. Ren, J. Almer, and Y. D. Wang, "Stress and strain partitioning of ferrite and martensite during deformation," *Metallurgical and Materials Transactions A-Physical Metallurgy and Materials Science*, vol. 40A, no. 6, pp. 1383–1387, June 2009.

[135] B. Clausen, T. Lorentzen, and T. Leffers, "Self-consistent modelling of the plastic deformation of FCC polycrystals and its implications for diffraction measurements or internal stresses," *Acta Materialia*, vol. 46, no. 9, pp. 3087–3098, May 1998.

[136] Y. Wang and E. Ma, "Strain hardening, strain rate sensitivity, and ductility of nanostructured metals," *Materials Science & Engineering, A: Structural Materials: Properties, Microstructure and Processing*, vol. 375 (special issue), pp. 46–52, July 2004.

[137] V. Vilamosa, A. Clausen, T. Borvik, B. Holmedal, and O. Hopperstad, "A physically-based constitutive model applied to AA6082 aluminum alloy at large strains, high strain rates and elevated temperatures," *Materials and Design*, 2016.

[138] O. Muransky, P. Sittner, J. Zrnik, and E. Oliver, "In situ neutron diffraction investigation of the collaborative deformation-transformation mechanism

in TRIP-assisted steels at room and elevated temperatures," *Acta Materialia*, vol. 56, no. 14, pp. 3367–3379, August 2008.

[139] R. Doherty, D. Hughes, F. Humphreys, J. Jonas, D. Jensen, M. Kassner, W. King, T. McNelley, H. McQueen, and A. Rollet, "Current issues in recrystallization: a review," *Materials Science & Engineering, A: Structural Materials: Properties, Microstructure and Processing*, vol. 238, no. 2, pp. 219–274, November 1997.

[140] Q. Zhan, T. Suo, C. Wang, K. Xie, and Z. Tang, "Temperature sensitivity and prediction of the mechanical behavior of ultrafine grain aluminum under uniaxial compression," *Acta Mechanica Solida Sinica*, vol. 27, no. 4, pp. 373–382, August 2014.

[141] E. Kroner, "Berechnung der elastischen Konstanten des Vielkristalls aus den Konstanten des Einkristalls," *Zeitschrift fur Physik*, 1958.

[142] J. Eshelby, "The determination of the elastic field of an ellipsoidal inclusion, and related problems," *Proceedings of the Royal Society of London Series A-Mathematical and Physical Sciences*, 1957.

[143] R. Hill, "The elastic behaviour of a crystalline aggregate," *Proceedings of the Physical Society of London Section A*, 1952.

[144] F. Bollenrath, V. Hauk, and E. Muller, "On calculation of polycrystalline elastic

constants from single crystal data," *Zeitschrift fur Metallkunde*, vol. 58, no. 1, 1967.

[145] P. Kovesi. MATLAB and Octave function for computer vision and image processing. [Online]. Available: http://www.peterkovesi.com/matlabfns/

Vita

Paul Keslar Lambert was born February 6, 1988 in Pittsburgh, Pennsylvania, USA. He received a B. Sc. degree in 2010 and a M. Sc. degree in 2012 from the Department of Materials Science and Engineering at the University of Maryland, College Park. He enrolled in the Materials Science and Engineering Ph. D. program at Johns Hopkins University in 2012, and received a M. Sc. degree from that department in 2015. He was awarded a Banneker/Key Scholarship from 2006-2010, an ASM International Morgan L. Williams Scholarship in 2010, a Department of Defense Science, Mathematics, and Research for Transformation (SMART) Scholarship from 2012-2017, and a Donald S. Rodbell Memorial Graduate Fellowship from 2013-2017. He was inducted into the Tau Beta Pi engineering honor society in 2009 and the Alpha Sigma Mu materials science and engineering honor society in 2011, and he received the University of Maryland, College Park's Materials Science and Engineering Department's Outstanding Senior Award

for the 2010-2011 academic year. His research focuses on developing stronger, tougher steels.

Starting in 2017, Paul will begin work at the Naval Surface Warfare Center, Carderock Division in Bethesda, Maryland, where he will be a ferrous metallurgist in the Physical Metallurgy and Fire Protection branch.

His publications and presentations related to this dissertation currently include:

Publications

P.K. Lambert, C.J. Hustedt, K.S. Vecchio, E.L. Huskins, D.T. Casem, S.M. Gruner, M.W. Tate, H.T. Philipp, A.R. Woll, P. Purohit, J.T. Weiss, V. Kannan, K.T. Ramesh, P. Kenesei, J.S. Okasinski, J. Almer, M. Zhao, A.G. Ananiadis, and T.C. Hufnagel, "Time-resolved x-ray diffraction techniques for bulk polycrystalline materials under dynamic loading," *Review of Scientific Instruments*, vol. 85, no. 9, 2014.

Research Talks and Posters

P.K. Lambert, C.J. Hustedt, A.F.T. Leong, D.T. Casem, N. Sinclair, X.J. Zhang, and T.C. Hufnagel, "*In situ* assessment of strain-induced martensitic transformation in 10% Nickel Multi-phase steels during dynamic compression," Materials Science and Technology Annual Meeting, Salt Lake City, UT, October 2016, Oral presentation.

C.J. Hustedt, **P.K. Lambert**, V. Kannan, K.T. Ramesh, N. Sinclair, D.T. Casem, J. Lloyd, R. Becker, and T.C. Hufnagel, "Deformation twinning in polycrystalline magnesium under dynamic compression," Society for Experimental Mechanics Annual Meeting, Orlando, FL, June 2016, Oral presentation.

C.J. Hustedt, T.C. Hufnagel, **P.K. Lambert**, V. Kannan, D.T. Casem, K.T. Ramesh, N. Sinclair, J.T. Lloyd, and R.C. Becker, "Deformation twinning in a polycrystalline magnesium alloy during dynamic compression," American Physical Society March Meeting, Baltimore, MD, March 2016, Oral presentation.

VITA

C.J. Hustedt, **P.K. Lambert**, E.L. Huskins, D.T. Casem, V. Kannan, K.T. Ramesh, S.M. Gruner, M.W. Tate, H.T. Philipp, A.R. Woll, T.C. Hufnagel, P. Purohit, J.T. Weiss, M. Zhao, and A.G. Ananiadis, "Sub-microsecond *in-situ* x-ray diffraction of bulk polycrystalline metals under dynamic compression," Society for Experimental Mechanics Annual Meeting, Costa Mesa, CA, June 2015, Oral presentation.

P.K. Lambert, K.S. Vecchio, E.L. Huskins, P. Kenesei, J.S. Okasinski, J. Almer, and T.C. Hufnagel, "Time-resolved x-ray diffraction of bulk metallic specimens during dynamic compression," Society for Experimental Mechanics Annual Meeting, Greenville, SC, June 2014, Oral presentation.

T.C. Hufnagel, K.S. Vecchio, **P.K. Lambert**, E.L. Huskins, P. Kenesei, and J.S. Okasinski, "*In situ* x-ray diffraction studies of polycrystalline metals under dynamic compression," Mach Conference, Annapolis, MD, April 2013, Oral presentation.